DTIC FILE COPY

PHOTOGRAPH THIS SHEET

AD-A199 279

DTIC ACCESSION NUMBER

LEVEL

1

INVENTORY

AFOSR-TR-88-1156

DOCUMENT IDENTIFICATION

17 JUNE 88

[redacted] has been approved for public release and sale; its distribution is unlimited.

DISTRIBUTION STATEMENT

ACCESSION FOR	
NTIS GRA&I	X
DTIC TAB	☐
UNANNOUNCED	☐
JUSTIFICATION	
BY	
DISTRIBUTION /	
AVAILABILITY CODES	
DIST	AVAIL AND/OR SPECIAL
A-1	

INSPECTED 4

DISTRIBUTION STAMP

DTIC ELECTE S D OCT 13 1988 E

DATE ACCESSIONED

DATE RETURNED

DATE RECEIVED IN DTIC

REGISTERED OR CERTIFIED NO.

PHOTOGRAPH THIS SHEET AND RETURN TO DTIC-DDAC

DTIC FORM 70A DEC 83

DOCUMENT PROCESSING SHEET

PREVIOUS EDITION MAY BE USED UNTIL STOCK IS EXHAUSTED.

SPATIAL LIGHT MODULATORS AND APPLICATIONS

1988 TECHNICAL DIGEST SERIES VOLUME 8

JUNE 15–17, 1988
SOUTH LAKE TAHOE, NEVADA

SECURITY CLASSIFICATION OF THIS PAGE

REPORT DOCUMENTATION PAGE

1a. REPORT SECURITY CLASSIFICATION: UNCLASSIFIED	1b. RESTRICTIVE MARKINGS
2a. SECURITY CLASSIFICATION AUTHORITY: UNCLASSIFIED	3. DISTRIBUTION/AVAILABILITY OF REPORT: Approved for public release; distribution unlimited.
2b. DECLASSIFICATION/DOWNGRADING SCHEDULE	
4. PERFORMING ORGANIZATION REPORT NUMBER(S)	5. MONITORING ORGANIZATION REPORT NUMBER(S): AFOSR-TR- 88-1156
6a. NAME OF PERFORMING ORGANIZATION: Optical Society of America; 6b. OFFICE SYMBOL (If applicable):	7a. NAME OF MONITORING ORGANIZATION: AFOSR/NE
6c. ADDRESS (City, State and ZIP Code): 1816 Jefferson Place NW, Washington, DC 20036	7b. ADDRESS (City, State and ZIP Code): Bldg 410, Bolling AFB DC 20332
8a. NAME OF FUNDING/SPONSORING ORGANIZATION: AFOSR; 8b. OFFICE SYMBOL (If applicable): NE	9. PROCUREMENT INSTRUMENT IDENTIFICATION NUMBER: AFOSR-88-0278
8c. ADDRESS (City, State and ZIP Code): Bldg 410, Bolling AFB DC 2-332-6448	10. SOURCE OF FUNDING NOS. — PROGRAM ELEMENT NO.: 61102F; PROJECT NO.: 2305/B4; TASK NO.: B4; WORK UNIT NO.:
11. TITLE (Include Security Classification): Spatial Light Modulators and Applications	
12. PERSONAL AUTHOR(S): Quinn	
13a. TYPE OF REPORT: Final REport; 13b. TIME COVERED: FROM 15-17 June TO 88	14. DATE OF REPORT (Yr., Mo., Day): ; 15. PAGE COUNT:
16. SUPPLEMENTARY NOTATION	

17. COSATI CODES			18. SUBJECT TERMS (Continue on reverse if necessary and identify by block number)
FIELD	GROUP	SUB. GR.	

19. ABSTRACT (Continue on reverse if necessary and identify by block number)

CONFERENCE WAS HELD SEE BOOKLET

20. DISTRIBUTION/AVAILABILITY OF ABSTRACT: UNCLASSIFIED/UNLIMITED ☐ SAME AS RPT. ☐ DTIC USERS ☐	21. ABSTRACT SECURITY CLASSIFICATION: UNCLASSIFIED
22a. NAME OF RESPONSIBLE INDIVIDUAL: GILES	22b. TELEPHONE NUMBER (Include Area Code): (202) 767-4931; 22c. OFFICE SYMBOL: NE

DD FORM 1473, 83 APR EDITION OF 1 JAN 73 IS OBSOLETE.

SECURITY CLASSIFICATION OF THIS PAGE

SPATIAL LIGHT MODULATORS
POSTDEADLINE PAPERS

POSTER SESSION
THURSDAY, JUNE 16, 6:00PM

PD1 Image Correlation Using a Deformable Mirror Device as a Programmable Fourier Plane Filter, James M. Florence, Texas Instruments Incorporated. Phase-only correlation filters are implemented with the Texas Instruments Deformable Mirror Device (DMD) light modulator. Experimental correlation results are compared with computer simulations to illustrate the performance characteristics of the DMD filters.

POSTER SESSION
THURSDAY, JUNE 16, 6:00PM

PD2 Optical Implementation of Association and Learning Based on Primo/Light Valve Devices, U. Efron and Y. Owecho, Hughes Research Laboratories. An outer-product associative memory system is proprosed which optically implements the learning of the association weights as well as the execution of the association operation. The simplest implementation is based on the concept of the correlation matrix associative memory. The system is based on the use of two 1-D PRIMO SLM layers as the input modulator, coupled with a liquid crystal light valve which represents the T matrix. The system can learn the relative importance of the input vectors by self-adjusting the weights of the T elements. The learning as well as the association with a given input are performed optically.

9:50AM-10:00AM
THURSDAY, JUNE 16

PD3 Multiple Quantum Well Spatial Light Modulators: Design Considerations, T. Y. Hsu, U. Efron, W. Y. Wu, and J. N. Schulman, Hughes Research Laboratories. The optimization of an MQW modulator for both phase and amplitude modulation is reported, along with preliminary structural design for a photoactivated MQW spatial light modulator.

IMAGE CORRELATION USING A DEFORMABLE MIRROR DEVICE AS A PROGRAMMABLE FOURIER PLANE FILTER

James M. Florence
Texas Instruments Incorporated
Central Research Laboratories
Dallas, Texas 75265

SUMMARY

The deformable mirror device (DMD) light modulator is a monolithic silicon integrated device that operates by the electro-static deflection of miniature mirror elements.[1] There are a variety of different mirror element structures and array sizes currently under development for different light modulating applications. For optical image processing applications, a pixel structure capable of phase modulation is of particular interest. A phase modulator can be used in the Fourier plane of a coherent optical system to implement phase-flattening filters for image correlation or other operations where manipulation of Fourier transform phase is required.

An example of a phase modulating DMD structure is the inverted cloverleaf mirror element shown in Fig. 1. The active portion of this element consists of four cantilever hinged leaflets that lie above an electrically addressable electrode integrated into the silicon substrate. Spacer material below the leaflets is removed leaving an airgap between the mirror leaflets and the electrode. When charge is placed on the electrode, the mirror leaflets deflect downward imparting a phase change to reflected light due to increased optical path length. This type of DMD element is currently being built in a 128 by 128 array that is addressable at frame rates as high as 180 Hz. The center to center mirror element spacing in this array is 50.8 μm making the entire array 6.5 mm square.

If the DMD array is placed in the Fourier plane of an optical processing system, the output will consist of a large number of output images, one for each diffraction order of the device. Assuming that the appropriate space-bandwidth-product constraints are imposed on the input to this optical processor, the (M,N)th output image will correspond to the input convolved with the effective impulse response for the (M,N)th diffraction order. In order to determine this effective impulse response, one must first determine the amplitude and phase response for a single DMD element as a function of the leaflet deflection in that diffraction order.

The DMD element response for a large number of different diffraction orders has been analyzed and verified experimentally.[2] It was found that phase modulation is found in all of the diffraction orders. However, the range of modulation is limited in the on-axis or 0,0 order due to the large percentage of non-active background associated with each DMD element. The effect of the background diminishes rapidly in the off-axis orders resulting in phase modulation over a full 2π

radians with easily attainable deflections of the mirror leaflets. The phase changes imparted by the leaflet deflections are, in all orders, coupled with amplitude changes. But, certain orders were found to exhibit strong phase changes in deflection ranges where amplitude changes were essentially flat. An example of these quasi-phase-only operating characteristics is the pixel response for the 7,4 diffraction order shown in Fig. 2. This figure shows the amplitude and phase responses as functions of the deflection at the innermost tips of the mirror leaflets. Note that in the deflection range between 0.4 and 1.0 wavelengths the phase changes by almost a full 2π radians while the amplitude varies by less than ±15%.

The existence of a quasi-phase-only operating mode of the device indicated the potential for implementation of image correlations with the DMD used as a programmable phase-only filter. To demonstrate this capability a correlator system was implemented with the DMD in the Fourier plane. The input to this system was a photographic transparency consisting of typewritten text. The DMD was operated in a binary mode between two deflection points with the same amplitude response but a phase difference of 2 radians. Deflection patterns were generated to produce binary phase-only correlation filters matched to characters in the input text transparency. The photographs shown in Fig. 3 show the impulse response of the DMD phase-only filter matched to the lower case letter "t" and a computer simulation of this type of filter. The close match between these impulse responses demonstrates very good agreement between the theoretical and experimental operation of the device. Image correlations were implemented with the DMD filter on a portion of the input transparency containing the words "to the". The optical correlation and a computer simulation of this operation are shown in Fig. 4. Again, the excellent agreement between these two images indicate the close match between theory and practice with the DMD filters.

The DMD light modulator has been shown to be very well suited for the implementation of phase modulating image correlation filters. The high frame rate capabilities and the simplicity of the electronic addressing indicate that this device can serve as the basis for an extremely powerful pattern recognition system.

REFERENCES

1. W.R. Wu, R.O. Gale, L.J. Hornbeck, and J.B. Sampsell, "Electro-Optical Performance of an Improved Deformable Mirror Device," Proc. SPIE, 825, 24 (1987).

2. J.M. Florence, M.K. Giles, and J.Z. Smith, "Operation of a Deformable Mirror Device as a Fourier Plane Phase Modulating Filter", in Digital and Optical Shape Representation and Pattern Recognition, Proc. SPIE, 938, April 1988.

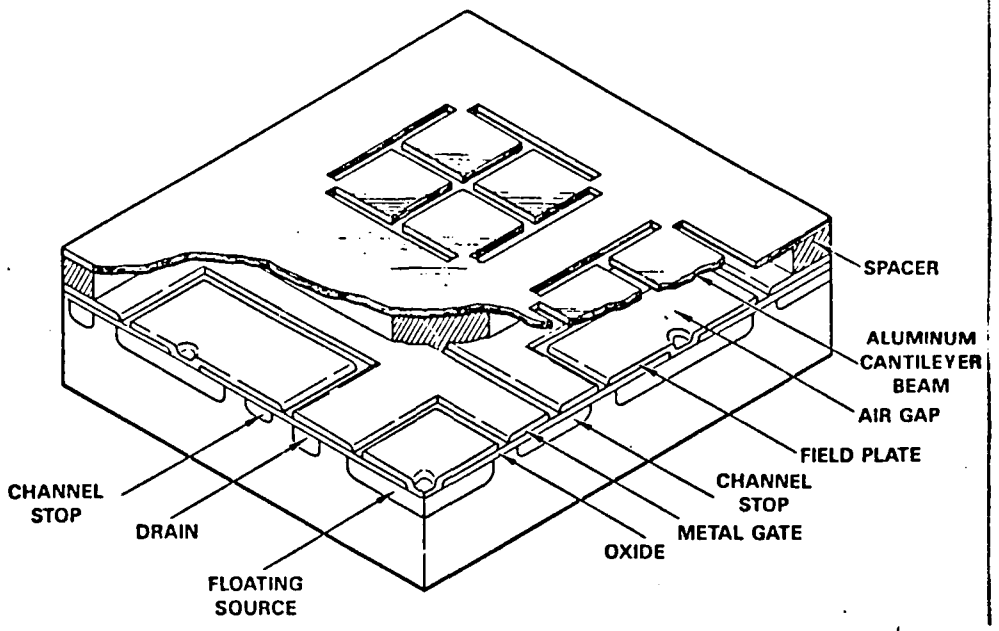

Fig. 1. Perspective view of an inverted cloverleaf DMD pixel.

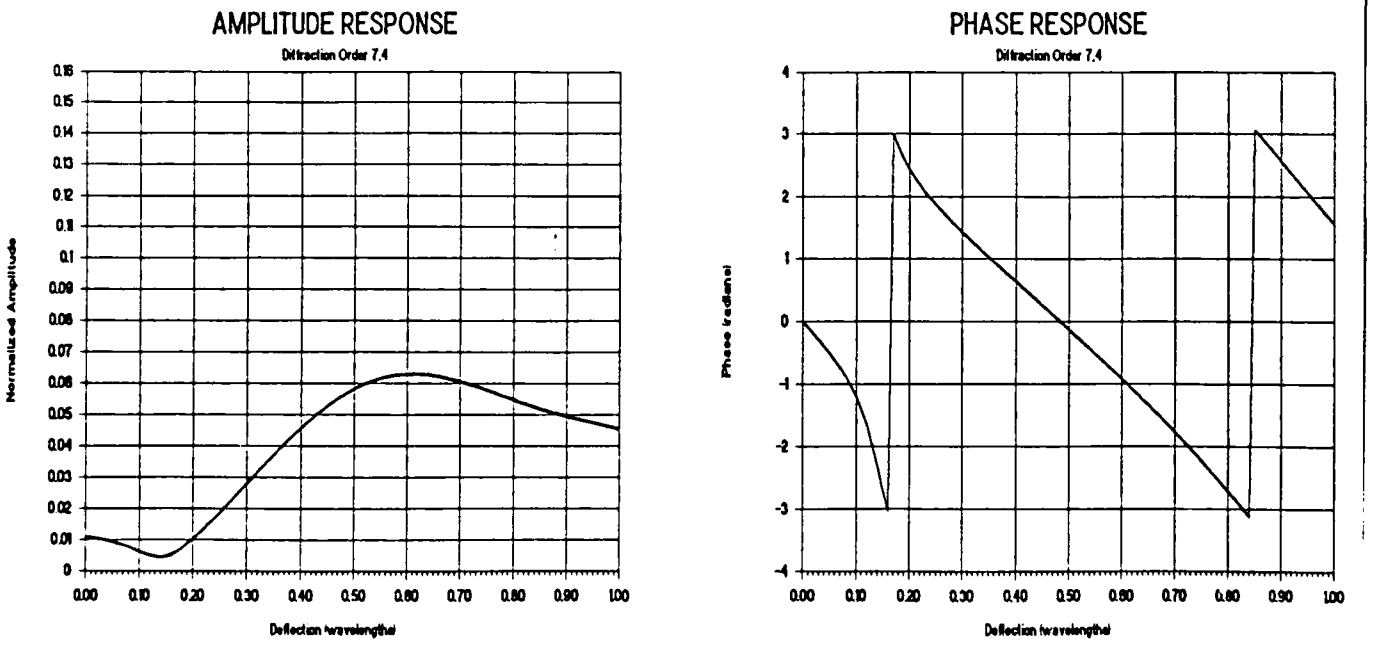

Fig. 2. Pixel response for the 7,4 diffraction order

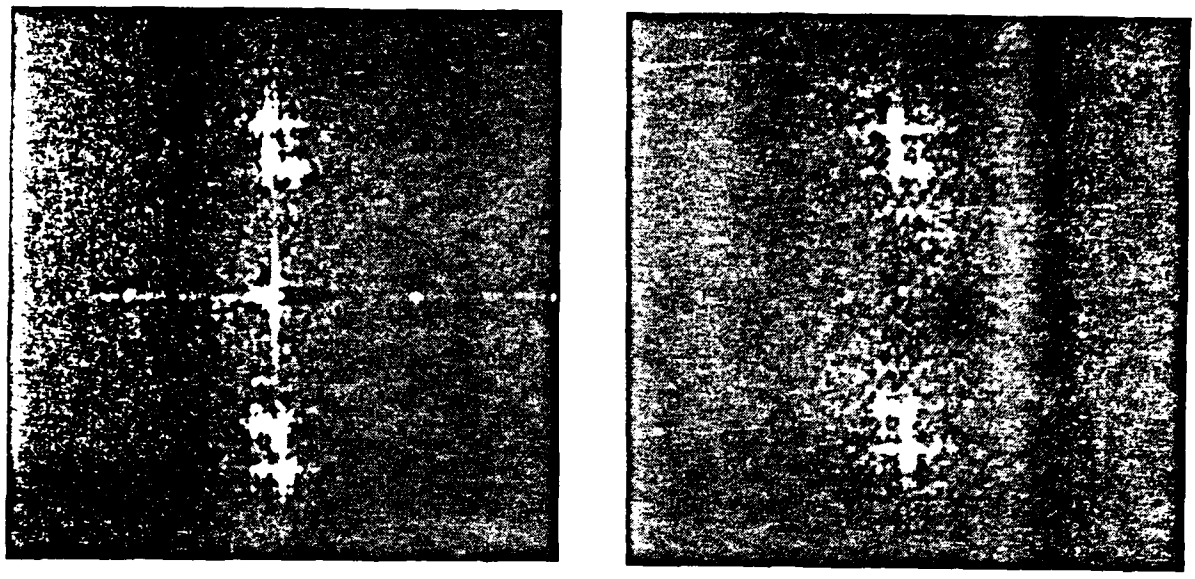

a) DMD Filter

b) Computer Simulation

Fig. 3 Comparison of DMD filter impulse reponse with a computer simulation

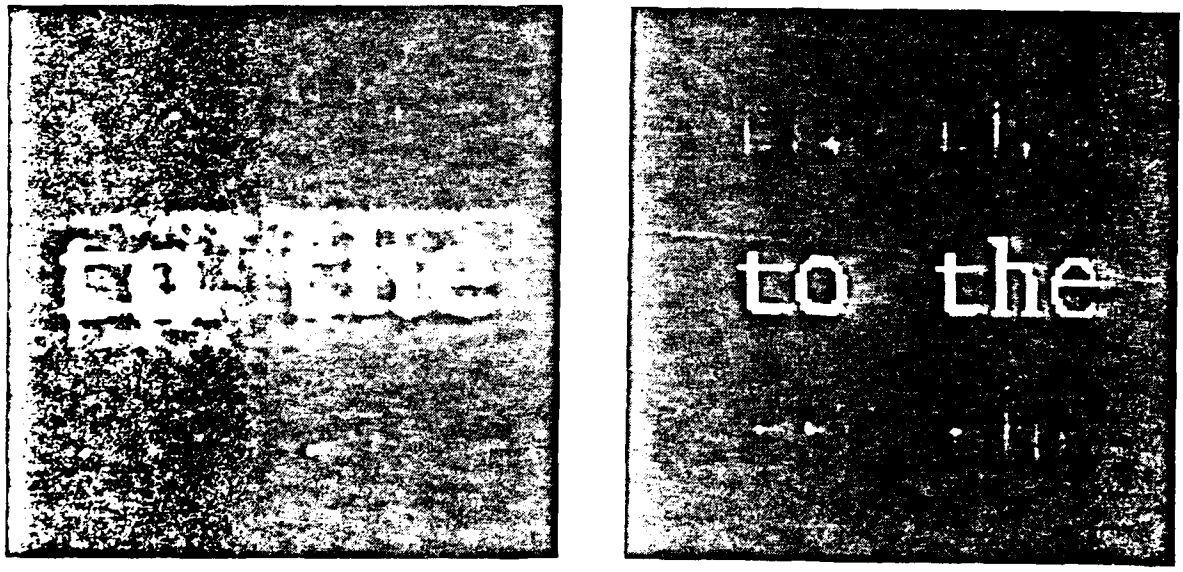

a) Optical Correlation

b) Computer Simulation

Fig. 4 Comparison of optical image correlation using DMD filter with a computer simulation

OPTICAL IMPLEMENTATION OF ASSOCIATION AND LEARNING BASED ON PRIMO/LIGHT VALVE DEVICES

U. Efron and Y. Owechko
Hughes Research Laboratories
3011 Malibu Canyon Road
Malibu, California 90265

Abstract

An outer-product associative memory system is proposed which optically implements the learning of the association weights as well as the execution of the association operation. The simplest implementation is based on the concept of the correlation matrix associative memory. The system is based on the use of two 1-D PRIMO SLM layers as the input modulator, coupled with a liquid crystal light valve which represents the T_{ij} matrix. The system can learn the relative importance of the input vectors by self-adjusting the weights of the T_{ij} elements. The learning as well as the association with a given input are performed optically.

Introduction

The effort proposed here is aimed at demonstrating the use of existing optical and electrooptical components in implementing adaptive neural network systems. Specifically, we propose a system which implements the outer product model[1,2] of auto- or hetero-association. Both learning and association operation can be executed using this system which is based on the use of 1-D striped-electrode fast input modulators (based on the PRIMO technology[3]) coupled with a time integrating photoactivated liquid crystal light valve.

The purpose of this concept is (1) to demonstrate the potential of adaptive optical systems for use as efficient parallel-addressed neural net systems, and (2) to study their capabilities and evaluate the ultimate performance expected in these implementations. The system is essentially based on three electrooptic components (Figure 1): (a) two 1-D PLZT modulators, (b) a liquid crystal light valve, and (c) a 1-D imaging detector. Linear array detectors are basically available as off-the-shelf items. As for the 1-D PLZT modulators, such devices have been under development for an optical computing PRIMO system.[3] Operation of a 64-element modulator at ~1 μSec response time was recently

demonstrated. For the integrating, photoactivated liquid crystal light valve either the CdS[4] or the silicon-based devices[5] can be used.

Structure and Operation of the PRIMO/LCLV Based Neural Net System

The main approach is shown in Figure 1. The system consists of two 1-D modulators (MOD1, MOD2) which will be based at this point on PLZT technology. These two layers will be used to construct the interconnect matrix, T_{ij}. Each of the 1-D modulators consists of striped-electrode patterns on PLZT. The two layers are oriented so that their electrodes are crossed. Thus by modulating one with a set of m vectors $U_i^{(m)}$ and the other with a set of m vectors $V_i^{(m)}$ supplied by the microprocessor, one optically forms the T_{ij} matrix as an outer-product[6,3] where:

$$T_{ij} = \sum_m U_i^{(m)} V_j^{(m)}$$

The vector elements are assumed to be ±1. The vectors $U_i^{(m)}$ and $V_j^{(m)}$ will be supplied at a relatively fast rate (≅10 μSec/vector) by the PLZT modulators. Since the LCLV has a response time of ≅10 msec, one will be able to integrate up to a few hundred outer products or vectors in this LCLV-based T_{ij} matrix. Bipolar analog T_{ij} values can be represented in PRIMO using temporal or spatial multiplexing.[3] Having completed the learning phase, the liquid crystal will be modulated with the T_{ij} information for a duration of ≅ 10 msec. During this period one can proceed with the interrogation or the association operation. A third 1-D PLZT layer (MOD3) will then input the vector $V_i^{(o)}$ to be associated. This 1-D vector, whose components are spread in the vertical dimension, will be optically multiplied by the T_{ij} (LCLV) matrix by illuminating the MOD3 modulator using the polarizing beam splitter as shown. Thus in each line, i, of the T_{ij} matrix the columns (running j) are multiplied by the (same) $V_j^{(o)}$ information. By using a cylindrical lens at the output of the beam splitter, as shown, we effectively sum:

$$\hat{V}_i = \sum_j T_{ij} V_j^{(o)}$$

for each i-line. Thus each of the i-pixels formed will correspond to the desired i^{th} component $\hat{V}_i$ of the matrix-vector product to be compared against a threshold level according to the outer-product model. This operation will be carried out by detecting the

resultant vector $\hat{V}_i$ using the linear detector and an electronic thresholder controlled by the microprocessor. To complete the association, the thresholded $\hat{V}_i$ is fed back into MOD3 and the matrix vector multiplication operation is repeated. The resultant sequence of $\hat{V}_i^{(n)}$ ($V_i^{(1)}$, $V_i^{(2)}$ ...$V_i^{(n)}$) will be tested for convergence which, once reached, will yield the closest association with the interrogating input vector, $\hat{V}_i^{(o)}$. One type of learning that this system can perform is a statistical learning as suggested by Anderson.(1) He showed that for a neuron system coupled in an auto association scheme the multiplication of the weight matrix W_{ij} by the interrogating vector $\hat{V}_i^{(o)}$ will result in the output vector being one of the stable state, with a weight which is proportional to the frequency in which this vector appeared during the learning phase.

The system can therefore learn to enhance common features which appear in different patterns during the teaching (learning) phase. Thus when a vector appearing during the interrogation phase has a feature which had appeared as a vector with a high frequency of repetition during the learning phase, the output of the system will tend to be that particular feature. The statistical learning capability is strictly true only for orthonormal state vectors. We do expect, however, that the enhancement of the T_{ij} weights associated with this effect will also occur to some extent for non-orthonormal vectors. It should be emphasized, however, that even without this interesting feature, the proposed system offers adaptive learning in the sense of learning the weights corresponding to the association of vectors U_i, V_j -- in other words, a modifiable-weight T_{ij} matrix.

Another interesting subject to be studied under this program is the possibility of using the vectors $\hat{V}_i$ obtained during the association (interrogation) phase as inputs for a new, modified T_{ij}. This opens up the possibility of demonstrating a system that would adapt itself to new state vectors (environment). this can be implemented if the interrogating vectors (which are input to MOD3 of Figure 1) are made to represent external vectors supplied by the environment which we wish to learn and recognize.

Finally, we wish to point out that an electro-optical implementation of the Hopfield-Anderson model was previously demonstrated.(7) The use of acoustooptic cells in conjunction with a 2-D spatial light modulator for similar implementation was recently suggested.(8)

References

1. J. A. Anderson et al, Psych. Rev. 84, 413 (1977).
2. J. J. Hopfield, Proc. Natl. Acad. Sci. 79, 2559 (1982).
3. B. H. Soffer et al, Appl. Opt. 25, 2295 (1986).
4. J. Grinberg et al, Opt. Eng. 14, 217 (1975).
5. U. Efron et al, J. Appl. Phys. 57, 1356 (1985).
6. R. Athale and W. C. Collins, Appl. Opt. 21, 2089 (1982).
7. D. Psaltis and N. Farhat, Opt. Lett. 10, 98 (1985).
8. A. D. Fisher et al, Appl. Opt. 26, 5039 (1987).

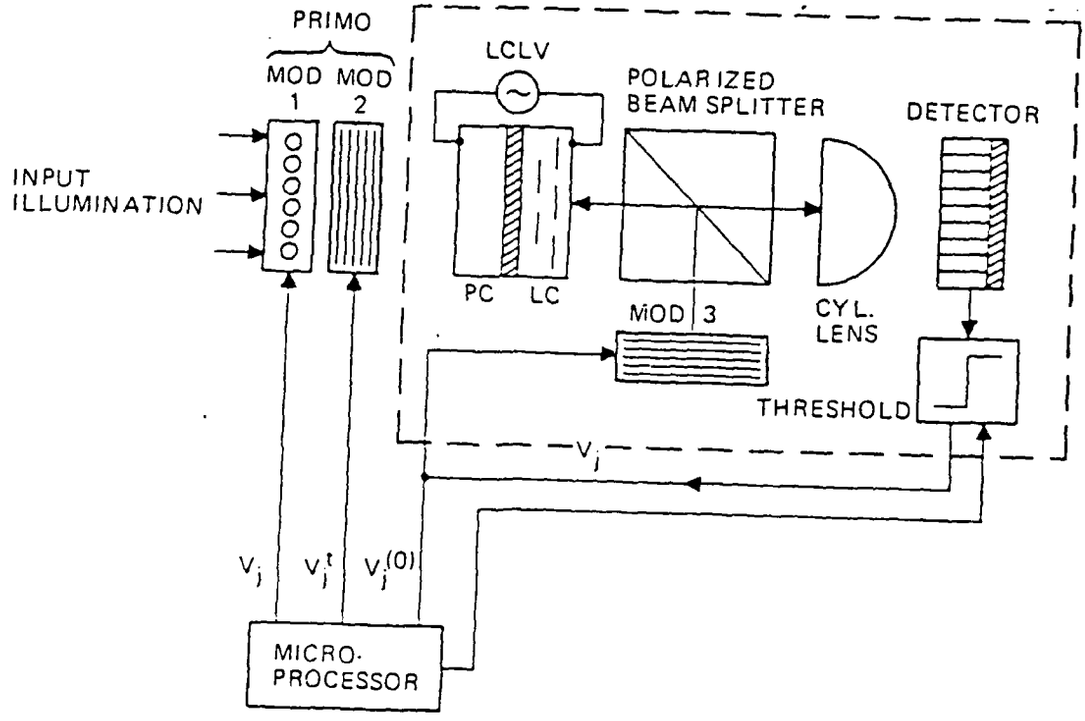

Figure 1. An optical associative memory system with learning capability using PRIMO/LCLV.

MULTIPLE QUANTUM WELL SPATIAL LIGHT MODULATORS: DESIGN CONSIDERATIONS

T. Y. Hsu, U. Efron, W. Y. Wu, and J. N. Schulman

Hughes Research Laboratories
3011 Malibu Canyon Road
Malibu, California 90265

ABSTRACT

The optimization of an MQW modulator for both phase and amplitude modulation is reported,along with preliminary structural design for a photoactivated MQW spatial light modulator.

Optimization of the MQW Modulator

The use of the multiple quantum well for spatial light modulators has rapidly progressed during the past few years.[1-4] The main advantage of this modulator is its *fast response and high electrooptic coefficient. However,* the MQW modulator is a narrow band device as its operation is based mainly on the excitonic effect resulting from the sharp and narrow exciton absorption peaks. It is nevertheless possible to design a MQW modulator to operate at almost any desired preselected wavelength by the suitable selection of the semiconductor material systems and the thickness of individual MQW layers, especially the well thickness. The strength of the exciton absorption peak in a narrow well is larger and less sensitive to electric fields than that of a wide-well structure. However, the shift of the absorption peak in the narrow well is also less sensitive to the applied field than that of the wide well. For an efficient modulator, a low applied voltage and high transmission are desirable. Thus, in view of the trade-off between the strength of absorption and the field sensitivity, we expect to have an optimum well thickness which will provide a compromise between these two factors. Shown in Table I are the results of experimental and theoretical calculation on MQW amplitude modulators of various well thicknesses; an on/off ratio of 100:1 is assumed. The results show that they all give acceptable performance, while the well thickness of $\cong$ 70 Å shows the best overall performance.

The utilization of electrorefraction in MQW phase modulation is a more complicated matter. The electrorefraction is related to the electroabsorption by the Kramers—Kronig analysis. The maximum refractive index modulation occurs at the energy level just below the zero applied field exciton absorption peak. As the applied field increases the exciton absorption is broadened, and the peak is reduced in height and shifted toward longer wavelengths. Therefore, if the probing laser wavelength is selected at the maximum refraction index modulation, the associated amplitude

Table I. Theoretical and Experimental Results on Amplitude Modulation of the MQW SLM.

WELL/BARRIER WIDTH (Å) / PARAMETER	50/50	60/60	70/70	80/80	90/90		94/94	
							THEORY	EXPRMT*
E(10^5 V/cm)	1	1	1	1	0.5	1	0.5	0.5
t (μm)	2.9	3.7	4.6	7.1	6.82	10.8	9.2	11.2
V (volts)	29	37	46	71	34.1	108	46	56
T (%)	17.6	29.5	52.5	58.7	15.3	58.3	6.3	3.5
$\alpha_{min}(cm^{-1})$	6000	3300	1400	750	2750	500	3000	3000
$\Delta\alpha$ (cm^{-1})	16000	12500	10000	6500	6750	4250	5000	4100**

Assumptions: (1) Contrast ratio = 100:1, (2) FWHM of exciton peak = 5.2 meV

* Extrapolated from data of 4 μm sample (Ref. 4).
** Possibly due to layer thickness nonuniformity and nonuniform applied field.

modulation and high absorption are unavoidable. The utilization of pure electrorefraction for a 2-D SLM may therefore become unrealistic due to the long optical path required in order to obtain a significant phase modulation. However, in applications where the low optical transmission is tolerable, a binary phase modulation can be achieved in a MQW modulator with a negligible amplitude modulation while maintaining a maximum refractive index modulation. As shown in Figure 1, a refractive index change, $\Delta n \cong 0.05$, may be obtained from a MQW modulator with 94 Å well thickness at $\lambda = 0.853$ μm as the applied electric field varies between 0 and 0.5×10^5 V/cm^{-1}. A half wavelength phase modulation may be obtained in an optical path of $\cong 8$ μm [4] (4 μm for reflective mode), which is feasible with MBE technology. The transmission of this modulator is $< 0.2\%$. A larger refractive modulation may be obtained using an MQW structure with a narrow well. As shown in Figure 2, at a well thickness of 50 Å a refractive index change of $\Delta n = 0.14$ is obtained, with a negligible absorption loss chang at $\lambda \cong 0.821$ μm, if the applied electric field is switched between 0 and 1×10^5 V/cm^{-1}. A half wavelength phase modulation may be obtained at the optical path of $\cong 3$ μm; however, the optical transmission of this modulator is still very low ($\approx 2\%$).

Photoactivated SLM Design

We have developed preliminary concepts for MQW-based spatial light modulators. These are based on both hybrid and monolithic approaches for the coupling of the

driver to the MQW modulator. The hybrid approach shown in Figure 3 is based on a GaAs substrate which is depleted by means of a metallic array of Schottky islands (e.g. tungsten) deposited and etched on its output side. Coupling to the MQW modulator is achieved via indium bumps contacting the corresponding metal pads on the modulator input side. Assuming a full depletion of the GaAs structure by back-biasing of the Schottky diode array, the photoconversion of the input image into a current pattern results in a proportional spatial voltage drop across the MQW modulator and consequently to a spatial modulation of the readout beam via electroabsorption. The monolithic approach to a photoactivated SLM is shown in Figure 4. The metallic mirror is replaced by the growth of a submicron wire grid structure over which the MQW modulator structure can be epitaxially grown. This solution allows monolithic integration of the GaAs driver to the MQW structure without the need for fabricating two separate structures. Epitaxial growth of GaAs over a submicron tungsten wire grid has been demonstrated by a group at MIT/Lincoln Laboratories.[6] The submicron wire grid structure (which is routinely produced in the Research Laboratories in periods of $d = 0.25\ \mu m$[7]) serves both as the Schottky contact and as a mirror reflecting a polarized light oriented parallel to the grid lines.

References

1. D. S. Chemla et al, Appl. Phys. Lett. 42, 864 (1983).
2. G. D. Boyd et al, Appl. Phys. Lett. 50, 1119 (1987).
3. B. F. Aull, B. E. Burke, K. B. Nichols and W. D. Goodhue, Proc. SPIE 825, 2 (1987).
4. T. Y. Hsu et al, Opt. Eng. 27, 372 (1988).
5. Y. C. Chang et al, J. Appl. Phys. 62, 4533 (1987).
6. B. A. Vojak et al, IEEE Elect. Dev. Lett. 5 , 270 (1985).
7. H. Garvin and A. Au, Proc. SPIE 240, 63 (1981).

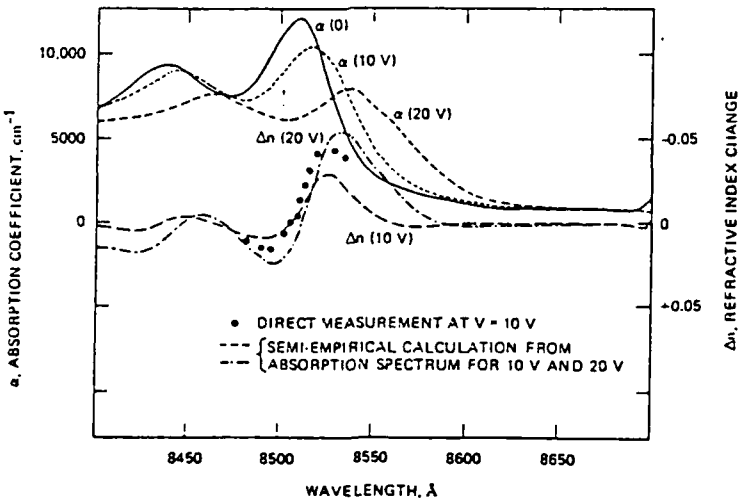

Figure 1. Experimental and theoretical results for electroabsorption and electrorefraction for a 200-period MQW structure with 100 Å / 100 Å well/barrier widths.

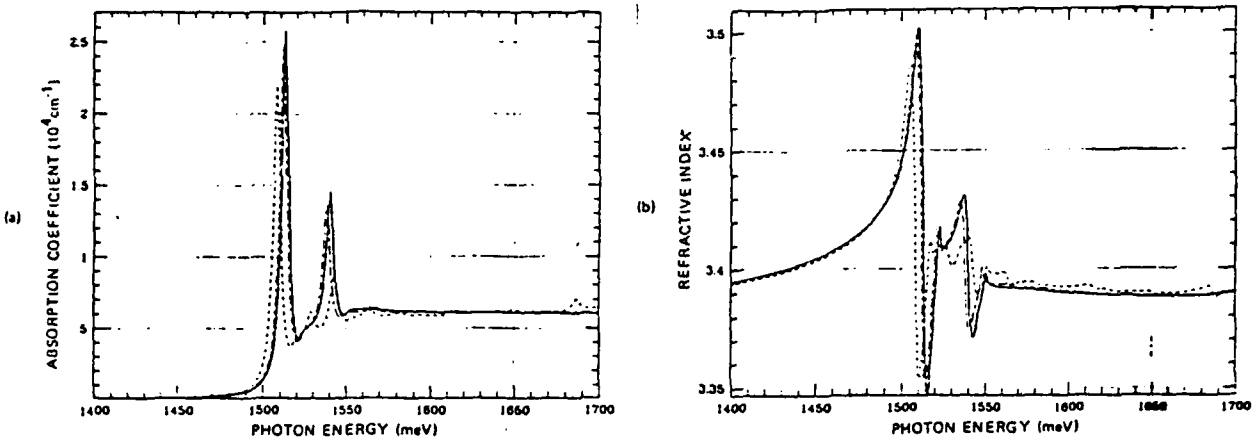

Figure 2. Theoretical results of (a) absorption spectra, and (b) refractive index spectra of 50-Å GaAs/50-Å GaAlAs MQW with applied field F = 0 (solid line), 0.5 x 10^5 V/cm (dashed-dotted line), and 1 x 10^5 V/cm (dashed line). A 5.2 meV full width at half-maximum (FWHM) of the exciton absorption peak is assumed (after Ref. 5).

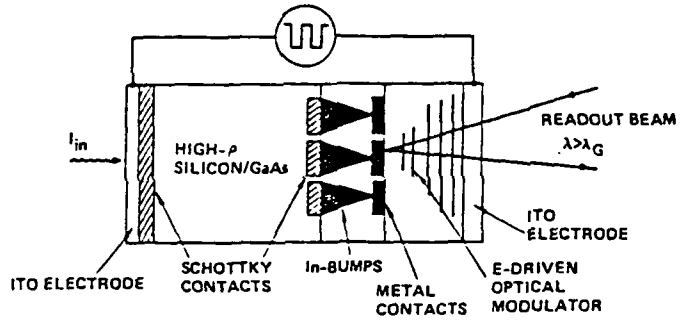

Figure 3. The photoactivated MQW-SLM: hybrid configuration, longitudinal field operation.

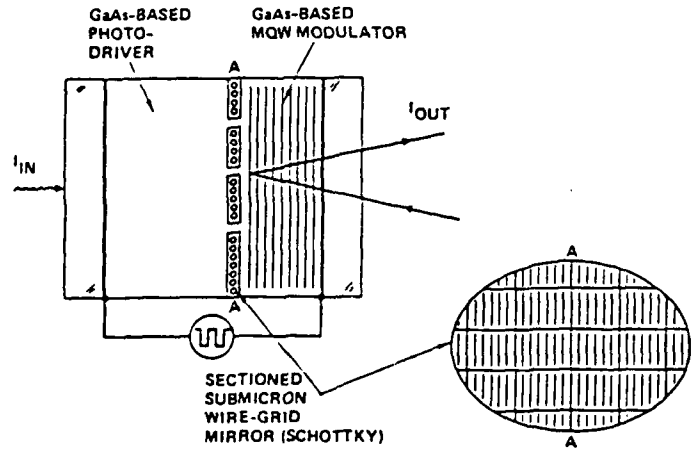

Figure 4. MQW SLM: monolithic approach using a submicrometer wire-grid interface.

SPATIAL LIGHT MODULATORS AND APPLICATIONS 1988 TECHNICAL DIGEST SERIES, VOLUME 8

CONFERENCE EDITION

Summaries of papers presented at the Spatial Light Modulators and Applications Topical Meeting

June 15–17, 1988

South Lake Tahoe, Nevada

Cosponsored by

Optical Society of America

Lasers and Electro-Optics Society of the Institute of Electrical and Electronics Engineers

Strategic Defense Initiative Organization/ Innovative Science and Technology Office

National Aeronautics and Space Administration

Office of Naval Research

Air Force Office of Scientific Research

Optical Society of America
1816 Jefferson Place, N.W.
Washington, D.C. 20036
(202) 223-8130

Articles in this publication may be cited in other publications. In order to facilitate access to the original publication source, the following form for the citation is suggested:

Name of Author(s), Title of Paper, Spatial Light Modulators and Applications, 1988 Technical Digest Series, Vol. 8, (Optical Society of America, Washington, D.C. 1988) pp. xx-xx.

ISBN Number
Conference Edition 1-55752-050-X (softcover)
Postconference Edition 1-55752-051-8 (hardcover)
(Note: Postconference Edition includes postdeadline papers.)
1988 Technical Digest Series 1-55752-045-3 (hardcover)

Library of Congress Catalog Card Number
Conference Edition 88-60862
Postconference Edition 88-60863

This work relates to a Department of the Navy Task from the Office of Naval Research. The U.S. Government has a royalty license through the world in all copyrightable material contained herein.

TABLE OF CONTENTS

PROGRAM v

WA LIQUID CRYSTAL DEVICES: 1 1

WB LIQUID CRYSTAL DEVICES: 2 23

WC PHOTOREFRACTIVE DEVICES 39

WD ELECTRO-OPTICAL DEVICES 55

WE INVITED SPEAKER SESSION 69

ThA III-V DEVICES 83

ThB DEFORMABLE STRUCTURES 101

ThC OPTO-ELECTRONIC DEVICES 119

ThD LIQUID CRYSTAL DEVICES: 3 137

ThE POSTER SESSION 159

FA APPLICATIONS: 1 207

FB APPLICATIONS: 2 225

KEY TO AUTHORS, PRESIDERS AND PAPERS 243

TUESDAY, JUNE 14, 1988

EMERALD BAY BALLROOM PREFUNCTION

6:00 PM-9:00 PM REGISTRATION/RECEPTION

WEDNESDAY, JUNE 15, 1988

EMERALD BAY BALLROOM PREFUNCTION

7:30 AM-5:00 PM REGISTRATION/SPEAKER CHECKIN

EMERALD BAY BALLROOM

8:30 AM-8:40 AM
OPENING REMARKS
Hua-Kuang Liu, *Jet Propulsion Laboratory, Conference Chair*

8:40 AM-10.20 AM
WA LIQUID CRYSTAL DEVICES: 1
Tien-Hsin Chao, *Jet Propulsion Laboratory, Presider*

8:40 AM
WA1 Schottky Diode Liquid Crystal Light Valve, Uzi Efron, W. E Stanchina, I. D. Rouse, W. Y. Wu, N. W. Goodwin, P. G. Reif, Shin-Tson Wu, M. S. Welkowsky, *Hughes Research Laboratories.* A Schottky diode liquid crystal light valve based on both silicon and GaAs has been developed. Resolution of 10 lp/mm with a contrast ratio of 10:1 was achieved in the silicon-based device. An operational GaAs-based Schottky LCLV has been demonstrated. (p. 2)

9:00 AM
WA2 Photoaddressed Liquid Crystal Spatial Light Modulators, D. Armitage, J. I. Thackara, W. D. Eades, *Lockheed Missiles & Space Company.* The development of photoaddressed spatial light modulators is discussed. Monocrystalline silicon or gallium arsenide photoadressing with nematic or ferroelectric liquid crystal readout structures is described. (p. 7)

9:20 AM
WA3 Development of an E-Beam Charge Transfer Liquid Crystal Light Modulator, Peter W. Hirsch, Ira Farber, Cardinal Warde, *Optron Systems, Inc.* An electron beam charge transfer liquid crystal light modulator is being developed. Preliminary results show great potential for optical computing displays. (p. 11)

9:40 AM
WA4 High-Performance Single Crystal Silicon Liquid Crystal Light Valve with Good Image Uniformity, K. Sayyah, M. S. Welkowsky, *Hughes Research Laboratories.* We introduce a silicon liquid crystal light valve with wavefront distortion better than λ/4 and 50% modulation at 16 lp/mm concurrent with a contrast ratio of 20:1. (p. 15)

WEDNESDAY, JUNE 15, 1988 — *Continued*

10:00 AM
WA5 Theoretical Resolution of a Thin Photoconductor Coupled Liquid Crystal Light Valve, Tae-Kwan Oh, *Sachs/Freeman Associates, Inc.;* Jack H. Davis, *U. Alabama in Huntsville;* Paul R. Ashley, *Redstone Arsenal.* A new concept of the modulation transfer function of a liquid crystal light valve has been developed. It utilizes light-induced spatial modulation of the conductivity of a thin photoconductor to predict the interfacial potential variation. (p. 19)

EMERALD BAY BALLROOM PREFUNCTION

10:20 AM-10:40 AM COFFEE BREAK

EMERALD BAY BALLROOM

10:40 AM-12:00 M
WB LIQUID CRYSTAL DEVICES: 2
Francis T. S. Yu, *Pennsylvania State University, Presider*

10:40 AM
WB1 Optimal Operation Temperature of a Si-LCLV, Shin-Tson Wu, Uzi Efron, *Hughes Research Laboratories.* The optimal operation temperature of a Si-LCLV using E-7 liquid crystal is characterized. Thermally generated dark current in the silicon photoconductor plays a significant role in determining this temperature. (p. 24)

11:00 AM
WB2 Performance Evaluation of a Transmissive Liquid Crystal Spatial Light Modulator, Shih-Chun Lin, R. Scott Boughton, *Aerospace Corporation;* John Hong, *Rockwell International Science Center;* Joe Reichman, *Grumman Corporate Research Center.* The performance of a liquid crystal SLM, fabricated by Grumman, was evaluated. Results on sensitivity, temporal response, uniformity, and resolution are presented and discussed. (p. 27)

11:20 AM
WB3 Microsecond Switching in Cholesteric Liquid Crystals, J. S. Patel, *Bell Communications Research.* The flexoelectric effect in cholesteric liquid crystals can be used to produce optical switching on a microsecond time scale. We have measured this reorientation time and found it to be independent of the magnitude of the electric field as expected. (p. 31)

11:40 AM
WB4 Real-Time Optical Edge enhancement Using a Hughes Liquid Crystal Light Valve, Tien-Hsin Chao, Hua-Kuang Liu, *Jet Propulsion Laboratory.* An edge enhancement effect obtained by using a Hughes Cd-S liquid crystal light valve is reported. Experimental demonstrations of this effect are also presented. (p. 35)

12:00 M-1:30 PM LUNCH BREAK

EMERALD BAY BALLROOM

1:30 PM-3:10 PM
WC PHOTOREFRACTIVE DEVICES
Pochi Yeh, *Rockwell International Science Center, Presider*

1:30 PM
WC1 Improved Photorefractive Performance from a Special Cut of $BaTio_3$, Joseph E. Ford, Yeshaiahu Fainman, Sing H. Lee, *UC-San Diego.* We have shown experimentally that a specially cut $BaTiO_3$ crystal provides improved gain, space-bandwidth product, and response time characteristics crucial for photorefractive spatial light modulator use. (p. 40)

1:50 PM (Invited Paper)
WC2 Spatial Light Modulation in GaAs, Li-Jen Cheng, Gregory Gheen, Tsuen-Hsi Liu, *Jet Propulsion Laboratory.* Spatial light modulation using the photorefractive effect in GaAs and its potential applications in optical processing are presented with experimental results as illustrations. (p. 44)

2:20 PM
WC3 Two-Beam Coupling Photorefractive Spatial Light Modulation with Positive/Negative Contrast in Sillenite Crystals, Abdellatif Marrakchi, *Bell Communications Research.* Photorefractive spatial light modulation with either positive or negative contrast is demonstrated. Contrast selection capability results from the particular polarization properties of Doppler-enchanced self-diffraction in sillenite crystals. (p. 48)

2:40 PM (Invited Paper)
WC4 Photorefractive Spatial Light Modulator as a 2-D Beam Steering Array, G. Roosen, *Institute of Theoretical & Applied Optics, France.* We discuss a reconfigurable $n \times n$ crossbar switch that could also perform beam steering. The first experimental results, using a photorefractive crystal, are presented. (p. 52)

EMERALD BAY BALLROOM PREFUNCTION

3:10 PM-3:30 PM COFFEE BREAK

WEDNESDAY, JUNE 15, 1988 — *Continued*

EMERALD BAY BALLROOM

3:30 PM-4:40 PM
WD ELECTROOPTICAL DEVICES
Cardinal Warde, *Massachusetts Institute of Technology, Presider*

3:30 PM
WD1 Highly Parallel Holographic Integrated Planar Interconnections, Tomasz Jannson, Shing-Hong Lin, *Physical Optics Corporation.* A planar holographic optical interconnection system is introduced, which has very high density interconnectability for communication and preserves the compatibility with monolithic electronic devices. (p. 56)

3:50 PM (Invited Paper)
WD2 Development Issues for MCP-Based Spatial Light Modulators, John N. Lee, Arthur D. Fisher, *U.S. Naval Research Laboratory.* Use of microchannel plates (MCPs) in electrooptic (MSLM) and membrane (PEMLM) modulators provides three-port operation on 2-D images, with gain, nonlinear thresholding, long-term storage and other special capabilities. (p. 60)

4:20 PM
WD3 Transfer Characteristics of Microchannel Spatial Light Moduators, Y. Suzuki, T. Hara, *Hamamatsu Photonics K.K., Japan;* M. H. Wu, *Hamamatsu Corporation.* The input-output characteristics, that is, the transfer characteristics of microchannel spatial light modulators are theoretically and experimentally discussed. (p. 64)

EMERALD BAY BALLROOM

8:00 PM-9:30 PM
WE INVITED SPEAKER SESSION
Demetri Psaltis, *California Institute of Technology, Presider*

8:00 PM (Invited Paper)
WE1 Future Roles of Spatial Light Modulators in Advanced Computing Architectures, John A. Neff, *Defense Advanced Research Projects Agency.* This paper discusses areas in which optics can address multiprocessor bottlenecks and the way in which 2-D spatial light modulators will likely play a key role. (p. 70)

8:30 PM (Invited Paper)
WE2 Recent Advances and Applications of Ferrolelectric Liquid Crystal Spatial Light Modulators, Kristina M. Johnson, *U. Colorado.* Characteristics of fast switching ferroelectric liquid crystal devices are reviewed, with emphasis on their use in optical interconnection network and neuromorphic computing. (p. 74)

WEDNESDAY, JUNE 15, 1988 — *Continued*

9:00 PM (Invited Paper)
WE3 Spatial Light Modulators: Fundamental and Technological Issues, C. Kyriakakis, P. Asthana, R. V. Johnson, A. R. Tanguay, Jr., *U. Southern California.* Fundamental physical constraints that affect spatial light modulator performance criteria are identified, against which the current status of such devices may be compared. In addition, important technological considerations that bear on certain device configurations are discussed. (p. 78)

THURSDAY, JUNE 16, 1988

EMERALD BAY BALLROOM PREFUNCTION

7:30 AM-5:00 PM REGISTRATION/SPEAKER CHECKIN

EMERALD BAY BALLROOM

8:30 AM-9:50 AM
ThA III-V DEVICES
William Miceli, *U.S. Office of Naval Research, Presider*

8:30 AM
ThA1 Spatial Light Modulators with Internal Memory, L. M. Walpita, *UC-San Diego.* A recently observed cross-modulation effect in GaAs is utilized to describe a spatial light modulator with internal memory. It has potential use in neural networks. (p. 84)

8:50 AM
ThA2 Optically Addressed Spatial Light Modulators by MBE-Grown nipi/MQW Structures, J. Maserjian, P. O. Andersson, B. R. Hancock, J. M. Iannelli, S. T. Eng, F. J. Grunthaner, *Jet Propulsion Laboratory;* K.-K. Law, P. O. Holtz, R. J. Simes, L. A. Coldren, A. C. Gossard, J. L. Merz, *UC-Santa Barbara.* Promising approaches for achieving optically driven light modulation are described. Initial results are given based on two kinds of device structure and two material systems [(In,Ga)As, (Al,Ga)As]. (p. 88)

9:10 AM
ThA3 InGaAs/GaAs and GaAs/AlGaAs MQW Spatial Light Modulators, Brian F. Aull, Kirby B. Nichols, William D. Goodhue, Barry E. Burke, *MIT Lincoln Laboratory.* We describe the fabrication and performance of charge-coupled-device-addressed spatial light modulators based on electroabsorption in MQW structures. (p. 92)

9:30 AM
ThA4 Investigation of a 1-D GaAs/GaAlAs MQW Spatial Light Modulator, J. P. Schnell, J. P. Pocholle, E. Barbier, J. Raffy, A. Delboulbe, C. Fromont, J. P. Hirtz, J. P. Huignard, *Thomson-CSF, France.* Fast SLMs are required for optical processing experiments. Elementary and 1-D GaAs/GaAlAs MQW SLMs have been investigated for this purpose. (p. 96)

EMERALD BAY BALLROOM PREFUNCTION

9:50 AM-10:20 AM COFFEE BREAK

EMERALD BAY BALLROOM

10:20 AM-11:50 AM
ThB DEFORMABLE STRUCTURES
Robert Sprague, *Xerox Palo Alto Research Center, Presider*

10:20 AM (Invited Paper)
ThB1 Deformable Mirror Device Spatial Light Modulator and its Use in Neural Networks, Dean R. Collins, Jeffrey B. Sampsell, James M. Florence, P. Andrew Penz, Michael T. Gately, *Texas Instruments, Inc.* A novel type of spatial light modulator—the deformable mirror device—is proposed as the answer to the neural network interconnect problem. (p. 102)

10:50 AM
THB2 Bistable Deformable Mirror Device, Larry J. Hornbeck, William E. Nelson, *Texas Instruments, Inc.* Operating characteristics are presented for the bistable deformable mirror device, a micromechanical, silicon-based IC spatial light modulator capable of precise, large angle deflections. (p. 107)

11:10 AM
ThB3 Limitations of Currently Available Deformable Mirror Spatial Light Modulators, Don A. Gregory, James C. Kirsch, *U.S. Army Missile Command.* Experimental limitations in light modulation using a deformable mirror spatial light modulator are discussed. These include reflectance, deflection angle, active area, and high-order diffraction effects. (p. 111)

11:30 AM
ThB4 Resolution Limits *of an* Imaging System with Incompressible Deformable Spatial Light Modulators, B. Kuhlow, G. Mahler, R. Tepe, *Heinrich-Hertz-Institut Berlin GmbH, F.R. Germany.* The behavior of deformable spatial-light-modulator materials is analyzed. Principal resolution limits caused by the incompressibility and the required imaging system are treated. (p. 115)

12:00 M-1:30 PM LUNCH BREAK

EMERALD BAY BALLROOM

1:30 PM-2:50 PM
ThC OPTOELECTRONIC DEVICES
C. Lee Giles, *U.S. Air Force Office of Scientific Research, Presider*

1:30 PM
ThC1 High-Performance TIR Spatial Light Modulator, Robert A. Sprague, William D. Turner, Mark S. Bernstein, David L. Steinmetz, David L. Hecht, Tibor Fisli, Joseph W. Kaminski, *Xerox Palo Alto Research Center;* Russell B. Rauch, *Xerox Electro-Optical Center.* We describe the design, fabrication, and performance of a 4735-element linear TIR spatial light modulator with a 256 Mpixel/s data rate. (p. 120)

THURSDAY, JUNE 16, 1988 — *Continued*

1:50 PM
ThC2 Two-Dimensional Electrically Addressed Silicon/-PLZT Spatial Light Modulator Arrays, J. H. Wang, Sadik C. Esener, T. H. Lin, S. Dasgupta, Sing H. Lee, *UC-San Diego.* An integrated 12 × 12 matrix addressed silicon/PLZT spatial light modulator array has been fabricated using laser-assisted diffusion and crystallization. *N*MOS transistors exhibiting electron mobility of 550 $cm^2/V\text{-}s$ are capable of driving the PLZT electrooptic light modulator at high speeds (100 kHz). (p. 124)

2:10 PM
ThC3 Two-Dimensional Optically Addressed Silicon/PLZT Spatial Light Modulator Array, T. H. Lin, J. H. Wang, S. Dasgupta, Sadik C. Esener, Sing H. Lee, *UC-San Diego.* An integrated optically addressed 2-D spatial light modulator array has been fabricated using laser recrystallization of silicon on PLZT. The performance of this array as well as that of the individual devices are discussed. (p. 128)

2:30 PM
ThC4 Spatially Segmented Approach to Designing Spatial Light Modulators, Ravindra A. Athale, *BDM Corporation;* Sing H. Lee, Sadik C. Esener, *UC-San Diego.* An approach to spatial light modulator design which involves lateral separation of the detector and modulator in each cell is described. Different electrode geometries allowed by this approach and their advantages are outlined. Experimental results are presented. (p. 132)

EMERALD BAY BALLROOM PREFUNCTION

2:50 PM-3:10 PM COFFEE BREAK

EMERALD BAY BALLROOM

3:10 PM-5:00 PM
ThD LIQUID CRYSTAL DEVICES: 3
Jeffrey Davis, *San Diego State University, Presider*

3:10 PM
ThD1 The Liquid Crystal Television Spatial Light Modulator: Progress, Hua-Kuang Liu, Tien-Hsin Chao, *California Institute of Technology.* the principle of operation of the liquid crystal television (LCTV) spatial light modulator (SLM) and the SLM properties of a new high-resolution research module LCTV are discussed. A comparison of this module with the Radio Shack and Epson LCTV SLMs is made. (p. 138)

3:30 PM
ThD2 Evolutionary Development of Advanced Liquid Crystal Spatial Light Modulators, N. Collings, W. A. Crossland, *STC Technology, Ltd, U.K.;* D. G. Vass, *Edinburgh University, U.K.* An overview is given of a strategy leading from two types of working liquid crystal SLM to possible future devices offering enhanced performance. (p. 142)

3:50 PM
ThD3 Ferroelectric Liquid Crystal Spatial Light Modulator: Materials and Addressing, Laura A. Pagano-Stauffer, Mark A. Handschy, Noel A. Clark, *Displaytech, Inc.* We discuss the implications and advantages of ferroelectric liquid crystal material properties for spatial light modulator performance and addressibility. (p. 147)

4:10 PM
ThD4 Development of a Spatial Light Modulator: a Randomly Addressed Liquid-Crystal-Over-*N*MOS Array, D. J. McKnight, D. G. Vass, R. M. Sillitto, *U. Edinburgh, U.K.* Electrical evaluation of a 50 × 50 pixel VLSI array in 1.5 μm *N*MOS for SLMs and the optical performance of 16 × 16 prototype SLMs are presented. (p. 151)

4:30 PM (Invited Paper)
ThD5 Nonlinear Optics of Liquid Crystals for Image Processing, Iam C. Khoo, *Pennsylvania State U.* Recently observed novel optical wave mixing effects, in conjunction with unique useful characteristics of liquid crystals throughout the visible-infrared region, offer new promises in image processing. (p. 155)

EMERALD BAY ROOMS

6:00 PM–7:00 PM
ThE POSTER SESSION/RECEPTION
Hua-Kuang Liu, *Jet Propulsion Laboratory, Presider*

ThE1 Optical Intensity and Polarization Coded Ternary Number System, Shing-Hong Lin, *Physical Optics Corporation.* An optical ternary number system is introduced, which utilizes both intensity and polarization codings for ternary combinatorial logic design and ternary arithmetical computation. (p. 160)

ThE2 Active-Matrix-Addressed Viscoelastic Spatial Light Modulator, R. Gerhard-Multhaupt, R. Tepe, W. Brinker, W.-D. Molzow, *Heinrich-Hertz-Institut Berlin GmbH, F.R. Germany.* Active-matrix addressing and spatial-frequency response of metallized viscoelastic layers are described. The results indicate satisfactory performance for light-valve and other electrooptical uses. (p. 164)

THURSDAY, JUNE 16, 1988 — *Continued*

ThE3 Pattern Recognition Utilizing Binary Light Modulators, Robert E. Hill, Donald K. Fronek, Calton S. Faller, *Louisiana Tech U.;* Richard A. Lane, *U.S. Army Missile Command.* The Optics Laboratory at Louisiana Tech University is developing capability for high-speed image processing and pattern recognition using a three-plane VanderLugt optical correlator. (p. 168)

ThE4 General Thin-Lens Action on Spatial Intensity Distribution Behaves as Noninteger Powers of Fourier Transform, Lester F. Ludwig, *Bell Communications Research.* Thin-lens action on spatial intensity distribution behaves generally as noninteger powers of the Fourier transform for separation distances within the lens-law boundary. (p. 173)

ThE5 Paper withdrawn. (p. 177)

ThE6 Paper withdrawn. (p. 178)

ThE7 Experimental Investigation of Photoemitter Membrane Spatial Light Modulator Performance Limit, Peter B. Rolsma, John N. Lee, *U.S. Naval Research Laboratory;* Tae-Kwan Oh, *Sachs/Freeman Associates, Inc.* PEMLM sensitivity and response time are enhanced by a proximity-focused visible light photocathode. Photocathodes and new membrane materials have been investigated. (p. 179)

ThE8 Application of Optical Logic on Ferroelectric Liquid Crystal Spatial Light Modulators to Neural Network Processing, Mark A. A. Neil, Ian H. White, *Cambridge University, U.K.* We discuss the use of ferroelectric liquid crystal spatial light modulators as optical polarization rotating logic elements in a direct storage implementation of the Hopfield model. (p. 183)

ThE9 Paper withdrawn. (p. 187)

ThE10 Paper withdrawn. (p. 188)

ThE11 Rotationally Invariant Joint Transform Correlation, F. T. S. Yu, S. Jutamulia, X. Li, E. Tam, *Pennsylvania State U.; Don A. Gregory, U.S. Army Missile Command.* Two methods of rotationally invariant joint transform correlation using liquid crystal televisions are described. These methods utilize multiple information-reduced references and single circular harmonics. (p. 189)

ThE12 Dynamic Interconnections with a Lenslet Array and an SLM, I. Glaser, A. A. Sawchuk, *U. Southern California.* Digital circuits can be implemented with a linear transformation and a point nonlinearity. Using a lenslet array and a mask on an SLM, we get a dynamically reconfigurable circuit. Examples are given. (p. 192)

ThE13 Real-Time Object Recognition and Classification by Code Division Multiplexed Phase-Only Encoded Filters, B. Javidi, S. F. Odeh, *Michigan State U.* A multiobject shift invariant pattern recognition system that uses code division multiplexed binary phase-only filters is presented. (p. 196)

ThE14 Spatial Light Modulators in Multimode Fibers, Mahmoud A. El-Sherif, *Air Defence College, Egypt.* An external field applied to a modified multimode fiber induces modal power redistribution. This technique is examined for spatial light modulators, and promising results are achieved. (p. 200)

ThE15 Optical Pattern Recognition using an Optically Addressed Spatial Light Modulator, Janine M. Vaerewyck, H. John Caulfield, *U. Alabama in Huntsville.* We consider the use of an optically addressed spatial light modulator in an optical pattern recognition system. A computer study conducted to determine the best use of an SLM in this type of system is discussed along with the experimental results. (p. 204)

EMERALD BAY ROOMS

7:00 PM-8:30 PM CONFERENCE BANQUET

EMERALD BAY ROOMS

8:30 PM-9:30 PM POSTER SESSION CONTINUED, COFFEE/DESSERT

EMERALD BAY BALLROOM PREFUNCTION

7:30 AM-11:30 AM REGISTRATION/SPEAKER CHECKIN

EMERALD BAY BALLROOM

8:30 AM-9:50 AM
FA APPLICATIONS: 1
David P. Casasent, *Carnegie-Mellon University, Presider*

8:30 AM
FA1 Optical Matrix-Vector Multiplication Using a Spatial Light Modulator and a Phase Conjugator, Arthur E. Chiou, Pochi Yeh, Monte Khoshnevisan, *Rockwell International Science Center.* We report concept and experimental results of an optical matrix-vector multiplication scheme using a phase conjugator in conjunction with a spatial light modulator. The finite storage time of the nonlinear medium and the optical phase conjugation are utilized to achieve automatic pixel-by-pixel alignment. (p. 208)

8:50 AM
FA2 Optical Associative Memory for Word-Break Recognition, Eung Gi Paek, A. von Lehmen, *Bell Communications Research.* A novel optical associative memory, able to identify and insert work breaks in a concatenated word string, is described. The system also has error correction capability. (p. 211)

9:10 AM
FA3 Adaptive Fraunhofer Diffraction Particle Sizing Instrument Using a Spatial Light Modulator, E. Dan Hirleman, *Arizona State U.*; Paul A. Dellenback, *Southern Methodist U.* Integration of a magnetooptic spatial light modulator into a laser diffraction particle sizing instrument is discussed. The concept gives the instrument the ability to reconfigure a detector array on-line and thereby adapt to the measurement context. (p. 217)

9:30 AM
FA4 Use of Binary Magnetooptic Spatial Light Modulators in Pattern Recognition Processors, David Flannery, John Loomis, Mary Milkovitch, *U. Dayton.* The construction and operating characteristics of binary magnetooptic SLMs are reviewed. Theoretical and experimental binary phase-only filter (BPOF) correlation results are presented to illustrate the agreement exhibited and the performance of BPOFs. (p. 221)

EMERALD BAY BALLROOM PREFUNCTION

9:50 AM-10:10 AM COFFEE BREAK

EMERALD BAY BALLROOM

10:10 AM–11:30 AM
FB APPLICATIONS: 2
Martin Sokoloski, *National Aeronautics and Space Administration, Presider*

10:10 AM
FB1 Real-Time Programmable Joint Transform Correlator with a Threshold Hard-Clipping Microchannel Spatial Light Modulator, F. T. S. Yu, Q. W. Song, *Pennsylvania State U.*; Y. Suzuki, *Hamamatsu Photonics K.K., Japan;* M. Wu, *Hamamatsu Corporation.* A programmable real-time optical joint transform correlator utilizing a threshold hard-clipping microchannel spatial light modulator to generate sharper and higher autocorrelation peaks is presented. (p. 226)

10:30 AM
FB2 Bipolar Joint Transform Image Correlator, B. Javidi, C. J. Kuo, S. F. Odeh, *Michigan State U.* We present a theoretical investigation of the bipolar joint transform image correlator. Analytical expressions for the output correlation signals of the bipolar joint transform image correlator are developed. (p. 230)

10:50 AM
FB3 Generating Tandem Coimponent Correlation Filters for Programmable Spatial Light Modulators, Stanley E. Monroe, Jr., *Lockheed Missiles & Space Company.* The iterative methods of Bartelt and Hormer for the generation of the distributed tandem component correlation filters have been adapted for use with a specific optical correlator. (p. 234)

11:10 AM
FB4 Mixed-Encoding Generalization of the Phase-Only Filter, Richard D. Juday, *NASA Johnson Space Center.* We have formulated a generalization of the phase-only filter (POF) theory that includes its concomitant amplitude modulation. The amplitude spectrum of the processed object enters the formulation, a feature missing in the classical POF. The POF solution is shown as a special case when the SLM's amplitude modulation is constant. (p. 238)

WEDNESDAY, JUNE 15, 1988

EMERALD BAY BALLROOM

8:40 AM–10:20 AM

WA1–5

LIQUID CRYSTAL DEVICES: 1

Tien-Hsin Chao, Jet Propulsion Laboratory, *Presider*

A SCHOTTKY DIODE LIQUID CRYSTAL LIGHT VALVE

U. Efron, W. E. Stanchina, I. D. Rouse, W. Y. Wu, N. W. Goodwin,
P. G. Reif, S. T. Wu, and M. S. Welkowsky
Hughes Research Laboratories
Malibu, California 90265
Tel. 213-317-5214

We have recently developed and demonstrated a Schottky-diode-based LCLV. The concept is to use a Schottky metal-semiconductor interface which allows depletion through the silicon to be attained and thus maintain the impedance match between the photoconductor and the liquid crystal. This match is critical in achieving the operation of a photoactivated SLM.[1] Since a high Schottky barrier-forming metal such as aluminum or platinum can be deposited on the n-type silicon substrate at low temperature, the silicon substrate can first be mounted on a flat glass substrate, polished, and then processed. This allows a high degree of output uniformity to be attained. Secondly, by eliminating the SiO_2 insulator present in our MOS LCLV version,[2] one can reduce the sheet conductivity at the Si/LC interface and achieve higher resolution and dynamic range.

Two Schottky LCLV configurations have been designed. A double Schottky layer structure (Figure 1), and a single Schottky configuration. The double Schottky configuration is designed to allow a balanced a.c. current to flow through the device, thus minimizing the LC decomposition which occurs due to d.c. current flow. The back (input) side Schottky diode layer (for a n-silicon based device) is fabricated using either a platinum grid or a thin platinum-layer (100 Å), followed by deposition of indium-tin-oxide to enhance the sheet conductivity of the back contact. Both structures have been fabricated and tested. The front Schottky contact consists of a metal matrix of platinum islands (17 μm x 17 μm) separated by chemical vapor

deposited oxide (3 μm channels). Results of the I-V characteristics of the Pt-nSi Schottky diode fabricated in the metal-matrix configuration are shown in Figure 2. Finally, in the single Schottky configuration, the back-contact is simply replaced by a highly doped n^+ layer similar to the back side structure of our Si-MOS LCLV.[2]

A single-Schottky diode layer LCLV was assembled and tested. Preliminary results show resolution of 10 line-pairs/mm, contrast ratio of 10:1 at the response time of the liquid crystal (≅20 mSec). A GaAs-based Schottky LCLV was also fabricated. A single Schottky configuration was also used in this case. The back contact consisted of silicon implantation ($6 \times 10^{13}/cm^2$). 2500Å of gold was used as the front side metal matrix Schottky contact on top of the 500-μm-thick 2-in. diameter n-type GaAs wafer ($\rho \approx 10^7$ Ω-cm). Due to the large thickness of the wafer and to difficulties in establishing an efficient back-side contact, the photo response was rather low. About 2 lp/mm of resolution was observed.

References

1. U. Efron, Proc. IOCC 1986 (SPIE 700, 132 (1986)).
2. U. Efron et al, J. Appl. Phys. 57, 1356 (1985).

FIGURE CAPTIONS

Figure 1. Structure of the double Schottky silicon liquid crystal light valve.

Figure 2. Forward- and reverse- bias characteristics of Pt-n Si Schottky diode fabricated in a metal matrix form.

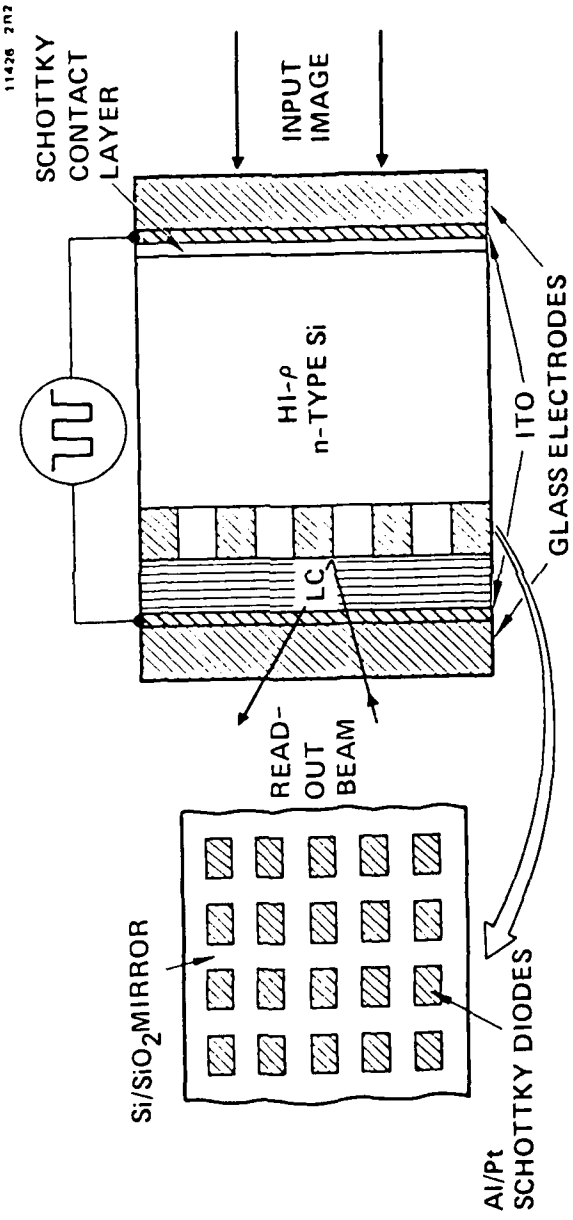
11426 2N2
SCHOTTKY CONTACT LAYER
INPUT IMAGE
HI-ρ n-TYPE Si
ITO
GLASS ELECTRODES
LC
READ-OUT BEAM
Si/SiO2 MIRROR
Al/Pt SCHOTTKY DIODES

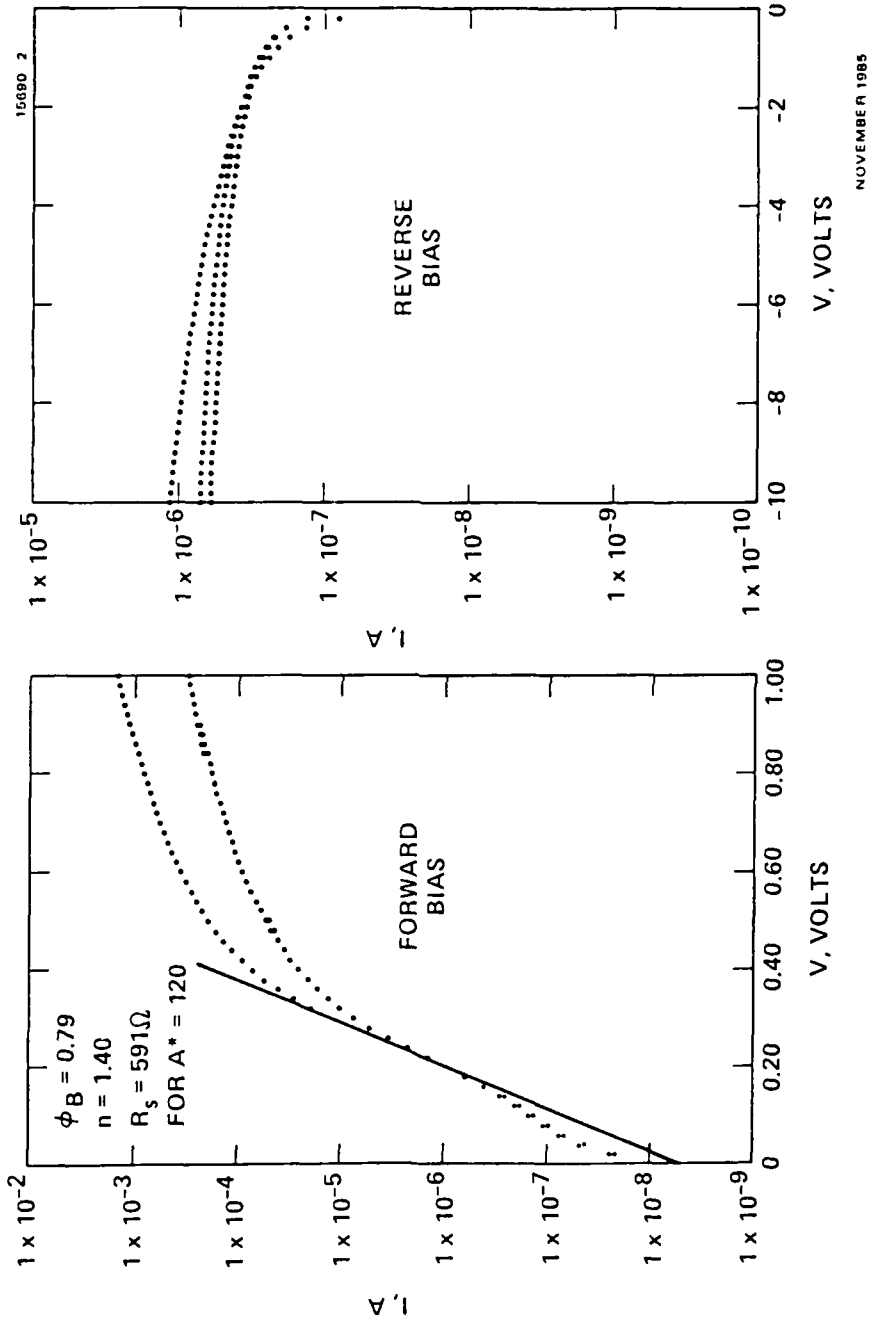
15690 2
NOVEMBER 1985
REVERSE BIAS
FORWARD BIAS
ϕ_B = 0.79
n = 1.40
R_s = 591Ω
FOR A* = 120
I, A
V, VOLTS
1 x 10^-2
1 x 10^-3
1 x 10^-4
1 x 10^-5
1 x 10^-6
1 x 10^-7
1 x 10^-8
1 x 10^-9
1 x 10^-5
1 x 10^-6
1 x 10^-7
1 x 10^-8
1 x 10^-9
1 x 10^-10
0
0.20
0.40
0.60
0.80
1.00
-2
-4
-6
-8
-10

PHOTOADDRESSED LIQUID-CRYSTAL SPATIAL LIGHT MODULATORS

D. Armitage, J. I. Thackara and W. D. Eades
Research & Development Division
Lockheed Missiles & Space Co., Inc.
3251 Hanover Street, Palo Alto, California 94304

Photoaddressed spatial light modulators (SLM) are an efficient means of modulating light with light and provide the benefits of optical parallelism in both write and read modes. Figure 1 shows the general form of a reflective-readout photoaddressed SLM. The input and output are optically isolated and the SLM can provide gain via an intense readout source. Incoherent-to-coherent light conversion is also readily achieved by the SLM.

The photoaddressed SLM structure is shown in Fig. 2. The optically flat glass substrates make up the bulk of the device. The liquid crystal layer is of order 0.01 mm thick. The photoreceptor could be a deposited photoconductor layer such as cadmium sulfide or a monocrystalline semiconducting wafer bonded to the substrate. The thickness of the photoreceptor is minimized in order to avoid compromising the SLM resolution.

There are several nematic liquid-crystal readout configurations. The hybrid-field effect mode employs a twisted structure which ensures a dark or nonbirefringent off-state, while providing a variable birefringence response. We have shown that the higher speed "surface mode" variable birefringent effect can be applied to a SLM readout[1]. If the optic axis of the nematic is aligned in the direction of the readout light as shown in Fig. 3, then a differentiating or edge enhancing readout is obtained. The basis of the effect is illustrated in Fig. 3 and is rooted in the fringe field realignment of the nematic director. Drive-on and drive-off is allowed in the differentiating nematic configuration and should provide increased frame speed in nematics.[2]

Ferroelectric liquid crystals (FLCs) have a permanent dipole moment which interacts on a first-order basis with an applied electric field, rather than the second-order response of the nematic. Therefore, the FLC can be switched between states by reversal of the electric field. FLC devices are in the early stages of development,[3] but switching speeds of 0.01 ms have already been demonstrated.

Photoconductors such as cadmium sulfide impose a limiting SLM frame rate of order 10 Hz associated with carrier detrapping times. The use of single-crystal material with low trap density is a route to higher frame rates.

Single crystal silicon and gallium arsenide photoreceptors have been used in a depletion mode configuration. The depletion mode implies the use of rectifying or blocking contacts rather than ohmic contacts. We have demonstrated a silicon-wafer photoreceptor structure based on capacitive

coupling which simplifies the fabrication and assembly process[1]. The fabrication of silicon-wafer devices is sensitive to the surface processing and passivation techniques.

We are investigating the behavior of gallium arsenide photoreceptors as an alternative to silicon. GaAs is available at much higher resistivity than silicon and the surfaces are less sensitive to processing and fabrication methods. However, GaAs has trap states in the bulk of the material in addition to surface traps. The frame speed of the SLM is compromised by such states.

A capacitively coupled GaAs-photoaddressed SLM was fabricated by cementing a polished wafer to a substrate and depositing a dielectric mirror composed of silicon oxide/amorphous silicon multilayers. Uniform parallel alignment of the nematic liquid crystal was provided by rubbed nylon surfaces. The nematic was configured in the high-speed surface mode readout[1]. The resolution demonstrated by the GaAs-photoaddressed SLM is shown by the USAF test target in Fig. 4, where 14 lp/mm is discernible. The image shown in Fig. 4 is taken from a TV camera, where the camera resolution is a limiting factor. The uniformity of this device is impressive and probably follows from the low leakage of the GaAs.

The frame rate of the device is slower than that achieved in silicon wafer addressing[1] and appears to be limited by the detrapping time constants of the GaAs. Further work is needed to establish the optimum form and inherent limitations of GaAs in this application.

A similar GaAs photoaddressing structure was used with a perpendicularly aligned nematic readout providing edge enhancement. The input image and edge-enhanced output are shown in Fig. 5.

We have experimented with FLC readout of various photoaddressing structures. The FLC is much more difficult to align than the well-known nematic liquid crystal. This is reflected in defects and nonuniformity in the output image. However, there appear to be other complications in the substitution of FLC for nematic readout. Transient imaging and image-blooming effects not present in the nematic are apparent in the FLC-photoaddressed devices. This behavior may be due to the sensitivity of the FLC to spurious dc components in the photoaddressing scheme.

A recent development in FLC technology employs the electroclinic effect to provide a linear birefringent response.[4] This effect trades sensitivity for increased response speed. Submicrosecond response speeds have been demonstrated. We are studying this effect in the context of photoaddressed SLMs.

---

1. D. Armitage et al., SPIE 824, 1987
2. D. Armitage and J. I Thackara, SPIE 613, 1986, p. 165
3. D. Armitage, J. I. Thackara, and W. D. Eades, SPIE 825, 1987
4. C. H. Bahr and G. Heppke, Liquid Crystals, 2, 825 (1987)

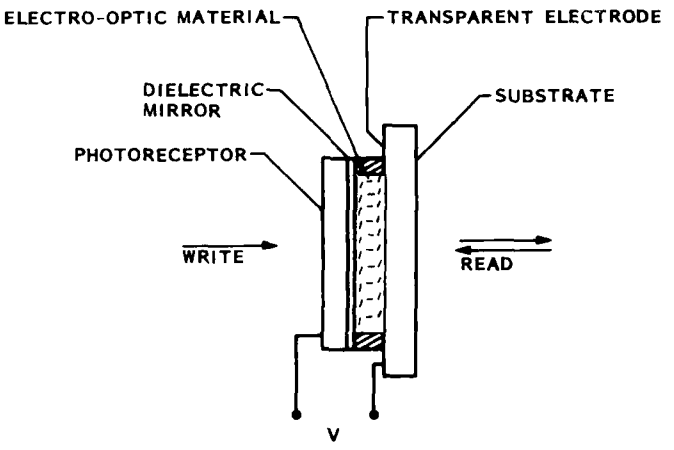

Fig. 1 Reflective-readout photoaddressed spatial light modulator

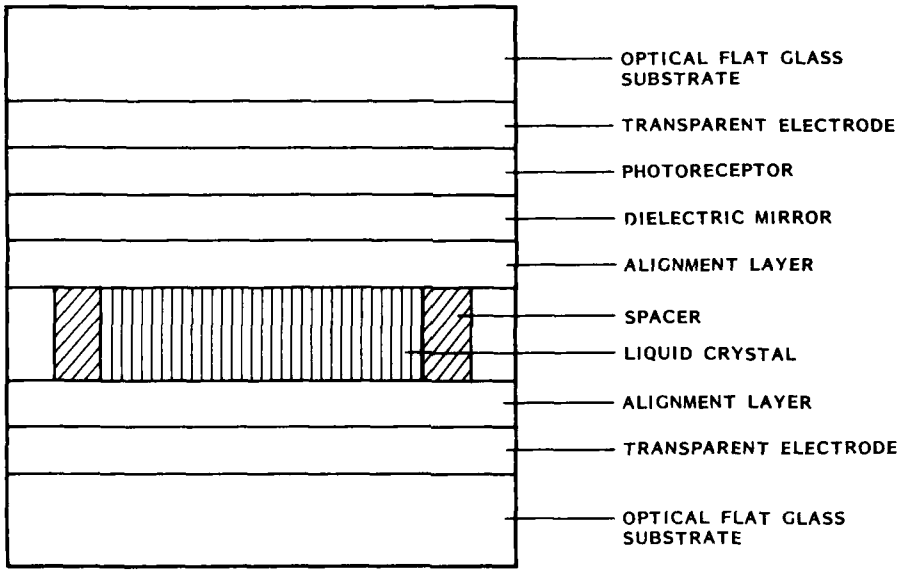

Fig. 2 Photoaddressed liquid-crystal spatial light modulator structure

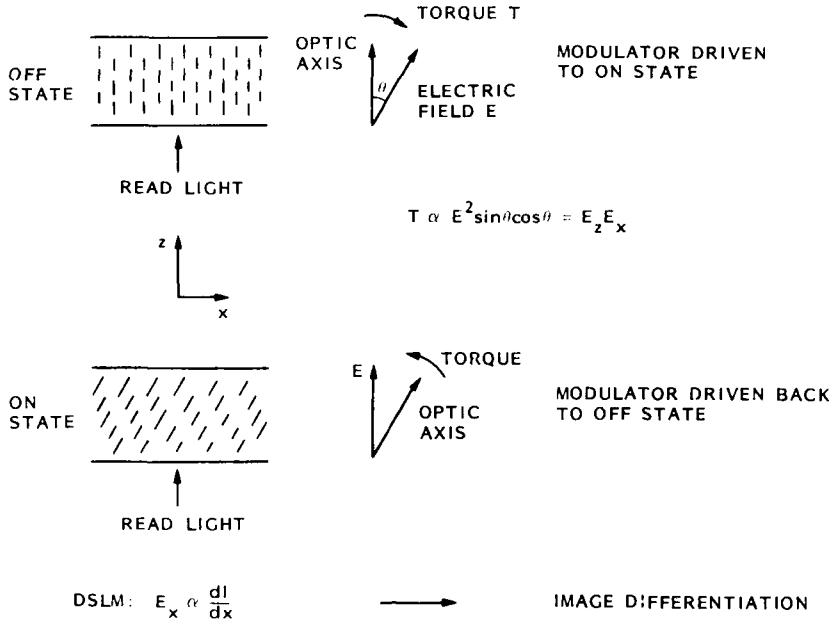

Fig. 3 Nematic liquid-crystal spatial differentiating configuration

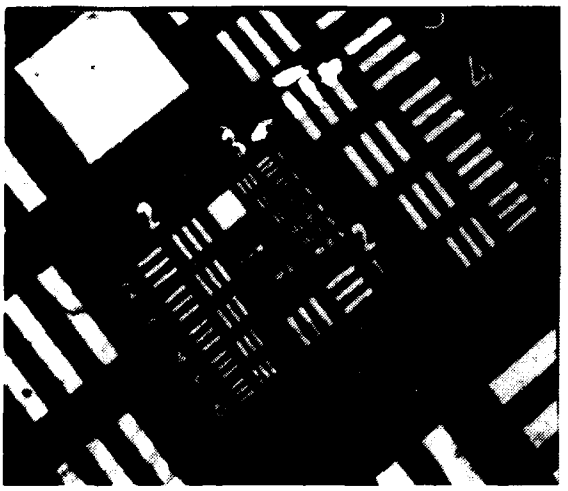

Fig. 4 Gallium arsenide photo-addressed nematic liquid-crystal SLM readout with USAF test target input

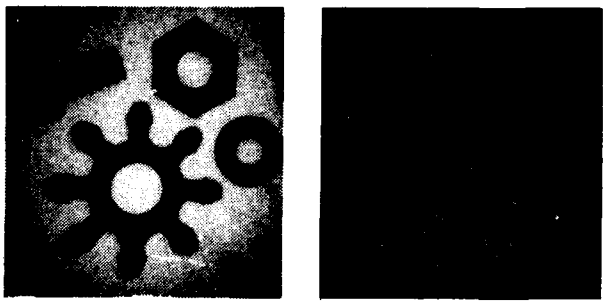

Fig. 5 Gallium arsenide photo-addressed nematic liquid-crystal differentiating SLM. Input image and edge-enhanced readout image.

Development of an e-Beam Charge-Transfer Liquid Crystal Light Modulator

Peter W. Hirsch, Ira Farber, Cardinal Warde
Optron Systems, Inc.
3 Preston Court
Bedford, MA 01730

An electron beam charge transfer liquid crystal light modulator is being developed and demonstrated. Preliminary results show great potential for optical computing displays.

INTRODUCTION

We have recently developed a computer-programmable, electron-beam-addressed liquid crystal light modulator (e-beam LCLM) which should have a broad range of applications in optical computing, displays, and robotic vision.

Some of the significant advantages of this device over existing commercial units include low cost, ease of fabrication, and potentially very high resolution. The simplicity of the device, which has very few layers associated with the liquid crystal, makes it relatively easy to fabricate very uniform liquid crystal layers. This could otherwise add significantly to the cost of manufacturing and ultimately to the cost of the device. High modulator resolution is achieved through the use of a high-resolution electron gun which is inexpensive and very common in many types of CRTs. The charge transfer plate, a proprietary Optron Systems invention, is an integral part of this device. It bridges the gap between vacuum and air, allowing for the high resolution transfer of charge to the modulator element which is a liquid crystal in this particular application.

DEVICE DESCRIPTION

The general design of the device is shown in Fig. 1. The modulator consists, esentially, of a high resolution electron gun tube assembly sealed to charge transfer plate (CTP) face plate. A grid is situated just inside the CTP for electron collection during the writing and erasing processes which utilize the secondary emission characteristics of the CTP surface. The liquid crystal is confined in a thin layer exterior to the tube body by the external surface of the CTP and an optically flat readout window coated with a transparent conductive coating of indium-tin-oxide (ITO). The readout window also has an alignment layer deposited over the ITO in the same fashion as the CTP. Either microspheres or glass fibers of the appropriate thickness can be used as spacers for the liquid crystal layer.

The CTP, which is illustrated in Fig. 2, consists of conductive longitudinaly extending pins interspersed throughout an insulative matrix so that electrical isolation is maintained between the pins. CTPs with 10μm pins on 14μm center-to-center spacing and 50μm conductors on 70μm centers are routinely fabricated at Optron Systems. Once charged, these conductive pins can then create an electric field across the modulating element (liquid crystal here) when an electrode is placed over the element and suitably biased.

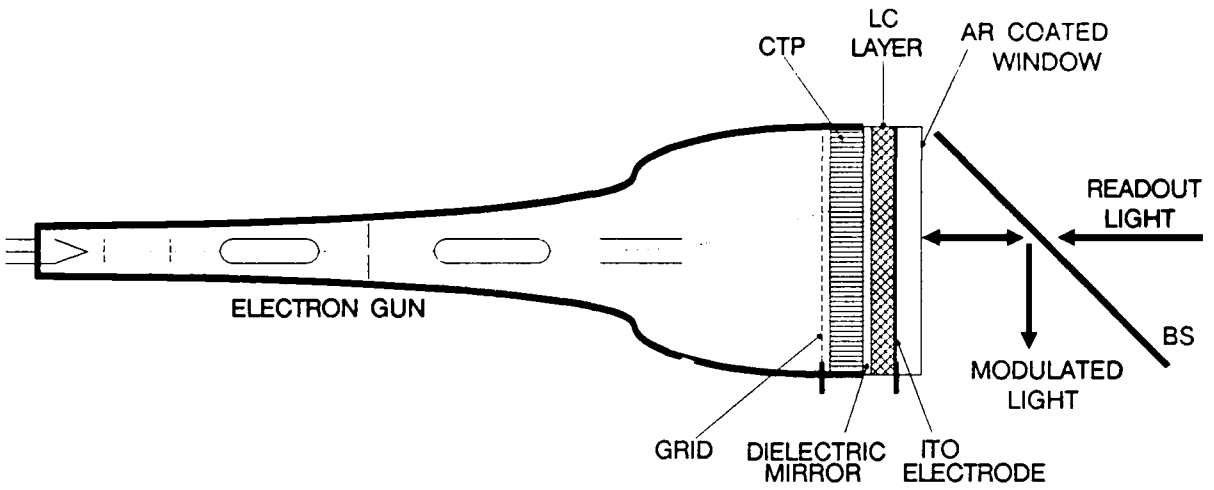

FIGURE 1: THE e-BEAM CHARGE TRANSFER LIQUID CRYSTAL LIGHT MODULATOR AS A SEALED OFF TUBE ASSEMBLY.

The CTP is polished flat on both surfaces and a dielectric mirror is deposited over its outer surface (away from the electron gun) to obtain a high reflectance. An alignment layer is then deposited over the dielectric mirror. This alignment layer consists either of a polymer material which is spun on and then buffed or of a layer of SiO which is evaporated at a grazing angle. Alignment for this particular liquid crystal device was parallel to the surface (homogeneous alignment).

The electron gun is driven by off-the-shelf high voltage power supplies and electronics for focussing and deflection. The driver electronics are in turn controlled by a specially designed board which inserts into an IBM PC. This board can drive the electron gun in either a vector or raster mode and allows images to be impressed onto the modulator either from the memory of the PC or from electronic image pick-up devices such as CCD or vidicon cameras.

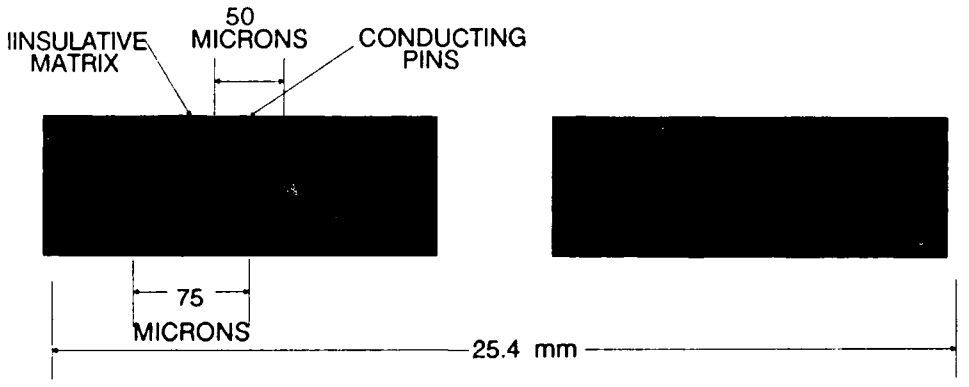

FIGURE 2: A CROSS SECTION OF THE CHARGE TRANSFER PLATE (CTP).

PRINCIPLE OF OPERATION

During operation of the modulator a small bias voltage (± 10 volts) is applied to the transparent electrode of the liquid crystal cell and the electron beam generated by the e-gun is scanned over the CTP in a pattern generated by the PC hardware and software. The resulting charge distribution created on the CTP surface is transferred through the CTP by means of its conductive pins to the liquid crystal interface. The charge distribution generated at the liquid crystal interface may be either positive of negative depending on the secondary electron emission characteristics of the CTP.

The charge patterns (images) are erased using the secondary emission process with the mesh grid operating as an electron collector. During this process the entire CTP can be flooded with electrons of a particular energy, while the externally applied voltage to the conductors is ramped back to zero volts, thus erasing the image.

PRELIMINARY RESULTS / FEASIBILITY STUDY

The preliminary results presented below were obtained with a prototype e-beam LCLM which employed a CTP with 50μm conductors on 70μm centers, and a high-resolution, electrostatically focussed and deflected Tektronix electron gun. Typically this e-gun is used in high resolution monitors and has a spot size of approximately 75-100μm. However, our actual spot size was somewhat larger, on the order of 250 microns, because we operated the gun with a cathode potential (-4kV) that was lower than the recommended values. The beam current of the e-gun is rated at 1-10μ/A but our output again fell short of this expected value due to in-house cathode activation. The operating current which was found to be necessary for liquid crystal modulation was on the order of 500nA. Control of the electron gun drive electronics was through a personal computer equipped with a specially designed board which vector scans the beam according to the software instructions (see Fig. 3). This provides a user-friendly system for generating modulation patterns on the liquid crystal device.

Our prototype device was fabricated with the CTP polished flat to λ/4 across its 18mm active area and an off-the-shelf window with approximately 10 fringes across its surface. A nematic liquid crystal used (a biphenyl, E-7 from Atomergic Chemetals). Alignment was accomplished through a spun on coating of polyimide from Merck Industries and spacers were 5μm spherical particles. The hybrid field effect mode[1,2] was used in this device due to its low off-state transmission, high on-state transmission, and rapid response time. On this particular device, no dielectric mirror was used; we simply relied on the surface reflection from the shiny CTP conductors. During operation, a signal generator provided a 1kHz sinusoidal signal to the transparent ITO electrode on the liquid crystal side of the readout window.

A representative sample of our preliminary data is shown in Figure 4 where we have written "OPTRON" onto the device. As mentioned earlier, the active area is 18mm in diameter so it is apparent that our resolution is limited by the electron gun to approximately 2 lines/mm. The framing speed of the prototype device currently appears to be limited by the low gun current to only a few Hz. The resolution and framing speed problems will be resolved by choosing a gun that offers a smaller spot size at low cathode potentials. The contrast and spatial uniformity of this early device will both be enhanced by flatter liquid crystal layers though the use of precision flat windows. We have routinely fabricated large-area, single-pixel liquid crystal cells with good spatial uniformity and greater than 40:1 contrast ratio so we are confident that rapid improvements will be forthcoming in the next few weeks.

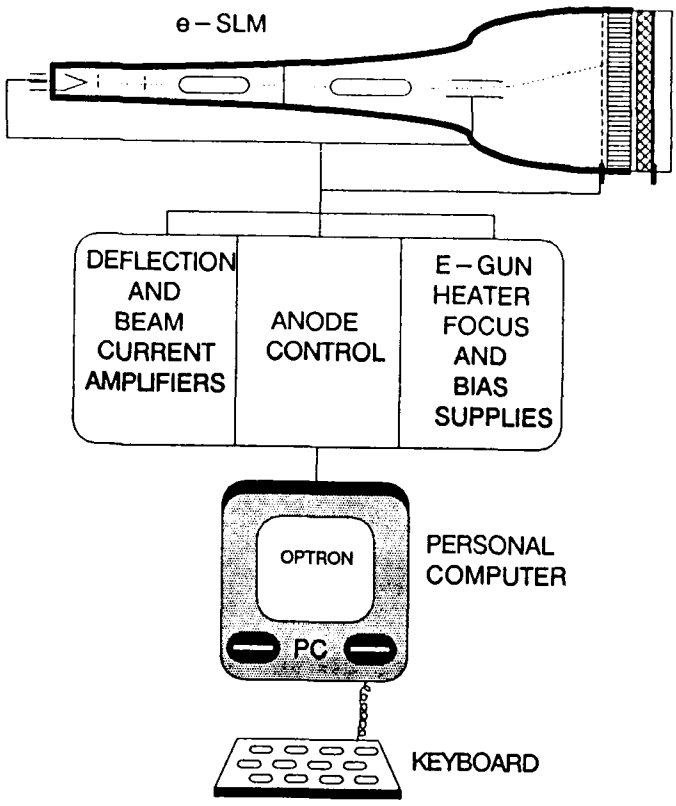

FIG. 3: SCHEMATIC OF ELECTRON GUN SLM WITH DRIVE ELECTRONICS AND PC CONTROL.

FIG. 4: EXAMPLE OF OUTPUT IMAGE FROM LCLM.

SUMMARY

A new type of liquid crystal light modulator has been developed at Optron Systems which holds great promise for the fields of optical computing and display technology. We have presented preliminary data which demonstrate feasibility and show the great potential for this device. With continuing refinements, the device should rival others in spatial resolution, contrast, speed, and cost. Central to the device design is the CTP which makes possible this type of device. The CTP can be easily scaled to larger diameters which would further improve the information capacity of the e-beam LCLM.

Device development is ongoing in several areas including resolution, contrast, speed and scalability. Improvements in resolution will result from the use of a higher resolution electron gun and implementation of 10μm-conductor CTP into the device. Speed should also be enhanced greatly by using an electron gun with a higher output current in order to more quickly erase charge from the CTP. We are also investigating the use of enhancer coatings over the CTP in order to tailor its secondary emission characteristics to the electron beam energy. Higher contrast will be achieved through the use of flatter, more parallel liquid crystal layers. Ferroelectric liquid crystals can also be incorporated into this device to realize kilohertz framing rates and improved contract ratio.

REFERENCES

1. Jan Grinberg, et. al., *Optical Engineering*, **14**, 217-225 (1975).
2. C. H. Gooch, H. A. Tarry, *J. Phys. D: Appl. Phys.*, **8**, 1575-1584 (1975).

High Performance Single Crystal Silicon Liquid Crystal Light Valve with Good Image Uniformity

K. Sayyah and M.S. Welkowsky

Hughes Research Laboratories
3011 Malibu Canyon Road
Malibu, CA 90265

Introduction

Spatial light modulators play the role of converting an input image written in certain wavelength, intensity and coherence conditions to an output image in which some or all of these parameters are varied. As image amplifiers, these devices can be used for large screen display applications while as image wavelength converters, they can be used for displaying visible images from IR scenery or for missile testing. For optical image processing applications, spatial light modulators can be used as incoherent-to-coherent image converters.

In all these applications, input sensitivity, spatial resolution, contrast, speed of response and output image uniformity are key parameters for a spatial light modulator. Different versions of the Hughes Single Crystal Silicon Liquid Crystal Light Valve (Si-LCLV) have been shown to meet almost all the above requirements and have been used as large screen display devices [1], IR dynamic image converters [2] and optical data processing devices [3]. The only exception has been the uniformity of the output image.

In this paper, we introduce a modified version of the Si-LCLV with good output image uniformity which not only maintains the high performance capabilities of its predecessors, but also provides means for improved performance.

Experimental

The nonuniformity of the output image of the Si-LCLV has been due to warpage of the unsupported 5 mils Si wafer used in this device. This warpage gives rise to subsequent nonuniformities in the thickness of the light modulating liquid crystal layer, hence the output image. The new device structure consists of chemically bonding a Si wafer 10-12 mils thick to a special glass substrate which has a thermal expansion coefficient similar to that of Si using a technique called electrostatic bonding [4]. After bonding, the Si wafer can be thinned and polished to the desired thickness and flatness using conventional chemomechanical polishing techniques. Flatnesses of $\lambda/4$ or better can routinely be obtained as shown by the interferogram in Fig. 1. The Si wafer is then processed for light valve fabrication with the limitation that all processing steps be performed below 700°C in order to maintain the flatness. Thus, many of the processing steps mentioned in detail in Ref. 1 for the conventional Si-LCLV have been changed in lieu of lower temperature ones. These include the use of only photoresist instead of a combination of photoresist and field oxide for implant masking, lower annealing temperature of the implants and the use of a low temperature gate insulator instead of the high temperature thermal oxide. We have shown that both Plasma Enhanced CVD (PECVD) and anodic SiO_2 have electrical properties approaching those of the state-of-the-art thermal oxides after a low temperature anneal step [5], and thus can be used in this device. The structure of this modified device is shown in Fig. 2.

The modified Si-LCLV was evaluated for its resolution, contrast, speed of response and input sensitivity. A scanning detector with a 25 μm pinhole in conjunction with an Air Force resolution target fabricated on the input side of the device were used for resolution measurements.

Results and Discussion

The modulation transfer function (MTF) of a Si-LCLV fabricated using our new low temperature process is shown in Fig. 3. This device had 20 μm center-to-center microdiodes with gaps of 3 μm between them implanted into the Si surface. The purpose of these microdiodes, which are merely n-type regions embedded in the Π-Si substrate, is to create surface potential wells to hold the photogenerated charge [1]. A 1500 Å PECVD SiO_2 was used as the gate insulator. Modulation was defined as $(I_{max}-I_{min})/(I_{max}+I_{min})$ and no normalization was performed. Thus all modulation values are absolute. The data in Fig. 3, indicates that 50% modulation occurs at 14 ± 1 lp/mm. The limiting resolution is about 30 lp/mm, while the dc contrast ratio with the device operating at the conditions mentioned in Fig. 3 is 20:1. This operating point is not quite optimum for best concurrent resolution and contrast as will be shown shortly.

The resolution and contrast of the Si-LCLV is strongly dependent on the various operating parameters of the device. These parameters are the depletion phase voltage (V_D) and duration (T_D), accumulation phase voltage (V_A) and duration (T_A) and the input light intensity (I_L). As discussed in detail in Ref. 1, this device basically works as an MOS capacitor which is deep depleted in the depletion phase wherein the photogenerated charge is swept to the Si/SiO_2 interface resulting in change in the liquid crystal bias. The accumulation phase is essential in preventing the total collapse of the deep depletion and hence loss in resolution through recombination of excess charge carriers. We have found that both the resolution and contrast are extremely sensitive to most of the above parameters, in particular to the accumulation voltage and pulse width. The dependence of the modulation at 16 lp/mm and the contrast ratio on the accumulation voltage are shown in Figs. 4 and 5, respectively. As noticed from these two figures, an increase of only 2 volts in the accumulation voltage above 25 V significantly reduces both the modulation at 16 lp/mm from close to 45% to 35% and the contrast ratio from about 20:1 to only 9:1. Figs. 4 and 5 also indicate that modulation levels close to 50% at 16lp/mm are possible with this device concurrent with contrast ratios of 20:1. The drop in the modulation level with increasing accumulation voltage above 24 V is due to the sharp drop in the contrast which in turn is due to the shift in the effective liquid crystal dark state bias. This bias is very sensitive to the accumulation voltage because during this phase a major portion of the accumulation voltage drops across the liquid crystal layer. Similar dependencies of the resolution and contrast on the other operating parameters will be shown and discussed in detail. Also the effect of 10 μm microdiodes and no microdiodes on device performance will be discussed.

The response time of the modified Si-LCLV was measured by using a pulsed red LED as the input excitation source. Basically, the response time of this device is limited by that of the liquid crystal layer which is a function of its material parameters and thickness [6]. The rise time of the liquid crystal also varies with its effective bias voltage, decreasing with increasing voltage. As expected, the fall time of this device was not dependent on the operating parameters and was measured to be about 16 mS for a liquid crystal layer 4 μm thick. The rise time of the device, however, was strongly dependent on the operating parameters, in particular the accumulation voltage and the input light intensity. The dependence of the device rise time on the input light intensity at 730 nm is shown in Fig. 6. As expected, the

rise time decreases with increasing input light intensity due to increase in the liquid crystal bias voltage in the on state. The input sensitivity of this device was measured to be about 10 $\mu W/cm^2$ at 730 nm excitation of the red LED.

Besides much improved output image uniformity, another advantage of our new approach is the added ability to reduce the Si thickness below 5 mils while maintaining yield and flatness. Theoretical calculations have indicated that reducing the Si thickness from 125 μm to 20 μm should improve the device resolution from 19 to 26 lp/mm at 50% modulation for a liquid crystal thickness of 4 μm [7]. This issue will be discussed.

Conclusion

We have introduced a modified version of the Hughes Si-LCLV which is capable of high resolution, contrast, speed of response and input sensitivity in conjunction with a very uniform output image. Wavefront distortions less than $\lambda/4$ have been achieved using our new device processing scheme. 50% modulations at 15-16 lp/mm and a limiting resolution of 30 lp/mm have been observed concurrent with contrast ratios of 20:1. Speed of response is limited by that of the liquid crystal layer. Rise times of less then 4 mS and fall times of 16 mS have been measured. The device input sensitivity at 730 nm was about 10 $\mu W/cm^2$. The resolution and contrast of the device was found to strongly depend on the various operating parameters.

References

[1] U. Efron, J. Grinberg, P.O. Braatz, M.J. Little, P.G. Reif and R.N. Schwartz, J. Appl. Phys. 57(1985)1356

[2] U. Efron, S.T. Wu, J. Grinberg and L.D. Hess, Opt. Eng. 24(1985)111

[3] M.S. Welkowsky, U. Efron, W. Byles and N.W. Goodwin, Opt. Eng. 26(1987)414

[4] P.R. Younger, J. Noncryst. Sol. 38 &39(1980)909

[5] K. Sayyah, to be presented in the Electrochem. Soc. Meeting in May 1988, Atlanta Ga.

[6] U. Efron, S.T. Wu and T.D. Bates, J. Opt. soc. Am. B 3 (1986)247

[7] Y. Owechko, Hughes Research Laboratories Internal Research Report 1985

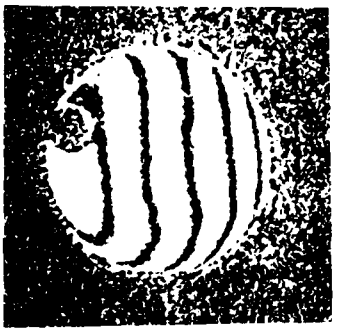

Fig. 1 Interferogram of an electrostatically bonded and flattened Si wafer showing flatness of $\lambda/10$ in the central region

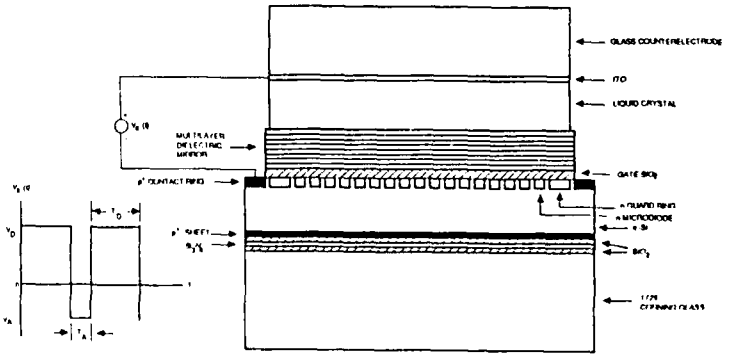

Fig. 2 Structure of the modified Si LCLV

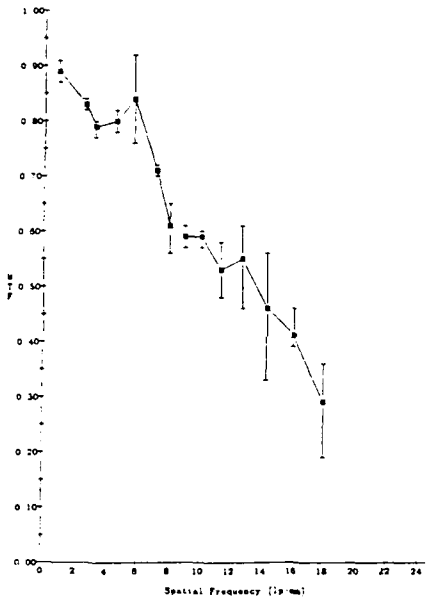

Fig. 3 Modulation Transfer Function (MTF) of a modified Si-LCLV operated at V_{μ}=20 V. T_{μ}=395 μS. V_{A}=-25 V. T_{A}=25 μS. I_{L}=38 $\mu W/cm^2$

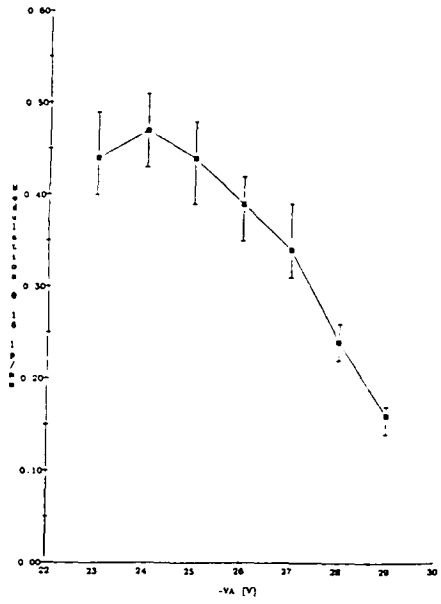

Fig. 4. Dependence of the modulation at 16 lp/mm on the accumulation voltage.

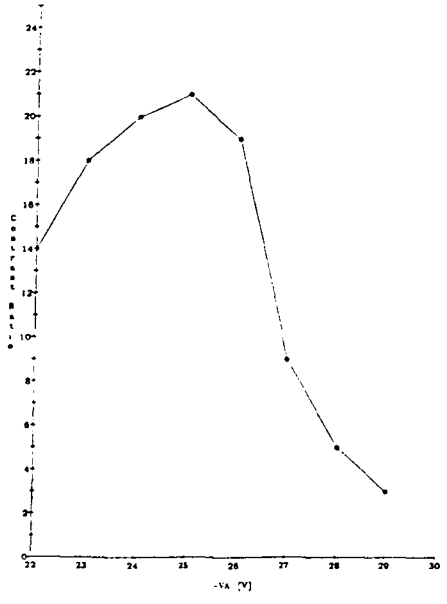

Fig 5 Dependence of the contrast ratio on the accumulation voltage

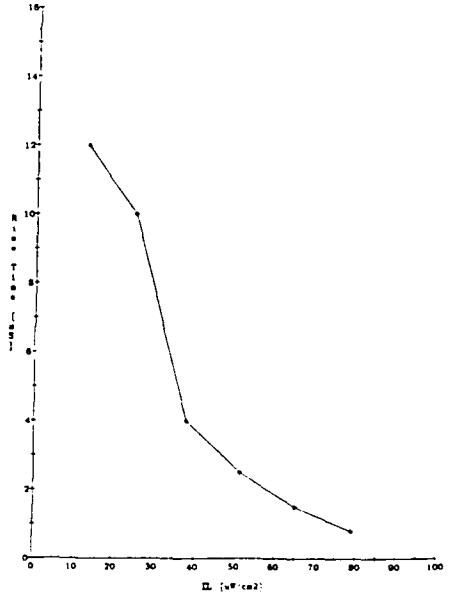

Fig 6 Dependence of the device rise time on the input light intensity at 730 nm

Theoretical Resolution of a Thin Photoconductor Coupled Liquid Crystal Light Valve

Tae-Kwan Oh

Sachs/Freeman Associates, Inc.
1401 McCormick Drive, Landover, MD 20785

Jack H. Davis
Department of Physics
University of Alabama in Huntsville, Huntsville, AL 35899

Paul R. Ashley
Research Directorate
Research, Development, and Engineering Center
Redstone Arsenal, AL 35898-5248

The hydrogenated amorphous silicon(a-Si:H) photoconductor and the nematic liquid crystal BDH-E44 combine to create a liquid crystal light valve(LCLV). The transmission of the readout light is determined by the voltage across the liquid crystal. When write light illuminates the current carrying photoconductor, the potential of each layer is rearranged through the photoconductor and liquid crystal.

A theoretical model for electrooptic modulation used to determine spatial resolution was developed by Roach [1] and later extended for use on 2 mm thick $Bi_{12}SiO_{20}$(BSO) LCLV [2]. Roach's model assumes an interface surface charge distribution of the form $\sigma_N \cos(\pi Nx)$ on a dielectric material represented by liquid crystal. Only dielectric effects of the photoconductor and liquid crystal are considered, and the image transfer from the input light to the charge distribution at the interface is assumed to be ideal with no charge spreading in the photoconductor. This implies a very high resistivity of the photoconductor. Owechko and Tanguay [3] predict the theoretical resolution of Pockels Readout Optical Modulator, which is a function of electrostatic field distribution arising from the stored point charges located within the BSO. Another important parameter is a bias voltage which does not affect the resolution in the Roach's model that is proved by Donjon, et al. [4].

In the case of thin(a few microns thick) photoconductors, the effects of losses due to the resistivity of the material cannot be neglected. In fact the resistivity itself is essentially the parameter which is modulated. Most of the photogenerated carriers are transitted through the photoconductors; it is supposed that the sum of drift lengths, l_c, before recombination is equal to or greater than the photoconductor thickness. For the thick photoconductor, space charges may be located inside the layer and we can apply the Owechko and Tanguay method. The applicable criterion for our model is the collection length which is expressed by

$$l_c = (\mu_p \tau_p + \mu_n \tau_n) E . \quad (1)$$

The sum of $\mu\tau$ product was determined to be 8.1×10^{-8} cm^2/V for the intrinsic amorphous silicon by photoelectromagnetic effect in blue or green light by Moore [5], and $1\text{-}6 \times 10^{-8}$ cm^2/V for the p$^+$-i-n$^+$ a-Si:H photodiode in AM1 white light by Crandall [6]. With 10 V dc bias, and a uniform field approximation [7], the collection length is about 9 μm for the intrinsic amorphous silicon. For thickness less than 9 μm, the loss of the resistivity of photoconductor directly causes a voltage shift across the liquid crystal.

A new model was used to determine spatial resolution, and was developed based on the previous arguments and criteria, and from a lumped element analysis of the equivalent circuit [8]. The modulator was divided into 2-D matrix of unit cells, each represented by equivalent values of its physical parameters, resistivity and capacitance. This generalized analysis allows the determination of potential and field throughout the liquid crystal as a result of any 2-D geometry or distribution of physical parameters imposed on the modulator structure. In order to evaluate the resolution, a step function of photoconductor resistivity is imposed on the photoconductor with the spatial wavelength which is defined by the reciprocal of spatial frequency S lp/mm. Then the output intensity as a function of spatial position x is given by

$$I^{\pm} = I_0 \sin^2 \left[\frac{\pi V}{2 V_\pi} \left(1 + \frac{V_s}{V_0} \alpha^{\pm} \right) \right] , \quad (2)$$

$$\text{where} \quad \alpha^{\pm} = \begin{cases} 1, & 0 \le x \le 1/2S \\ -1, & 1/2S \le x \le 1/S . \end{cases}$$

The amplitude of the potential variation across the liquid crystal in the x direction along the interface is V_s. The value of V_s was obtained numerically by the same method. The result is normalized to S to obtain V_s/V_0. When the liquid crystal light valve is operated in the near linear region of transmission, the value of V/V_π becomes 0.5 [9]. The normalized contrast transfer function is then given by

$$CTF = (I^+ - I^-) / (I^+ + I^-) . \quad (3)$$

Finally the MTF can be calculated from the conversion of CTF [10].

Figure 1 shows the amplitude of potential variation across the liquid crystal as a function of spatial frequency. Leftmost and rightmost points represent the middle of half spatial wavelength, dark and bright patterns, and the x scale represents 50, 10, 5, 2.5 and 1.25 μm for 5, 25, 50, 100 and 200 lp/mm spatial frequency. Here d and L are the thickness of LC and a-Si:H respectively. It is clearly shown that the potential variation V_s is decreased as spatial frequency is increased.

It is pointed out that the normalized modulation transfer function and unnormalized modulation transfer function have direct

interpretations useful for comparison of different parameters of the device. The light transmission of a LCLV is mostly determined by the potential across the liquid crystal. The unnormalized contrast transfer function is defined, considering the sublinear region of light transmission of a liquid crystal, as

$$CTF_v = (V_b - V_d) / (V_b + V_d) \qquad (4)$$

where V_b and V_d are the potentials at the middle of bright and dark step spatial wavelength patterns. The result in Figure 2 shows that the LCLV with a larger thickness of a-Si:H and a smaller thickness of the liquid crystal give more CTF_v. It might be interpreted as a measure of the sensitivity of the device. This unnormalized contrast transfer function indicates the manifest effect of dark conductivity of a-Si:H even in the low spatial frequency as shown in Figure 3.

For the 5 μm thick amorphous silicon with 64 $\mu W/cm^2$ white light, the calculated MTF is shown in Figure 4. Here $\rho_A = 2.6 \times 10^9$ ohm-cm and $\rho_L = 1.6 \times 10^9$ ohm-cm with 10 V dc bias, and the photoconductivity change is about 2.3. Values of the liquid crystal thickness of 6.25, 12.5 and 25 μm were used. For d = 12.5 μm, 50% MTF occurs at around 37 lp/mm. Up to 50 lp/mm are predicted for d = 6.25 μm with 50% MTF.

Roach's model [1] neglects the resistivity and thus holds in the high frequency limit. Our model neglects the dielectric constants and thus holds in the low(temporal) frequency limit. Thus neither is connected, although Roach's model(high frequency) and our model(low frequency) are based on the same form of the Laplace equation, which is applied to each layer separately. But Roach's model is confined to surface charge and dielectic properties, while our model utilizes spatial conductivity variation, which gives direct potential values at the interface. The resistive model of the MTF in the LCLV neglects the dielectric effect in the dc bias, which might change the charge at the interface. With an ac bias the dielectric constants should be considered.

REFERENCES

1. W. R. Roach, IEEE Trans. Electron Devices ED-21, 8(1974).
2. P. Aubourg, J. P. Huingnard, M. Hareng and R. A. Mullen, Appl. Opt. 21, 3706(1982).
3. Y. Owechko and A. R. Tanguay, Jr. Proc. SPIE 202, 110(1979).
4. J. Donjon, M. Decaesteker, B. Monod, and R. Petit, Acta Electonica, 18, 187(1975).
5. A. R. Moore, Appl. Phys. Lett. 37, 327(1980).
6. R. S. Crandall, Appl. Phys. Lett. 44, 537(1984).
7. R. S. Crandall, J. Appl. Phys. 53, 3350(1982).
8. Tae-Kwan Oh, Ph.D. Thesis, "The a-Si:H Photoconductor Coupled Liquid Crystal Light Valve," Univ. of Alabama, Huntsville(1987).
9. P. R. Ashley and J. H. Davis, Appl. Opt. 26, 241(1987).
10. J. W. Coltman, J. Opt. Soc. Am. 44, 468(1954).

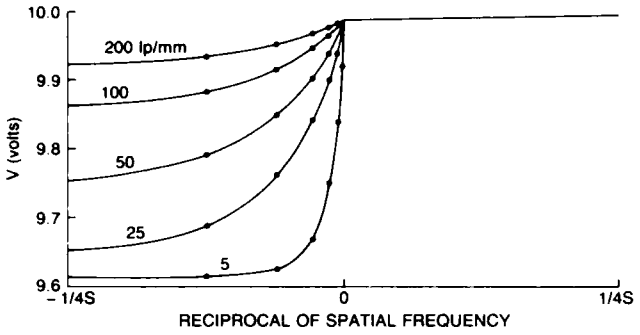

Fig. 1 - Potential Variation across the Liquid Crystal as a Function of the Reciprocal of Spatial Frequency. The d = 12.5 μm, L = 5 μm, ρ_A = 5E9 Ω cm, and ρ_L = 5E10 Ω cm. The Photoconductivity change is 100.

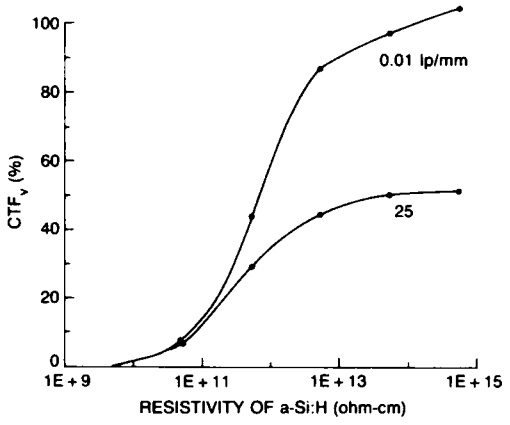

Fig. 3 - Unnormalized Contrast Transfer Function of the Dark Resistivity of a-Si:H. The d = 12.5 μm, L = 2 μm, and ρ_L = 5E10 Ω cm.

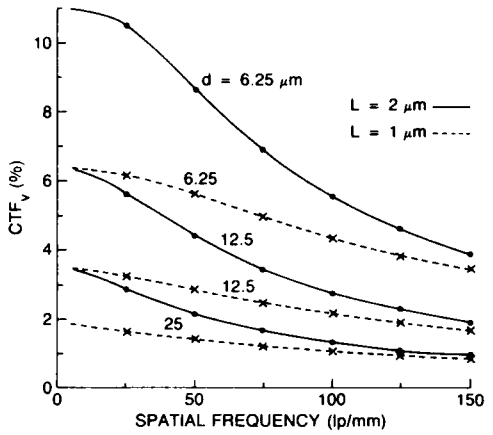

Fig. 2 - Unnormalized Contrast Transfer Function for Liquid Crystal Light Value

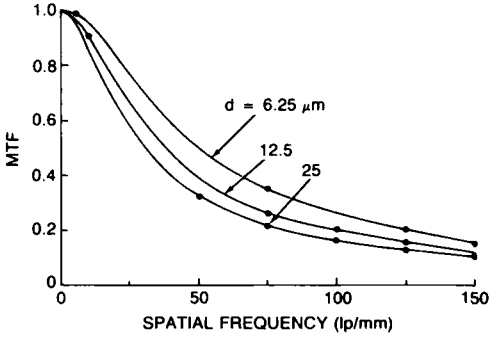

Fig. 4 - Theoretical Modulation Transfer Function of LCLV with 5 μm Thick a-Si:H

WEDNESDAY, JUNE 15, 1988

EMERALD BAY BALLROOM

10:40 AM–12:00 M

WB1–4

LIQUID CRYSTAL DEVICES: 2

Francis T. S. Yu, Pennsylvania State University,
Presider

OPTIMAL OPERATION TEMPERATURE OF A Si-LCLV

Shin-Tson Wu and Uzi Efron
Hughes Research Laboratories
3011 Malibu Canyon Road
Malibu, California 90265

Summary

A silicon liquid crystal light valve (Si-LCLV) is a useful device for converting an input image written in certain wavelength, intensity, and coherence conditions to an output image in which some or all of these parameters are varied. For examples, IR-to-visible[2] and visible-to-IR[3] image conversions using a Si-LCLV have been demonstrated successfully.

The structure of a reflective mode Si-LCLV consists of three major parts: (1) photoconductor: a 125-μm-thick, high resistivity (~5000 ohm-cm) π-silicon, (2) dielectric mirror: for reflective mode operation, and (3) nematic LC layer: for modulating the readout beam. In operation, a periodic asymmetric voltage waveform is applied to the Si-LCLV so that the device alternates between a long (~0.5 ms) depletion phase and a short (~40 μs) accumulation phase. In the depletion (active) phase, the high resistivity π-silicon is depleted completely, and electron-hole pairs generated by the input light are swept by the electric field, thereby producing a spatial voltage pattern that activates the liquid crystal. Since the liquid crystal film is birefringent, the electric-field-induced LC reorientation causes phase retardation of the incoming linearly polarized readout beam. A polarization analyzer completes the image transformation to a two-dimensional intensity pattern which replicates the input pattern originally imposed on the silicon photoconductor. A projection lens placed approximately one focal length from the output face of the LV relays the output image to the observer or detector.

When a Si-LCLV (with a parallel or perpendicular aligned LC layer) is used as an amplitude or phase modulator, large dynamic range and fast response times are the two important parameters. However, for a given LC material, these two parameters are conflicting issues; faster response times are often associated with a smaller dynamic range, or vice versa. To evaluate the trade-off between dynamic range and response times, we obtain a figure of merit (F.M.) as

$$F.M. = K\Delta n^2/\gamma_1 \qquad (1)$$

for a LC cell. Where $K = K_{11}$ or K_{33} represents the splay or bend elastic constant, Δn is the birefringence and γ_1 the rotational viscosity of the LC. Since K, Δn, and γ_1 are all temperature dependent, the F.M. is expected to depend on temperature. Optimizing the merit factor, we derived an optimal operation temperature (T_{op}) for a LC modulator:[4]

$$T_{op} = \frac{E}{6\beta k}\left[\left(1 + 12\beta k T_{NI} / E\right)^{1/2} - 1\right] \qquad (2)$$

where E is the activation energy of the LC, β is a material constant, k the Boltzmann constant, and T_{NI} the nematic-isotropic phase transition temperature. T_{op} is calculated to be ~48° and ~87°C for E-7 and E-44 LC mixtures, respectively. By operating a LC modulator at its T_{op}, the merit factor can be improved significantly. Good agreement between experiment and theory has been obtained.

In the Si-LCLV, in addition to the LC temperature effect, one more factor has to be taken into account, which is thermally-generated dark current (J_S) in the reverse-biased silicon photoconductor. J_S is strongly dependent on the temperature as[5]

$$J_s \sim T^3 \exp(-E_g/kT) \quad (3)$$

where E_g is the bandgap of the Si photoconductor. J_s increases by a factor of ~50 as the temperature increases from room temperature to 48°C, the optimal operation temperature of E-7 liquid crystal. The increase in dark current would alter the required bias voltage of the Si-LCLV and greatly affect its performance. On the other hand, operation at a higher temperature would result in a decreased threshold voltage for the LC. These effects conspire to lower the optimal operating temperature of the light valve to a value less than that predicted for the LC layer alone. We have found experimentally that the optimal operation temperature of the E-7 Si-LCLV occurs at 33°C, rather than at 48°C as anticipated for an isolated LC cell. Even at this slightly elevated temperature (33°C), a 60% improvement of the overall figure-of-merit was found relative to that at 22°C.

References

1. U. Efron, J. Grinberg, P. O. Braatz, M. J. Little, P. G. Reif, and R. N. Schwartz, J. Appl. Phys. 57, 1356 (1985).
2. S. T. Wu, U. Efron, and T. Y. Hsu, Opt. Lett. 13, 13 (1988).
3. S. T. Wu, U. Efron, J. Grinberg, L. D. Hess and M. S. Welkowsky, Proc. SPIE, 572, 94 (1985).
4. S. T. Wu, A. M. Lackner and U. Efron, Appl. Opt. 26, 3441 (1987).
5. S. M. Sze, Physics of Semiconductors, (Wiley Interscience, New York, 1981).

PERFORMANCE EVALUATION OF A TRANSMISSIVE LIQUID CRYSTAL SPATIAL LIGHT MODULATOR

Shih-Chun Lin, R. Scott Boughton, John Hong*
The Aerospace Corporation
P.O. Box 92957, Los Angeles, CA 90009

and

Joe Reichman
Grumman Corporate Research Center
Bethpage, New York 11714

I. Introduction

Liquid crystal spatial light modulators (LCSLM) have been used in many optical data processing systems. The one most often cited is the reflective type produced and marketed by Hughes Aircraft Company. Its construction, performance, and applications to real-time optical data processing have been reported before[1,2]. Grumman has recently developed an LCSLM, which allows both the write and the read beams to enter from the same side. The CdS photoconductor used is transparent to light of wavelength longer than 600 nm, so a red light, such as a He-Ne laser, will transmit through. Otherwise, the light valve operation is similar to the Hughes device.

An experimental evaluation was carried out at Aerospace on one of the devices for its sensitivity, temporal response, uniformity, and resolution. The results are summarized below.

II. Performance Measurements and Results

The basic experimental set-up is shown in Fig. 1. A collimated, incoherent write beam was generated from a 75 W xenon arc lamp, filtered by a blue filter. A collimated, coherent read beam was generated by a 10 mW He-Ne laser (λ = 632.8 nm), expanded to overfill the 1" diameter device aperture. Both beams were linearly polarized in the same direction and their intensities were adjusted individually by ND filters. An 8 V peak-to-peak sinusoidal voltage was applied across the device. The frequency of the voltage was adjustable. The input object was imaged onto the LCSLM by a diffraction-limited lens system. The output from the SLM was imaged through a red filter to a detector, a TV camera, or film, depending on what parameter was being measured.

*Present address: Science Center, Rockwell International Corp., P.O. Box 1085, Thousand Oaks, CA 91360

A. Sensitometry

Sensitometry measurement enables us to determine the device sensitivity, the linear dynamic range, and the contrast ratio. The bias voltage was 8 V, peak-to-peak. The sensitometry results are shown in Fig. 2. The curves show saturation at the high end of the input intensity, a linear region, and an increased sensitivity as the driving frequency is increased. From these curves, we conclude that the device, under the operational conditions, has a linear dynamic range of 10 dB or better, a contrast ratio of 15 dB or larger, and a sensitivity better than 21 $\mu w/cm^2$.

A separate set of transmission measurements were carried out at Grumman. The driving voltage was not set at 8 V peak-to-peak, but at values corresponding to points of minimum transmission when the write light was switched off. The data show that the sensitivity of a similar device can be as low as a few $\mu w/cm^2$.

B. Temporal Response

The temporal response of the LCSLM was measured by gating the write light with an electronically-controlled mechanical shutter, while monitoring the photodetectors and intensities of the write light and the output laser light. Typical responses are shown in Fig. 3, where the lower trace is the detector response to the gated write light and the upper trace is the response to the transmitted laser light. Results show that the rise time increases with increased driving frequency and decreased write intensity. The shortest rise time is 45 ms for 1 KHz, 50 ms for 2 KHz, and about 50 ms for 5 KHz. The decay time is much longer than the rise time. An initial delay between the onset of the read light and the onset of the write light was observed when the driving frequency was 1 KHz. The delay disappeared in the 2-KHz and 5-KHz cases. The delay time ranges from 5 ms to 60 ms depending on the writing intensity. Such a phenomenon has not been reported before and is worthy of future study.

C. Uniformity

1. Intensity Uniformity

The transmitted beam fringe pattern is shown in Fig. 4(a). The pattern is not a function of driving voltage, frequency, and the light intensities. A more quantitative measure was obtained by scanning the transmitted intensity with a small pinhole. The detector output is shown in Fig. 4(b).

2. Phase Uniformity

Phase uniformity was measured by two independent techniques. The first one employed a Mach-Zehnder interferometer. Fig. 5(a) shows the fringes of the interferometer before the device is

inserted, whereas Fig. 5(b) shows the fringe pattern after the active device is inserted. There is very little distortion in the fringes even though the intensity fringe pattern is still visible. The second measurement used was a rapid-scanning triangular interferometer originally developed for MTF measurement[3]. The envelope of the interferometer output is the MTF. The MTF of the well collimated, diffraction-limited He-Ne beam over a 1-cm circular aperture is shown in Fig. 6(a), whereas the beam after transmitting through the operating SLM is given in Fig. 6(b). The degradation in MTF due to phase non-uniformity may be estimated at about $1/4\lambda$ (Ref. 4), a result consistent with that of the first technique.

D. Resolution

The resolution of the device was measured by using the Air Force resolution chart, Sayce gratings, and a four-bar pattern as the input objects. Fig. 7 shows the output image of the Air Force resolution chart. The resolution is about 38 lp/mm and is limited by the graininess of the film. Using Sayce gratings and a four-bar pattern, a resolution of 45 lp/mm was measured by a CCD array.

III. Conclusion

Performance data show that the Grumman device is comparable to, if not better, than the other type. A transmissive device may provide more flexibility in designing optical processor architectures.

IV. References

1. J. Grinberg, et al., "A new real-time non-coherent to coherent light image converter - The hybrid field-effect liquid crystal light valve," Opt. Eng.,Vol. 14, p 17 (1975)

2. W.P. Blea, et al., "Applications of the liquid crystal light valve to real-time optical data processing," Opt. Eng., Vol. 17, p. 371 (1978).

3. D. Kelsall, "Rapid interferometric technique for MTF measurement in the visible or infrared region," Appl. Opt., Vol. 12, p. 1398 (1973).

4. E.L. O'Neill, Introduction to Statistical Optics, Addison, Reading, Mass., 1963, Chapter 6.

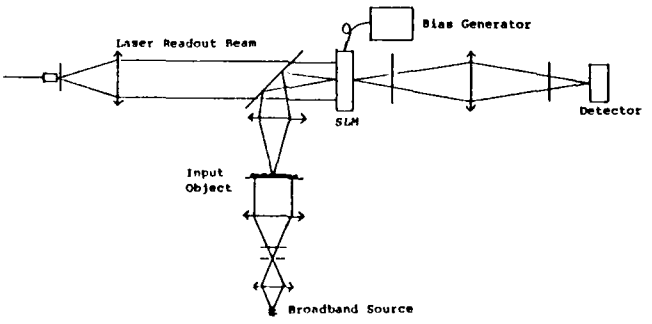

Fig. 1 OPERATION OF SPATIAL LIGHT MODULATOR

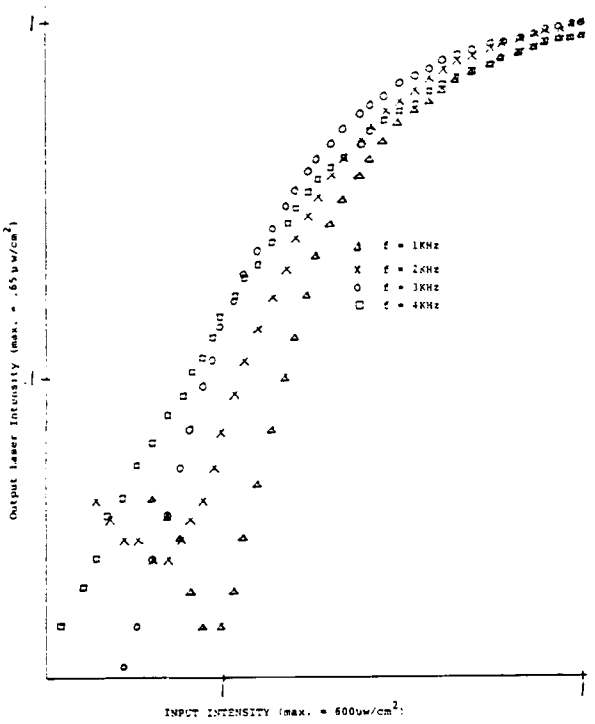

Fig. 2 Sensitometry Results (8V, p-p)

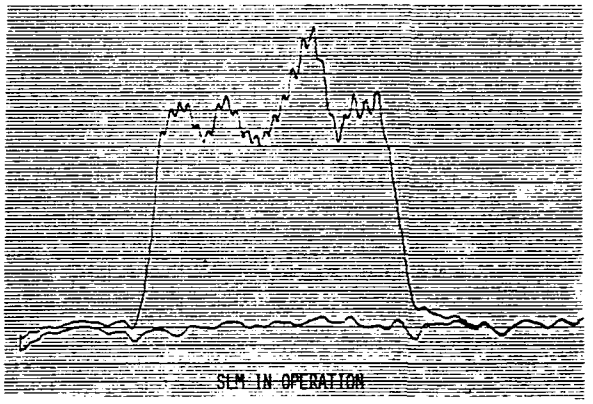

Fig.4(b) Intensity Nonuniformity Radiometry Scan

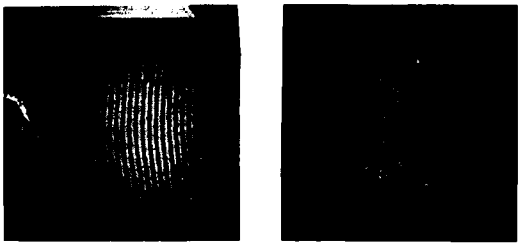

(a) M-Z Interferometer only (b) LCSLM in Interferometer

Fig. 5 Phase Uniformity by Interferometry

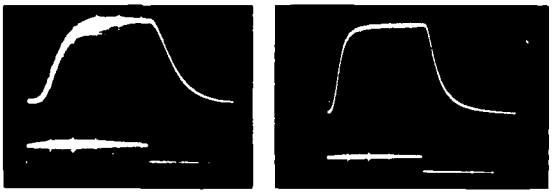

(a) 1KHz,50ms/div (b) 2KHz 0.25s/div

Fig. 3 Temporal Response

(a) Laser Beam Only (b) LCSLM output

Fig. 6 Phase Uniformity by MTF

Fig. 4(a) Intensity Nonuniformity

Fig. 7 Output Image of the Air Force Resolution Chart

MICROSECOND SWITCHING IN CHOLESTERIC LIQUID CRYSTALS

J. S. Patel
Bell Communications Research
331 Newman Springs Road
Red Bank NJ 07701

The helical structure of a cholesteric liquid crystal can be modified or even completely unwound by an applied electric field. This is well understood in terms of the coupling of the electric field to the dielectric anisotropy of the liquid crystal, an effect which is quadratic in the amplitude of the electric field. In this paper we report the measurements of optical switching times for a new effect in cholesteric liquid crystals which arises because of flexoelectric coupling[1] and which is linear in the electric field.[2]

The effect is easily observed in a well aligned parallel plate cell in which the helix axis of the cholesteric liquid crystal lies in the plane of the plates. In this configuration, in absence of an electric field, The cholesteric liquid crystal behaves as a uniaxial material with its optic axis perpendicular to the helix axis. When an electric field is applied, the helix distorts, as shown in figure 1, to lower the free energy of the system as describes elsewhere.[2] The net result of an applied electric field is that the system behaves as if the optic axis has been rotated about the electric field direction. The direction and the magnitude of this rotation depends on the direction and the magnitude of the applied electric field. Thus this effect is a linear electro-optic effect and phenomenologically resembles the ferroelectric effect in liquid crystals.

We have constructed a test cell containing a cholesteric liquid consisting of a mixture of 30% cholestryl nonate and 70% ZLI2141-100 nematic liquid crystal from MERCK which

has a low $\Delta\epsilon$. The cell was made of conductive indium tin oxide coated glass, with a cell gap of 7.5 microns. The alignment was obtained by coating both surfaces of the cell with alignment polymer and buffing the surface as described before[3]. The sample was filled in the isotropic state and cooled into the cholesteric phase with 40V DC across the sample to improve the alignment quality.

By placing the sample between cross polarizer and applying an AC voltage, optical modulation could be easily observed by monitoring the transmission through the cell. Since the rotation of the optic axis was small in this sample, a linear relationship between the depth of modulation and the applied electric field is expected if the sample is placed with its zero field optic axis at a small angle to the polarizer axis. This can be easily seen by noting that the transmission for the two optical states,is given by

$I_1 \propto \sin^2[2(\Theta - \Phi)]$ and $I_2 \propto \sin^2[2(\Theta + \Phi)]$

and the difference $\Delta I \propto \sin(4\Theta)\sin(4\Phi)$

where Θ is the angle that the zero field optic axis makes with the polarizer axis and Φ is the change in the angle that the optic axis undergoes as a result of applied field. This angle Φ can be shown to be proportional to the applied electric field at least for small fields[2]. Thus the difference in the intensity should be proportional to the applied electric field.

Experimentally the optical response to an applied square wave of various amplitudes were recorded digitally for further analysis. The data points demonstrating the linear relationship between ΔI and voltage are shown in figure 2. Figure 3. shows the optical response due to an applied square wave. The intensity has been normalized to compare the rise and the fall time at different voltages. The data clearly shows that these time are

independent of applied electric field although, the absolute electro-optic effect is proportional to the magnitude of the electric field. The rise and the fall time are equal as expected since the switching is field driven for both the states. The field independence of the switching time can be explained by noting that the torque on the molecules is proportional to the field, but the molecules have to swing through an angle Φ which is also proportional to the field. It can be shown that[2] $\tan\Phi = \mathbf{e}.\mathbf{E}/t_o K$, where **e** is the flexoelectric coefficient[3], K is the elastic constant, $2\pi/t_o$ is the helical pitch, and **E** is the electric field. Thus for small values of Φ the switching speed is field independent because of the compansating effects of the greater torque and larger optic axis rotation.

REFERENCES

1. R. B. Meyer, *Phy. Rev. Letts.* **22,** 918 (1969).

2. J. S. Patel and R. B.Meyer, *Phy. Rev. Letts.* **58,** 1538 (1987)

3. J. S. Patel, T. M. Leslie and J. W. Goodby, *Ferroelectrics,* **59,** 129 (1984).

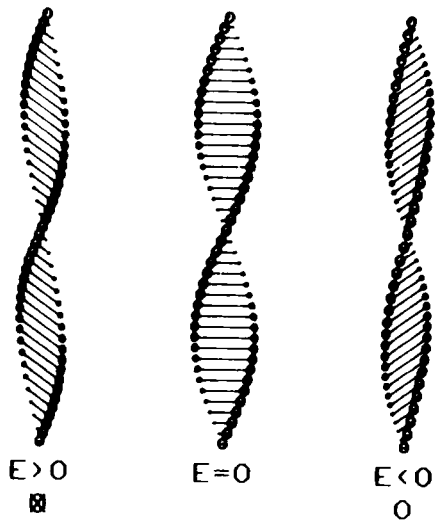

Fig. 1 (a), (b), and (c): The helical structure viewed normal to the helix axis, (a), in the absence of an electric field, and, (b) and (c), in the presence of an electric field perpendicular to the plane of the drawing, showing the induced director rotation.

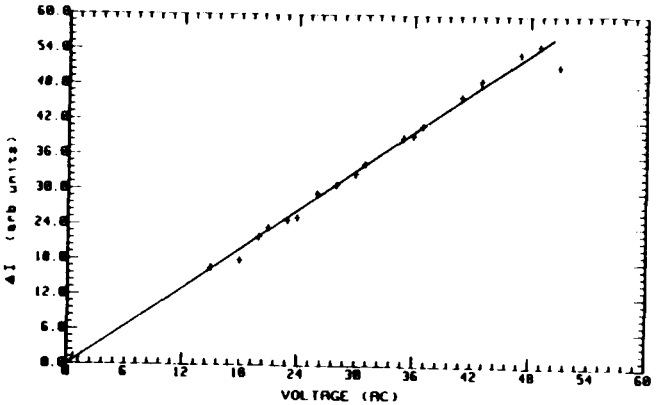

Fig. 2 Observed change in optical transmission as a function of applied voltage

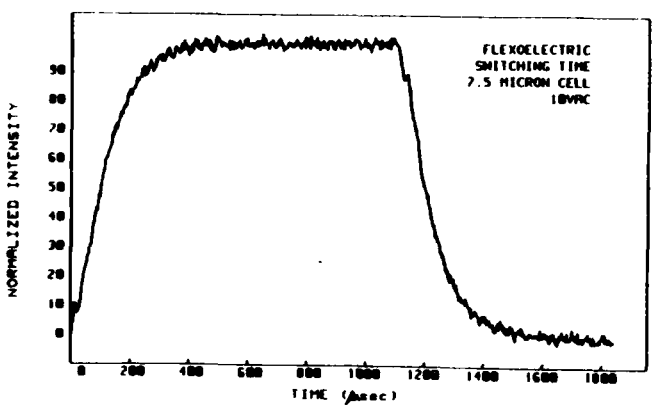

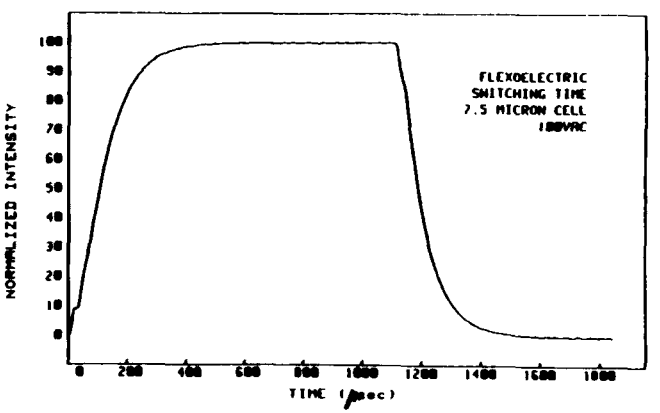

Fig. 3 Optical response time due to an applied square wave voltage. The Transmission intensity has been normalized to compare the response times corresponding to an applied 10V AC (Fig.3A) and 100V AC (Fig 3B).

Real-Time Optical Edge Enhancement Using a Hughes Liquid Crystal Light Valve

Tien-Hsin Chao and Hua-Kuang Liu
Jet Propulsion Laboratory
California Institute of Technology
Pasadena, CA 91109

Edge enhancement is one of the most important preprocessing techniques utilized in optical pattern recognition. In an optical correlator, cross-correlations among similar input objects can be greatly reduced by using the edge enhancement technique. Traditionally, optical edge enhancement is obtained by high-pass filtering at the Fourier plane. However, the system SNR is generally lowered by this filtering process. Recently, two differentiating spatial light modulators, specifically designed to generate edge-enhanced output, have been reported. Casasent et al. have demonstrated real-time edge enhancement using a Priz light modulator [1]. The Priz light modulator is a transverse modification of the Pockel's Read-out Optical Modulator (PROM) with a [111] BSO crystal cut. Armitage and Thackara have designed a BSO photo-addressed nematic liquid crystal differentiating spatial light modulator [2, 3]. A layer of liquid crystal is tuned in a transverse configuration (i.e. the electro-optic response is optimized for E_x and E_y rather than E_z) to achieve the edge-enhancement. The BSO crystal is used as a photo-addressing medium. This SLM is functionally optimized as an edge-enhancing SLM.

In one of our recent artificial neural network experiments, we discovered an interesting edge enhancement effect by using a Cd-S Hughes Liquid Crystal Light Valve.

In our experiment, the edge-enhancing effect started to appear as the biasing frequency was lowered. This effect was optimized at a bias frequency of 500 Hz and voltage of 6 V_{rms}. (For normal operation, the values are 10 KHz and 10 V_{rms}). The input writing light intensity was about 50 $\mu w/cm^2$. Experimentally, a linearly polarized read-out beam was employed. First, a continuous tone image was obtained, through using a polarizing beam splitter, at the above stated biasing condition. The edge-enhanced output was obtained when the LCTV was rotated about 30° ccw.

The interpretation of this edge enhancement phenomenon is as follows: It was generally understood that in a photo-addressed SLM, the transverse field components are proportional to the spatial gradient of the writing image. Thus, a transverse SLM acts as a differentiating or edge-enhancing device [3]. As a low frequency biasing signal is applied to the Hughes LCLV, the liquid crystal molecules align themselves along the direction of the applied field that is perpendicular to the electrode surfaces. The LCLV is thus switched to a transverse mode under this bias condition and functions as an edge-enhancing spatial light modulator.

The experimental results are shown in Fig. 1. Fig. 1 (a) shows an edge-enhanced Air Force resolution chart. Fig. 1 (b) shows an edge-enhanced picture of a continuous-tone image. In this picture, the outline of the girl's head is clearly displayed and the halo in the background is reduced to a ring.

Further experiments using this real-time edge-enhancing effect in an optical correlator are underway at JPL. The results will also be presented in the meeting.

The research reported in this paper was performed at the Jet Propulsion Laboratory, California Institute of Technology, as part of its Innovative Space Technology Center, which is sponsored by the Strategic Defense Initiative Organization/Innovative Science and Technology through an agreement with the National Aeronautics and Space Administration (NASA). The work described was also co-sponsored by NASA OAST and the Physics Division of the Army Research Office.

References

1. D. Casasent, F. Caimi, M. Petron, and A. Khomenko, Appl. Opt., **21**, p. 3846 (1982).

2. D. Armitage and J. I. Thackara, Proc. SPIE, **613**, p. 165 (1986).

3. D. Armitage and J. I. Thackara, Technical Digest of Topical Meeting on Machine Vision of OSA, **12**, p. 58 (1987).

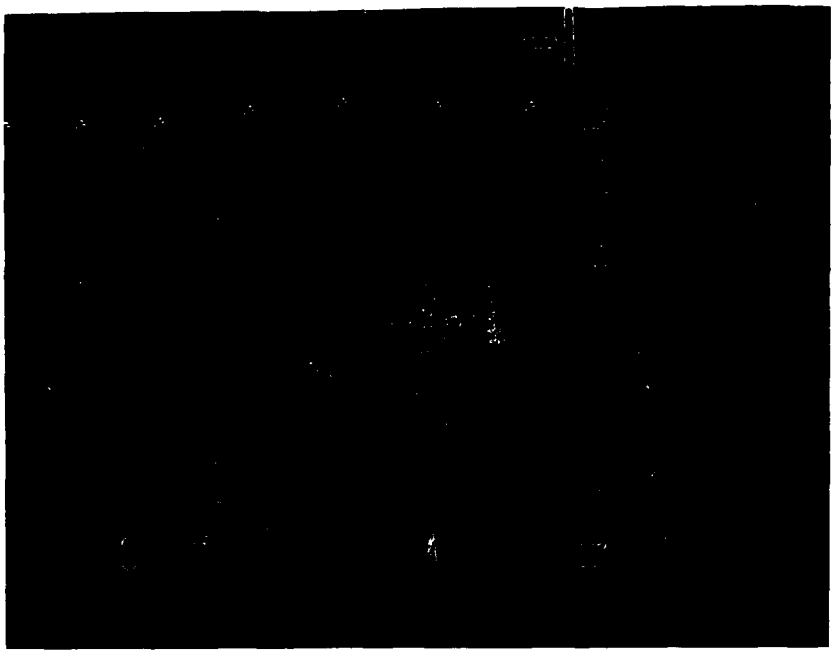

(a)

(b)

Fig. 1 Edge enhancement experiments using a Hughes Liquid Crystal Light Valve. (a) Edge-enhanced image of an Air Force resolution chart. (b) Edge-enhanced image of a continuous-tone image.

WEDNESDAY, JUNE 15, 1988

EMERALD BAY BALLROOM

1:30 PM–3:10 PM

WC1–4

PHOTOREFRACTIVE DEVICES

Pochi Yeh, Rockwell International Science Center,
Presider

Improved photorefractive performance from a special cut of $BaTiO_3$.

Joseph E. Ford, Yeshaiahu Fainman and Sing H. Lee
Department of Electrical and Computer Engineering,
University of California at San Diego, La Jolla, CA 92093

1. Introduction

Photorefractive materials have been used to construct optically controlled spatial light modulators (SLMs) using incoherent erasure of an index grating[1] and using photorefractive gain[2]. An SLM should provide high resolution, large aperture, low noise and crosstalk, and fast time response. If gain is to be provided it should be high, and uniform to within the 3db criterion[3]. Among the currently available photorefractive materials, barium titanate has the best performance characteristics for optical signal processing applications requiring gain. It provides large index modulation, high sensitivity, reasonable response times, and crystals of good optical quality are available. However, utilization of these characteristics in a regularly cut crystal (with faces parallel to the (100), (010) and (001) crystallographic planes) introduces certain operational difficulties. To overcome these difficulties we have prepared a specially-cut crystal of $BaTiO_3$, with faces parallel to the (100), (011), and $(01\bar{1})$ crystallographic planes. In this paper, we will evaluate the performance of crystals with this orientation for information processing and particularly for SLM applications.

2. Characteristics of photorefractive $BaTiO_3$

The use of $BaTiO_3$ for coherent image amplification is discussed in detail in reference 3. The optical configuration for two-beam coupling is shown in fig. 1. Briefly, the signal gain, G, is given by

$$G=\frac{(1+r)e^{\Gamma L}}{1+re^{\Gamma L}} \tag{1}$$

where r is the ratio of input beam intensities; L is the effective optical interaction length in the crystal; and Γ, the exponential gain factor, is a material characteristic which depends on the input beam angles θ and β (see fig. 2).

2.1 Regular-cut $BaTiO_3$

For a regular-cut crystal in air, the interior beam angles necessary to obtain high gain ($\beta \sim 20°, \theta \sim 2°$) can be reached only if either the pump or the signal beam enters the crystal at near grazing incidence, resulting in several adverse effects on SLM performance. First, crystal's volume is not uniformly illuminated, reducing the gain near the sides, and so decreasing the usable crystal aperture. Second, the slope of the Γ curve is very steep in the accessible high-gain regions. This means that the signal gain will be a sharply varying function of input angle, reducing the allowed angular bandwidth of the input signal, and therefore the resolution of the SLM.

To avoid these problems, it is possible to decrease β and to increase θ, trading in the gain coefficient for increased bandwidth. However, to produce the same gain as before, the interaction length--and therefore the crystal's thickness--must be substantially increased. Furthermore, in SLM applications, both the signal and the pump (the modulator control beam) carry information, therefore the pixel size must be large enough that pixels do not significantly overlap one another in the crystal. The combination of a larger beam angle and a thicker crystal forces an increase in the minimum pixel size, with a corresponding decrease is the SLM's space bandwidth product. Also, it is not possible to apply an external electric field aligned with $\hat{\mathbf{k}}_g$, which can be useful in some information processing applications[4].

2.2 Special-cut $BaTiO_3$

Our solution to these problems was to have the $BaTiO_3$ crystal cut at 45° to the conventional orientation[3], so that its faces are on the (100), (011) and (011) planes, as shown in figure 3. This orientation allows coupling to the peak exponential gain coefficient ($\beta \sim 45°$, $\theta \sim 2°$) with both the pump and signal beams at nearly normal incidence to the crystal face. This results in full use of the crystal aperture with uniform gain. The increased Γ means that a thinner crystal will produce the same gain as before, while reducing crosstalk and decreasing the minimum pixel size. Furthermore, since $\hat{k}_g$ will be nearly perpendicular to the crystals sides, an external electric field aligned with $\hat{k}_g$ can be applied, so that higher gains can be achieved[5].

2.3 Experimental results

The first special-cut crystal we examined was the same thickness as the regular-cut crystal we use (4.5 mm). The resultant gain was so large that the amplification of scattered light (fanout) dominated, depleting the pump beam and reducing the available gain. We then examined a special-cut crystal only 2.5 mm thick which gave improved results. We have characterized these crystals and compared them to a regular-cut crystal 4.5 mm thick which produced comparable gain.

A comparison between the two crystals of the gain measured as a function of input beam angle is shown in figure 4. The special-cut crystal gave much more uniform gain, with a peak Γ of 2.45/mm compared to 1.39/mm for the regular cut. The maximum gain for the special-cut crystal occured at θ=8° rather than the predicted 2°. This is a result of fanout: to avoid depletion of the signal beam, it must propagate through the crystal at an angle for which the fanout is low. Unlike the regular-cut crystal, the gain observed showed a strong positive dependance on the incident intensity, probably due to a nonlinear dependance of fanning on the total input intensity.

An important material performance characteristic for SLM applications is the spatial frequency response of the photorefractive amplifier. This was determined by simultaneously amplifying two signal beams and calculating their gain ratio, in effect measuring the contrast ratio of an amplified image of a grating. The result, plotted in figure 5, showed that the special-cut provides uniform gain for images with spatial frequencies of over 500 lp/mm. The regular-cut crystal has by comparison uneven performance: at spatial frequencies below 100 lp/mm, the signal closer to the pump beam tends to dominate the gain. Above 100 lp/mm, the angle between the two signal beams has become large enough that the second beam can begin to extract energy from the first (see fig. 2), resulting in a dynamic transfer of energy back and forth between the two signal beams, further reducing the contrast. When an external electric field was applied to the special-cut crystal, the gain increased, especially at low photorefractive grating spatial frequencies and low pump beam intensities. At θ=2°, the gain more than tripled when 1 kV was applied (see figure 6).

One of the most critical characteristics of an SLM is its response time. Regular-cut $BaTiO_3$ has a relatively slow response compared to, for example, BSO. A large reduction in the response time of the special-cut $BaTiO_3$ crystal was observed, independant of the applied field. The response times of a 2.5 mm thick special-cut and a 4.5 mm thick regular-cut crystal were measured under conditions producing the same gain (pump intensity 25 mW/cm^2, signal/pump ratio 10^{-4}, gain ~ 650). The special-cut crystal had a response time of only 2.1s compared to 54s for the regular-cut crystal. This improvement is most probably due to a decrease in the effective dielectric constant experienced by the beams interacting in the special-cut crystal[6].

3. Conclusions

We have shown that a special-cut $BaTiO_3$ crystal is very well suited for use as an amplifying SLM. Such crystals provide more uniform gain, better response to high spatial frequency input, more effective use of crystal aperture, and faster response times than conventional $BaTiO_3$ crystals. In other words, an amplifying spatial light modulator using this unconventionally cut $BaTiO_3$ crystal will provide uniform gain for large space bandwidth product signals and will operate with improved response time.

References

1. Y. Shi, D. Psaltis, A. Marrakchi and A.R. Tanguay, "Photorefractive incoherent-to-coherent optical converter," Appl. Opt. 22(23), 3665 (1983).

2. Y. Fainman, C. C. Guest and S. H. Lee, "Optical digital logic operations by two-beam coupling in photorefractive material," Appl. Opt. 25(10), 1598 (1986).

3. Y. Fainman, E. Klancnik and S. H. Lee, "Optimal coherent image amplification by two-wave coupling in photorefractive $BaTiO_3$, Opt. Eng. 25(2), 228 (1986).

4. E. Ochoa, L Hesselink and J. W. Goodman, "Real-time intensity inversion using two-wave and four-wave mixing in photorefractive $Bi_{12}GeO_{20}$," Appl. Opt. 24(12), 1826 (1985).

5. J. C. Jonathan, R. W. Hellwarth and G. Roosen, "Effect of applied electric field on the buildup and decay of photorefractive gratings," IEEE J. Quant. El. 22(10), 1936 (1986).

6. G. C. Valley and M. B. Klein, "Optimal properties of photorefractive materials for optical data processing," Opt. Eng. 22(6), 704 (1983).

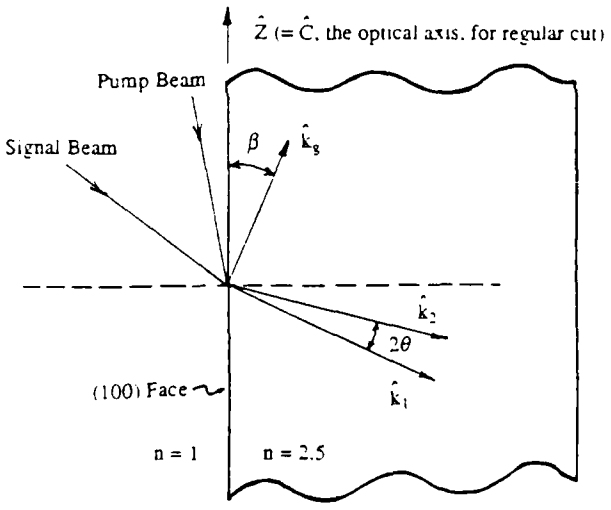

Fig. 1. Geometric configuration of two-wave mixing in $BaTiO_3$. $\hat{k}_1$ and $\hat{k}_2$ are the wave vectors of the pump and signal beams respectively; $\hat{k}_g$ is the wavevector of the index grating induced from the two interacting beams; 2θ is the interior angle between the two beams; $\hat{C}$ is the optical axis of crystal, and β is the angle between $\hat{k}_g$ and $\hat{C}$.

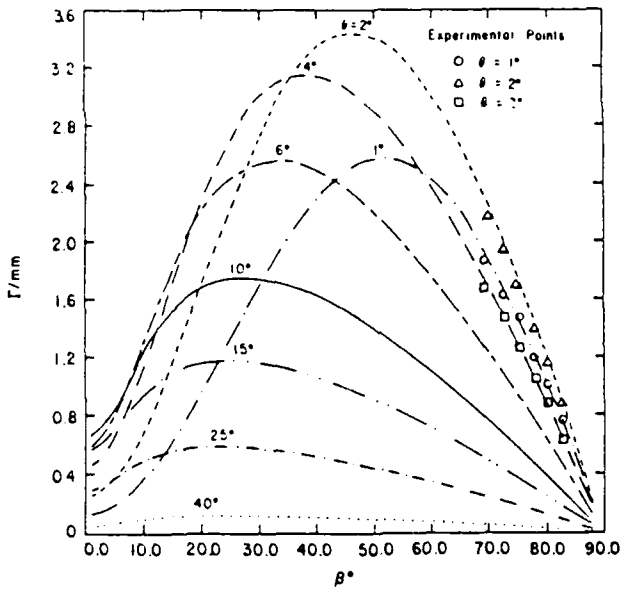

Fig. 2. The exponential gain coefficient, Γ, as a function of externally controlled angles θ and β (as measured inside the crystal). Experimental gain measurements shown are for the regular-cut crystal.

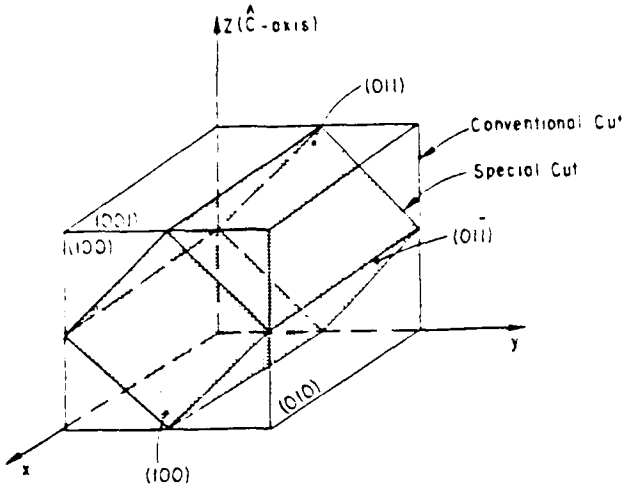

Fig. 3. Orientation of the special-cut $BaTiO_3$ crystal (with faces on the (100), (011), and (01$\bar{1}$) crystallographic planes) relative to the regular-cut crystal.

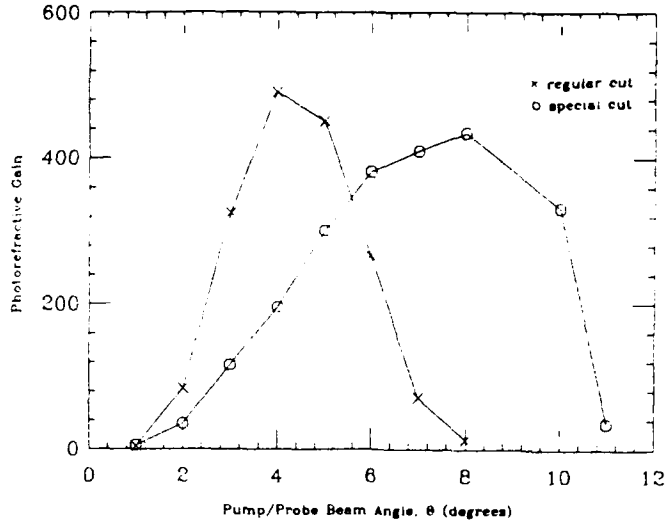

Fig 4. Photorefractive gain vs internal pump/probe beam angle, θ, for both regular (4.5 mm crystal thickness, β=15°) and special (2.5 mm thick, β=0°) cut $BaTiO_3$. The special-cut crystal had an applied voltage of 1kV (1.92kV/cm). Pump intensity was 20 mW/cm^2.

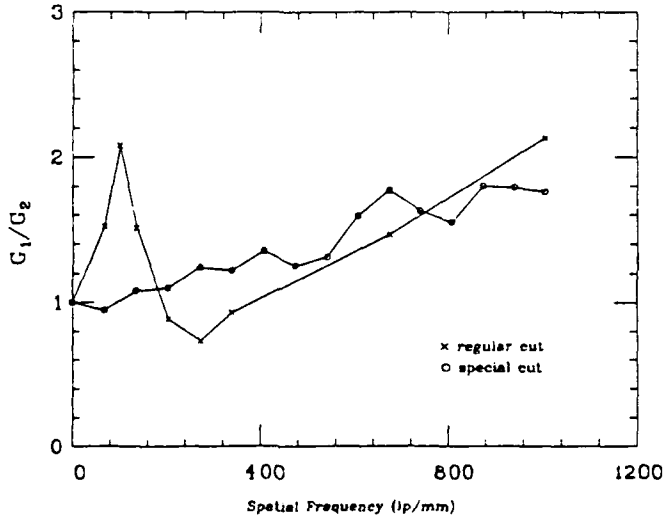

Fig. 5. Frequency response of $BaTiO_3$ for both regular and special cut crystals. Interior bias angle $\theta = 4°$. The response is defined as the ratio of the gain of two signal beams simultaneously amplified in the crystal.

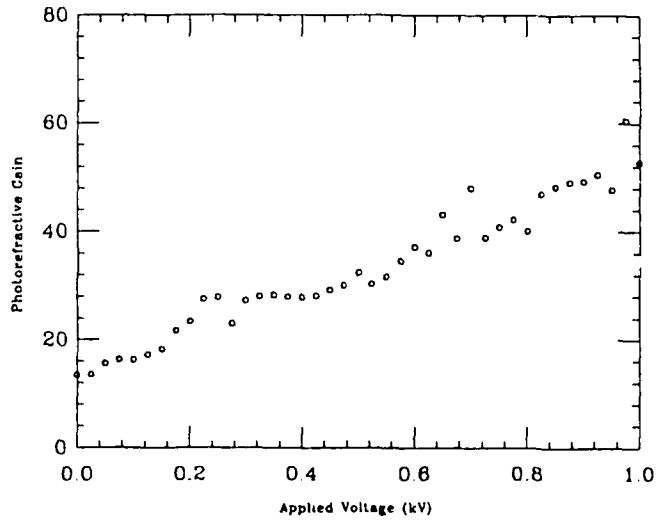

Fig. 6. Photorefractive gain vs applied voltage for special-cut $BaTiO_3$. Pump intensity $I_p = 20mW/cm^2$, $r = 2x10^{-4}$, $\theta = 2°$ (grating period Λ=3μm), and β=0°.

SPATIAL LIGHT MODULATION IN GaAs

Li-Jen Cheng, Gregory Gheen, and Tsuen-Hsi Liu
Jet Propulsion Laboratory
California Institute of Technology
Pasadena, California 91109

Gallium Arsenide(GaAs) is the most technologically-important compound semiconductor for electronics and optoelectronics. Semi-insulating Cr-doped and undoped GaAs crystals are known to be photorefractive.[1,2] This provides opportunities to use GaAs for optical processing, including spatial light modulation. In this paper, we will present recent results of our investigation on the feasibility of using GaAs in this area.

Volume holographic grating can be written in the photorefractive crystal using two coherent light beams, which can diffract light. If the grating is written with information-bearing beams, the diffracted beam is spatially modulated in accordance with the information. Spatial light modulation in photorefractive GaAs uses this principle. The light to be diffracted is not necessary to be coherent with and/or have the same wavelength as the write beam. However, the diffraction can occur only when the Bragg angle condition is satisfied. The diffracted beam can carry the information stored in the hologram by means of the spatial variation in intensity and phase. The information storage can be achieved either by encoding write beams(one or both) or illuminating the uniform grating in the crystal with an information-bearing incoherent light. The former is commonly used for optical processing. The latter is the mechanism used in the photorefractive incoherent-to-coherent optical converter[3].

In comparison with conventional photorefractive oxides, such as barium titanate, bismuth silicon oxide(BSO), and strontium barium niobate(SBN), photorefractive GaAs does provide several distinguishable advantages. They include fast response,

compatibility with semiconductor lasers, availability of large, high quality crystals, and potential to be integrated with optoelectronic components. In addition, the optical isotropy and the tensor nature of the electro-optic coefficients of GaAs crystals allow the possibility that the polarization of the diffracted light is perpendicular to that of the incident beam[4-6]. This provide a convenient method to separate the diffracted beam from background noises and opportunities to create innovative applications.

The responsible mid-gap level in LEC-grown, undoped, semi-insulating GaAs for the photorefractive effect is known to be the EL-2 level, an arsenic anti-site defect. This particular defect is also known to be responsible for compensating the residual electrical activity, making undoped crystals semi-insulating. The level is located about 0.75 eV below the conduction band. Typical density of the defect in undoped, semi-insulating GaAs crystals currently available is in the order of 10^{16} cm^{-3}, among which only about 10^{15} cm^{-3} are in the empty state, acting as acceptors. The electron mobility in photorefractive GaAs is typically about 5000 $cm^2/sec\text{-}V$, which is about four-orders of magnitude larger than those of the oxides.

The response time of a photorefractive material is the time required to form an index grating which depends on beam intensities, grating periodicity, as well as material properties. Carrier mobility, donor concentration, photoionization cross section of the donor, and carrier capture rate at the acceptor are material factors determining the response time. It is reported that the response time in LEC-grown, undoped GaAs is about 1 millisecond[7] and 20 microseconds[2] under a total intensity of 0.1 and 4 W/cm^2. These numbers are, at least, about two orders of magnitude larger than those of the oxides under the same intensities. The response time of GaAs can be in the picosecond time scale, if intense picosecond light pulses are used. For example, under a total intensity of $5x10^7$ W/cm^2, the response time of GaAs was reported to be 43 picoseconds[8].

The volume holographic grating written in a photorefractive material has a finite lifetime. This lifetime determines the information storage time in the crystal, an important parameter for evaluating the information processing capability. For a given wavelength, the read beam intensity and the grating periodicity are two process-related parameters determining the lifetime. Recently, a beam coupling technique using a 1.15 micron He-Ne laser was employed to measure the grating lifetime in GaAs[9]. The largest lifetime measured is about 8 seconds under a read beam intensity of 0.7 mW/cm^2 with the grating periodicity being 0.63 microns. The measured value decreases to milliseconds as the read beam intensity and the grating periodicity increase to about 10 mW/cm^2 and 4 microns, respectively. In addition, the results suggest that lifetime is sensitive to residual imperfections in the crystal.

There are two generic configurations utilizing the photorefractive effect: beam coupling(two-wave mixing) and four-wave mixing. In the beam coupling, two coherent beams interact with each other, resulting in a net energy transfer or a polarization shift. Spatial light modulation and image transfer using the polarization shift were successfully demonstrated[10,11]. In the four-wave mixing, two coherent beams write an index grating. A third beam reads the grating, creating a fourth output beam by diffraction. Four-wave mixing is more useful and versatile. A number of basic optical information processes including imaging using phase conjugation[12], correlation[13] and convolution, and matrix-vector multiplication[14] were demonstrated using the degenerate four-wave mixing configuration. Experimental results will be presented and their potentials for practical applications will be discussed.

The work described in this paper was carried out by the Jet Propulsion Laboratory, California Institute of Technology, and was sponsored by the Defense Advanced Research Projects Agency and the Strategic Defense Initiative Organization/Innovative Science and Technology through agreement with the National Aeronautics and Space Administration.

References:

1. A.M. Glass, A.M. Johnson, D.H. Olsen, W. Simpson, and A.A. Ballman, Appl. Phys. Lett., 44, 948 (1984).

2. M.B. Klein, Opt. Lett., 9, 350 (1984).

3. Y. Shi, D. Psaltis, A. Marrakchi, and A. R. Tanguay, Jr., Appl. Opt., 22, 3665 (1983).

4. P. Yeh, J. Opt. Soc. Am. B, 4, 1382 (1987).

5. A. Partovi, E. Garmire, and L.J. Cheng, Appl. Phys. Lett. 51, 299 (1987).

6. L.J. Cheng and P. Yeh, Opt. Lett. , 13, 50 (1988).

7. G. Gheen and L.J. Cheng, Appl. Phys. Lett. 51, 1481 (1987).

8. G.C. Valley, A.L. Smirl, M.B. Klein, K. Bohnert, and T.F. Boggess, Opt. Lett. 11, 647 (1986).

9. L.J. Cheng and A. Partovi, Appl. Opt., May 1 issue, 1988.

10. L.J. Cheng, G. Gheen, T.H. Chao, H.K. Liu, A. Partovi, J. Katz, and E. Garmire, Opt. Lett. 12, 705 (1987).

11. L.J. Cheng, G. Gheen, F.C. Wang, and M.F. Rau, J. Appl. Phys. 62, 3991 (1987).

12. G. Gheen and L.J. Cheng, Appl. Phys. Lett. 51, 1481 (1987).

13. G. Gheen and L.J. Cheng (to be published).

14. L.J. Cheng and G. Gheen (to be published).

Two-Beam Coupling Photorefractive Spatial Light Modulation with Positive/Negative Contrast in Sillenite Crystals

Abdellatif Marrakchi
Bellcore
331 Newman Springs Road, Red Bank, NJ 07701-7020

Dynamically programmable optical processing and switching systems rely heavily on the availability and performance of spatial light modulators (SLMs). Several devices based on the refractive index change of a photosensitive material have been already demonstrated.[1] However, their performance has been shown to be limited, both in terms of sensitivity and resolution. As a result, new concepts are being investigated that would perform the SLM function. One alternative is to utilize the photorefractive effect.

In the following, we demonstrate and characterize photorefractive spatial light modulation based on Doppler-enhanced two-beam coupling in bismuth silicon oxide crystals ($Bi_{12}SiO_{20}$, or BSO). Even though the intrinsic erasure efficacy is not large enough to allow direct visualization of the spatial light modulation, the polarization properties inherent to optically active materials, such as BSO crystals, extend the dynamic range of this erasure process, making such a configuration attractive both for its performance and its simplicity. In addition, for a specific orientation of the crystal, the particular polarization properties allow control over the contrast of the modulation. Indeed positive or negative contrast can be achieved by proper selection of the polarization state of the image-bearing coherent transmitted beam.

When two coherent beams are allowed to interfere within the bulk of a photorefractive material, the resulting intensity distribution is mapped onto a corresponding refractive index modulation due to charge generation, transport, and trapping. This process gives rise to a space charge field which is responsible for the refractive index change through the linear Pockels effect. Under certain conditions, this holographic recording occurs with an energy exchange between the two writing beams. Photorefractive grating recording does occur with the appropriate phase mismatch in the diffusion regime, i.e., no external field is applied to the material. However, in this case, beam coupling in BSO crystals is weak due to the small value of the electrooptic coefficient (r_{41} is about 4.5 pm/V). In order to take advantage of the effect of large applied electric fields and the proper phase mismatch, it was found that a moving grating enhances coupling,[2] both by increasing the space charge field amplitude and by optimizing the phase mismatch. Large values of energy transfer could then be observed in BSO crystals.

Schematically, the principle of photorefractive incoherent-to-coherent optical conversion (PICOC) based on self-diffraction is illustrated in Fig. 1. Two coherent plane waves impinge upon the BSO crystal, from the same side to form a transmission-type refractive index grating. The reference (or pump) beam has a much larger intensity compared to the signal beam. Under proper conditions, at the exit of the crystal, the weak signal beam intensity is increased due to coherent self-diffraction from the grating being written simultaneously. In addition to the two writing beams, a third beam is also incident on the crystal. This illumination could originate either from a white light source combined with a color filter, or from a laser source incoherent with respect to the writing beams. The effect of the incoherent spatial information is two-fold. First, its DC part locally reduces the phase grating modulation depth (related to sensitivity); and second, its spectral content affects the induced harmonics of the space charge field (related to resolution). Although for a complete device performance analysis both effects should be considered, only the reduction of the grating modulation depth is taken into account in the proposed simple model. The locally induced reduction of the fringe modulation subsequently decreases the amount of energy transferred onto the weak coherent signal beam. Note that the intensity distribution in the signal beam after the crystal is a negative replica of the incoherent information.

In the derivation of the transmitted signal intensity, we shall not be concerned with the device spatial resolution issues. Consequently, the conversion process is described in terms of the effect of the local modulation decrease on self-diffraction. The reduction of the transmitted weak output intensity is illustrated in Fig. 2, for two different crystal thicknesses. The plots are normalized to the intensity that would result in the presence of coupling but without erasure. They represent the function

$$N_{out} = \exp[-\Gamma_0 d(\frac{\sigma R}{1 + \sigma R})] \qquad (1)$$

in which Γ_0 is the exponential gain in the absence of the incoherent erasure beam, $\sigma = \alpha_S \lambda_S \exp(-\alpha_S d)/\alpha_G \lambda_G \exp(-\alpha_G d)$ is the relative efficiency of generating charges at each wavelength, and $R = I_S/I_G$ is the incoherent-to-coherent intensity ratio. Note that even for the 2 mm-thick crystal (which is used in our experiment), most of the reduction happens for a range of ratios between zero and one. (The typical values of the different parameters used in the model are $\alpha_G = 2\ cm^{-1}$ and $n_G = 2.615$ at the coherent wavelength $\lambda_G = 514$ nm; $\alpha_S = 10\ cm^{-1}$ at the incoherent wavelength $\lambda_S = 442$ nm; $I_{20}/I_{10} = 10^{-3}$; and $E_{sat} = 12.3\ kVcm^{-1}$.) Defining the sensitivity of the conversion as the slope of these plots around the origin, one finds that it is given by

$$S = -\Gamma_0 \sigma d \qquad (2)$$

which shows that the larger the gain in two-wave mixing, the more sensitive the device will be. This expression also shows that the sensitivity is enhanced by the use of an incoherent wavelength that is efficiently absorbed by the material.

The polarization properties in sillenite crystals have been extensively studied.[3,4] The simultaneous presence of field-induced linear birefringence and natural optical activity in these materials brings about a large degree of freedom in terms of polarization control of the beams that emerge behind the crystal. The results of the theoretical model developed in Ref. 4 as applied to the present experiment are shown in Fig. 3. The transmitted signal beam (I_2) is weakly elliptical in the stationary case, and becomes fatter with the running grating condition (2 mm-thick BSO crystal; 8 $kVcm^{-1}$ applied field along the <001> axis; 7 μm fringe spacing; linear incident polarization along the modulated axis). In addition, the angle between the major axes of the optical fields that correspond to the two configurations is about 30 deg., illustrating the fact that the increase in the space charge field amplitude due to the Doppler shift combines with the optical activity to further rotate the polarization state. Consequently, the contrast ratio of the optical conversion can be improved using such properties. To achieve this, the experimental conditions are chosen so as to extinguish the transmitted coherent beam with a polarization analyzer, in the presence of an applied field but without running gratings; then the fringes are allowed to move, with a velocity that optimizes self-diffraction. Addition of the incoherent beam decreases the diffracted intensity in the signal beam, but now, the contrast ratio is enhanced with the use of the analyzer, since the background intensity and the scattered noise are drastically reduced. This technique has been successfully applied to the photorefractive incoherent-to-coherent optical conversion of two-dimensional transparencies, as shown in Fig. 4 for a USAF target. (The rings in this figure are due to imperfections in the parallelism of the opposite faces of the crystal.)

An additional feature affordable with two-beam coupling in photorefractive crystals is contrast reversal. The direction of energy transfer is determined by the intrinsic anisotropy of the c-axis in the case of ferroelectric recording media, and by the polarity of the applied field in the case of sillenite materials. Consequently, contrast reversal is easily achievable with BSO crystals by reversing the polarity of the applied field. However, the technique we chose to explore relies rather on the polarization properties of self-diffraction in a <110> oriented BSO crystal.

For simplicity, let's assume that the polarization states shown in Fig. 5 can be realized. This figure shows the state of the transmitted beam with ($\Gamma \neq 0$), and without coupling ($\Gamma = 0$). (The case without coupling corresponds to a perfect erasure.) For these two cases, the polarizations are assumed weakly elliptical (they could be linear), with orthogonal major axes (or a large angle between them). A rotating analyzer helps enhance the intensity of the erased area over the undisturbed one, or vice versa. Consequently, if the angle α of Fig. 5 is equal to zero, the intensity in the undisturbed region is weaker than in the erased area, and hence the contrast is positive (erasure increases intensity). On the other hand,

with an angle equal to $\pi/2$, the intensity in the erased region is weaker, and hence the contrast is negative. According to the study of Ref. 4, situations like these can happen with a <110> oriented BSO crystal; unlike the case of a <001> crystal, for which the major axes are always almost parallel, and contrast selection is not possible. Figure 6 illustrates this positive/negative spatial light modulation in which the choice is made with a rotating analyzer placed behind the crystal.

In summary, photorefractive spatial light modulation is achievable with two-beam coupling configurations. The particular case of BSO crystals is interesting to study because the Doppler-enhancement technique, and the polarization properties of different cuts, not only allow incoherent-to-coherent optical conversion, but also positive or negative contrast selection with simple means, such as a rotating polarization analyzer.

Critical review of this summary by G. A. Hayward and S. Jain is acknowledged.

References

[1] See other papers in this issue, for example.
[2] J. P. Huignard and A. Marrakchi, Opt. Comm. 38, 249 (1981).
[3] A. Marrakchi, R. V. Johnson, and A. R. Tanguay, Jr., J. Opt. Soc. Am. B3, 321 (1986).
[4] A. Marrakchi, R. V. Johnson, and A. R. Tanguay, Jr., IEEE JQE-23, 2142 (1987).

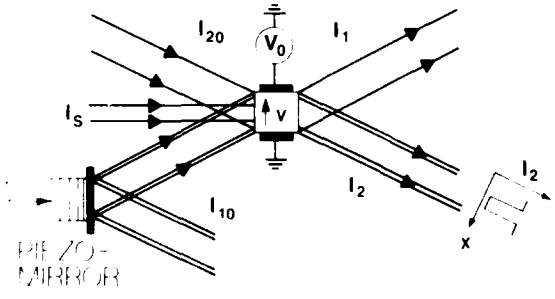

Fig. 1 Photorefractive spatial light modulation based on Doppler-enhanced two-beam coupling.

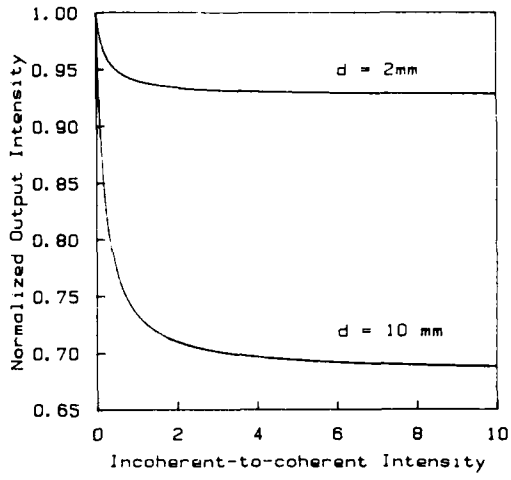

Fig. 2 Normalized intensity after the crystal as a function of the incoherent-to-coherent intensity ratio.

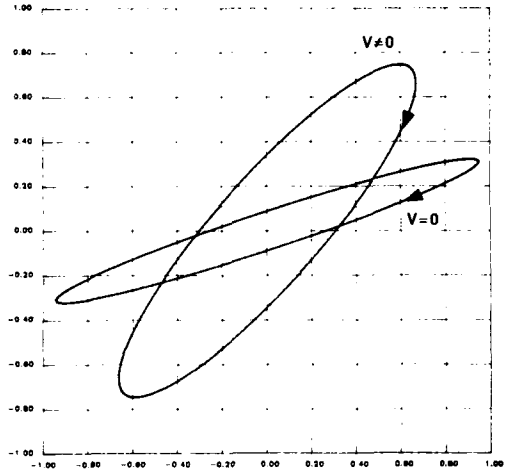

Fig. 3 Polarization state of the transmitted beam for the stationary and the Doppler-shifted grating cases.

Fig. 4 Incoherent-to-coherent conversion of a USAF resolution chart.

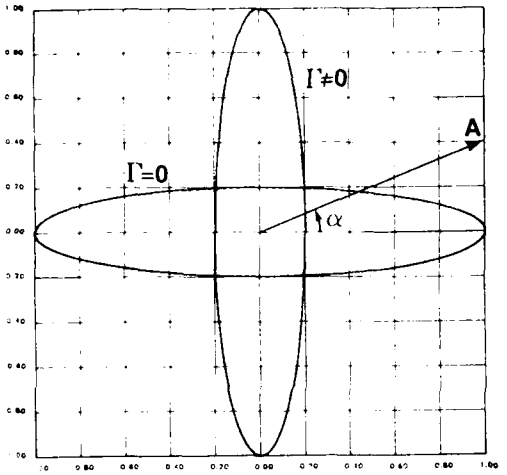

Fig. 5 Polarization state of the transmitted beam for a configuration with coupling ($\Gamma \neq 0$), and without ($\Gamma = 0$).

Fig. 6 Incoherent-to-coherent conversion with contrast reversal.

Photorefractive Spatial Light Modulator as a 2-D Beam Steering Array.

G. ROOSEN

Institut d'Optique Théorique et Appliquée, U.A. CNRS
Bâtiment 503, Centre Universitaire d'Orsay, B.P. 43
914006 ORSAY Cédex - FRANCE

Free space optical interconnections are of prime importance for both optical communications[1] and optical computing[2].

Indeed optics offers a naturally parallel environment with a potential for dynamic, arbitrary and global interconnects between two dimensionnal arrays of processing elements or fiber optic networks.

Optics is attractive for interconnects because the inherent non interaction properties of light beams. This means that in a linear medium optical pathes can cross without any effect and that light travelling in one channel does not affect light travelling in another channel.

An obvious manner for exploiting these powerful properties of optics is to use a 2-D holographic method to steer free space beams between n^2 input ports and n^2 receiving ports. However this has to be done in such a manner that a change in any particular interconnect link will not affect any other interconnect links.

The deflection matrix to implement could consist of a 2-D array of independent cells in which independent gratings will be recorded with different parameters so that a multitude of input beams will be steered independently of one another in different directions[3].

The realization of reconfigurable interconnect patterns will be reached by modification of either the whole deflection matrix or any single cell independently. This requires both a dynamic method for establishing and changing the desired pattern of subholograms and nonlinear optical materials for efficient recording of these steering gratings.

As very likely, high diffraction efficiencies will be desired, the deflection matrix will certainly consist of thick holograms. Therefore the issue of Bragg selectivity will have to be carefully considered.

In this conference, we will first present one of the solution, we propose for achieving large scale dynamic optical interconnections. It is based on real time holography that is diffraction of signal beams by optically induced transient gratings.

Variation of the diffraction direction of signal beams is achieved by shifting the optical frequency of a control beam[4]. A method allowing a minimization of Bragg detuning and thus a maintain of an optimum efficiency over large scan angles will be described and its performances discussed. First experimental results will be given, showing the possibility of simultaneously steering more than 10^4 independent channels.

The non linear medium used in these experiments was a crystal of bismuth silicone oxyde (BSO). It belongs to a class of photoconductive and electro-optique materials that exhibits a strong optical non linear behavior through the photorefractive effect. An important feature is the possibility of generating this non linearity with low power laser beams. On the other hand fast response times are obtained with pulse excitations[5,6]. The photorefractive effect has been found in a large variety of crystals, resulting in a broad range of spectral sensitivities, spatial resolutions, efficiencies and speeds.

We will briefly discuss on these properties in the light of the interconnect problem, choosing BSO as an exemple[7].

(1) P. Gravey, Proceed., 7th ECOC 81, 1981

(2) J.W. Godman, F.I. Leonberger, S.Y. Kung, R.A. Athale, Proceed. IEEE, 72, 850, 1984

(3) G. Pauliat, J.P. Herriau, A. Delboulbé, G. Roosen, J.P. Huignard, J. Opt. Soc. Am. B, 3, 306, 1986

(4) G.T. Sincerbox, G. Roosen, Appl. Opt., 22, 690, 1983

(5) G.C. Valley, A.L. Smirl, M.B. Klein, K. Bohnert, T.F. Boggess, Opt. Lett., 11, 647, 1986

(6) J.M.C. Jonathan, Ph. Roussignol, G. Roosen, Opt. Lett., 13, 1988.

(7) G. Pauliat, M. Allain, J.C. Launay, G. Roosen, Opt. Comm., 59, 266, 1986 and 61, 321, 1987.

WEDNESDAY, JUNE 15, 1988

EMERALD BAY BALLROOM

3:30 PM–4:40 PM

WD1–3

ELECTRO-OPTICAL DEVICES

Cardinal Warde, Massachusetts Institute of Technology, *Presider*

Highly-Parallel Holographic Integrated Planar Interconnections

Tomasz Jannson and Shing-Hong Lin
Physical Optics Corporation
2545 W. 237th St.
Torrance, CA 90505

1. Introduction

The concept of using holograms or holographic devices to realize optical interconnection has been subjects of recent investigations [1,2]. In conventional holographic architectures, the holographic optical elements (HOEs) that interconnect signals between the input sources such as laser diodes (LDs) and the output receivers such as photodiodes, fibers, etc., are generally not located in the plane of the optoelectronic and VLSI elements. This type of 3D free-space holographic interconnect has important limitations. First, alignment problems are critical. If the sources and detectors are not in exact 3D alignment with the opposing holographic elements, performance suffers possibly to the point where the interconnect becomes inoperative. Second, and more importantly, even assuming ideal conditions, conventional Bragg holographic interconnect previously proposed cannot, in theory or practice, provide the large number of interconnections ($N >> 10$) needed in the typical VLSI systems. In short, the interconnectability of such bulk holographic system is limited by the small hologram thickness (~10 to 20 μm).

The optical interconnect approach being investigated in this paper has its basis in holography; however, it utilizes a radically different class of holograms known as *planar multiplex holograms*. This new class of *volume holograms* operate on guided waves in the monolithic integrated optic substrates and is very compatible with microelectronic elements. Most notable among its features, the Bragg selectivity of a planar multiplex hologram, first described by Jannson[3], is not limited by hologram coating thickness. Thus, the interconnectability of the resulting *highly parallel integrated optical interconnects* can be very large, reaching up to 10^8 channels per cm^2 for full interconnects.

2. Holoplanar Optical Inteconnects

The proposed holoplanar optical interconnections are based on the planar Bragg holography [3]. The resulting interconnect configuration combines the technology of integrated optics, total internal reflection (TIR) hologram [4], and planar Bragg holograms in a monolithic form. As depicted in Figure 1, the laser diode array, driven by electronic signals, emits spherical wavefronts which are ideally transformed (i.e., in a diffraction-limited manner) to waveguide zig-zag waves by the TIR holograms. The guided waves are in turn redirected or distributed to various target connections by a multiplexed thick 2D planar Bragg hologram which is co-planar with the waveguide. The planar Bragg structure can be fabricated in either passive or active material, resulting in static or dynamic interconnections. This configuration achieves the advantage of free-space interconnections and yet allows the compact packaging of integrated optics.

3. Theory of Planar Bragg Holography

If we introduce with prism coupling, for instance, two or more planar guided waves interferring within the thin photosensitive coating (e.g., dichromated gelatin), a planar hologram can be recorded. Assuming, for simplicity, only two elementary planar waves, with planar wavevectors $\underline{h}_o$ and $\underline{k}_o$ (i.e., the (x,y)-projections of zig-zag guided wave wavevectors), they will record a planar holographic grating with grating vector $\underline{K}$ as shown in Figure 2. Thus, we can adopt the conventional 3D theoretical models of Bragg holograms, especially including Kogelnik's coupled wave theory [5] in describing planar Bragg holograms. In particular, all basic properties of Bragg holograms, such as angular/wavelength selectivity, peak diffraction efficiency, wavelength dispersion, etc., can be easily calculated on the basis of their horizontal or planar dimensions. At this point, we have arrived at a very interesting fundamental property of planar Bragg holograms, namely these holograms can be very "thick" in the sense of planar dimensions (i.e., T_x or T_y in Figure 2). This large effective hologram thickness enables highly-efficient Bragg holograms with excellent angular/wavelength Bragg selectivity to be obtained.

4. System Interconnectability for Single Mode Waveguides

In order to determine the interconnectability of the typical holoplanar interconnect system in the single mode waveguide, it is necessary to estimate the angular Bragg selectivity of multiplex planar Bragg holograms. Using Rayleigh resolution criterion [3], the theoretical minimum angular distance between two planar waves recognizable by the system is approximately given by [6], $(\Delta\theta)_{min} = \lambda_m / T$, where T is planar hologram "thickness" (equivalent to T_x or T_y), and λ_m is an effective wavelength of the waveguide mode corresponding to λ/n_m, where λ is the optical wavelength in vacuum. Assuming λ_m = 0.5 μm and T = 1cm, we obtain an outstanding value of $(\Delta\theta)_{min} = 0.003^o$, which is equivalent to more than 10^4 spatial degrees of freedom stored and later to be reconstructed for the planar hologram in a 30°-total scanning angle.

5. Experimental Results

(1) TIR Holograms

The basic function of the TIR holograms is to transfer the diverging light from laser diodes or LEDs into directional planar guided waves for processing the planar Bragg hologram. We have designed and fabricated efficient TIR holograms based on dichromated gelatin coatings. The experimental result ofthe TIR hologram is shown in Figure 3. Experiments on dichromated gelatin coatings have successfully shown the wavefront transforming operation.

(2) Planar Bragg Holograms

In order to demonstrate the interconnects in the monolithic planar waveguide, based on the proposed planar Bragg holograms, POC has conceived a special proprietary technique that enables the free-space recording of multiple-grating planar holograms with a 488 nm Argon laser while reconstructing the holograms with a 632.8nm He-Ne laser. Several one-to-many channel planar Bragg holograms were successfully fabricated on dichromated gelatin.

The experimental results for 1-to-3 (2-gratings) and 1-to-9 (8 gratings) fan-out are illustrated in Figures 4.

6. Conclusions

The proposed interconnect configuration combines two holographic technologies (TIR and planar Bragg holograms) in an integrated optics monolithic format that performs ultra-high density interconnect operations in a co-planar manner. We have demonstrated successfully that the holoplanar interconnect technology is experimentally feasible. It should be emphasized that the successful realization of highly-rugged, fully-parallel, high-density (N > 100) and highly-efficient holoplanar Interconnects will be breakthrough in many areas of optical computing, optical information processing and optical telecommunication, where the low-loss full-parallelity is of vital importance.

References

1. J. W. Goodman, et al, "Optical interconnections for VLSI applications," IEEE Proc. 72, 850 (1984).
2. R.K. Kostuk, J.W. Goodman and L. Hesselink, "Design considerations for holographic optical interconnects," Appl. Opt. 26, 3947 (1987)
3. T. Jannson, "Information capacity of Bragg holograms in planar optics." JOSA 71, 342 (1981)
4. W. Lukosz and A. Winthrich, "Holograms recording and read-out with the evanescent field of guided waves," Optics Comm. 19, 232 (1976)
5. H. Kogelnik, "Coupled wave theory for thick hologram gratings, Bell Syst. Tech, J. 48, 2909 (1969)
6. T. Jannson, et al, "The interconnectability of neurooptic processors," SPIE 698, 157 (1986)

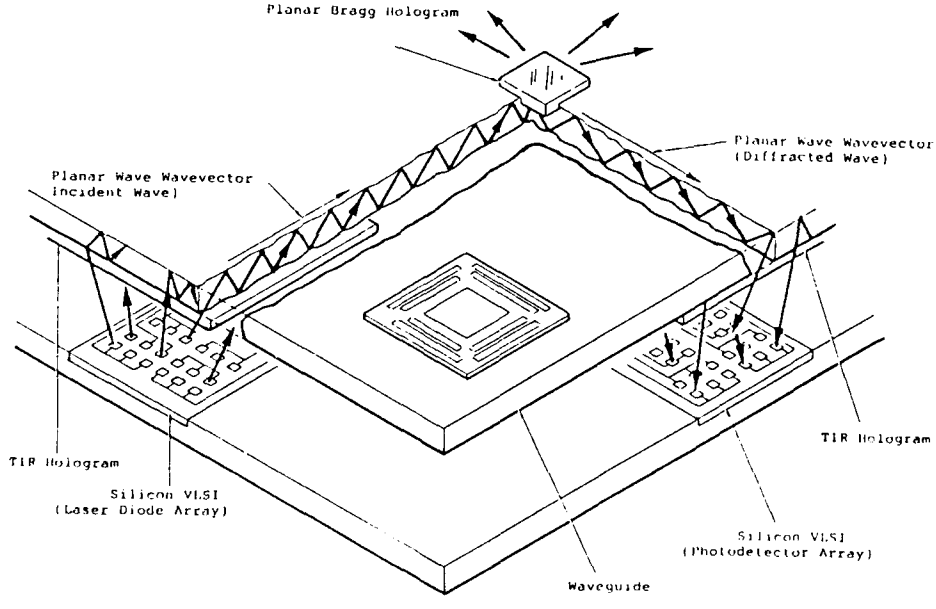

Figure 1 Overall holoplanar optical interconnection architecture layout.

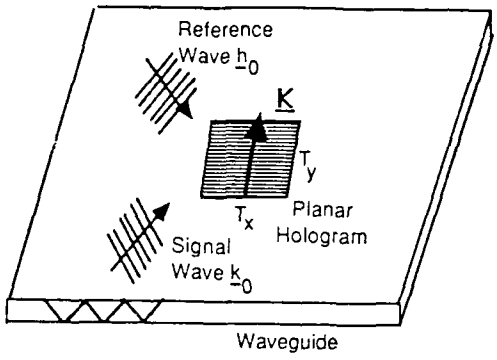

Figure 2 Geometry of planar Bragg hologram in a waveguide.

Figure 3 Photograph from experimental fabrication of TIR hologram.

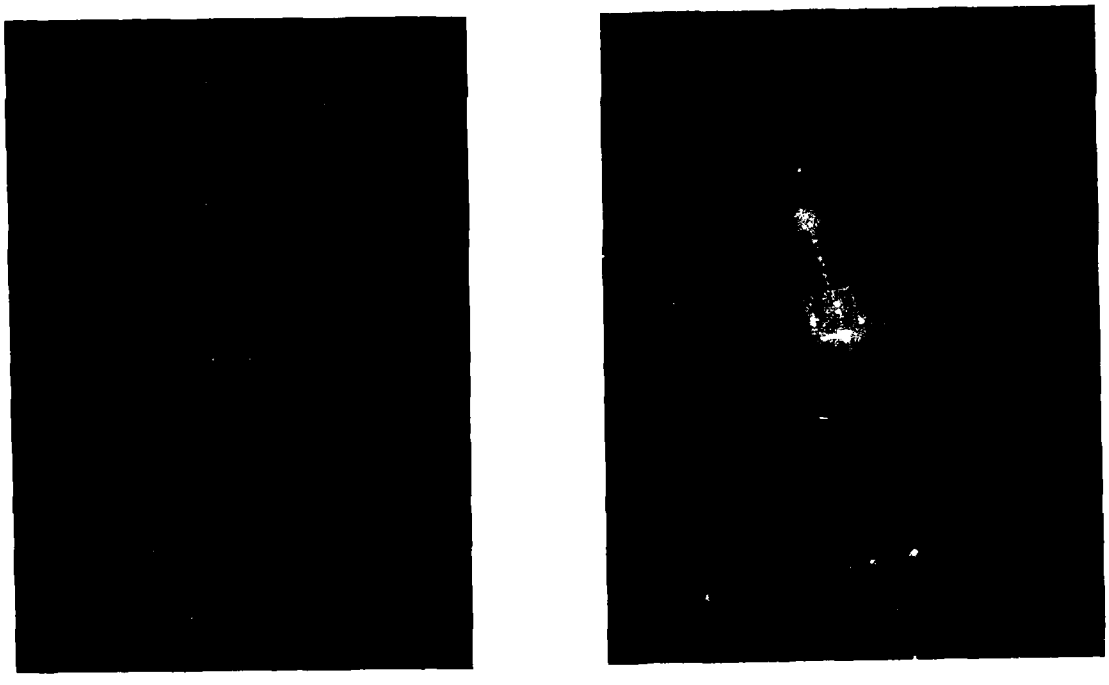

Figure 4 Photograph from experimental fabrication of one-to-many interconnect holograms.

Development Issues for MCP-Based Spatial Light Modulators

John N. Lee and Arthur D. Fisher
Optical Sciences Division, Naval Research Laboratory, Washington, DC 20375

I. Introduction

Several of the most critically needed characteristics for two-dimensional (2-D) spatial light modulators (SLMs) include i)high input sensitivity, ii)high resolution, iii)long storage times, iv)high speed, and v)large dynamic range. One would desire to maximize all these characteristics simultaneously, but in actuality there exist tradeoffs that prohibit complete freedom in optimizing one parameter in isolation from the others. The microchannel-plate (MCP) devices, however, can be shown to have tradeoff points allowing unique performance in several of the above characteristics. The use of an MCP electron amplifier allows for internal signal gain, unlike most other SLMs where the output signal gain can be increased only by increasing the readout light level. Thus, detection and processing of very low signal levels, such as often encountered in multistage and feedback processing, becomes feasible. Further, MCP-based devices can intrinsically perform special image-processing operations (see Sec. III below).

The basic stucture of an optically-addressed SLM incorporating an MCP is shown in Fig. 1. The input, writing image impinges on basically an image-intensifier structure, consisting of a photocathode-MCP arrangement, but followed by an optical modulating material, instead of a by a phosphor screen (as in an intensifier tube). The most extensively investigated modulator materials have been electro-optic crystals such as $LiNbO_3$ and $LiTaO_3$, used in the Microchannel-plate Spatial Light Modulator (MSLM)[1,2], and 50-nm thick nitrocellulose membranes, used in the Photoemitter Membrane Light Modulator (PEMLM)[3]. Upon deposition of charge onto the modulating material both types of modulator provide phase modulation of the readout beam, and amplitude modulation with subsequent polarizing or interferometric optics. Charge of either polarity may be deposited. Charges are removed by bias voltage polarity reversal and using secondary emission characteristics[2,3]. An electrically addressed variant of Fig. 1 replaces the input optical beam with an electrical addressing mechanism such as a scanned electron beam. An extensive amount of development has been done; the MSLM is available in both optically and electrically addressed versions[4,5], and a number of prototypes are being developed for both the MSLM and the PEMLM[6]. We review the major performance advances achieved, and discuss the some of the major developments still needed.

II. Device Performance

Sensitivity: The sensitivity can be made to be virtually quantum limited, due to the gain provided by the MCP and the ability to integrate charge on the membrane or crystal. Full contrast responses can be obtained with only a few photons/pixel, but it is usually desirable to operate with reduced gain to collect more photons for increased quantum-limited signal-to-noise ratio. For the specific case of the PEMLM[3] with a 6μm-radius membrane, a photocathode quantum efficiency of 10% at 633 nm, and MCP gain of 8400, full contrast modulation can be obtained with 50 photons/pixel, corresponding to a calculated write energy of only 140 pJ/cm^2 or 0.016 fJ/pixel. This is about 50x less than the lowest reported energy required to switch a single bistable optical element[7], although the switching speed there is about 1 ns; on the other hand, the MSLM and PEMLM are three-port, image-multiplying, devices with isolation between input and output.

Speed and Resolution: These cannot be optimized independently of each other. As is the case for most SLMs, the intrinsic material response time of the electro-optic crystal (psec) or a membrane element (< μsec[6]) is not the

limitation. Rather, it is the maximum rate at which charge can be deposited onto the material and the capacitance of the system. Capacitance can be decreased, but not without also decreasing the resolution. For example, in the MSLM the electro-optic crystal capacitance can be decreased by increasing its thickness, but this will reduce resolution, since increased fringing of the electric field lines will occur between the charge deposited on one side of the crystal and the transparent electrode on the other side. The product of number of resolution cells and the frame speed (or pixels/sec) tends to remain constant for a given type of SLM, and is therefore useful as a figure of merit. For the MSLM it is possible to obtain frames with 3×10^5 cells with 30 msec update time, or about 10^7 pixels/sec. For the PEMLM one can extrapolate a figure of merit of 10^{10} pixels/sec, based on constructed devices with 10^7 cells and observations of about 1 msec response times.

Storage Time: Images have been stored on an MSLM for several months[2]. On the PEMLM, storage times ranging from minutes to hours have been observed[3]. The storage times of the MSLM can be attributed somewhat to the high values of dielectric constant, but mostly to the bulk and surface resistivity for $LiNbO_3$; the product of these two quantities gives a time constant for charge decay of several months. Surface resistivities, however, are not well understood, and large variabilities are observed[8].

III. Threshold and Other Special Operations

The MSLM and PEMLM also have intrinsic capabilities for bipolar operation and nonlinear thresholding[9]. The former allows addition and subtraction on arrays of data, and synchronous detection of a temporally modulated intensity object (i.e., a pixel array of lock-in detectors). The thresholding operation utilizes the electron dynamics for charge deposition and removal from the modulating material. One type of thresholding operation on an optical field begins by first uniformly pre-charging an insulating target with electrons and then using the electrons generated by the optical information to "erase" the uniform charge. Erasure of the charged target occurs only where the input intensity is above a critical level, determined by the rate-of-change of a bias voltage (V_b) applied on the target [3,8]. This behavior can be qualitatively understood by referring to Figs. 2 and 3, which model the MSLM device as a parallel-plate capacitor system, where i_g is the current flowing to the crystal (XTAL in Fig. 2), V_g is the voltage between the crystal and a metal grid that follows the electron source, V_b is the voltage applied to the transparent electrode on the crystal, V_c is the applied grid voltage, and V_x is the voltage drop across the crystal itself. Depending on the value of V_g, the polarity of i_g may be either positive (deposition of electrons) or negative (secondary emission removal of electrons). The basic dependence of i_g on V_g is shown in Fig. 3 for two intensities (A > B); these solid curves are simply scaled versions of each other. Normally, a stable equilibrium occurs at $V_g = V_{go}$, where $i_g = 0$. An increase of V_g causes electron buildup on the crystal ($i_g > 0$), driving V_g more negative, back towards V_{go}. A decrease of V_g allows more secondary emission electrons to escape from the crystal ($i_g < 0$), driving V_g more positive.

Examination of Fig. 2 reveals that a change in the bias voltage V_b induces the additional capacitive displacement current

$$i_g = C_x(\dot{V}_b - \dot{V}_g) \qquad (1)$$

where C_x is the capacitance across the crystal (or between the membrane and transparent electrode in the PEMLM). In the absence of any electrons from the MCP, this capacitive current also changes V_g ($\dot{V}_g = i_g/C_g$). However, in the presence of an MCP photocurrent, a new stable equilibrium of V_g can still be maintained, despite the changes in V_b; then $\dot{V}_g = 0$ and Eq. (1) becomes $i_g = C_x\dot{V}_b$.

The new equilibrium occurs at $V_g = V_{g1}$ in Fig. 3, where the i_g vs. V_g curve for intensity A intersects the $i_g = C_x\dot{V}_b$ load line (horizontal dashed line, for $\dot{V}_b < 0$). At this equilibrium the MCP-driven current (secondary emission) transports charge between the crystal and grid at the same rate displacement-current charge is being capacitively applied from V_b, preventing any net charging of C_g and resulting in the total capacitive charge from V_b being applied to the crystal, V_x (i.e., $\Delta V_g = 0$ and $\Delta V_x = \Delta V_b$). The stability of this equilibrium can be understood by considering two cases. If $V_g > V_{g1}$, then the MCP-driven current($|i_g|$ on the i_g vs. V_g curve of Fig. 3) is smaller than$|C_x\dot{V}_b|$, and there is an excess, uncompensated capacitive current driving V_g more negative (remember, $\dot{V}_b < 0$). If $V_g < V_{g1}$, then $|i_g| > |C_x\dot{V}_b|$ and the excess i_g charges C_g more positive.

There is no equilibrium point if the optical intensity is too low to make the i_g vs V_g curve intersect the load line (e.g., intensity B in Fig. 3). The full capacitive charge from V_b is then coupled into V_g, i.e., $\Delta V_g = \Delta V_b$ and $\Delta V_x = 0$ (Note: $C_x >> C_g$). There are thus two operating regimes, separated by a distinct intensity threshold, occurring at the intensity where the i_g vs. V_g curve shifts to just cross the $C_x\dot{V}_b$ load line. Writing-image regions with intensities I_w below the threshold I_t produce no change in output modulation (since $\Delta V_x = 0$), and the intensities exceeding the threshold produce a full change in modulation (with $\Delta V_x = \Delta V_b$). This threshold intensity is given by

$$I_t = \left[\frac{h\nu}{\eta q G A}\right]\frac{C_x\dot{V}_b}{F(V_{gp})} \qquad (2)$$

where $F(V_{gp})$ is the most negative value of i_g on a normalized i_g vs. V_g curve in Fig. 3, and the bracketed term converts current into optical intensity. A more rigorous analysis[8] shows that for $I_w < I_t$, the crystal or membrane charge (or voltage change) is proportional to $\ln(1 - I_w/I_t)$, which often gives a very distinct threshold for typical device parameters. The two output modulation levels can be arbitrarily set by the choice of starting and ending voltages for the decreasing ramp in V_b. These photo-electronic SLMs therefore offer a fully programmable thresholding operation, with independently settable input threshold intensity and output modulation levels. Figure 4 shows an experimental demonstration of the hard-clip thresholding operation with the MSLM; the 6-level grey scale image in Fig. 4 was thresholded at five different adjustable threshold levels in Figs. 4b-4f. The two output levels were set for an inverted-contrast response. This threshold capability then allows other operations to be performed, such as edge enhancement[9], Boolean logic, and nonlinear transfer functions, e.g., logarithmic[10].

IV. Development Directions

While enormous performance potential is evident, there are a number of shortfalls in present devices in manufacturability, applicability, and performance. These devices rely on photocathode technology which is still somewhat of an art, expensive, and limited to wavelengths shorter than 700 nm. Also, fabrication and materials must be compatable with the fabrication and characteristics of photocathodes which are notoriously susceptible to poisoning and must be baked and kept under ultrahigh vacuum; this is a particular worry with the nitrocellulose membrane in the PEMLM. Work continues on investigation of PEMLM operation with other membrane materials that can withstand high vacuum bakeout temperatures, such as SiO_2, Al_2O_3, and parylene, and using physical isolation techniques between the membrane and the photocathode region such as electron permeable membranes.

Many optical processors operate at laser diode wavelengths near 830 nm, so photocathodes sensitive at this wavelength need to be incorporated (e.g., standard S1 or GaAs photocathodes). However, recent demonstration of arrays of

sharply-pointed silicon or metal field emitters[11], raises the possibility of VLSI production of "synthetic" photocathodes with very high current carrying capability and tailored spectral response; such structures could also increase device speed and obviate many materials compatability issues. Speed can also be significantly enhanced by employing recently developed MCP technology having very high strip current (which is directly related to the ultimate device charging times); strip currents of 100 mA/cm^2 appear feasible[12], or about 10^3 times present levels.

References

1. C. Warde, A.D. Fisher, D.M. Cocco and M.Y. Burmawi, Opt. Lett. 3, 196 (1978).
2. C. Warde, A. Weiss, A.D. Fisher and J. Thackera, Appl. Opt. 20, 2066 (1981).
3. A.D. Fisher, L.C. Ling, J. N. Lee and R.C. Fukuda, Opt. Eng. 25, 261 (1986).
4. T. Hara, K. Shinoda, T. Kato, M. Sugiyama and Y. Suzuki, Appl. Opt. 25, 2306 (1986).
5. K. Shinoda and Y. Suzuki, Proc. SPIE 618, (1986).
6. L.C. Ling, R. C. Fukuda, A.D. Fisher and J. N. Lee, Proc. SPIE 684, 7 (1986).
7. M Dagenais and W. F. Sharfin, Opt. Eng. 25, 219 (1986).
8. A.D. Fisher, "Techniques and devices for high-resolution adaptive optics," PhD Thesis, Massachusetts Institute of Technology (1981).
9. J.A. McEwan, A.D. Fisher and J. N. Lee, Digest of Postdeadline Papers, Fifth IEEE/OSA Conference on Lasers and Electro-Optics, paper PD-1, (1985).
10. H. Kato and J.W. Goodman, Appl. Opt. 14, 1813 (1975).
11. A. Campiri and H. Gray, Proc. 1987 Matl. Res. Soc. Symp. 76, 67 (1987).
12. J. Anderson, Galileo Electro-Optics, private communication.

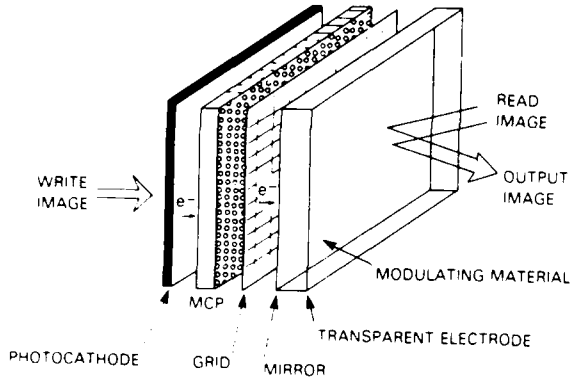

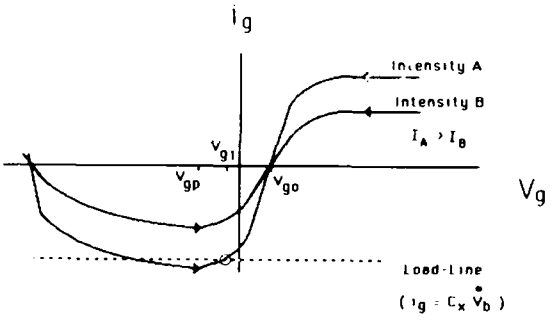

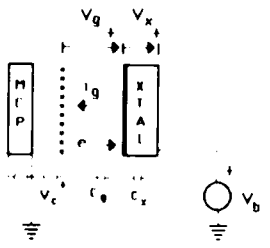

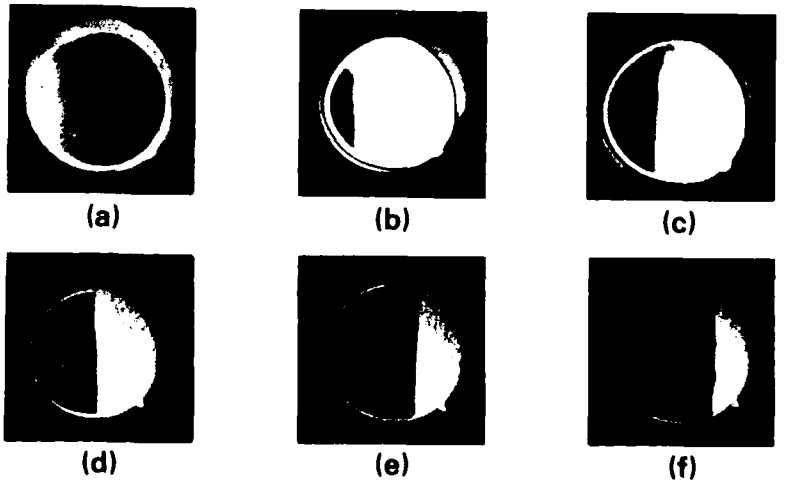

Transfer characteristics of Microchannel Spatial Light Modulator

Y. Suzuki, T. Hara and M. H. Wu*

Hamamatsu Photonics K. K.
1126-1 Ichino-cho, Hamamatsu 435 Japan

*Hamamatsu Corporation
360 Foothill Road, P. O. Box 6910, Bridgewater, N. J. 08807-0910

Introduction

Microchannel Spatial Light Modulator (MSLM) [1),2),3)] can be used as a key device in the system for optical computing and optical neural network because this device has many functions [4),5),6)]. The MSLM is an optical addressing spatial light modulator, that is, the read-out light intensity is modulated by the writing light energy. Therefore it is important to recognize its input-output characteristics (the transfer characteristics) when we design the optical system with this device. In this paper the transfer characteristics of the MSLM will be theoretically and experimentally discussed.

Principle of operation

The principle of the basic operation of the device is shown in Fig. 1. When the photocathode, on which the input image is usually projected, is illuminated with a uniform light, the photoelectrons are emitted. For writing light, various wavelengths can be used. The photocurrent i_w [A] is written by a following equation.

$$i_w = SAL \tag{1}$$

where S [A/W] is the photocathode sensitivity, A [m^2] is the effective area of the photocathode and L [W/m^2] is the light intensity on the photocathode.

The electric current i_{in} [A] on the input side of a microchannel plate (MCP) after undergoing accerelation and focusing from the grid and the anode is

$$i_{in} = \alpha_1 SAL \tag{2}$$

where α_1 is an electron transmittance of the grid.

When the MCP gain is G, the output current i_{out} [A] from the MCP is shown as follows.

$$i_{out} = \alpha_1 SALG \tag{3}$$

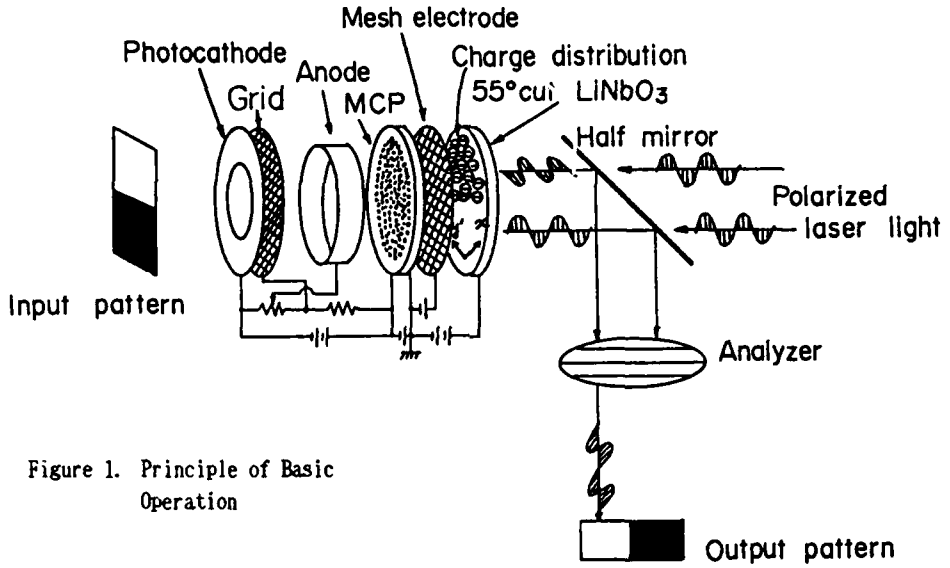

Figure 1. Principle of Basic Operation

The current i [A] which can reach the crystal surface (the top layer of the dielectric mirror) through the mesh electrode mounted between the MCP and the electrooptic crystal (55 degree cut $LiNbO_3$) is written by

$$i = \alpha_1 \alpha_2 SALG \tag{4}$$

where α_2 is the electron transmittance of the mesh electrode.

Then the electric charge is deposited onto the surface of the crystal. This electric charge can be controlled by the mesh electlode. The electric charge Q [q] is

$$Q = \alpha_1 \alpha_2 SALGT(\delta - 1) \tag{5}$$

where T [sec] is the writing time and δ is the average value of the secondary electron emission ratio in the operating region. These electric charges create a change in the voltage across the crystal.

This voltage V [V] is written by

$$V = Q / C \tag{6}$$

$$C = (\varepsilon_0 \varepsilon^* A) / d \tag{7}$$

where C [F] is the capasitance of the crystal, ε_0 is the dielectric constant of the vacuum, ε^* is the dielectric constant of the crystal and d [m] is the thickness of the crystal. The electric field associated with the voltage modulates the refractive index of the crystal.

By illuminating the crystal from the back with a coherent light which is polarized at 45 degrees to the x axis of the crystal, the light reflected back from the dielectric mirror experiences a phase retardation Γ [rad] corresponding to the change in the

refractive index.

Consequentlly Γ is written as the function of the voltage[2].

$$\Gamma = \{ (V+V_0) / V\pi \} \pi \quad (8)$$

where V_0 is the voltage corresponding to the phase retardation by the natural birefringence of the crystal or uniformly supplied surface charge on the crystal and $V\pi$ is the half wave voltage.

Then an analyzer, which is oriented 45 degrees to the x axis, is now inserted to convert a phase modulated light to an intensity modulated light. The output light intensity I [W/m^2] will be given by

$$I = K \sin^2 (\Gamma/2)$$
$$= K \sin^2 [(\pi/2) \times \{ (V+V_0) / V\pi \}] \quad (9)$$

where K is a constant. By using equations (5), (6) and (7), the equation (9) becomes

$$I = K \sin^2 [(\pi/2V\pi) \times \{\alpha_1\alpha_2 SGLT(\delta-1) \times (d/\varepsilon_0\varepsilon^*) + V_0\}] \quad (10)$$

Transfer characteristics

From equation (10), the transfer characteristics (the relation between LT and I) of the MSLM can be calculated. The results are shown in Fig. 2 and Fig. 3.

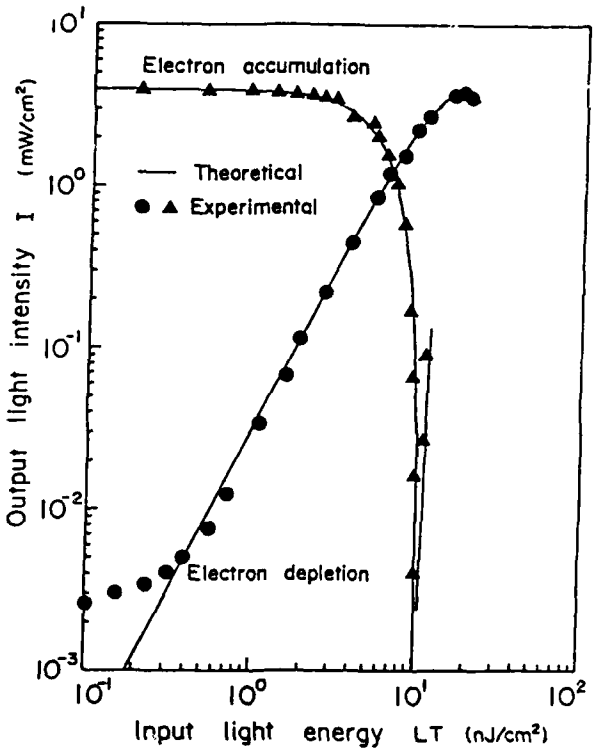

Figure 2. Transfer characteristics for Ar laser

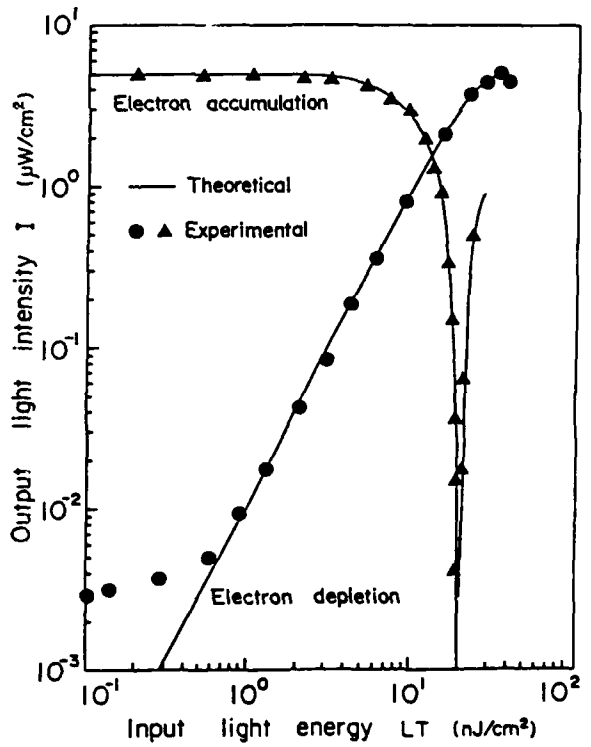

Figure 3. Transfer characteristics for He-Ne laser

In our calculation, we use the following values. K=4 [mW/cm^2] (Ar laser), 5 [uW/cm^2] (He-Ne laser): Vπ = 2.0 [kV] (Ar laser), 2.4 [kV] (He-Ne laser): α_1 = 0.6: α_2 = 0.7: S = 40 [mA/W] (Ar laser), 25 [mA/W] (He-Ne laser): G = 4000: δ = 1.6 (electron depletion), 0 (electron accumulation): ε^*= 30: d = 70 [um]: V_0 =0 (electron depletion), Vπ (electron accumulation), the natural birefringence is compensated in both cases. In this case the electron depletion mode corresponds to the writing mode of the positive charge image and the electron accumulation mode corresponds to the writing mode of the inverse positive charge image [2].

The experimental results also shown in Fig. 2 and Fig. 3 correspond to the calculated results fairly well. The minimum writing light energy for the full modulation (input sensitivity) is 10~30 nJ/cm^2. The maximum output light intensity for Ar laser which is mainly determined by the optical damage of the crystal is 4 [mW/cm^2] on the screen. This value corresponds to 0.1 [W/cm^2] of the light intensity at the crystal.

Conclusion

The transfer characteristics of the MSLM have been discussed. The MSLM can be used at a very low writing light level and at a high read-out light level with the same wavelength. Therefore this device can be used as a key device involving optical feedback, cascading [7] and regeneration of the signal levels in the optical computing [8),9)], optical neural network [10] and other related areas [11].

Acknowledgment

The authors would like to thank Mr. T. Hiruma, President of Hamamatsu Photonics K.K., for giving us the opportunity to carry out these experiments. Thanks are also due to Mr. N. Mukohzaka for assisting the experiment.

References

1) C. Warde, A. D. Fisher, D. M. Cocco and M. Y. Burmawi, Opt. Lett., 3, 196 (1978)
2) T. Hara, M. Sugiyama and Y. Suzuki, Adv. Electronics and Electron Phys., 64B, 637 (1985)
3) T. Hara, Y. Ooi, T. Kato and Y. Suzuki, Proc. SPIE, 613, 153 (1986)
4) C. Warde and J. Thackara, Opt. Eng., 22, 695 (1983)
5) J. A. McEwan, A. D. Fisher and J. N. Lee, CLEO paper PD-1, (1985)
6) T. Hara, K. Shinoda, T. Kato, M. Sugiyama and Y. Suzuki, Appl. Opt., 25, 2306 (1986)
7) Y. Suzuki, T. Hara, Y. Ooi and M. H. Wu, SPIE's OE/Lase'88, LA (1988)
8) T. Hara, N. Mukohzaka and Y. Suzuki, Proc. SPIE, 625, 30 (1986)
9) A. D. Fisher, M. H. Wu, Y. Suzuki, T. Hara and N. Mukohzaka, OSA Meeting, Rochester (1987)
10) A. D. Fisher, W. L. Lippincott and J. N. Lee, Appl. Opt., 26, 5039 (1987)
11) F. T. S. Yu, X. J. Lu, Y. Suzuki and M. H. Wu, Opt. Comm., 63, 371 (1987)

WEDNESDAY, JUNE 15, 1988

EMERALD BAY BALLROOM

8:00 PM–9:30 PM

WE1–3

INVITED SPEAKER SESSION

Demetri Psaltis, California Institute of Technology, *Presider*

FUTURE ROLES OF SPATIAL LIGHT MODULATORS IN ADVANCED COMPUTING ARCHITECTURES

By
John A. Neff
Defense Sciences Office
Defense Advanced Research Projects Agency
Arlington, VA 22209

INTRODUCTION

One of the areas of computer architecture with the most rapid growth is that of parallel multiprocessors - an interconnection of anywhere from a few processing elements (PEs) to millions of PEs operating in parallel on the same problem. Attempts at solutions to many difficult problems in the past resulted in a rapid increase in complexity of software. With the continuing decline in the cost of hardware, attention has turned toward mapping such problems on massively parallel machines. For example, knowledge base searching can be done by pursuing many paths in parallel rather than following a complex algorithm that attempts to guide a serial search in an optimum fashion. The result is that many more computations are performed when following the parallel approach, with most not leading to a solution; however, the correct solution will most often be arrived at much sooner.

For most problem domains, a large number of processors, say n, working in parallel, but independent of one another, will fall far short of solving the problem by a factor of "n" more efficiently than a single processor. Without adequate communication amongst the "n" processors, a great deal of redundant effort often results. The power of the multiprocessing systems is most often in direct proportion to the degree of system interconnection. Nature provides convincing evidence that powerful parallel processors can result from a large number of processors of relatively low complexity being massively interconnected. Highly functional neural systems can result from the use of only thresholding elements (the PEs in this case) heavily interconnected. The fan-out in neural systems can reach as high as tens of thousands.

It is this issue of interconnection being such a powerful factor in parallel multiprocessor performance that suggests a role for optics. Whereas electronics is the superior technology for switching due to the greater ease of charged particles effecting one another, optics is superior in cummunications since the uncharged photons do not exert influence on one another.

The focusing of optics on problems in multiprocessor development is important for more than just the reason that multiprocessors have communication bottlenecks. The maturity of parallel processing is comparable to that of optical processing; therefore, the two technologies can mature in parallel. This presents an easier challenge than attempting to break into a field that has a great deal of momentum behind it. The relatively early

new technology, and if those of us with an interest in the development of optical processing are alert, we will search for ways that optics can aid in the growth of this companion field. This paper will discuss areas in which optics can address multiprocessor bottlenecks, and the way in which 2D spatial light modulators (SLMs) will likely play a key role.

RECONFIGURABLE INTERCONNECTS

Although the foundation of optical interconnects will be fixed point-to-point links between modules, boards, and maybe even chips, the real excitment among computer architects comes upon consideration of reconfigurable interconnects. An SLM based crossbar switch, illustrated in Figure 1a, is being developed for replacing a VLSI crossbar in the MOSAIC multiprocessor shown in Figure 1b. The SLM, whose elements are used as switches, can interconnect any input port with any output by selecting the proper switch to open, permitting the fiber guided light to pass. A 16 x 16 x 1 (the "1" indicating that each port is one channel) will replace the 16 x 16 x 32 VLSI switch that forms the foundation of the MOSAIC, interconnecting numerous special purpose microprocessors such as Fixed Systollic (FSP) and Programmable Systollic (PSP) processors.

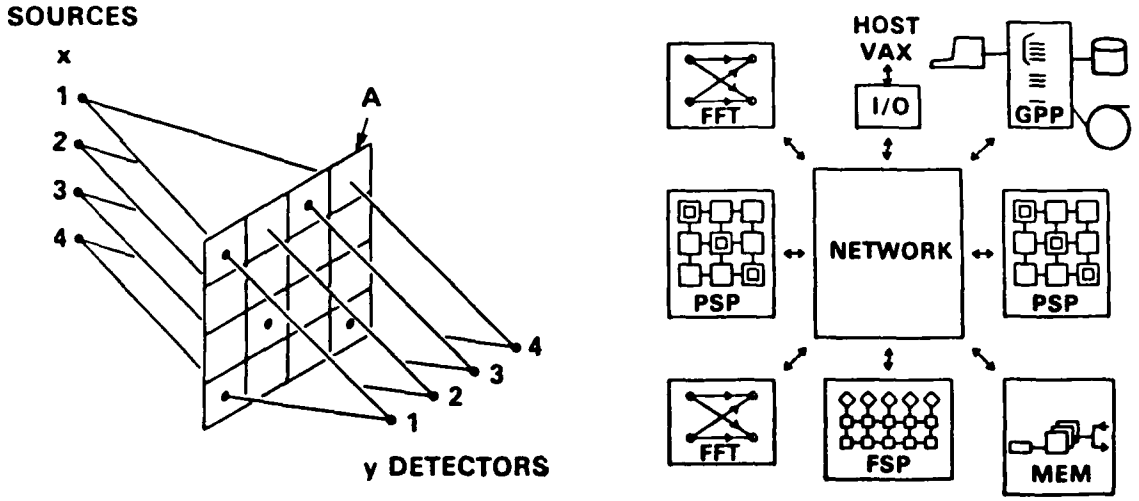

(a) (b)

Figure 1. (a) SLM based optical crossbar switch which will be demonstrated in the MOSAIC multiprocessor shown in (b).

An SLM with varying transmissivities for each pixel could be used to place a weight on each interconnect. This is important for neural network implementation since the weights form the basis of information storage in these networks. Varying the weights results in a change in the information represented by the network, thus a network that can adapt or learn must contain a device which can vary the strengths of the interconnects.

For interconnection via free-space propagation of light beams, a hologram can serve to steer the beams to their proper

provide reconfiguration. Such may be possible someday using wave-mixing in a photorefractive material; however, a near-term solution can use an SLM to select a certain subset of holograms from a hologram array. Similar to the crossbar switch application, the SLM would act as a switch capable of activating the desired set of holograms out of a large array of holograms.

OPTICAL ACCELERATORS

Accelerators are high performance special purpose processors that, upon being added to a parallel computer, can significantly improve the machine's overall performance. For those parallel computers that must routinely perform such operations as correlation and Fourier transforms, optical accelerators will likely prove quite successfull. Work is currently underway to build a digital optical correlator for the MOSAIC, as is illustrated in Figure 2. The correlator will have thousands of digital filters available for read-in on the magneto-optic SLM in the correlation plane. The projected throughput is 50,000 frames/second which equates to 100,000 MOPS for a 128 x 128 SLM. Note that the optical accelerator will be connected to the optical crossbar switch discussed above.

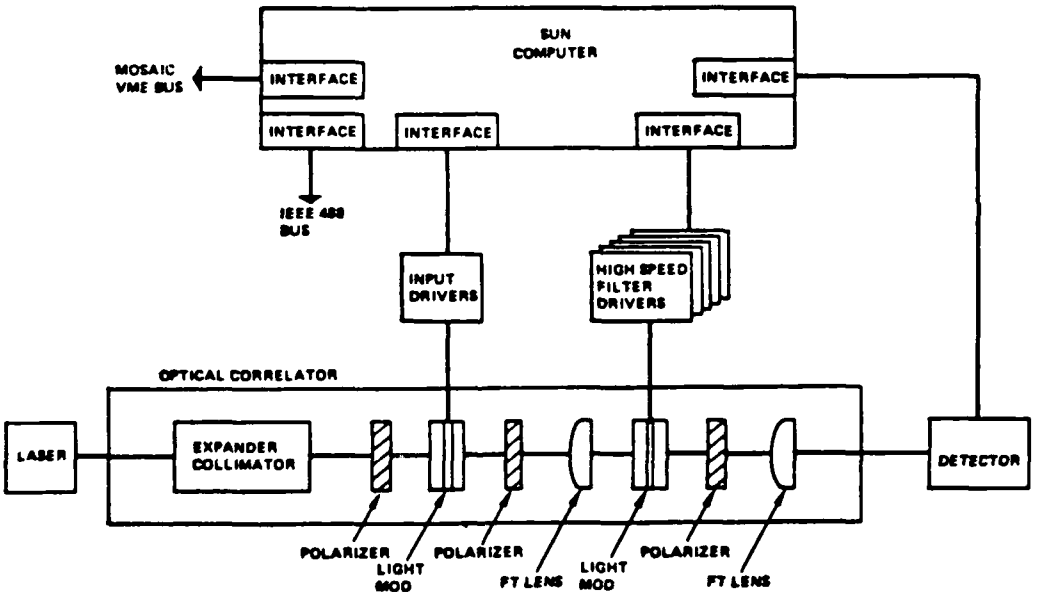

Figure 2. Optical Accelerator for the MOSAIC.

OPTICAL LOGIC ARRAYS

The MOSAIC is a coarse-grained architecture; i.e., the system is an interconnection of several relatively complex microprocessors. At the other end of the multiprocessor spectrum are the fine-grained architectures such as the Connection Machine and neural networks. These architectures are far more interconnect intensive and, in the long run, may benefit even more from the use of optics. As the role of optical interconnects increases, the need to perform optical switching and logic operations will also increase in order to avoid

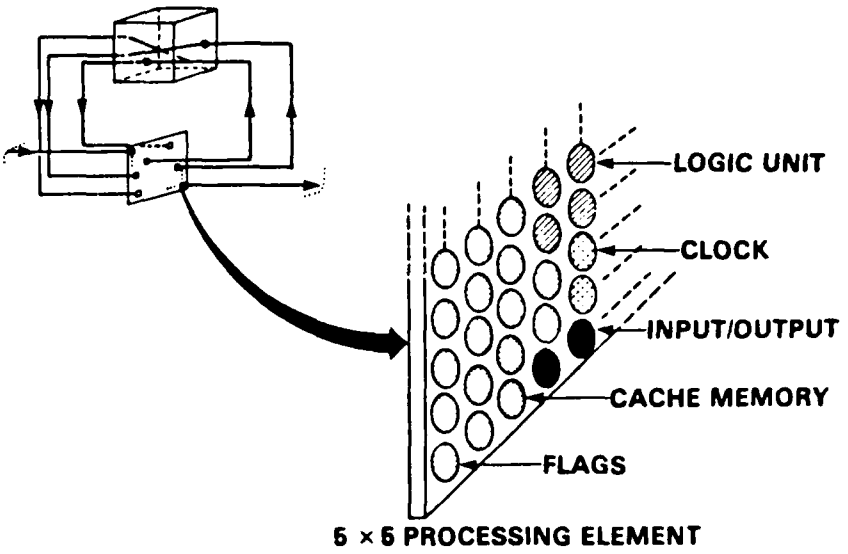

Figure 3. Optical connectionist architecture.

excessive electron/photon conversions. An example of a very basic optical computing unit, shown in Figure 3, can be realized by one SLM exhibiting a nonlinear response and a reconfigurable interconnect unit. The SLM pixels will realize logic operations through use of their nonlinear response, and will be interconnected in various groupings via the interconnect element to form functional circuits.

Figure 3 illustrates a PE of complexity along the line of a Connection Machine. Several logic elements could be interconnected as a PE, and the input/output pixels of the PEs would be interconnected to form the parallel fine-grained multiprocessor. For example, the pixels within each PE could be interconnected to form several registers, an arithmetic & logic unit, and some cache memory. The example shown is for n = m = 5 (25 logic elements per PE) which would permit 40,000 PEs for SLMs and interconnect arrays of 1000 x 1000.

SUMMARY

Realization of optical logic array processors are likely a decade or more away, but they are part of a logical progression of optics for multiprocessing. The success of the progression relies heavily on the initial stages which involve providing reliable optical components for the next generation of these machines. Although the initial insertion of optics will involve fiber-guided interconnects, it should be followed closely by optical crossbars and accelerators. It must be realized that optical computing will come about through an evolutionary process rather than through one day just providing the computing community with machines based on a technology very foreign to them.

Recent Advances and Applications of Ferroelectric Liquid Crystal Spatial Light Modulators

Kristina M. Johnson, Mark A. Handschy*, and Garret Moddel

Center for Optoelectronic Computing Systems
University of Colorado
Boulder, Colorado 80309-0425

*Displaytech, Inc., 2200 Cenral Ave., Suite A, Boulder, CO 80301

Introduction

Optical computing systems offer increased information processing throughput rates by taking advantage of parallel optical architectures. The fundamental component in these architectures is a device which can modulate two-dimensional optical data. These devices, known as spatial light modulators (SLMs) have many applications including input/output data displays, spatial and matched filtering, incoherent-coherent light converters, optical crossbar switches, optical interconnection networks, and neurocomputing. The ideal system requirements placed on SLMs include high resolution (100 lp/mm), 1000 x 1000 pixels, megahertz frame rate, 100 grey levels, 1000:1 contrast ratio, and low cost [1]. An operating characteristic which often prevents SLM's from reaching these goals is device power dissipation [2]. Furthermore, devices which have large commercial markets have a better chance of meeting these systems requirements. In this paper we will discuss a new class of materials, ferroelectric liquid crystals (FLCs), that potentially can meet all the above system requirements.

Material Properties

FLCs are strongly birefringent uniaxial materials whose optic axis can lie anywhere on a cone of angle ψ; the cone axis is fixed to the material's structure. They are ferroelectric, with spontaneous polarization P perpendicular to both the optic axis and the cone axis. The electrooptic effects arise form the fact that the optic axis can easily be reoriented by the torques produced by applied electric fields E that align P parallel to E.

These electrooptic properties can be exploited by placing a thin slab of FLC between electrode plates, with the cone axis parallel to the plates. This device can function as an intensity modulator when placed between crossed polarizers, with the optic axis states selected by opposite signs of applied voltage lying parallel to the plates, but differing in orientation by 2ψ. When $\psi = 22.5^{o}$ and the slab thickness is approximately matched to the FLC birefringence, the device is a half-wave plate which yields light linearly polarized at an angle 90^{o} to the incident polarization. This light is then completely transmitted through the analyzer. Without its polarizers, this device functions as a polarization modulator, rotating the light's polarization by either 0^{o} or 90^{o}. Phase modulators of arbitrary modulation depth can

be made by setting the polarizer parallel to one of the optic axis states, and setting the analyzer perpendicular to the other optic axis state, with the phase difference between the two states controlled by the device thickness. This mode of operation gives a throughput of $\sin^2 2\psi$. All three modes of operation are equally feasible, and operation in reflection requires only that the FLC slab be half as thick as for transmission, and that the second plate be reflective. a These electrooptic properties lead to the following expectations for the characteristics of SLM elements made from FLCs:

1. Size. The minimum size of a switched element is determined by the wavelength of light being switched and the strength of its interaction with the switching medium. By comparison to most other electrooptic effects, the interaction of light with FLCs is extremely strong. For a two-state element ("switched" and "unswitched") the interaction strength may be characterized by the length in which a ray of polarized light propagating through the switched state experiences a 180° phase shift relative to what it would experience propagating through the unswitched state. For the FLC, this length is $\lambda/(2\Delta n)$, where λ is the vacuum wavelength of the light and Δn is the birefringence of the FLC. With typical Δn's = 0.1 - 0.2, the factor $1/(2\Delta n)$ takes values between 2.5 and 5. Thus, the element could have a square cross section, with side dimension about equal to the vacuum wavelength, and length 2.5 to 5 times longer than the vacuum wavelength. This volume is hundreds of times smaller than for similar switches exploiting electrooptic effects in solids such as $LiNiO_3$.

2. Switching speed. The switching speed of the FLC element for a given field strength E is largely determined by the FLC material's ferroelectric polarization P and its orientation viscosity n, through the relation $t = n/(PE)$, with 10% to 90% response times t_s being about 1.8 t. Presently available broad temperature range materials have viscosities of abut 50 cP and polarizations of about 5 nC/cm^2, giving response times about 180 us at 25°C with a modest 10 V/um applied. Present record-holding materials have polarizations of 250 nC/cm^2, giving response times 50 times shorter, or about 3.6 us. Materials that are ferroelectric at elevated temperatures have much lower viscosities, e.g. 5 cP at 70°C, allowing another order of magnitude reduction in switching speeds. Improvements of polarization by a factor of three seem likely within the next few years, bringing near-term switching speeds down to about 1 us at 25°C and 120 ns at elevated temperatures.

3. Energy dissipation. Switching a unit area of FLC by reversing an applied voltage V dissipates an energy 2PV through reversal of the polarization P. If this switching is repeated as frequently as possible (i.e. once every t_s), the power dissipated is $2PV/t_s = 3.6nd/t_s$, where d is the FLC thickness ($E = V/d$). Thus, for a given maximum allowable power dissipation per unit area W, the shortest achievable switching time is given by $t_s = [3.6nd/W]^{1/2}$. For an SLM with 10 um x 10 um pixels (1000 x 1000 elements in 1 cm^2) and 1 um thick, operating at room temperature with a 50 cP material and all elements switched every t_s, a dissipation bound of 100 mW/cm^2 (about equal to the heat of the noon sun) would limit t_s to 13 us. With a device operating in reflection, one could use water cooling to achieve $W = 10$ W/cm^2; with room temperature, 50 cP materials this would give $t_s = 1.3$ us; with high temperature, 5 cP materials it would give $t_s = 400$ ns. A comparison of the frame rates attainable for a 1000 x 1000 SLM which dissipates 10 W/cm^2 has been made with conventional electrooptic materials; $LiNbO_3$, and PLZT, and FLC materials [3]. For the conventional

materials, the dissipation is assumed to be $W = (1/2)CV^2$; the parameters necessary to calculate the half-wave voltage and capacitance C are taken from a handbook [4] in the case of $LiNbO_3$, and a description of an optically addressed SLM [5] in the case of PLZT. FLCs approached the megahertz frame rate, while PLZT was a factor of 20 slower, and a $LiNbO_3$ device would be limited to 1.3 ms frame rate. Power dissipation limits are more important than intrinsic switching speeds for applications requiring densely packed interconnection networks and neurocomputers.

4. Addressing. The bistability and sharp threshold characteristics of the FLC element makes possible the electrical addressing of a matrix of elements by row and column electrodes. Multiplexing up to 1000:1 has been demonstrated by Wahl et al. [6]. Thus, an N x N element SLM can be electrically reconfigured with 2N electrical connections, even for N up to 1000. Optical addressing has also been demonstrated on a slower photoconductor [7], and devices with fast amorphous Si photosensors have been proposed [8] and recently demonstrated [9]. The bistable feature of the FLC element allows the write light to be turned off when the crossbar is not being reconfigured. The amorphous silicon FLC/SLM test devices currently show millisecond rise times with 60% modulation of the read beam [9]. The first generation devices have design specifications of 100 microsecond rise time for 50 mW/cm^2 illumination intensity, resolution of 50 lp/mm, and 1" diameter cell size.

Applications

Two applications for FLC/SLMs are in optical interconnects for high density packet routing and neurocomputing. Currently we have demonstrated a 4 x 4 exchange network using an FLC device sandwiched between two polarizing beamsplitters [10]. This experimental arrangement occupied the better part of a Newport Research Corporation 4' x 6' optics table. We are currently investigating more integrated structures such as those built by Soref and McMahon using nematic liquid crystals [11] and Clark et al. in FLC's [12].

For neurocomputing, we are building an optical system with a 1 x 128 FLC columnar array as the input, followed by a two-dimensional Seiko liquid crystal television (LCTV), which stores the weight matrix. A hidden layer is comprised of another 1 x 128 FLC columnar array, again followed by a second LCTV weight matrix. The output is currently detected by a Panasonic camera and input to an IBM AT personal computer which calculates the error between desired and output response.

Our future goals include using photoaddressed FLC and nematic liquid crystals to replace the electrically controlled hidden layer and LCTV weight matrices, respectively. Work in progress on this system will be reported.

References

[1] J. W. Goodman, Optical Computing Short Course, OSA Annual Meeting, Seattle, WA (1986).

[2] A. Tanguay, Soc. Phot. Inst. Eng., Vol. 456, 130 (1984).

[3] M. A. Handschy, K. M. Johnson, G. Moddel, and L. A. Pagano-Stauffer, to appear in Ferroelectrics (1988).

[4] Bruce H. Billings, in America Institute of Physics Handbook, Dwight E. Gray, ed. (McGraw-Hill, New York, 1972) Chap. 6, pp. 6-239.

[5]] Sing H. Lee, Sadik C. Esener, Mark A. Title, and Timothy J. Drabik, Opt. Eng. **25**, 250 (1986).

[6] J. Wahl, T. Matuszczyk, and S. T. Lagerwall, Mol. Cryst. Liq. Cryst. **146**, 148 (1987).
[7] D. Armitage, J. I. Thackera, N. A. Clark, and M. A. Handschy, Mol. Cryst. Liq. Cryst. **144**, 309 (1987).
[8] G. Moddel , K. M. Johnson, and M. A. Handschy, Proc. SPIE **754**, 207 (1987).
[9] W. Li, C. T. Kuo. G. Moddel, and K. M. Johnson, Proc. SPIE **936** (1988).
[10] K. M. Johnson, M. Surette and J. Shamir, to appear in Appl. Opt. , May (1988).
[11] R. A. Soref and D. H. McMahon, Opt. Lett **5**, 147 (1980).
[12] N. A. Clark et al., JOSA Special Issue Abstracts **4**, 106 (1988).

SPATIAL LIGHT MODULATORS: FUNDAMENTAL AND TECHNOLOGICAL ISSUES

C. Kyriakakis, P. Asthana, R. V. Johnson, and A. R. Tanguay, Jr.

Optical Materials and Devices Laboratory,
and Center for Photonic Technology
University of Southern California
University Park, MC-0483
Los Angeles, California 90089-0483

Numerous applications have been envisioned for spatial light modulators in optical information processing and computing systems [1, 2]. These applications can be summarized within the context of a generalized optical information processor or computer as shown schematically in Fig. 1 [2]. The principal functional roles of both one- and two-dimensional spatial light modulators include those of format, input, output, CPU, and memory devices. In addition, spatial light modulators can be effectively utilized to provide certain types of feedback interconnections, as for example in the case of optical crossbar switches and holographically encoded weighted interconnections.

Such a wide variety of applications has of course led to an equally wide variety of interrelated, and at times conflicting, device requirements. In this presentation, we examine these requirements from three complementary perspectives: fundamental physical limitations that affect the performance of any spatial light modulation function; the current status of spatial light modulator development with respect to such fundamental limits; and technological considerations that impact present and future device design and development. Each of these three perspectives will be discussed in detail, and is outlined briefly below.

Study of the fundamental physical limitations that affect an emerging technology is at once an exciting and somewhat sobering endeavor. The excitement arises naturally from the discovery of what we can in fact achieve; the sobering impact often occurs with the realization of what we <u>have</u> in fact achieved. Numerous such fundamental physical limitations pertain to the process of spatial light modulation. For example, two principal attributes of incident wavefronts can be conveniently modulated: amplitude and/or phase. In most applications, it is desirable to modulate one or the other, but not both. Yet these two parameters are intimately related, such that modulation of one has a deterministic impact on the other through the Kramers-Kronig relations. Analysis of this interrelationship can yield fundamental limits on the phase/amplitude cross-talk

anticipated for various physical device configurations, as well as appropriate figures of merit.

A second important fundamental limitation pertains to the minimum (quantum limited) energy required per unit resolution element to achieve a given level of modulation within predetermined accuracy constraints. Different limits can be derived for both analog and digital spatial light modulation [2, 3], as well as for the important cases of optically addressed and electrically addressed devices. For purposes of discussion, consider the case of optically addressed spatial light modulators, for which the modulation function inherently involves a detection process within each resolution element. The quantum limits for binary switching are well known, and are summarized for optical devices in Fig. 2 (after P. W. Smith, Ref. [3]). For analog modulation, quantum restrictions place much stricter boundary limitations on the minimum allowable photon flux for a given pixel resolution, error rate, and device framing rate [2].

For envisioned systems applications involving one or more spatial light modulators, analysis of fundamental limitations such as that described above are essential for determining whether an analog or digital approach is favorable from the point of view of a fixed input power budget at a given desired computational throughput rate. In general, a given processing or computation function can be partitioned into the cost (energy or otherwise) of representation, the cost of computation, and the cost of detection and utilization of the answer. For operation at the quantum limits, analog representations are favored for architectures and algorithms that implement a high degree of computational complexity (irreducible number of equivalent binary operations) per unit detected output resolution element, whereas binary representations favor operations with a somewhat lower degree of computational complexity.

The current status of spatial light modulator development depends strongly for its assessment on the nature of the application and its resultant requirements. It is interesting to note at the outset that for certain applications (such as incoherent-to-coherent conversion with high analog accuracy), spatial light modulator technologies have been developed which approach quantum limited performance. On the other hand, a broad spectrum of applications exists for which current spatial light modulators fall far short of such ultimate performance boundaries. In making such comparisons, it is of critical importance to identify interrelated sets of performance parameters that cannot be arbitrarily separated, and to assess the conjoint figure of merit achievable within a given device technology (rather than the minimum value obtained across many different types of devices, or even within the same device under different operating condistions).

A large number of technological considerations apply to the eventual incorporation

of spatial light modulators in optical information processing and computing systems. For systems of given size, spatial frequencies are inherently limited by the acceptance apertures of finite F-number lenses. Phase modulation, which is capable of much larger diffraction efficiencies at a given spatial frequency than amplitude modulation, is more difficult to implement in imaging configurations and is more sensitive to substrate nonuniformities and polish figure. Amplitude modulation, on the other hand, can present formidable thermal dissipation problems for applications involving spatial light modulation with high optical throughput gain. Applications exist for both optically addressed and electrically addressed spatial light modulators, with distinct requirements for each. In fact, several recently conceived applications such as the utilization of spatial light modulators in neural network implementations could advantageously employ both address modes simultaneously.

Electrically addressed spatial light modulators lead quite naturally to inherently pixelated structures. Such structures can be advantageous from several points of view, including the convenient merging of optical and electrical inputs, interpixel cross-talk, strictly limited space-bandwidth product, and fixed system registration. However pixelation can yield additional difficulties such as inherently incomplete fill factors, scattering from metallic interconnections, and fixed pattern noise. Similar types of considerations apply to the utilization of reflective as opposed to transmissive device geometries.

A final technological consideration that will continue to strongly affect device design and development is that of available optical sources, both CW and pulsed. For fixed (and usually limited) external power, size, and weight considerations, the maximum achievable pulsed energy densities available set stringent requirements on the magnitudes of usable higher order material nonlinearities. Recent achievements of enhanced nonlinearities in both bulk and multiple quantum well compound semiconductor structures, as well as in nonlinear organic polymers, lend importance to the question of whether or not $\chi^{(3)}$ materials as well as $\chi^{(2)}$ materials will provide useful spatial light modulation functions in future devices.

1. C. Warde and A. D. Fisher, "Spatial Light Modulators: Applications and Functional Capabilities", in *Optical Signal Processing*, J. Horner, Ed., Academic Press, Inc., San Diego, (1987), 477-518.

2. A. R. Tanguay, Jr., "Materials Requirements for Optical Processing and Computing Devices", Opt. Eng., 24(1), 2-18, (1985).

3. P. W. Smith, "Applications of All-Optical Switching and Logic", Phil. Trans. R. Soc. Lond., A313, 349-355, (1984).

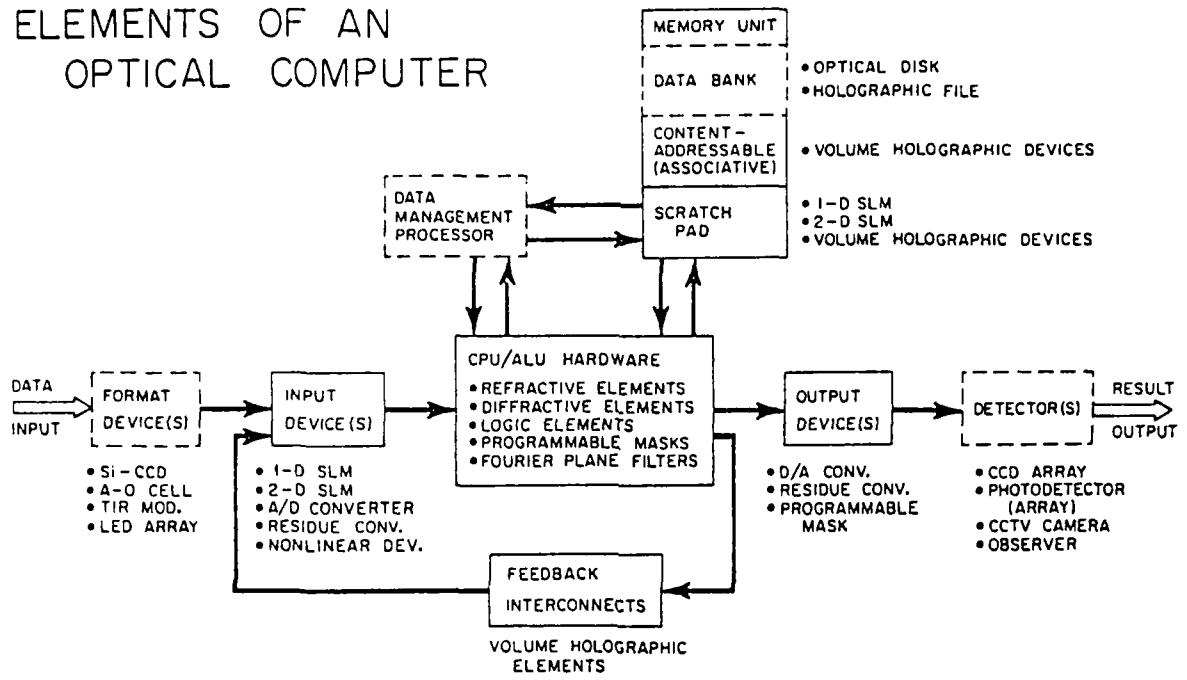

Fig. 1 Schematic diagram of the principal elements of a generalized optical processor or computer.

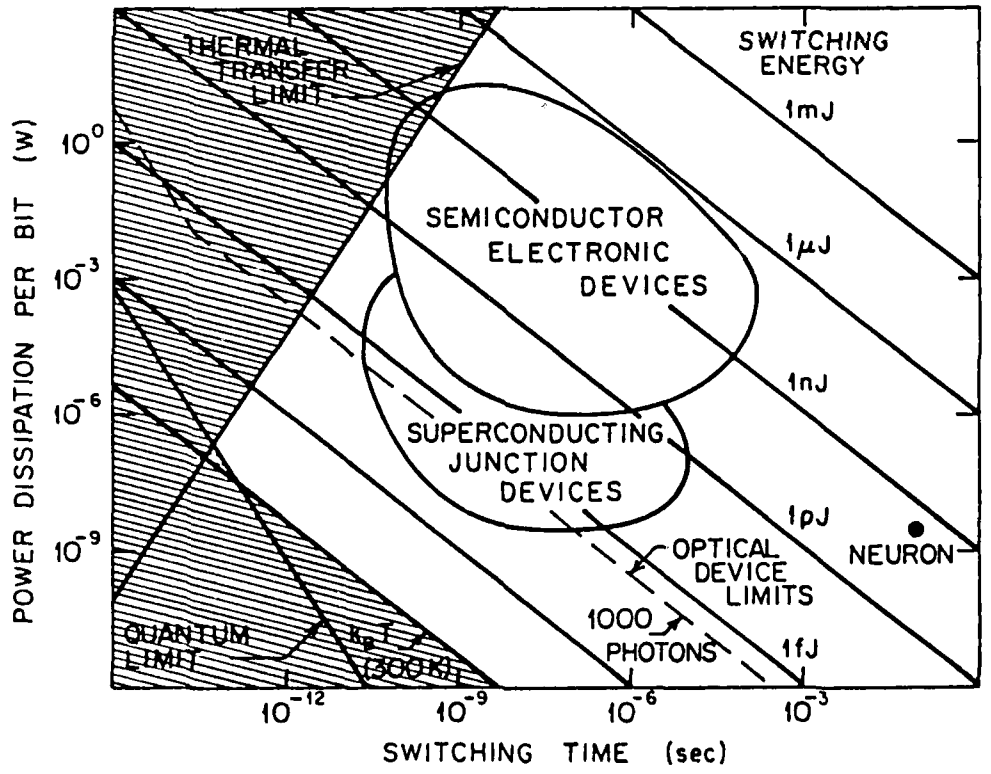

Fig. 2 Power dissipation per bit as a function of switching time, showing several fundamental and technological limitations (after Ref. 3).

THURSDAY, JUNE 16, 1988

EMERALD BAY BALLROOM

8:30 AM–9:50 AM

ThA1–4

III-V DEVICES

William Miceli, Office of Naval Research, *Presider*

Spatial Light Modulators with Internal Memory

L.M. Walpita

Department of Electrical and Computer Engineering, C-014
University of California, San Diego
La Jolla, CA 92093, U.S.A.

It is increasingly recognized that the ability for optical techniques to provide parallel processing may enable us to greatly enhance the speed capability of computing. To satisfy requirements of parallel optical processing many types of spatial light modulators (SLMs) are now being investigated. In this paper we discuss a SLM with internal memory which is electrically addressable and digitally operated.

The properties of the SLM is based on newly observed optical cross modulation effect in Semi-insulating GaAs[1]. To demonstrate this effect we pass a beam of LED (light emitting diode) light through a semi-insulating GaAs sample which has transparent electrodes on both surfaces (Figure 1). In the presence of an electric field the LED light is slightly absorbed due to the Franz-Kaldysh effect. However, when an optical pulse tuned to the absorption edge of the GaAs hits the sample, the absorption of the LED light is instantaneously reduced but then increases substantially beyond the initial absorption after the pulse and this level is maintained by the presence of the electric field (Figure 2). In this effect, the optical pulse generates many conducting carriers which are kept at high energy by the applied voltage. The LED light generates trapped carriers below band gap. It has been suggested that the LED generated trapped carriers are released to the conduction band to reach thermal equilibrium with the conducting high energy carriers[2]. In this process below band gap LED light is further absorbed resulting in the observed enhanced absorption. The enhanced absorption, triggered by the optical pulse gives rise to a memory effect.

During the demonstration of the effect, we have used LED (line width 0.2μm) light intensity of 50 m watts/cm^2 and typically optical pulse energy of 10×10^{-6}J/pulse/cm^2 (includes reflection loss of 30%); after the optical pulse, approximately about 10% of LED light absorption has been observed in the presence of 200v applied across 400μm thick sample. The effect of the optical pulse intensity, on the LED light absorption and on the photo current through the sample is given in Figure 3; both the LED absorption and the photo current tend to saturate at increased optical pulse intensities. We estimate that an array of 10^4 devices of area $100(\mu m)^2$ will dissipate power of approximately 250 m watts/cm^2. We also estimate that for line width of the LED light reduced by ten fold, approximately 70% absorption of LED light is caused by the optical pulse of energy 10×10^{-6}J/pulse/cm^2 and voltage 40v applied across 100μm thick sample for similar amount of power dissipation for 10^4 devices; the power dissipation can be minimized by optimization of the operating parameters and array dimensions. In this modulation effect the enhanced absorption of the LED light after the optical pulse can be adjusted by the strength or time delay of the subsequent voltage pulses (Figure 4). At present, the speed of the modulation effect is limited by the RC time constant of the external electronics.

The schematic of an integrated array of the proposed spatial light modulator is shown in Figure 5. An array of cells can be fabricated on a single semi-insulating GaAs substrate. Each

cell has transparent InSnO electrodes with further deposited aluminum electrodes. The aluminum electrodes are arranged in a cross bar fashion so that each element can be accessed independently. On the basis of an elementary calculation, we have estimated that for $100(\mu m)^2$ cells separated by $100\mu m$, the carrier diffusion and fringing effects will be negligible for $100\mu m$ thick samples.

The proposed SLM, apart from providing memory capability, has many other useful qualities, it is externally programmable and digitally operated. Eventhough digital processing might be at present slower than analogue processing, digital processing can give better signal to noise capability. A digitally operated SLM can be more readily interfaced with a digital computer. The SLM with memory is well suited for neural network applications[3]. Optical implementation of artificial neural models has been already achieved by others[4], where a single dimensional input field maps into a single dimensional output field through a two dimensional spatial light modulator. If two dimensional fields are to be processed, the SLM should be provided with a third dimension. In the SLM with memory, where a train of optical pulses can be involved, time can be taken to be the third dimension. The SLM with memory is easy to fabricate as there are no other semiconductor device incorporated or multilayer deposition techniques involved.

References

1. L.M. Walpita, W. S. C. Chang, H. H. Wieder, T. E. Van Eck, "Cross Modulation of Light in SI Semiconductor Materials in the Presence of Electric Fields", *Applied Optics*, **Vol 24**, 2481 (1985).
2. L.M. Walpita, "Memory Effects in Semi-Insulating GaAs Optical Modulator" Technical Digest OSA Annual Meeting, Vol 22, 63 (1987).
3. L. M. Walpita, "Electro-Absorption Cell for Artificial Neural Networks" *Applied Optics*, **Vol 26**, 2631 (1987).
4. N. H. Farhat, D. Psaltis, A. Prata, E. Paek, "Optical Implementation of the Hopfield Model", *Applied Optics*, **Vol. 24**, 1469 (1985).

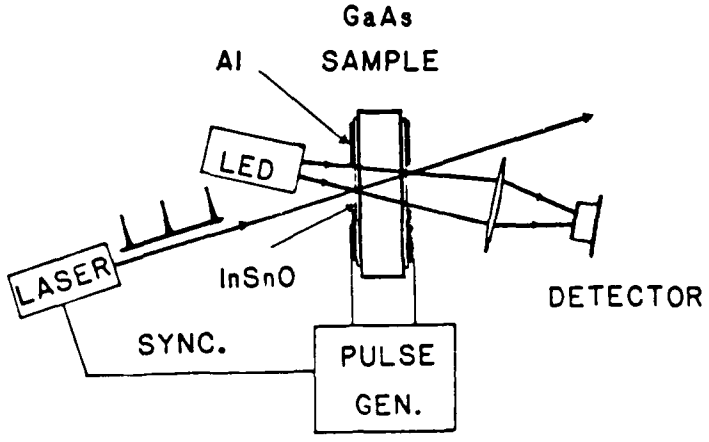

Figure 1. Schematic of the experimental set up

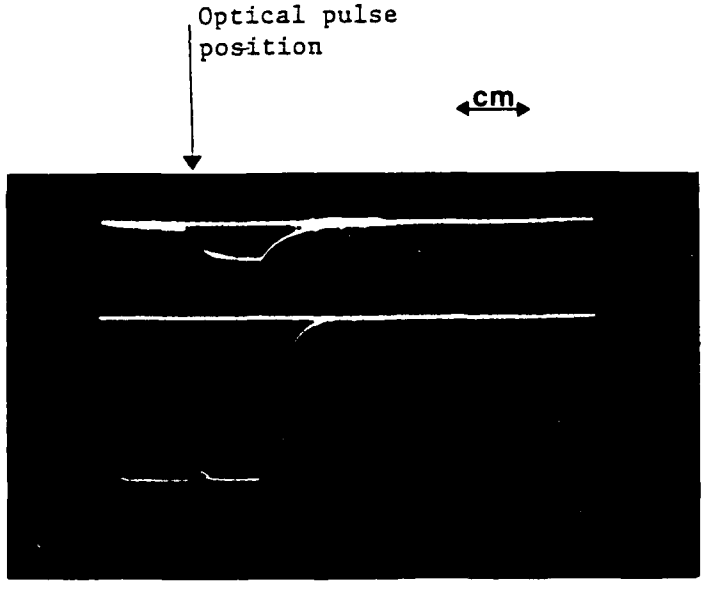

Figure 2. The effect of the optical pulse of 1 kwatt/cm^2 on the LED absorption is shown. The bottom trace is the voltage pulse with horizontal scale 15μsec./cm and vertical scale 150v/cm. The upper trace represents the absorption caused by both optical and voltage pulse, with vertical scale 75%/cm.

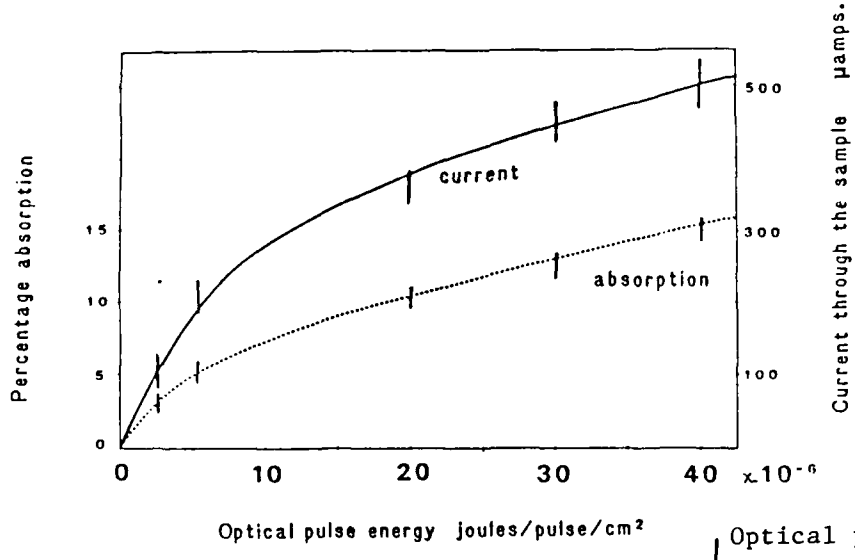

Figure 3. The enhanced absorption of the LED light and increased sample current after the optical pulse in the presence of the voltage pulse of 200v is shown.

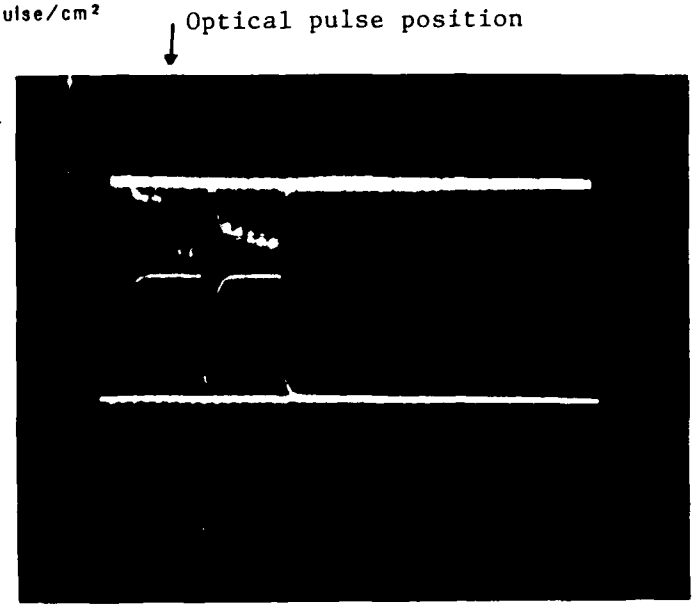

Figure 4. The effect of the second voltage pulse on LED absorption is shown. The bottom trace is the voltage pulse: horizontal scale 30 μsec./cm and vertical scale 150v/cm. Upper trace represent absorption: vertical scale 8%/cm

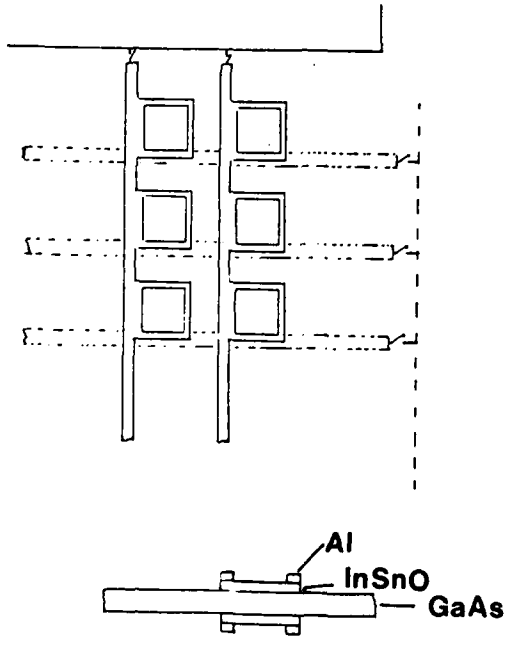

cm

Figure 5. Schematic of the proposed integrated device and unit cell.

Optically Addressed Spatial Light Modulators by MBE-Grown nipi/MQW Structures

J. Maserjian*, P.O. Andersson, B.R. Hancock, J.M. Iannelli, S.T. Eng, F.J. Grunthaner
Jet Propulsion Laboratory, California Institute of Technology, Pasadena, California 91109
* presently at University of California, Santa Barbara

K-K. Law, P.O. Holtz, R.J. Simes, L.A. Coldren, A.C. Gossard, and J.L. Merz
Electrical and Computer Engineering Department, University of California, Santa Barbara, California 93106

The development of high performance, reliable spatial light modulators (SLMs) has been slow over past years, primarily due to the limitations of materials technology[1]. New opportunities have been made possible by the greatly enhanced electro-optic properties of multiple quantum well (MQW) structures[2]. Such MQW structures are now being incorporated into a variety of new electro-optic devices[3]. Approaches for SLMs using MQWs have been proposed [4-8] and early results are encouraging[5,6,8].

In this work, we pursue new promising approaches for achieving optically addressed SLMs, based on combining nipi doping structures with MQWs. Figure 1 summarizes two photo-optic modulation effects that we utilize. In Fig. 1a, the quantum wells are located at the conduction band potential minima of the doping superlattice. A write signal with energy greater than the band gap of the host material (e.g., GaAs) generates electron-hole pairs which are separated by the internal field of the pn junctions (photovoltaic effect). At steady state, a flux Φ_p deposits δn_Q electrons/cm^2 in the quantum wells - determined by the absorption coefficient α, the spacing b, and the recombination time τ. These electrons fill the quantum states by an amount δE due to the finite state density per unit energy ($\pi h^2/m^*$), causing a shift in the absorption edge.

In Fig. 1b the quantum wells are located in the constant field region of the nipi superlattice. The write signal again produces a photovoltaic effect, but in this case we use the change of the internal field E(see expression in Fig. 1), due to the photocarrier separation. This field in turn induces a shift of the exciton energy E_{ex} due to the quantum confined Stark effect (QCSE)[2] which is quadratic (an E^2 term in Fig. 1) at low to moderate fields. In both cases (Figs. 1a and b), the energy range of the write signal ($hv > E_g$) lies well above the absorption edge of the quantum well. Modulation is accomplished by selecting the wavelength of the read signal in the range over which the quantum well absorption edge is shifted. The modulation depth will depend on the sharpness of the absorption edge, which in turn depends on the quality and uniformity of the quantum wells.

Figure 2 shows theoretical plots[9] of the change in absorption α with field for different well widths due to the QCSE. Also shown are contours of constant (initial) absorption. The curves are normalized to the zero field absorption α_o. We desire large $d\alpha/dE$ for maximum response, small $d^2\alpha/dE^2$ for linear response, and large α for maximum contrast. Clearly, these conditions are seen to be incompatible and we must select a compromize. We have initially chosen a well width of 79Å (28 monolayers) and an internal quiescent field of about 1.5 x 10^5 V/cm, giving for α_o^{-1} $d\alpha/dE$, 0.5 and α/α_o, about 2/3. This field will also prevent MQW trapping of photocarriers generated by the write signal.

The SLM device structures envisioned are shown in Figs. 3 and 4. Figure 3 uses a back surface metal reflector and therefore requires a transparent substrate. We are currently investigating (In,Ga)As/GaAs quantum wells grown by molecular beam epitaxy (MBE) on GaAs substrates for this purpose. In this case we use the quantum state filling effect of Fig. 1a which offers potentially much higher sensitivity than the QCSE of Fig. 1b. However, it has the disadvantage of having the MQWs occupy a smaller fraction of the active layers which limits the maximum possible contrast . In spite of this, we still hope to achieve contrast ratios above 10:1 in optimized structures. Figure 4 uses a distributed-Bragg reflector (DBR) with an opaque GaAs substrate. In this case we can make use of the more mature (Al,Ga)As/GaAs MBE technology. In Fig. 4a the DBR is simply a passive reflector for the read signal. The active nipi/MQW layers are configured as in Fig 1b to use the QCSE and are grown to a total thickness the order of the absorption depth of the write signal ($\approx$2 μm). The read signal is modulated by absorption as it passes (twice) through the active layers. In Fig. 4b, the active nipi/MQW layers are incorporated within the DBR (at alternative quarter-wavelength layers of the DBR stack), providing an active DBR. In this case we make use of both changes of index of refraction and α to modulate the reflectance of the DBR. By matching the read signal and exciton wavelength near the edge of the DBR reflectance band, we predict large sensitivity and contrast ratios. This effect can be further enhanced by "chirping" the DBR. Another

approach (not shown) would make use of two DBRs to obtain a Fabry-Perot resonator. Unfortunately, in this case the changes of index and α tend to oppose one another. However, this approach may still prove useful through careful design.

In Fig. 5 we show photoluminescence from a nipi superlattice in GaAs for different levels of irradiance. The sample was MBE-grown with 40 nm p^+ layers (1.10^{18} cm^{-3} Be), 40nm n^+ layers (1.10^{18}cm Si), and no undoped layers. The result shows the expected GaAs sub-bandgap photoluminescence which shifts approximately logarithmically with irradiance[10]. This behavior is too weak to be used for our SLMs, but assures us that we are achieving the internal nipi fields we need in the nipi/MQW structures.

We have spent considerable effort trying to perfect MBE growth of InAs/GaAs strained-layer superlattices[11]. We would like to incorporate these superlattices into our quantum wells with the prospect of achieving higher degree of order and quality. Unfortunately, this approach is still limited by our ability to reproduce precise MBE growth temperatures. Therefore, we have recently chosen to take an intermediate approach using In_xGa_{1-x} As alloys with moderate values of x (≈0.2) in the quantum wells to test our device approach. Our first results on a nipi/MQW test structure using the InGaAs alloy are encouraging. The structure was grown with 20 periods, each consisting of $2x10^{18}$ cm^{-3} Be acceptors 60 nm thick, $1x10^{18}cm^{-3}$ Si donors 60 nm thick, and a 12 nm quantum well of $In_{.2}Ga_{.8}$ As/GaAs. The transmission through the structure, without an AR coating or back surface reflector, was measured versus wavelength near the absorption edge (≈920 nm). Figure 6 shows this transmission with a GaAs laser pump (≈ 50mW/cm^2) turned on and off causing a relative modulation change of about 7%. The maximum transmission in this case is limited by front and back surface reflection. By optimum device design we should increase this modulation depth by a factor of at least five; however, we also anticipate a much greater improvement as we perfect the MBE growth process for these quantum wells.

Our SLM effort using (Al,Ga) As and DBRs (Fig.4) are also just getting underway at this writing. Figure 7 shows our first attempt at MBE growth of a DBR. The structure consists of a stack of ten pairs of alternating quarter-wavelength layers (64 nm $Al_{.2}Ga_{.8}As$ and 74 nm AlAs). A small thickness gradient (≈1%) occurs because of system drift which lead to the observed reflectance curves. This effect is qualitatively modeled by the theoretical curves which assumes a constant 1% layer thickness gradient. This kind of chirping can be optimized to achieve very sharp turn on of the reflectance curve which is important for the active DBR approach. For the passive DBR, the structure is not critical as long as the main reflection band includes the quantum well exciton wavelength.

The first nipi/MQW structure was MBE grown using (Al,Ga)As according to Figs. 1b and 4b. The structure consists of a ten period DBR stack (58nm $Al_{.2}Ga_{.8}As$ and 65 nm AlAs) upon which was grown 1.62 um of nipi/MQW ($Al_{.2}Ga_{.8}As$/GaAs) active material. The n^+ and p^+ layers consisted of 10 nm $4x10^{18}cm^{-3}$ Si doping and 10 nm $4x10^{18}cm^{-3}$ Be doping, respectively, and were separated by an undoped i region containing four 79Å quantum wells with 79Å barriers. Our photoluminescence results are shown in Fig. 8. The insert shows two quantum well exciton peaks and the position of these peaks are plotted versus irradiance level. The left peak does not shift and has been identified as due to the MQWs located at the outer layers of the nipi structure. We had neglected to allow for a sufficiently thick p^+ cap to accommodate surface states, and consequently, the outer (p-i-n) leg of the nipi is pinned at low fields. However, the remaining 19 nipi legs are not affected and we observe the expected shift with irradiance level. The large shift at low levels (≈10 $\mu W/cm^2$), combined with the narrow exciton half width (≈60Å) for 76 MQWs, projects to high modulation sensitivity. We are currently in the process of setting up modulation reflectance measurements.

Acknowledgement:
This work was supported by NASA, AFSRO and SDIO/Innovative Science and Technology Office.

1. A.R. Tanguay, Jr., Opt. Eng. 24, 002 (1985).
2. D.A.B. Miller, et al, Phys. Rev. B32, 1043 (1985).
3. D.A.B. Miller, Opt. Eng. 26, 368 (1987)
4. D.A.B. Miller, U.S. Patent 4, 564, 244 (1985).
5. W.D. Goodhue, et al, J. Vac. Sci. Tech. B4, 769 (1986).
6. T.H. Wood, et al, Electronics Lett. 23, 916 (1987).
7. U. Efron, et al, Proc. SPIE, Vol 792, 197 (1987).
8. G. Livescu, et al, submitted to Optics Lett. (1988).
9. Obtained as described in Ref. 2, and assuming an exciton half width of 10 meV.
10. G.H. Dohler, Science 13, 97 (1987).
11. F.J. Grunthaner, et al, Appl. Phys. Lett. 46, 983 (1985).

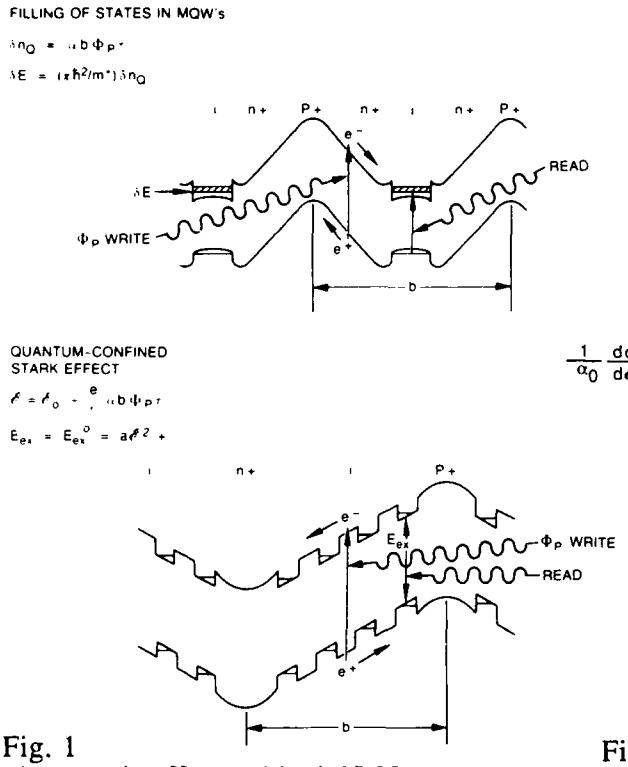

Fig. 1
Photo-optic effects with nipi/MQW structures:
a) Filling of states.
b) Quantum Confined Stark Effect.

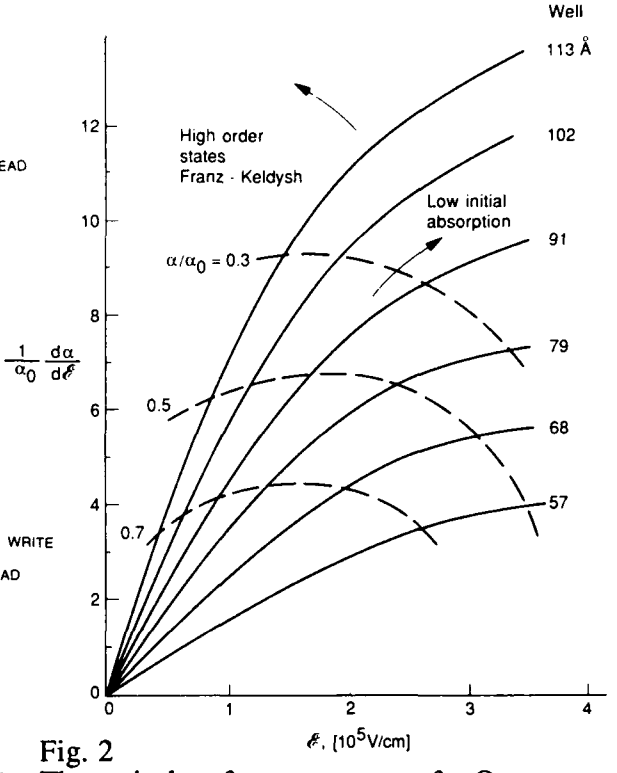

Fig. 2
Theoretical performance curves for Quantum Confined Stark Effect.

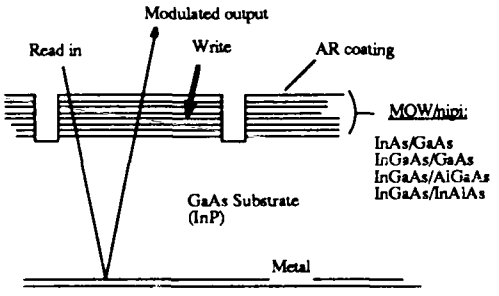

Fig. 3
SLM device structure - transparent substrate.

Fig. 4a

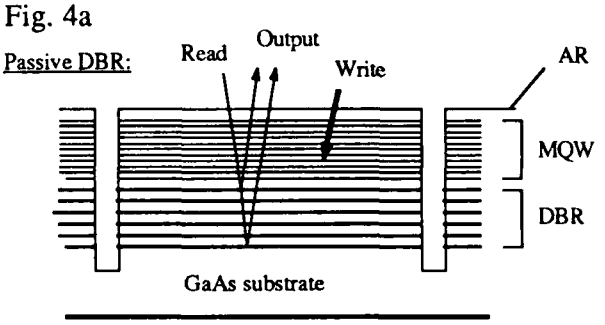

Fig. 4b

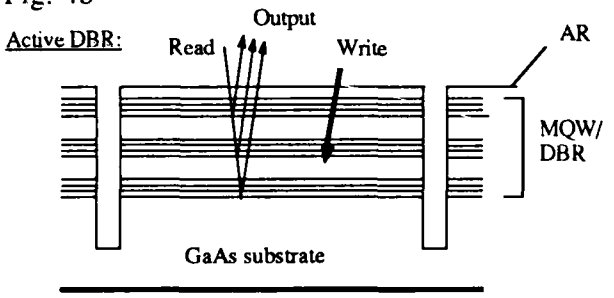

Fig. 4
SLM device structure - opaque substrate:
a) Passive DBR b) Active DBR

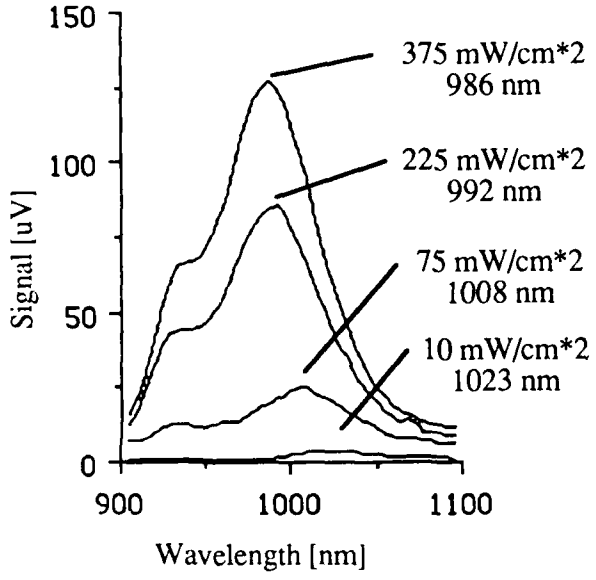

Fig. 5
Photoluminescence from GaAs nipi structure.

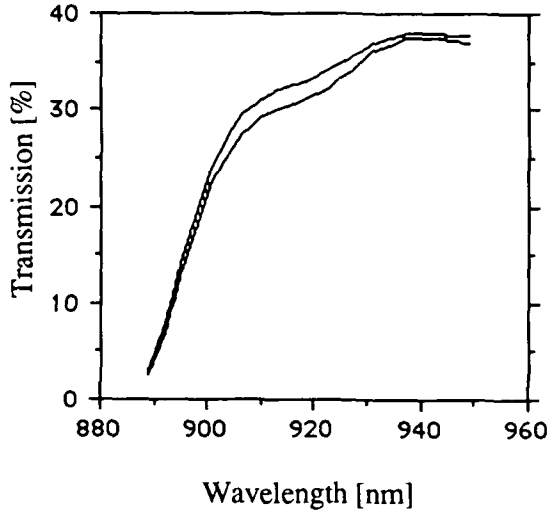

Fig. 6
Transmission modulation from MQW/nipi test structure.

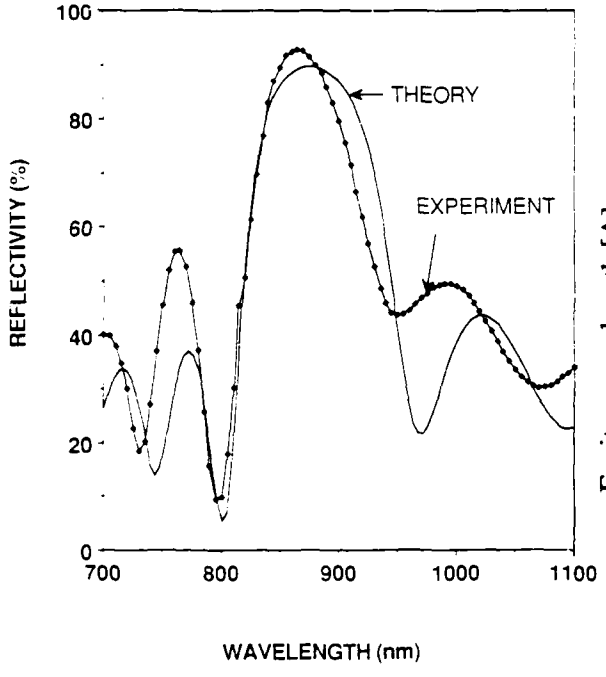

Fig. 7
Distributed Bragg reflector with linearly graded layer thicknesses.

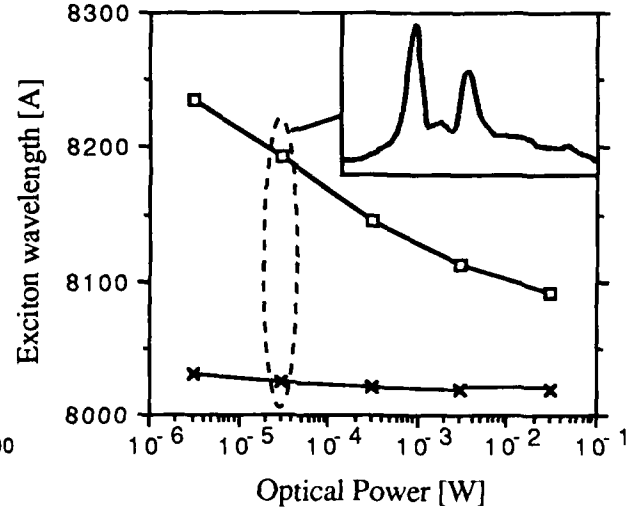

Fig. 8
Exciton photoluminescence shift with irradiance.

InGaAs/GaAs and GaAs/AlGaAs Multiple-Quantum-Well Spatial Light Modulators

Brian F. Aull, Kirby B. Nichols, William D. Goodhue, and Barry E. Burke

Lincoln Laboratory, Massachusetts Institute of Technology
Lexington, Massachusetts 02173-0073

The need for spatial light modulators (SLMs) with high-speed electrical addressing capability motivates the development of SLM devices based on GaAs and related ternary alloys. These materials are amenable to the growth of superlattices with good optical modulation properties and to the fabrication of high-speed addressing circuitry on the same wafer.

We have fabricated monolithic one- and two-dimensional spatial light modulators based on excitonic electroabsorption in multiple quantum wells (MQWs).[1] The SLM is electrically addressed using a charge-coupled device (CCD). CCD-addressing supports large space-bandwidth products in an SLM without the drawback of needing a separate electrical input to each pixel. The device concept is shown in Fig. 1. A p^+-type ground plane, an undoped MQW, and an n-type layer are grown sequentially on a semi-insulating GaAs substrate. The n-type layer serves as a channel layer for a three-phase buried-channel CCD fabricated on the surface of the wafer. The SLM is addressed by storing a pattern of charge packets in the CCD array; the charge packets are sequentially injected through an ohmic contact. (However, optical addressing is also possible by using the CCD as an imager.) At

1. T. H. Wood, C. A. Burrus, D. A. B. Miller, D. S. Chemla, T. C. Damen, A. C. Gossard, and W. Wiegmann, Appl. Phys. Lett. **44**, 16 (1984).

each pixel, the magnitude of the stored charge packet determines the electric field across the underlying portion of the MQW. This in turn determines the absorption coefficient of the MQW material at wavelengths near the band-edge exciton peaks and, therefore, the optical transmission of the pixel. The CCD electrodes are patterned from an ultra-thin layer of metal so that they are semitransparent to incident light. One of the three CCD phases is arbitrarily selected as the optically active pixel, and the other portions of the CCD array are masked with an aluminum light shield. The SLMs include 16-pixel and 32-pixel one-dimensional arrays, as well as 16-by-16-pixel two-dimensional arrays.

SLMs that operate at 965 nm have been fabricated using InGaAs/GaAs strained-layer MQWs, and SLMs that operate at 847 nm have been fabricated using GaAs/AlGaAs MQWs. The active device layers are grown by molecular beam epitaxy (MBE), and the details of the growth are reported elsewhere.[2] For the GaAs/AlGaAs device, the GaAs substrate is opaque at the operational wavelength and is therefore removed in its entirety. In this case, a 35-μm-thick AlGaAs support layer is grown by organometallic vapor phase epitaxy prior to the MBE growth of the active device layers in order to facilitate removal of the substrate and transfer of the device to a glass slide.

The InGaAs/GaAs-based SLM was characterized as follows. Light from a cw xenon arc lamp was filtered through a

2. W. D. Goodhue, B. E. Burke, B. F. Aull, and K. B. Nichols, "MBE-Grown Spatial Light Modulators with Charge-Coupled-Device Addressing," 8th MBE Workshop of the American Vacuum Society, Los Angeles, CA, September, 1987.

monochromator set at 965 nm and then focused on a selected pixel of a one-dimensional SLM. The transmitted light was detected with a dry-ice-cooled S-1 photomultiplier tube. The CCD was clocked at 166 kHz. The transmitted intensity as a function of time was obtained by ensemble averaging the detected signal with a waveform analyzer that was triggered synchronously with the CCD frame time. A charge packet of magnitude zero yields an optical transmission 20% greater than a full charge packet, consistent with dc electroabsorption spectra. The time-resolved optical signal shows transients of several microseconds duration at the beginning and end of a burst of large charge packets. This is due to trapping effects associated with strain-induced dislocations at the interface between the MQW and the n-type layer. Electrical measurements of charge-transfer losses in the CCD indicate no trapping effects on longer time scales.

The GaAs/AlGaAs-based device was characterized as follows. A selected pixel of a 16-pixel one-dimensional device was illuminated with a pulsed AlGaAs laser diode operating at 847 nm. The CCD was clocked at 0.5 MHz, and the laser diode was pulsed synchronously with the frame time of the CCD. The transmitted light was detected with a silicon photodiode. The light beam was chopped at 1 kHz with no synchronization to the CCD clock to facilitate lock-in amplification. A charge packet of magnitude zero yields an optical transmission 45% greater than a full charge packet, consistent with dc electroabsorption spectra. No trapping effects have been observed in electrical measurements of charge-transfer losses in the CCD at clock frequencies up to 1 MHz.

Although these SLMs have been operated at CCD clock speeds only up to 1 MHz, they are capable of clocking speeds in excess of 1 GHz. For an analog SLM with one electrical input, this yields a computational throughput of a billion multiplications per second. Parallel loading of the CCD would yield an even higher throughput.

This work was sponsored by the Departments of the Navy and the Air Force.

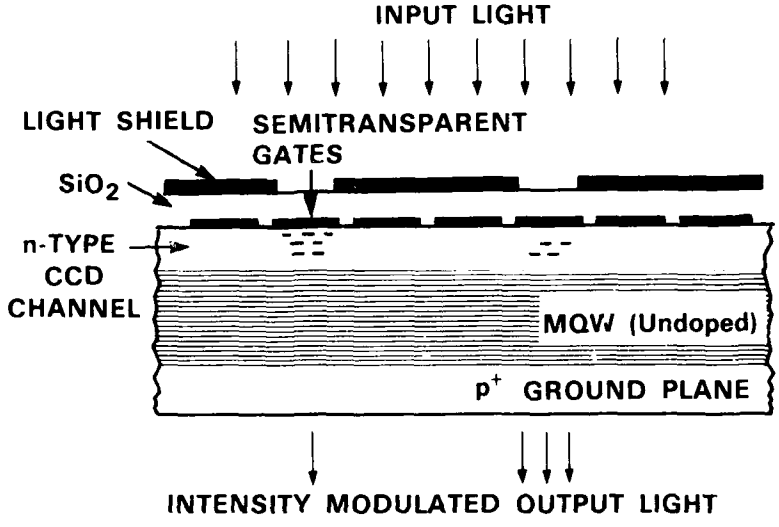

Fig. 1 Structure of multiple-quantum-well spatial light modulator

INVESTIGATION OF A 1D GaAs-GaAlAs MULTIPLE QUANTUM WELLS SPATIAL LIGHT MODULATOR

J.Ph.SCHNELL, J.P.POCHOLLE, E.BARBIER, J.RAFFY,

A.DELBOULBE, C.FROMONT, J.P.HIRTZ, J.P.HUIGNARD

THOMSON-CSF, Laboratoire Central de Recherches

Domaine de Corbeville, B.P. N° 10

91401 ORSAY Cedex (France)

Introduction

Semiconductors multiple quantum wells (MQW's) are promising optical materials for their fast response speed, their tailorable optical properties and their technological compatibility with electronic circuits.

The electroabsorption modulation in MQW structures used as SLM's makes them suitable devices for fast optical signal processing (Ref.1). A particularly interesting application is the fast generation of reference images in an optical correlator. This paper describes the realization and first characterizations of elementary and 1D-GaAs/GaAlAs MQW's SLM's which are a step toward 2D MQW SLM's.

SLM structure

The epitaxial structures were grown by MBE. The structure is shown schematically in figure 1. The substrate was a (100) orientated GaAs wafer. The following layers were successively epitaxied : a 200 nm - thick AlAs etch stop, an $Al_{0.3}Ga_{0.7}As$ buffer, a superlattice buffer, the 100 periods of 8 nm - thick GaAs wells and 20 nm - thick $Al_{0.3}Ga_{0.7}As$ barriers calculated to present a heavy hole

excitonic resonnance at 840 nm, an $Al_{0.3}Ga_{0.7}As$ buffer and an n-doped $Al_{0.3}Ga_{0.7}As$ layer.

The expitaxied layers were transferred on a transparent substrate (a glass slice) by sticking and complete ablation of the GaAs epitaxy substrate (H_2O_2 : NH_4OH etch solution). Several samples of various sizes (up to 2 mm x 10 mm) were realized.

Gold electrodes were deposited by sputtering so that MQW's are inserted in the intrinsic region of a MIN diode. The electric field is applied to the MQW's by using a couple of MIN diodes (figure 2) ; the forward-biased diode applies the positive potential to the underlying n-layer ; the second MIN diode is thus reverse-biased and is the region of electroabsorption. The gold electrode serves as a reflector for the optical beam which crosses twice the MQW's. Elementary and 1D-SLM's with 30 pixels photolithographically patterned were created as shown in figure 3. Connections were made by thermocompression.

Results

The transmission spectrum with no applied electric field (figure 4) shows well resolved heavy and light hole excitonic resonnances. The observed peaks are in good agreement with those calculated. Electroabsorption were investigated with an argon laser-pumped dye laser (LDS 821) at several wavelengths in the range 838-864 nm. Both the elementary devices and 1D-SLM were tested. In the latter case, pixels were individually addressed with an AC electric field of 4×10^4 V/cm (applied voltage V = 15 V). Modulation ratios higher or equal to 25 % were observed at 846 nm in an explored frequency range from DC to 100 KHz.

Conclusion

In this study, the interest is focused on extended areas of MQW SLM's based on the GaAS/GaAlAs systems. A 30 pixels - 1D SLM with MIN structure working in

a reflection configuration were made. The first characterizations are encouraging future application of these devices for high speed data input in optical correlators.

Acknowledgements

The technical assistance of Mrs LEHOUX and Miss SAMSO were greatly appreciated.

References

1. D.S.CHEMLA, T.C.DAMEN, D.A.B.MILLER, A.C.GOSSARD and W.W.WIEGMANN, Appl. Phys. Lett. **42**, 864 (1983).

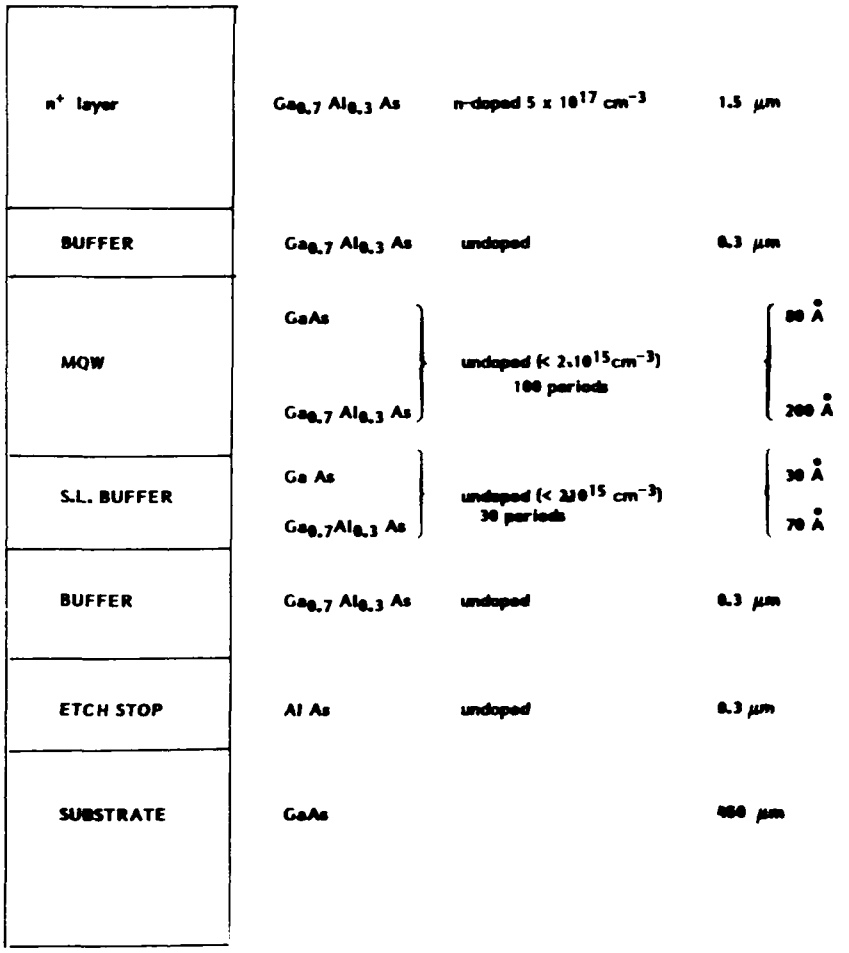

Figure 1 - Epitaxial structure grown by MBE

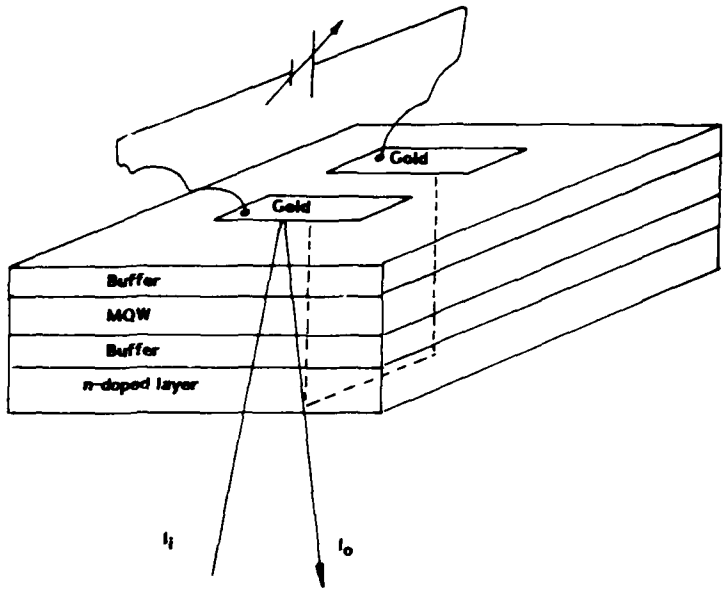

Figure 2 - Elementary MIN light modulator

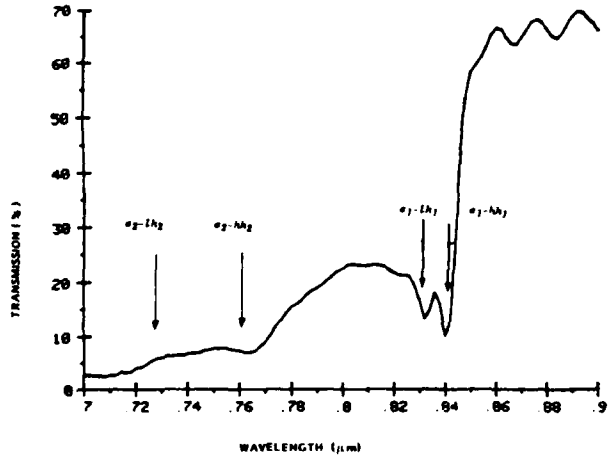

Figure 3 - Transmission spectrum of the expitaxied structure

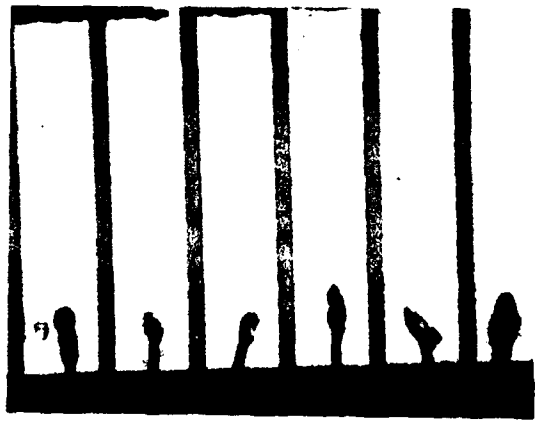

Figure 4 - Part of a 30 pixels MQW SLM

THURSDAY, JUNE 16, 1988

EMERALD BAY BALLROOM

10:20 AM–11:50 AM

ThB1–4

DEFORMABLE STRUCTURES

Robert Sprague, Xerox Palo Alto Research Center,
Presider

Deformable Mirror Device Spatial Light Modulators and its Application to Neural Networks

Dean R. Collins, Jeffrey B. Sampsell, James M. Florence,
P. Andrew Penz, and Michael T. Gately

Central Research Laboratories
Texas Instruments Incorporated
Dallas, Texas

Summary

Neural Networks are a nontraditional method for performing computations. Neural Network architecture is a fine grain, parallel architecture with simple processors coupled at long range to the inputs. Figure 1 shows a simple picture of a layered neural network. Computation is performed by multiplying each input to every processor (node) by a weighting factor and then summing the products. The sum is then thresholded and an output is obtained from each node. The nonlinear thresholding operation provides the decision making mechanism.

In general neural networks execute matrix/signal processing type operations. Neural networks recognize/reorganize by correlating inputs with learned states. Neural Networks have the novel ability to:

- Cluster stored information
- Recall information when the query is both incomplete and erroneous
- Be trained rather than programmed.

All neural networks are characterized by extensive interconnects between processor nodes. The extent of these interconnections is shown in Figure 2. Figure 2 contrasts the interconnections required for a cellular automata node, which interacts with only its nearest neighbors, to a neural network node, which interacts with every other node. Figure 2 also shows a regular matrix formulation of the interconnects for four nodes. In general there is no intermediate formulation between simple nearest neighbor interconnects and the fully interconnected matrix case. This means that N nodes will in general require N^2 interconnections. Since most practical neural network problems require a minimum of 100 to 1000 nodes, the minimum number of interconnects ranges from 10^4 to 10^6. Most neural networks require the interconnection to have analog values. Furthermore, in order for learning to take place, these interconnects must be variable. The large number, the analog values, and the variable nature of the interconnects pose an extreme challenge for conventional semiconductor technology.

In this paper we describe both a novel type of Spatial Light Modulator (SLM), called the Deformable Mirror Device (DMD), and its applicability to neural network computation. We believe that optical technology is the breakthrough needed to make neural network technology practical. Since the number of interconnections of a neural network are perceived to be the limiting factor, it is natural to advocate optical technology to solve the interconnect problem. It is very easy to make complex interconnection-light beams pass through each other; however, it is very difficult to build a light switch. Light switches, or two dimensional arrays of light switches called Spatial Light Modulators exist and have been used by Farhat[1], Psaltis[2], and

others to build Optical Neural Networks. These systems were either very expensive, slow, or tied to TV format. In general these systems were quite limited by the performance of the SLM. Several holographic techniques using film have been demonstrated, but they suffer from the inability to vary the interconnections.

The SLMs described here are based on an all solid state silicon technology, called Deformable Mirror Devices[3]. The light switch elements are small metal mirrors, approximately 15 microns by 15 microns in area. We have produced fully functional two dimensional arrays of 64,000 mirrors. The addressing circuitry is also included on the silicon chip reducing the number off off-chip leads required.

Certain aspects of the DMD are ideally matched to neural network computations:

1. The mirror deflections are both variable and electronically controlled in an analog mode.
2. The degree of mirror deflections is equivalent to the value of the interconnects used in neural network computations.
3. The mirror deflections are limited, and sigmoidal in nature, providing an ideal threshold function.

Several neural network configurations using DMDs are described. Special consideration is given to the electrical addressing constraints imposed on the optical operation of the DMD arrays. System partitioning between optical and electrical subsystems is shown to allow rapid execution of highly parallel matrix computations, while retaining timing, synchronization, and dynamic range consistency.

References

1. N.H. Farhat, S. Miyahara, and K.S. Lee, "Optical Analog of Two-Dimensional Neural Networks and Their Application in Recognition of Radar Targets," p. 146, Neural Networks for Computing, Snowbird, UT 1986 AIP Conference Proceedings 151, American Institute of Physics, NY 1986.
2. D. Psaltis, and N. Farhat, "Optical Information Processing Based on an Associative-Memory Model of Neural Nets with Thresholding and Feedback," Opt. Lett. 10, 98, (1985).
3. D.R. Collins, J.B. Sampsell, P.A. Penz, and M.T.Gately, "Optical Neurocomputers Implementation Using Deformable Mirror Arrays," p. III-631, Proceedings of the IEEE First Annual International Conference on Neural Networks, June 1987 (IEEE Catalog #87TH0191-7).

FIGURE 1.
NEURAL NETWORKS MODEL

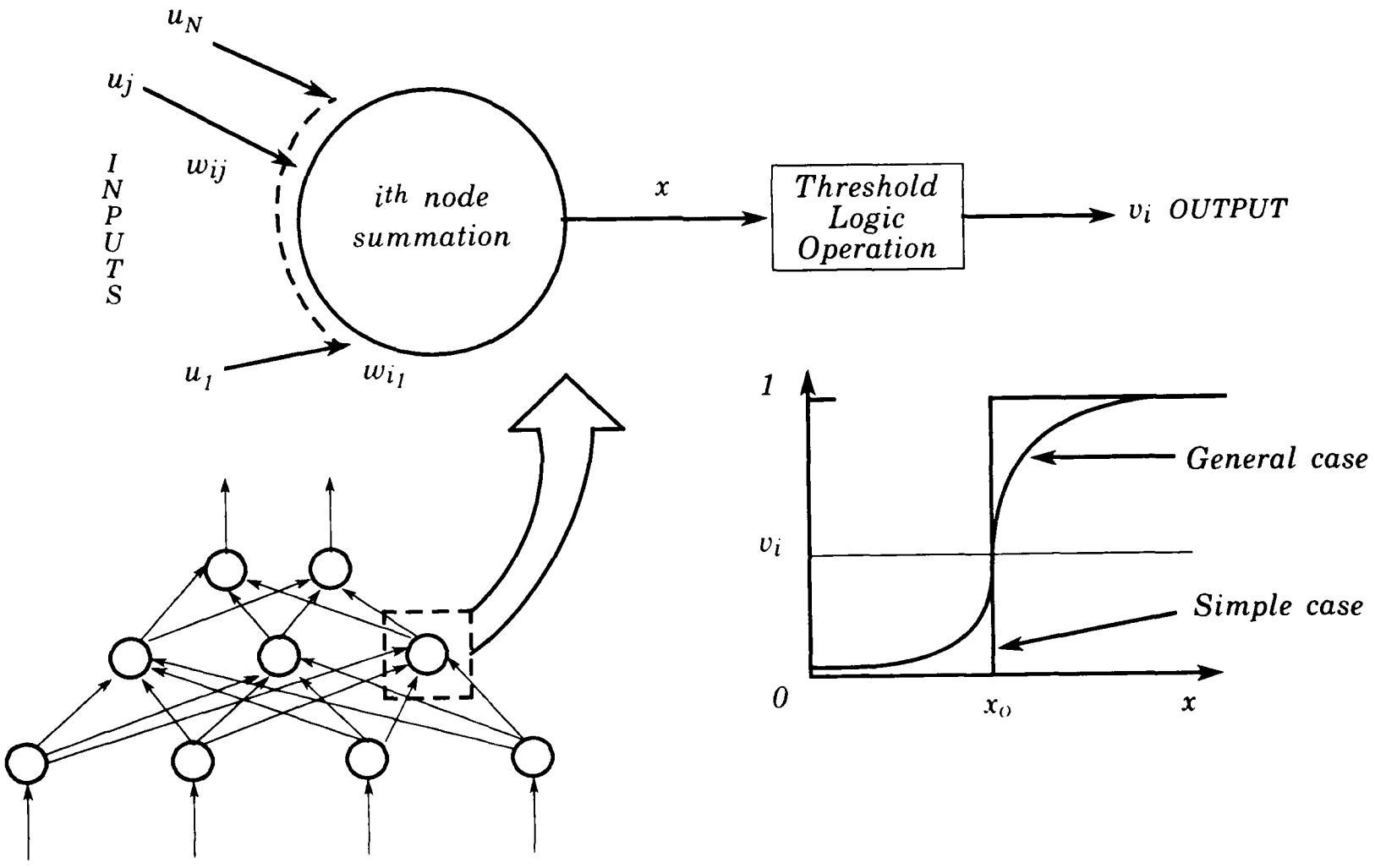

FIGURE 2.
INTERCONNECTIONS
NEURAL NETWORK / CELLULAR AUTOMATA

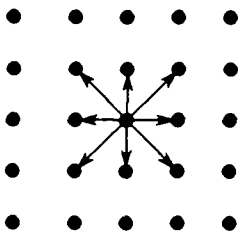

Cellular Automata

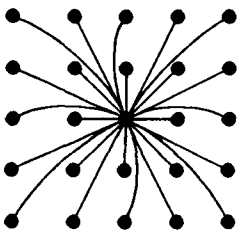

Neural Network

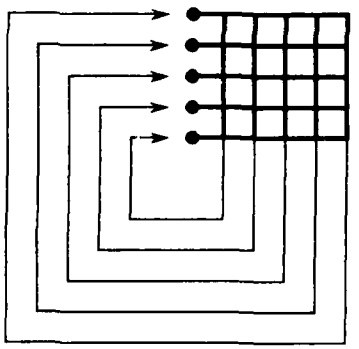

Matrix Form of Neural Network

Bistable Deformable Mirror Device

Larry J. Hornbeck
Texas Instruments Incorporated
Central Research Laboratories
POB 655936/MS 134
Dallas TX 75265

William E. Nelson
Texas Instruments Incorporated
Data Systems Group
5701 Airport Rd/MS 3237
Temple TX 76503-6012

1. Introduction

The bistable DMD is the digital version of a class of reflective, micromechanical spatial light modulators (SLMs) known as deformable mirror devices (DMDs). In its earliest form the DMD was a hybrid SLM consisting of a metalized polymer mirror bonded to an underlying silicon address circuit[1,2].

From this technology evolved a monolithic, analog DMD consisting of an array of aluminum alloy cantilever beams integrated over an underlying silicon address circuit [3]. The monolithic, analog DMD is capable of being line-addressed at TV rates, and contains on-chip, all of the necessary serial-to-parallel converters and decoders. Its small analog deflections (1°-2°) make it suitable for correlation and other optical processing applications [4-5], as well as neurocomputing [6].

There has been a growing interest in the DMD for optical crossbar switching[7], and for printing applications[8] using both photoreceptor and film media. For these applications, precise, large angle digital deflections (10°) are required. The bistable DMD described in this paper meets these criteria. It features a large deflection angle which is precisely determined by the device architecture and not by a balance of forces, as in the case of analog DMDs. Flatness in the zero deflection state is ensured by a torsion beam pixel design. In a printing application requiring gray shades, pulse width modulation produces uniform, accurate shades of gray.

In the following sections, the architecture and operating characteristics of the bistable DMD will be described. Because the bistable DMD is a very recent development, more details of device performance in printing applications will be presented at the conference.

2. Device Description

The architecture of the bistable DMD is shown in Figures 1 and 2. Each pixel consists of a torsion beam, made from a layer of thick reflecting metal, connected to a surrounding conducting support layer by two thin metal torsion rods at diagonal corners. A planarizing, insulating spacer material underlying the torsion beam is removed by isotropic plasma etching to form an air gap under each torsion beam. Underlying each torsion beam are four electrodes, two landing electrodes and two address electrodes. The landing electrodes are electrically connected to the torsion beam. Flatness of the torsion beam is ensured by the fact that the torsion rods are under tension.

When an address electrode is energized, the electrostatic force of attraction between the beam and address electrode causes the beam to rotate about its diagonal in the direction of the address electrode until its tip touches the landing electrode (dotted line in Fig. 2). The angle that the fully deflected beam makes is called the landing angle, θ_L. The beam rotates to $+\theta_L$ or $-\theta_L$ depending on whether the (+) or (-) address electrode is energized. Both landing electrodes are maintained at the torsion beam potential, and function to reduce the landing torque and to provide an electrically neutral contact to the landing surface.

In order to operate the bistable DMD, positive potentials are applied to one or the other of the address electrodes and a negative potential called the differential bias, is applied to the beam

and landing electrodes. The function of the differential bias is to lower the address voltage requirement by providing a torque gain to the applied address torque. The term differential bias reflects the fact that no torque results unless there is a potential difference between the address electrodes, or the torsion beam is deflected. The bistable DMD may be operated in any of three modes, monostable, tristable, or bistable, depending on the magnitude of the differential bias. This is illustrated in the potential energy plot of Figure 3. With no differential bias, and in the absence of an applied address voltage, the torsion beam is monostable, with only one potential energy minimum and hence only one stable state at $\theta = 0$. In order to deflect the beam to the landing angles $\theta = \pm \theta_L$, a constant address voltage must be applied. When this voltage is removed, the beam returns to $\theta = 0$.

As differential bias is introduced, the potential energy at the landing angles begins to decrease, and eventually two potential energy minima develop at $\theta = \pm \theta_L$. The torsion beam is now tristable, with stable states at $\theta = -\theta_L, 0, +\theta_L$. In order to address the beam from its undeflected state at $\theta = 0$, an address voltage is applied with a magnitude sufficient to momentarily lower the potential barrier between $\theta = 0$ and the desired landing angle, $\theta = -\theta_L$ or $+\theta_L$. The beam rotates to the landing angle, and when the address voltage is removed, the beam remains in a statically stable state at $\theta = \pm \theta_L$ until the differential bias is removed.

As the magnitude of the differential bias is increased further, the potential barriers between $\theta = 0$ and $\theta = \pm \theta_L$ disappear and the beam becomes bistable. Momentary application of the address voltage causes the beam to rotate to the desired landing angle and to remain there until the differential bias is removed. The lowest address voltage requirement is achieved by operating in the bistable mode.

At the end of each address cycle the deflected beams must be returned to the undeflected state, or reset, before being readdressed. To accomplish this, the differential bias is momentarily returned to ground and a short duration reset pulse is applied to the beams and landing electrodes via the differential bias bus. The reset pulse acts to store potential energy in the torsion rods by deflecting the beam and torsion rods downward towards the electrodes. When released, this additional potential energy assures a uniform, reliable reset action of all deflected pixels to the undeflected state.

Because the reset and differential bias functions are common to every pixel, they can be provided by a single off-chip driver. Only the address electrode signals (10 volts or less) need to be switched by on-chip circuitry and this funciton is supported by conventional C-MOS structures.

3. Operating Characteristics

The present chip design is a linear array of 512 pixels consisting of four rows of 128 pixels, with an effective center-to-center spacing of 19 microns. Because this embodiment is meant to demonstrate only the electrooptical characteristics of a bistable DMD, it does not include on-chip address circuitry, but is hard-wired on-chip into 32 blocks of 16 independently addressable pixels.

The beam landing angle is 8.9 degrees, determined by the torsion beam diagonal length and spacer thickness. The electromechanical response time at atmospheric pressure is six microseconds as measured by a photomultiplier. The measured pixel deflection cycle lifetime is greater than 12 billion cycles.

Using a conventional darkfield microscope, an image of one portion of the chip is shown in Figure 4. Here 10 of every 16 pixels are addressed in the tristable mode from $\theta = 0$ (dark state) to $\theta = \theta_L$ (bright state). Gray shades are accurately produced by using pulse width modulation. Because of the short response time of the DMD, the address pulse can be delayed after reset to control the duty factor and therefore produce precise gray shade modulation. Table 1 is a summary of the design and operating characteristics of the bistable DMD.

Table 1
Bistable DMD Summary

Array Size	512 x 1 (Four rows of 128 pixels)
Effective Pixel Spacing	19 Microns at Unit Magnification
Address Configuration	32 Blocks of 16 Independently Addressable Pixels
Address Voltage	+ 10 Volts (Tristable), + 5 Volts (Bistable)
Differential Bias	-10 Volts (Tristable), -18 Volts (Bistable)
Reset Pulse	+ 60 Volts, 1 Microsecond Pulse Width
Angular Deflection	± 8.9 Degrees
Angular Nonuniformity	
Undeflected State	± 0.2 Degree
Deflected State	± 0.1 Degree
Response time ($\theta = 0$ to θ_L)	6 Microseconds at Atmospheric Pressure
Pixel Lifetime	Greater than 1.2×10^{10} Cycles

4. Summary

The architecture and operating characteristics of the bistable deformable mirror device (DMD) have been presented. The bistable DMD is a reflective, micromechanical spatial light modulator, monolithically formed on silicon. Large angle digital beam deflections (± 8.9 degrees) are achievable with a very high degree of uniformity. Because of its fast response time (6 microseconds) it can be pulse width modulated to produce accurate gray shade modulation. A differential biasing technique lowers address voltage requirements to 10 volts or less so that conventional C-MOS on-chip drive circuits can be employed. Applications currently under evaluation at Texas Instruments include printing and optical crossbar switching.

5. References

1 L J Hornbeck, "128 x 128 Deformable Mirror Device," IEEE Trans. Electron Devices ED-30(5), 539(1983)

2. D R Pape and L.J.Hornbeck, "Characteristics of the Deformable Mirror Device for Optical Information Processing," Optical Engineering 22(6), 675 (1983)

3. W R Wu, R O Gale, L.J.Hornbeck, and J.B.Sampsell, "Electrooptical Performance of the Deformable Mirror Device," Proc SPIE 825 (1987).

4 J M Florence, M K Giles, and J.Z.Smith, "Operation of a Deformable Mirror Device as a Fourier Plane Phase Modulating Filter," submitted to SPIE 1988 Technical Symposium Southeast, Orlando, April 1988

5 D Gregory, R.Juday, J Sampsell, R.Gale, R.Cohn, and S.Monroe, "Optical Characteristics of a Deformable-Mirror Spatial Light Modulator," Optics Letters 13(1), 10(1988).

6. D R Collins, J.B. Sampsell, P.A.Penz, M.T.Gately, "Optical Neurocomputers Implementation Using Deformable Mirror Arrays," Proc. IEEE First Annual International Conference on Neural Networks, 1987.

7 R Cohn, "Link Analysis of a Deformable Mirror Device Based Optical Crossbar Switch," Proc. SPIE 825 (1987)

8 W E Nelson, L J Hornbeck, "Micromechanical Light Modulator for Electrophotographic Printer," to be presented at SPSE 4th International Congress on Advances in Non-Impact Printing Technologies, 20 March 1988

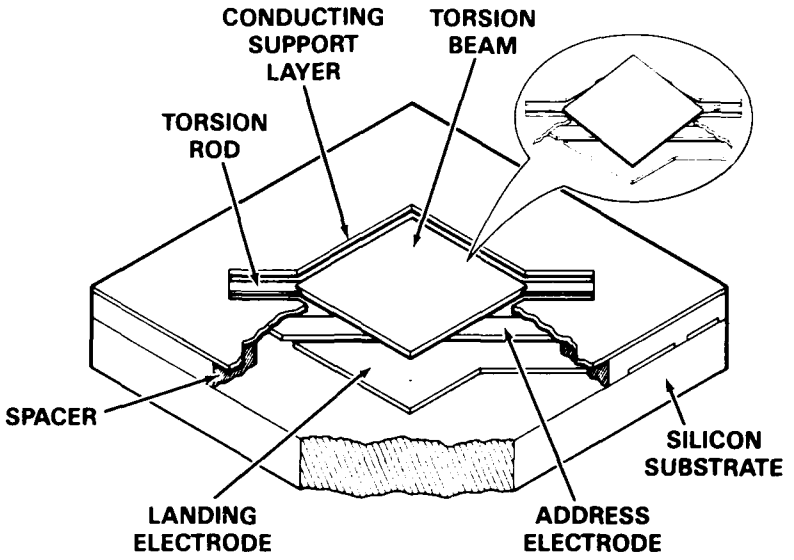

Fig. 1. Bistable DMD with cutaway showing electrodes.

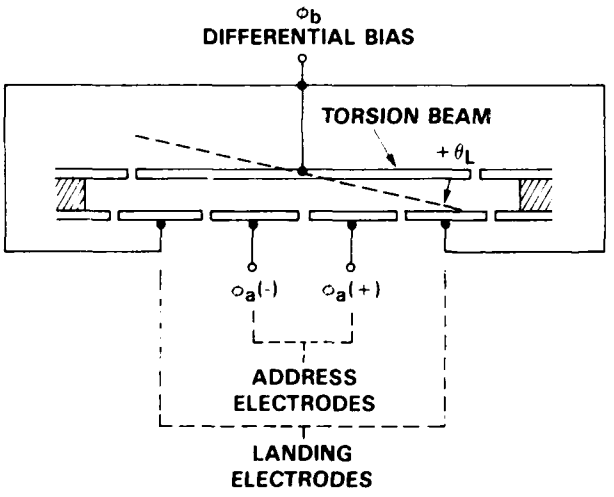

Fig. 2. Cross section of bistable DMD.

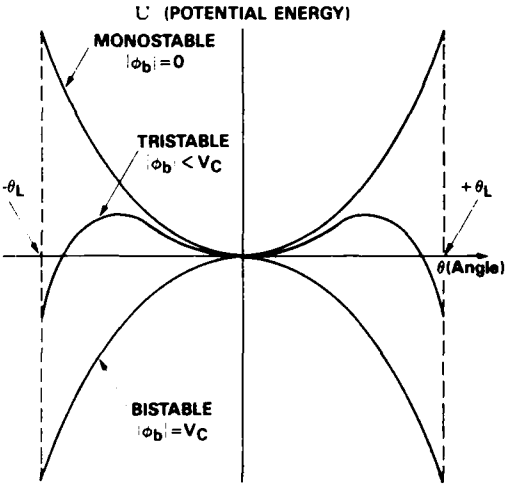

Fig. 3. Potential energy for three modes of operation.

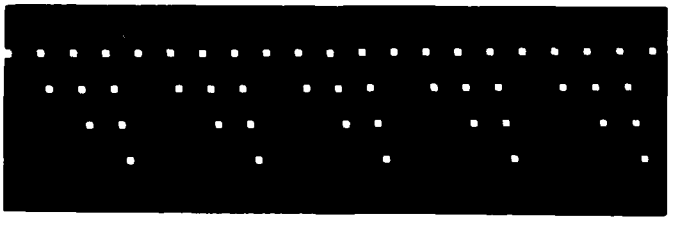

Fig. 4. Darkfield projected image of bistable DMD.

Limitations of Currently Available Deformable Mirror Spatial Light Modulators

Don A. Gregory
and
James C. Kirsch

U. S. Army Missile Command
AMSMI-RD-RE-OP
Research Directorate
Redstone Arsenal, AL 35898-5248

SUMMARY

The Spatial Light Modulator (SLM) is perhaps the most critical element in several optical processing architectures such as the Vander Lugt Matched Filter Correlator and the Joint Transform Correlator. The SLM is a device used to encode information onto a laser beam so that it may be processed by a coherent optical system. Several devices are available which perform this critical task. The optical characteristics of these devices will determine, to a large extent, the speed, resolution, and efficiency of an optical system since the SLM is responsible for supplying the system with new information. The Hughes Liquid Crystal Light Valve (LCLV) is a reflection type SLM that is both optically addressed and read. The limitations of the LCLV are its low sensitivity to the write light, low resolution, and slow response time. The Semetex/Litton Magneto-Optic Device (MOD) is a transmission type SLM that is electrically addressed and optically read. The MOD is comparable in resolution to the LCLV but the optical throughput of the device is only 3-5%. Neither device will operate at high frame rates.

A new device, recently developed by Texas Instruments, is electrically addressed and optically read in a reflection mode. The Deformable Mirror Device (DMD) is capable of megahertz pixel rates and can be addressed by either a camera or a computer.[1] The monolithic device is a 128x128 array of pixels on a silicon substrate. The silicon substrate also contains the necessary drive and line addressing electronics.

Figure 1 is a drawing of an individual pixel of the DMD. Each pixel of the array consists of four tiny mirrors which are hinged on one corner. The mirrors are 12.57 μm square and are formed on 51μm centers. An air-gap capacitor is formed between each set of mirrors and an underlying electrode. The electrodes are connected to the sources of an array of metal-oxide semiconductor (MOS) transistors. The addressing

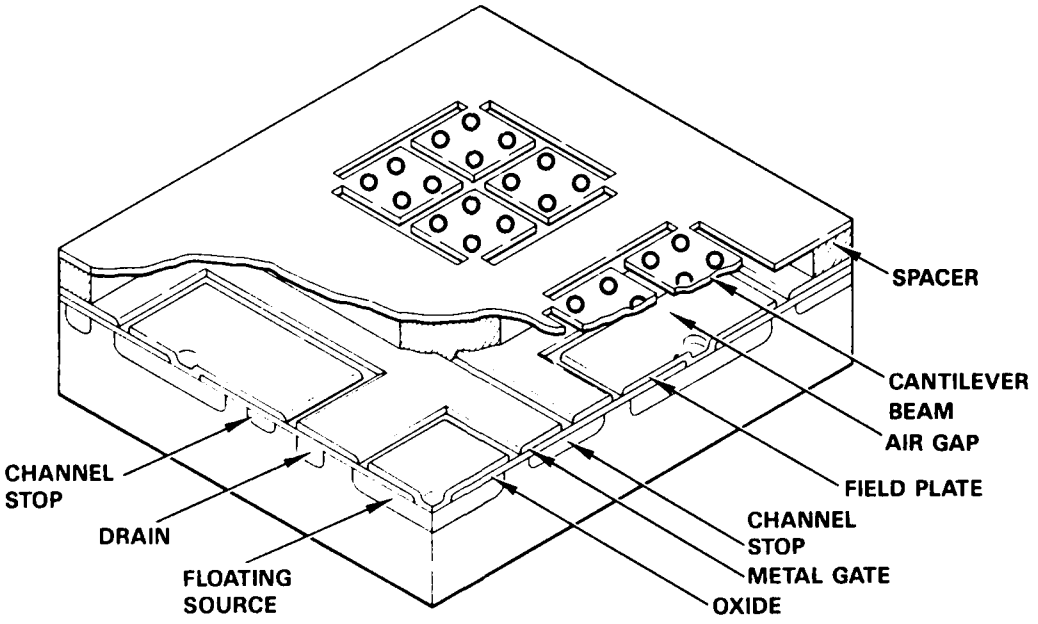

Figure 1. A cut-away drawing of the DMD spatial light modulator.

electronics drive each electrode to a voltage corresponding to a given video signal. The electric field created between the electrodes and the mirrors causes the mirrors to deflect slightly.[1] The amount of deflection in each pixel will correspond to a phase change in the light reflected from the mirrors. In this manner, a video signal can be encoded into the phase of a laser beam.

Several optical characteristics of the DMD have been examined. These include reflectance, deflection angle of the mirrors, active area, and high order diffraction effects. The diffraction effects have been experimentally investigated and theoretically modeled. The results will be used to determine the effectiveness of using a DMD as a spatial light modulator.

The reflectance of the DMD determines, in part, how efficiently the available light is used. A high reflectance alone, however, does not ensure efficient use of the light. The light must be reflected at a small enough angle to ensure that vignetting does not occur. This condition places an upper limit on the deflection angle of the mirrors. The smallest useful deflection angle is determined by the minimum usable phase shift in the reflected wave.

The high order diffraction effects will also play a large role in determining the usefulness of the DMD as a spatial light modulator. Each mirror has four tiny holes to aid in etching the wells under each pixel. These holes along with inactive areas around the pixels will cause high order diffraction effects when viewed in the Fourier plane. The optical Fourier transform of the DMD with no input signal is shown in Figure 2. The Fourier transform of an input scene displayed on the DMD would be convolved with this diffraction pattern. The result of this convolution would yield the Fourier

transform of the input scene at each element in the diffraction pattern of Figure 2. Only one order is useful in many optical processing applications so light diffracted into the higher orders is wasted.

The results of these investigations will be presented along with optical processing architectures which could make use of a DMD spatial light modulator. Future research will focus on the phase modulating properties of the device. The pixel design for the next generation of DMD's will also be presented. This design should result in larger active areas and greater phase modulation.

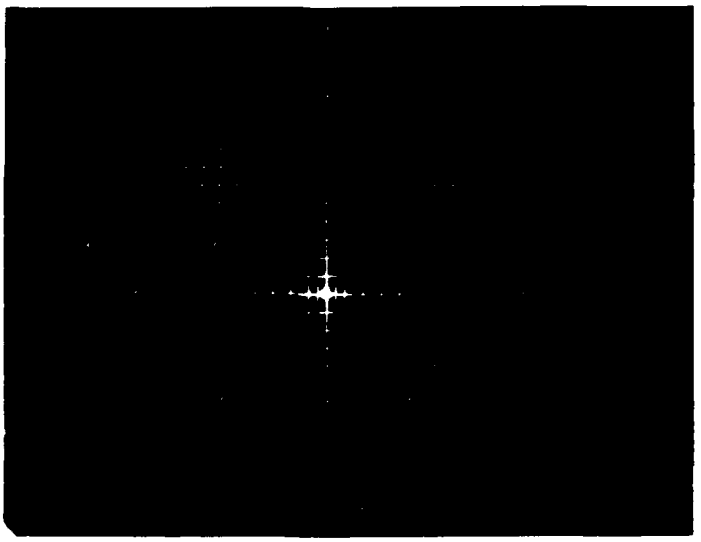

Figure 2. The far field diffraction pattern of the DMD with no input signal.

REFERENCES

1. Gregory, D., Juday, R., Sampsell, J., Gale, R., Cohn, R., and Monroe, S., "Optical characteristics of a deformable-mirror spatial light modulator," Optics Letters, vol. 13, pp. 10-12 (1988).

Resolution Limits of an Imaging System with Incompressible Deformable Spatial Light Modulators

B.Kuhlow, G.Mahler, and R.Tepe
Heinrich-Hertz-Institut Berlin GmbH, Einsteinufer 37,
D-1000 Berlin 10, Federal Republic of Germany

Introduction

The spatial light modulator (SLM) considered here consists of a thin incompressible viscous fluid layer and is addressed by an electron beam. As a consequence of the deposited charge image, the fluid surface is deformed by electrostatic stresses. For the incident light, this surface deformation represents a phase object causing phase modulation and thus diffraction. The conversion of this (invisible) phase modulation into a (visible) intensity modulation is achieved by means of a schlieren-optical imaging system. In previous publications [1,2], the transfer characteristics of the system for sinusoidal charge patterns, which lead to sinusoidal deformations because of the control-layer's linear transfer function, were extensively described; here, the transfer characteristics of the same system for spatially non-periodic structures are analyzed, and the resolution limits caused by the incompressibility of the SLM material and by the optical filtering are determined.

Surface-Charge Pattern

In order to study the non-periodic deformation behavior of the fluid SLM, an isolated line on a dark background is considered. For writing one line, the electron beam is scanned horizontally with the constant velocity v_x; at the same time, it is wobbled vertically with a very high frequency according to the line modulation. The position of the beam spot on line n at time t is thus given by

$$\xi(t)=v_x t \quad \text{and} \quad \eta(t)=nd+c\cdot\sin(2\pi f_w t), \tag{1}$$

where d is the line pitch (for an extended carrier grating, d represents the grating period), and c and f_w are the wobbling amplitude and frequency, respectively. Assuming a spatially invariant current-density distribution $g(\xi,\eta)$, the charge-density distribution on the fluid surface is found as

$$\sigma_n(x,y)=\int_{-\infty}^{\infty} g(x-\xi(t),y-\eta(t))\,dt. \tag{2}$$

Fourier transformation of Eq.(2) leads to the charge-density spectrum:

$$Q_n(f_x,f_y)=S(f_x,f_y)K(f_x,f_y) \tag{3}$$

here, $S(f_x,f_y)$ is the Fourier transform of $g(\xi,\eta)$ and $K(f_x,f_y)$ is a function which describes the effects of the beam modulation and is defined as

$$K(f_x,f_y)=\int_{-\infty}^{\infty} \exp\left[j2\pi(f_x\xi(t)+f_y\eta(t))\right]\cdot dt. \tag{4}$$

If a current-density distribution of the form $g(\xi,\eta)=g_o\cos^2(\pi\xi/a)\cos^2(\pi\eta/b)$, whose shape is similar to a Gaussian distribution, is assumed, and if the spot dimensions are chosen to be $a=v_x/f_w$ and $b=d$, as required for an ideal dark-field adjustment, the normalized spectrum of a horizontal line becomes

$$Q_n(0,f_y)=\frac{\sin(\pi f_y d)}{\pi f_y d(1-f_y^2 d^2)}\cdot J_o(2\pi f_y d), \tag{5}$$

where J_o is the zero-order Bessel function; this equation forms the basis for the following analysis of non-periodic surface deformations.

Surface Deformation of the Spatial Light Modulator

In order to find the fluid-layer surface deformation resulting from a sinusoidal charge pattern, the electrostatic potential has to be calculated by means of Laplace's equation $\Delta V=0$; subsequently, the electrostatic deformation stresses are derived from the electric field at the SLM surface. Then, the resulting hydrodynamic deformation of the viscous fluid is determined on the basis of the linearized Navier-Stokes equation. For a sinusoidal deformation of arbitrary spatial frequency, the time dependence of the amplitude is [1]:

$$a(t)=a_o \cdot \left[1-\exp(-t/\tau_1)\right] \cdot \exp(-t/\tau_2), \qquad (6)$$

where the parameters a_o, τ_1, and τ_2 are functions of spatial frequency, layer thickness, and such material properties as viscosity, capillarity constant, conductivity, and dielectric permittivity (for details see Ref. [1]).

Assuming a linear system, the spatial-frequency response for a given periodic charge pattern was calculated for different times; the resulting band-pass curves are shown in Fig.1. The decrease towards low spatial frequencies is essentially caused by the incompressibility of the SLM material, the decline at high spatial frequencies is a consequence of the surface tension.

In general, the transfer characteristics of the SLM can be represented by a multi-dimensional linear system in which a spatially varying charge pattern as input leads to a space- and time-dependent surface deformation as output. Thus, the deformation at time t_o caused by an arbitrary charge distribution can be calculated according to the following general formula:

$$a(x,y,t_o)= \int_{-\infty}^{\infty}\int H(f_x,f_y,t_o)Q_n(f_x,f_y)\exp\left[j2\pi(f_x x+f_y y)\right] df_x df_y \qquad (7)$$

where $H(f_x,f_y,t_o)$ is the time-dependent spatial-frequency response of the SLM as depicted in Fig.1. When considering a single line on a dark background [4] the integration is restricted to the variable f_y. Fig.2(a) shows the charge-density distribution of a single line; the corresponding deformation is given in Fig.2(b). According to Eq.(5), the writing of a single line on the fluid leads to side lobes of the charge pattern and also of the deformation; it should be noted, that, because of the SLM incompressibility, the deformation pattern contains side lobes even for charge distributions without side lobes; thus, the image of a single line is always a triplet. Unfortunately, this feature, which is characteristic for all incompressible SLM's, is not adequately discussed in the existing literature. Furthermore, it is found that the deformation pattern widens with time (Fig.4), since, according to Fig.1, the components with low spatial frequencies are dominant in this range.

Schlieren-Optical Imaging System

As already mentioned in the Introduction, the surface deformation of the SLM is made visible by means of a special schlieren-optical system, a dark-field imaging system, that acts as a high-pass filter for the deformation pattern. The transmission of the phase object represented by the SLM can be written as

$$t(x,y,t_o)= \exp\left[j\,\frac{2\pi}{\lambda}\cdot(n-1)\cdot a(x,y,t_o)\right], \qquad (8)$$

here, n and λ are the refractive index of the SLM material and the wavelength of the light, respectively.

The dark-field imaging system is schematically shown in Fig.3; along the optical axis, five planes are labeled by numbers: 1-the light sources, 2-the control layer, 3-the principal plane of the schlieren lens, 4-the diffraction pattern, and 5-the image plane. For periodically arranged narrow light sources as necessary for high brightness and good resolution, the filter in plane 4 has to be a periodic arrangement of slots and of bars that block the undiffracted light of the source images (cf. the optical system of the General Electric light valve [3]).

The light distribution in plane 4 is proportional to the Fourier transform $T(x_4, y_4, t_o)$ of the transmission $t(x_2, y_2, t_o)$ given by Eq.(8), and the coordinates x_4 and y_4 of the diffraction pattern are defined as [2]

$$x_4 = f_x \lambda Q - M x_1 \quad \text{and} \quad y_4 = f_y \lambda Q - M y_1 \tag{9}$$

where $M = z_{34}/z_{13}$ is the magnification factor of the source image, and $Q = z_{12} z_{34}/z_{13}$ is a scaling factor. Behind the high-pass exit filter of transmission function $P(x_4, y_4)$ in plane 4, the modified light distribution is proportional to

$$T'(x_4, y_4, t_o) = T(x_4, y_4, t_o) P(x_4, y_4). \tag{10}$$

Finally, the desired intensity distribution of plane 5 is obtained from a further Fourier transformation of the light distribution given by Eq.(10). Apart from magnification factors, the intensity distribution of a single line whose surface-deformation pattern varies only with the y coordinate, becomes

$$I(y_5, t_o) = I_o \cdot \left| t'(-y_5, t_o) \right|^2, \tag{11}$$

where $t'(-y_5, t_o)$ is the Fourier transform of $T'(y_4, t_o)$. Fig.4 depicts the deformation patterns and the resulting intensity distributions at three instances within the frame period T. For the calculation of the distributions, light sources with a Gaussian shape and a broad spectrum were assumed. In spite of the temporally widening deformation pattern (see above), the line image remains narrow because of the optical high-pass filter. The widths of its exit slots are chosen so that the diffraction maxima of a single line move in time from the centers to the inner edges of the slots and that towards the end of a frame period the lower spatial frequencies are blocked by the bars. Thus, the filter always keeps the image of a single line relatively narrow. In case of an extended carrier grating, its period d should be designed to be so small that the light diffracted from it passes the slots close to their outer edges; then the largest possible part of one modulation side band can be transmitted.

Acknowledgements

The authors like to thank R.Gerhard-Multhaupt for stimulating discussions and L.Emich for valuable assistance. This work was supported by the German Federal Minister for Research and Technology under contract No. TK 140; the responsibility for the contents rests, however, solely with the authors.

References

1. R.Tepe, J.Appl.Phys. 57, 2355 (1985).
2. B.Kuhlow, Th.Sinnig, Appl.Opt. 26, 2659 (1987).
3. W.E.Glenn, SMPTE J. 79, 788 (1970).
4. G.Mahler, IEEE Trans.Consum.Electron. CE-30, 563 (1984).

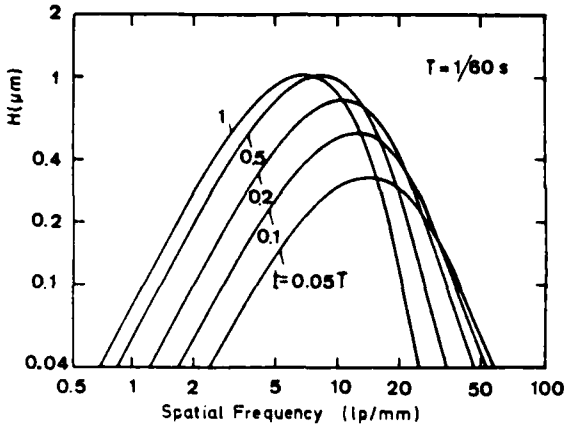

Fig.1 Time dependent spectral-frequency responses of deformable SLM; for chosen parameters see Ref.(1).

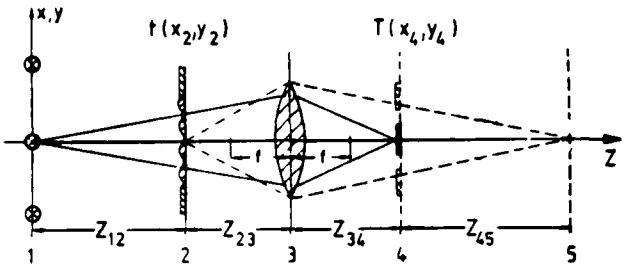

Fig.3 Schematic arrangement of the dark-field imaging system.

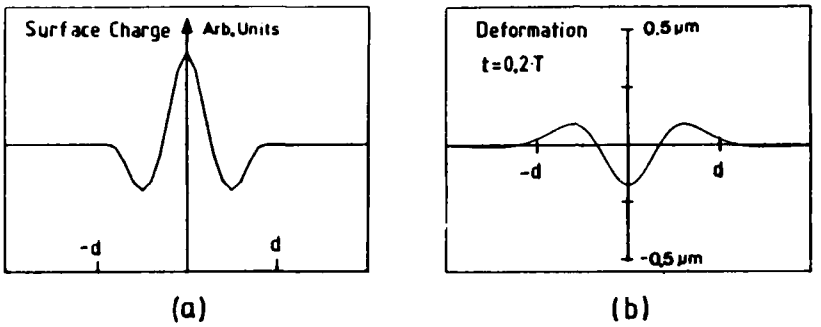

Fig.2 Single groove in an incompressible fluid formed by electron beam.

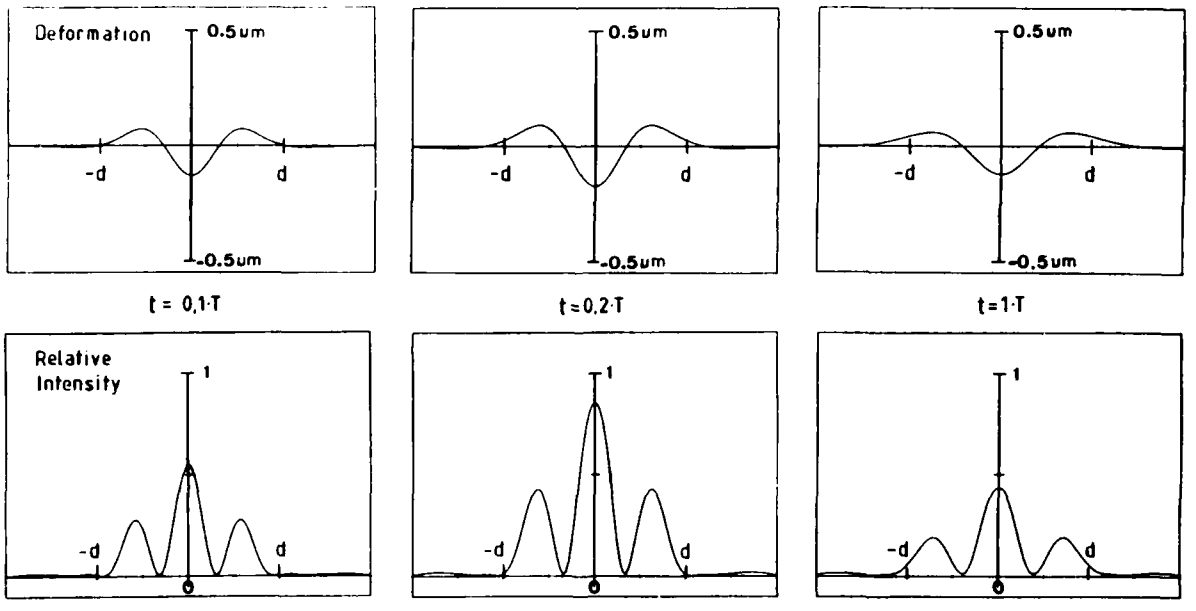

Fig.4 Surface deformation of a fluid and the resulting image at three different times during frame repetition period T.

THURSDAY, JUNE 16, 1988

EMERALD BAY BALLROOM

1:30 PM–2:50 PM

ThC1–4

OPTO-ELECTRONIC DEVICES

C. Lee Giles, Air Force Office of Scientific Research, *Presider*

High Performance TIR Spatial Light Modulator

Robert A. Sprague, William D. Turner, Mark S. Bernstein,
David L. Steinmetz, David L. Hecht, Tibor Fisli, Joseph W. Kaminski
Xerox Palo Alto Research Center
3333 Coyote Hill Road
Palo Alto, California 94304

Russell B. Rauch
Xerox Electro-Optical Center
701 South Aviation Boulevard
El Segundo, California 90245

Summary

Introduction

The TIR linear spatial light modulator, which has been discussed in a number of previous publications,[1-4] is a VLSI-driven device which utilizes phase change in lithium niobate to achieve modulation of a line of light at a number of positions along a line. It does this by coupling fringing fields from a set of electrodes on a VLSI chip into the crystal and interacting with these fringing fields in a total internal reflection mode of illumination. The device is used to phase modulate the light and can be either directly read out or used in a Schlieren readout system to create intensity modulation. In this paper we present information on design, fabrication, and performance of a new high performance device which has 4735 elements and operates with a 256 MPixel/second data rate.

Device Structure

The basic configuration of the device is shown in Figure 1. It consists of a thin flat plate of lithium niobate which has electrodes deposited on one surface and has two sides polished to allow interaction with a beam of light in a TIR mode. In this case, the electrodes are 3.5 mm long, have a spacing of 10 microns, and there are 4736 of them spaced over 47.35 mm. Individually selectable voltages are applied to each of these electrodes by addressing them with two integrated circuits which have complementary sets of electrodes and are pressure-contacted to the electrodes on the crystal.

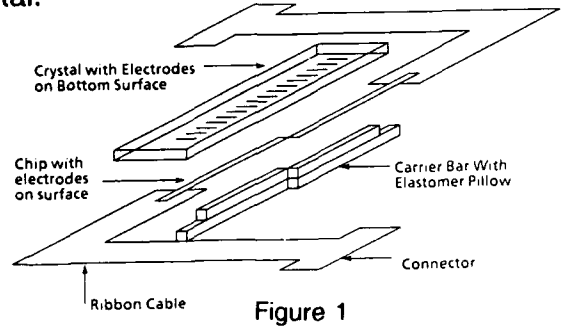

Figure 1
TIR modulator assembly.

Figure 2 shows a circuit layout for each chip. The design utilizes 16 lines of data which are sequentially written to each successive group of 16 electrodes on the device with a shift register addressing technique. There is a CMOS transmission gate for each electrode so that the voltage is held on each electrode until it is to be changed. The electrodes on the VLSI chip are .5 mm long and on 10 micron spacings. They are patterned in a second layer of metal which is located at the highest elevation on the chip so that when it is pressed against the crystal electrodes good electrical contact is achieved. The chip stores up to 15 volts on the electrodes, which is enough to achieve 50 percent diffraction efficiency into the two first orders (i.e., 50% of the light is scattered out of the undiffracted zero order beam). The shift register operates at an 8 MHz data rate, providing a chip bandwidth of 128 MHz (16 lines x 8 MHz) and a modulator bandwidth with 2 chips of 256 MPixels/second.

A modulator of the type shown diagrammatically in Figure 1 and using two of the chips shown in Figure 2 is illustrated in the picture of Figure 3. Each chip is mounted on a carrier bar consisting of pieces of aluminum with an elastomer layer mounted underneath each chip. When the carrier bar with its associated chip is assembled to the crystal, the elastomer is compressed, forcing the chip electrodes against the crystal electrodes with a uniformly distributed pressure on the order of 100 psi. This pressure is sufficient to break the oxide layers and provide good electrical contact between the chip electrodes and the crystal electrodes. The pressurizing structure of the modulator shown in Figure 3 utilizes two spring metal plates which are curved in opposition to apply the pressure. When these metal plates are flattened by the force exerted by the screws clamping them together, the elastomer is fully compressed. Their complementary reverse curvature applies a balanced pressure along the length of the modulator, thus producing a flat surface at the chip/crystal interface. This is important in achieving a good interaction with a line of light which is focused in the sagittal axis.

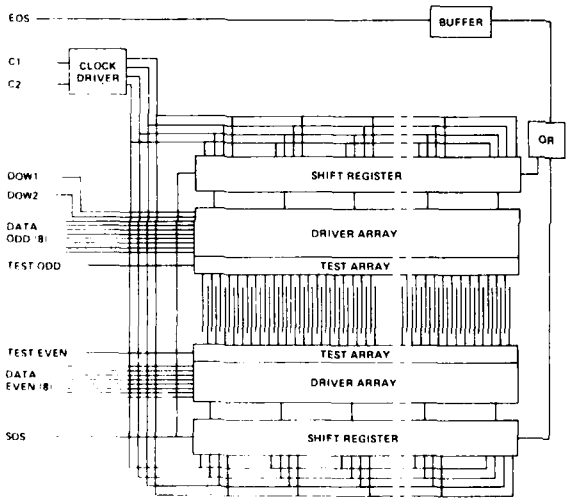

Figure 2
VLSI circuit configuration.

Figure 3
Photograph of the TIR modulator.

Device Testing

In order to test the modulator, it is illuminated with a narrow laser beam and the modulator is reimaged onto a detector plane. A slit which is the size of the image of one modulator element is placed in the detector plane. The modulator is translated across the beam, and the detected intensity passing through the slit is plotted on a chart recorder. This scheme is shown in Figure 4. By using such a testing technique, nonuniformities in the illuminating beam are eliminated from the measurement, since the same part of the beam is always used for testing. Figure 5 shows a typical plot of modulator output. The efficiency is between 40% and 50% (as measured by the ratio of light measured with the stop in place and all pixels turned on to that with the stop taken out of the system and all pixels turned off). It can be seen that all pixels work, but there is some local nonuniformity from element to element. Overall contrast is about 100:1, as indicated by the background trace on the same plot.

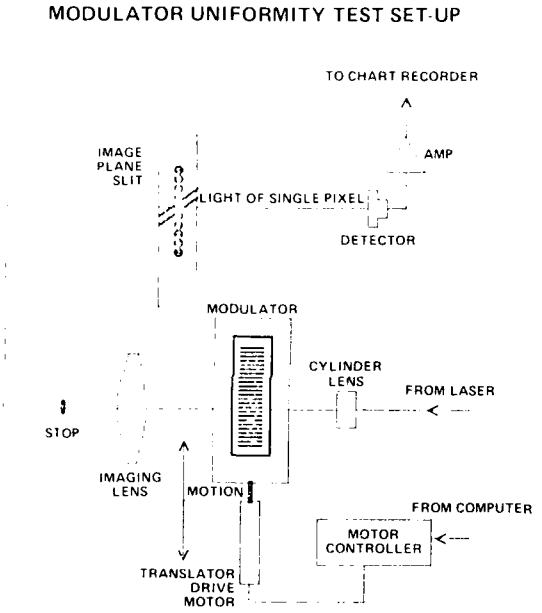

Figure 4
Configuration and methodology used to test modulator performance.

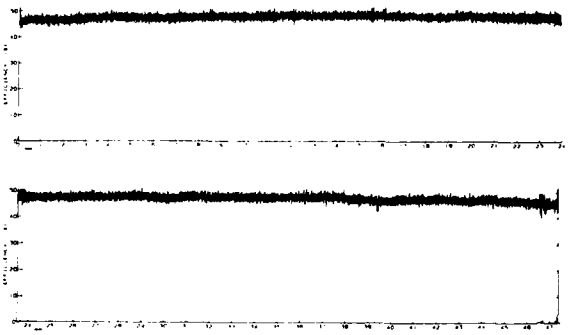

Figure 5
Modulator uniformity and background measured in apparatus of Figure 4.

Device Application

Figure 6 shows a typical optical system in which this spatial light modulator is incorporated in order to achieve intensity modulation in an output image plane. This particular system is used for laser printing, but other applications are suggested which might utilize the same basic device at different magnifications and with different types of illumination sources. The laser light is expanded in the tangential direction by lens L1 and collimated by a combination of L2 and L3. It is brought to focus in the sagittal (vertical) direction by lens L3 so that it is focused into the modulator and onto the lower surface of the crystal in the center of the electrodes. Lenses L2 and L3 are aspheric in nature so that some of the light in the center of the Gaussian laser beam is redirected towards the outside of the beam to produce a tangentially uniform beam in the plane of the modulator. After this light illuminates the modulator, it is brought to focus inside the imaging lens

onto a stop which blocks out the zero order diffraction. The imaging lens collects the diffracted light and images the modulator, with some magnification, onto the output image plane. For laser printing, this particular set of optics was used to image the modulator at 300 spots per inch on a 15.7 inch format. An example of the type of image spots produced at the output of such a system in shown in Figure 7.

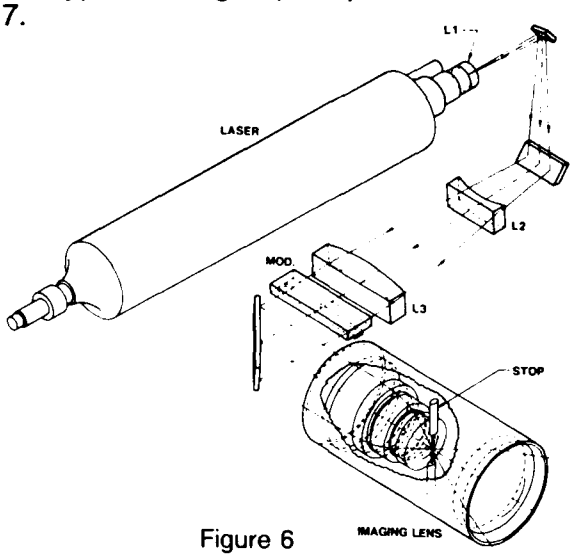

Figure 6
Optical system using the TIR spatial light modulator for laser printing.

Figure 7
Highly magnified output image of the system shown in Figure 6.

Conclusion

We have shown the design, construction, and test evaluation of a TIR spatial light modulator with 4735 individually controllable elements and a bandwidth of 256 MPixels per second. Such a device has potential application in areas of printing, optical computing, and addressing of large optical memories.

References

1. Sprague, R. A.; Turner, W. D.; Flores, L. N. *Linear total internal reflection spatial light modulator for laser printing*. Proceedings of the SPIE; 1981; 299: 68-75.

2. Turner, W. D.; Sprague, R. A. *Integrated total internal reflection (TIR) spatial light-modulator for laser printing*. Proceedings of the SPIE; 1981; 299: 76-81.

3. Johnson, R. V.; Hecht, D. L.; Sprague, R. A.; Flores, L. N.; Steinmetz, D. L.; Turner, W. D. *Characteristics of the linear array total internal reflection electro-optic spatial light modulator for optical information processing*. Optical Engineering. 1983; 22 (6): 665-674.

4. Sprague, R. A.; Turner, W. D.; Hecht, D. L.; Johnson, R. V. *Laser printing with the linear TIR spatial light modulator*. Proceedings of the SPIE; 1983 April 19; 396: 44-49.

Two-Dimensional Electrically-Addressed Si/PLZT Spatial Light Modulator Arrays

J. H. Wang, S. C. Esener, T. H. Lin, S. Dasgupta and S. H. Lee
Department of Electrical and Computer Engineering, C-014
University of California, San Diego
La Jolla CA 92093

1. INTRODUCTION

In the last few years extensive efforts have gone into the development of spatial light modulators (SLMs) for the realization of massively parallel optical processors[1,2]. The silicon-PLZT SLM approach is one of the promising approaches and has the potential of combining the computational power of silicon and the communication power of optical interconnects. By using the third direction normal to the processing plane, the Si/PLZT approach allows the optical interconnects to provide the advantages of high speed parallel and global interconnections to simple silicon electronic circuits performing local computational operations. In this paper, we report on the successful fabrication of two-dimensional electrical matrix-addressed SLMs by integrating silicon MOSFETs and electro-optic PLZT light modulators on the same substrate (PLZT) using a simultaneous laser crystallization and diffusion technique[3]. When fully developed into large arrays this Si/PLZT electrically addressed SLM (ESLM) can be used efficiently as an input device to optical processors, transducing electrical information into optical form while being fully compatible in data format with the optically addressed Si/PLZT SLMs presently under development at UCSD. In what follows we describe the theory and design consideration for the Si/PLZT ESLM, detail the experimental techniques used and discuss the results obtained.

2. OPERATING THEORY AND DESIGN CONSIDERATIONS

The fabricated matrix addressed ESLM consists of a 12x12 array of identical unit cells as shown in the photomicrograph in Fig.1. As all Si/PLZT SLMs, it has a spatially segmented format and can be operated in transmissive as well as in reflective mode[1,4,5]. A unit cell of such an array is shown in the photomicrograph in Fig.2a and consists simply of a MOSFET that connects the PLZT modulator to the electrical modulating input as shown in the schematic of the circuit in Fig.2b. The operation of the cell is very similar to the operation of a single transistor dynamic RAM cell. When the gate of the pass MOSFET is high, the electrical modulating input is directly connected to the PLZT modulator electrode. At this time a charge proportional to the electrical input is deposited across the PLZT modulator capacitance. Once the gate of the pass transistor is returned to a low state, this charge remains stored in the PLZT capacitance until the pass transistor is activated again at which time the charge in the modulator capacitance is refreshed. The stored charge in the modulator establishes a transverse electrical field in the PLZT modulator, which then modulates a read beam with a modulation depth proportional to the electrical input. Thus the Si/PLZT ESLM can work in both analog as well as in binary mode on the proper choice of the input.

Critical parameters involved in the fabrication of large ESLM arrays involve the storage time and the response time of the cell and the output dynamic range. In order to increase the storage time or the refresh time, the leakage current of the MOSFET must be minimized. Therefore, for successful operation, Si/PLZT SLMs require good Si crystal quality with a long carrier recombination time. The time response of the cell must also be minimized by maximizing the MOSFET transconductance, another parameter closely related to the silicon crystal quality. Finally, in order to achieve good modulation depth the transistors must have a large breakdown voltage, yet another parameter related to the silicon crystal characteristics.

The next section describes the experimental methods utilized in achieving good silicon crystal on PLZT and in the fabrication of Si/PLZT ESLMs.

3. EXPERIMENTAL METHODS

The fabrication of the Si/PLZT ESLM arrays entailed several crucial issues. The samples were prepared by depositing a 3.5μm layer of SiO_2 on to the front surface of the PLZT substrate by PECVD at 250°C. This layer is used as both thermal and electrical isolation. A 0.6μm thick layer of polysilicon is then deposited on both sides of the composite by LPCVD at 640°C. The front side polysilicon layer is later on crystallized and used to host the silicon transistors while the backside layer is used as a masking layer protecting the PLZT

substrate throughout the process. A PECVD grown SiO_2 layer is then deposited on the poly layer and used as a mask for the drain and source regions of the MOSFETs to be fabricated. A phosphosilica film with impurity concentration of $1 \times 10^{20} cm^{-3}$ is spun on to the front surface of the sample for use as a diffusion source. The thickness of the impurity layer was 2000A. These wafers are then baked in an oven at 100°C for 1 hr to form a thin, highly-doped SiO_2 film.

The dopant is incorporated into the film by an Ar^+ laser assisted diffusion that is carried out simultaneously with the laser crystallization process of the silicon film . The various considerations that went into the implementation of this technique are detailed in Reference 3. A rectangular aperture is placed across the laser beam to reduce the beam width in the direction of the scan to 25μm. The beam width normal to the scanning direction was 70μm and the spacing between adjacent scan lines was 10μm. The PLZT substrate was held at room temperature during the laser scanning procedure. The laser power was kept at 7W. The masking SiO_2 layer was then removed and the standard VLSI device fabrication procedures followed except for the gate oxidation step which was performed at the relatively low temperature of 850°C in a pyrogenic oxidation tube. This low temperature oxidation is necessary since PLZT is damaged at temperatures above 900°C. Prior to the gate oxidation process, the samples are stripped of the polysilicon layer on the backside of the PLZT. In case the layer is left on, the strain induced at the interface of the PLZT and polysilicon during the oxidation process damages the PLZT and degrades the electro-optic performance.

RESULTS AND DISCUSSION

Following the laser-assisted diffusion, the Si films were characterized by measuring the average resistivity, the average Hall mobility and the impurity concentrations. These results are summarized in table 1. The I-V characteristics of the NMOS transistors were then tested. Figure 3 shows the characteristics of a typical NMOS transistor that was fabricated. The breakdown voltage obtained from the characteristics is ~ 48V which is at least a factor of 2 larger than previously reported thin film transistors. The transconductance is 200μS. From the obtained characteristic, the electron mobility was calculated to be $550 cm^2/Vs$. This value is within 15% of electron mobilities obtained in bulk silicon devices. This suggests that the technique of laser-assisted diffusion provides an excellent means of fabricating MOSFETs on PLZT.

The time response characteristics of the devices were also measured. Figure 4 is a photograph of a typical response characteristic. As can be read from the picture, rise and fall times within 10μs are achieved for a 30V peak-to-peak voltage swing. Presently, we are measuring the storage time, leakage current and optical modulation depth. These parameters will be presented at the conference.

In summary, we have demonstrated the successful fabrication of integrated 2-D array of a matrix addressed Si/PLZT SLMs. Initial measurements performed on the device show that the performance is in the expected range.

References:

1. S. H. Lee, S. Esener, M. Title and T. Drabik, "Two-dimensional silicon/PLZT spatial light modulators: design considerations and technology," *Opt. Eng.* **25** (2):250-260. February 1986, also in *Proc. SPIE*, Los Angeles, January 1986.

2. D. A. B. Miller, " Quantum Wells for Optical Information Processing," *Opt. Eng.* **26** (5):368-372. May 1987.

3. J.H. Wang, T.H. Lin, S.C. Esener, S. Dasgupta and S.H. Lee "NMOS Transistors Fabricated by Simultaneous Laser Assisted Crystallization and Diffusion on Silicon on Electrooptic PLZT," *Proc. of Mat. Res. Soc. Symposium*, Boston, Massachusetts (November 1987).

4. S. Esener, J. Wang, M. Title, T. Drabik and S.H. Lee "One-dimensional silicon/PLZT spatial light modulators," *Opt. Eng.* **26** (5):406-413. May 1987, also in *Proc. SPIE*, San Diego, (August 1986).

R. Athale, S. H. Lee and S. Esener, "A spatially segmented design approach to spatial light modulators," in these *Proceedings*, Lake Tahoe, 1988.

Table 1. The electrical characteristics of silicon film after simultaneous laser assisted crystallization and diffusion.

average resistivity	ohm · cm	0.0048
average Hall mobility	$cm^2V^{-1}sec^{-1}$	72
impurity concentration	cm^{-3}	1.8×10^{19}

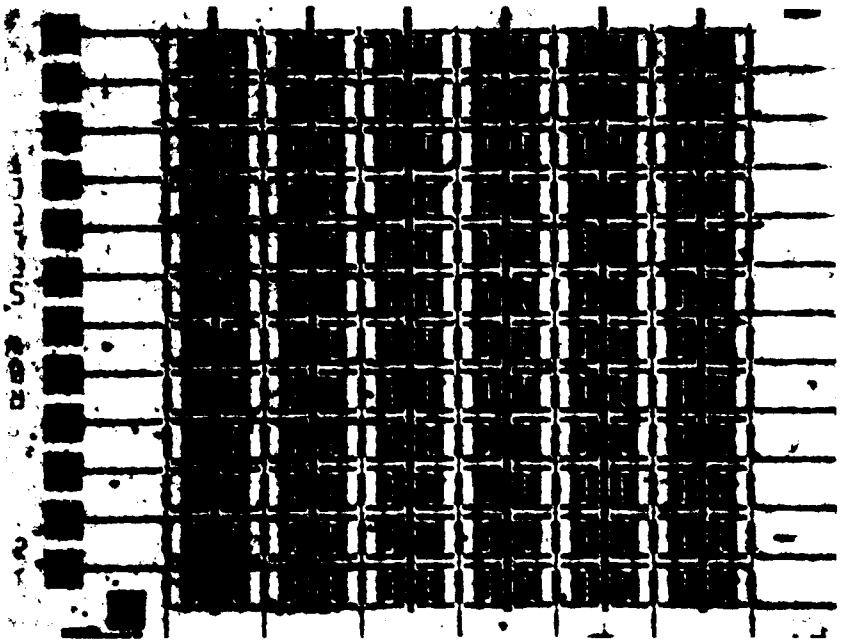

Fig. 1. Photomicrograph of the fabricated 12 x 12 ESLM.

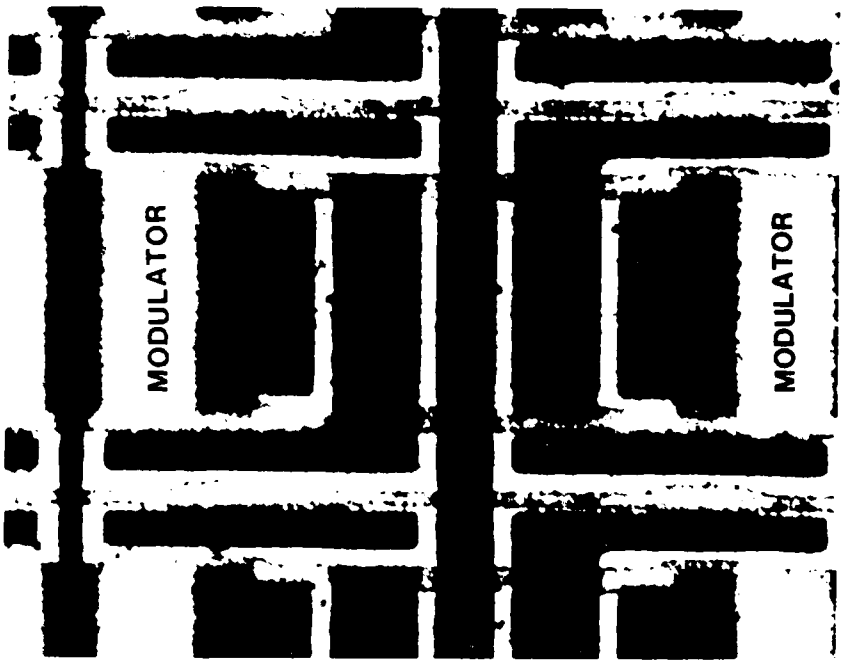

Fig. 2a. Photomicrograph of 2 unit cells of the ESLM.

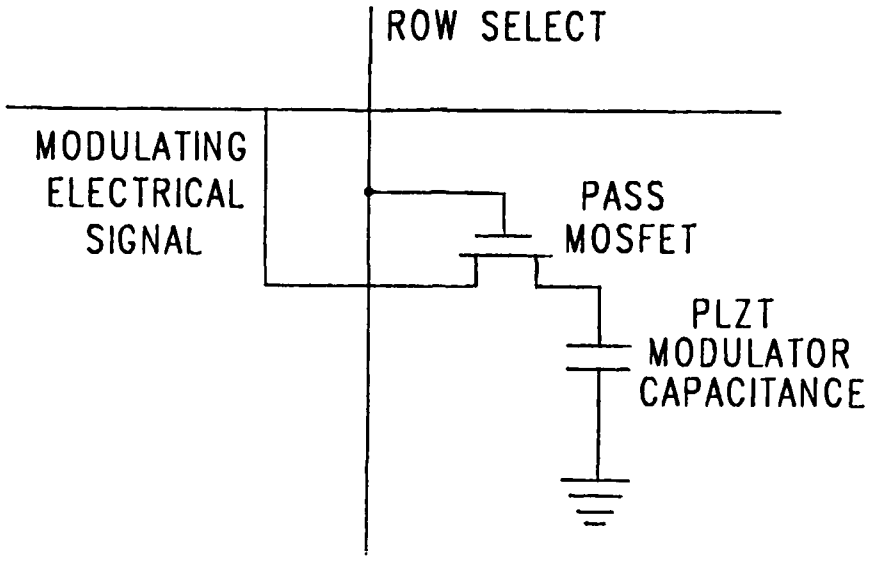

Fig. 2b. Schematic of the ESLM cicuit.

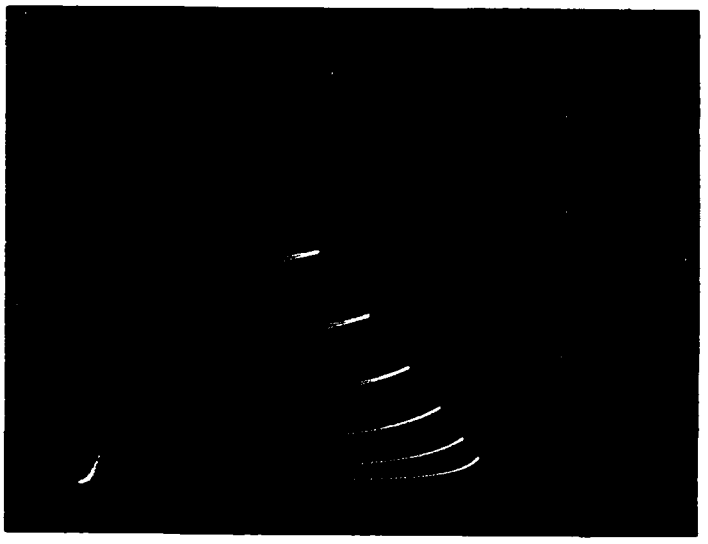

Fig. 3. I-V characteristics of a typical NMOS pass transistor used in the ESLM circuit.

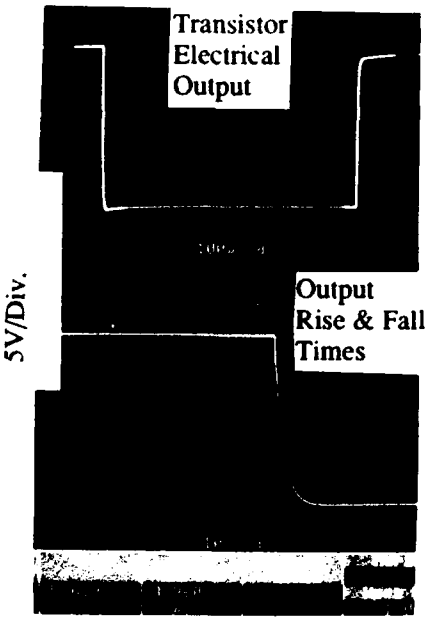

Fig 4. Response time characteristics of ESLM. The upper curve is plotted on a longer time scale. The lower curve shows the rise and fall times in detail on a shorter time scale.

A 2-D Optically Addressed Silicon/PLZT Spatial Light Modulator Array

T. H. Lin, J. Wang, S. Dasgupta, S. C. Esener, and S. H. Lee
Department of Electrical and Computer Engineering
University of California, San Diego
La Jolla, CA 92093

I. Introduction

Optically addressed spatial light modulators (OSLM) are an important component for the implementation of massively parallel high performance opto-electronic computers. Such devices are particularly useful for applications such as optical logic and memory, wavelength and coherence transformations and 2-D filtering. The technology which combines silicon for detection and computation and electro-optic PLZT ($Pb_{0.9}La_{0.1}[Zr_{0.65}Ti_{0.35}]_{0.975}O_3$) for optical modulation allows the realization of such SLMs. These two materials combine the computational power of silicon and the parallel communication capability of optics. In this paper we report the successful fabrication of 2 x 2 OSLM arrays using polycrystalline silicon deposited on a PLZT substrate. We detail the device design considerations, describe the experimental techniques utilized and discuss the resulting OSLM performance.

Depositing polysilicon on PLZT by chemical vapor deposition (CVD) is one approach for SLM fabrication. However, silicon of good crystalline quality is necessary to obtain a high breakdown voltage and high detection efficiency in the driving circuitry. Laser recrystallization of polycrystalline silicon is a useful technique for the growth of large grained silicon. Crystals ~100μm by ~25μm have been previously obtained. An electronic circuit including a light detector and an amplifier to drive the electro-optic light modulator was designed, fabricated on silicon on PLZT and their optical and electronic performance characterized.

II. Design Considerations

A schematic of the circuit fabricated for the OSLM is shown in Fig 1. The circuit includes a phototransistor, the driving circuitry and an optical modulator. On sensing the light from the input beam, the photodetector produces an output which is then used as an input to the driving circuit. To achieve a dynamic range of 100:1 from the modulator, the necessary output from the driver is around 25V[2]. Fig. 2 is a photomicrograph of a 2 x 2 Si/PLZT SLM array. Each pixel of the array consists of a field and light induced current-punch through transistor (FLIC-PTT) as the photodetector and the driver of additional PMOS and NMOS transistors. A fraction of the photodetector output is fed back to the photodetector gate through a CMOS inverter in order to achieve a large gain through a positive feedback.

The fabrication of such a device requires careful investigation of certain materials and device processing issues. As mentioned before, laser recrystallization is used to obtain larger grained material. In addition, low temperature processes for device fabrication have been developed to prevent damage to the PLZT.

III. Experimental Techniques

In the next section we describe the experimental techniques utilized to obtain the OSLM arrays. The device fabrication was carried out using mostly the standard VLSI fabrication procedure. For the NMOS devices, the source and drain are implanted with phosphorous doses of $3\times10^{13}/cm^2$ at 30KeV and $1.05\times10^{14}/cm^2$ at 60KeV. For the PMOS devices, the source and drain are implanted by boron with doses of $1.14\times10^{14}/cm^2$ at 30KeV, and $3.5\times10^{13}/cm^2$ at 80KeV. An Ar^+ laser was then used to crystallize the film and activate the dopants. The output power from the laser was 16.5W, which melted a zone 60μm wide when scanned at a speed of 22 cm/s with 10μm steps between consecutive scans.

Since PLZT is prone to damage when heated to temperatures higher than 900°C:[3], the following steps were taken to limit the temperature rise in the PLZT substrate.

1. A 3.5 μm thick plasma enhanced chemical vapor deposited (PECVD) SiO_2 film was used as a thermal buffer layer between the polysilicon film and the PLZT substrate.
2. The beam dwell time on the polysilicon film was limited to 0.1 ms to reduce heat conduction into the substrate. This dwell time was achieved by using a combination of beam shaping and controlled scan

speed.

3. A 100nm thick gate oxide is grown by pyrogenic oxidation at 850°C.

IV. Results and Discussion

The devices thus fabricated were then individually tested for their I-V characteristics, their response time and modulator performance. Fig. 3 is a photograph of the I-V characteristics of the photodetector fabricated on Si/SiO_2/PLZT. The breakdown voltage measured from the I-V curve is ~ 28V. The mobility calculated is 442 cm^2/V-s. The transconductance is 100 μS/V. The PMOS transistors fabricated demonstrate characteristics shown in Table 1. To calibrate the process parameters, silicon on sapphire (SOS) samples were included with the Si/PLZT samples in the device fabrication procedure. The performances of these devices are listed in Table 1. We are in the process of measuring the sensitivity, the modulation depth, the time response and the leakage current of the optical gates. These results will be discussed at the conference.

V. Conclusions

Laser crystallization was used to implement a Si/PLZT optically addressed spatial light modulator. We have demonstrated NMOS transistors with electron mobilities of 442 $cm^2/V-s$ and transconductances of 100μS/V. PMOS transistors with hole mobilities of 40$cm^2/V-s$, and transconductances of 10μS/V were also fabricated. These devices are used as the detector and the driver of the OSLM array.

References

1 J. P. Colinge, E. Demoulin, M. Lobet, IEEE Tran. Elect. Dev., **ED-29**, 4, 585 (1982).

2. S. C. Esener, Ph.D dissertation, Univ. of California, San Diego, p82 (1987).

3. T. H. Lin, M. L. Burgener, S. C. Esener, and S. H. Lee, Mat. Res. Soc. Symp. Proc., **74**, 135 (1987).

Table 1. Performance of PMOS Transistor

Material	Mobility ($cm^2/v-s$)	Breakdown Voltage (V)	Transconductance (μS/V)
Si/PLZT	40	28	9
SOS	101	32	28

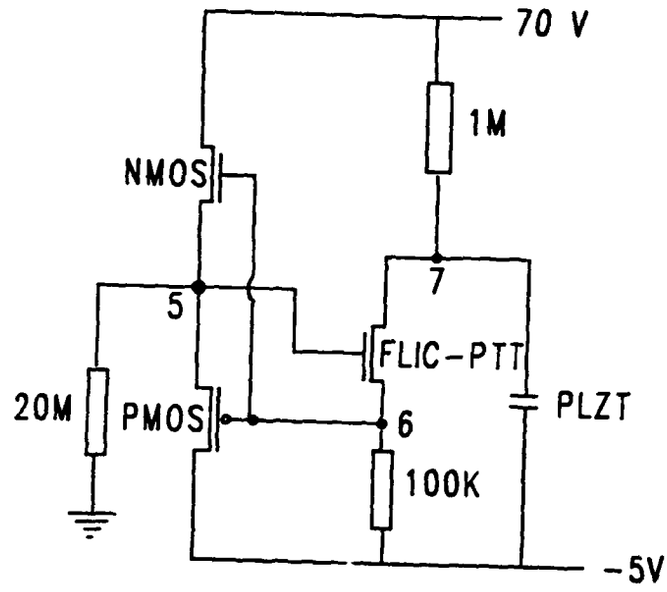

Fig. 1. Schematic of the fabricated OSLM circuit.

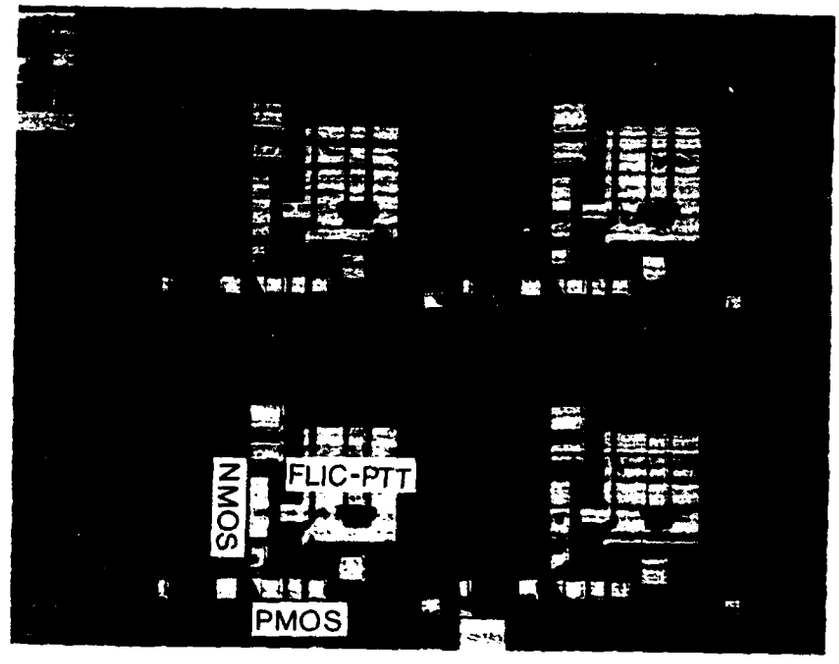

Fig. 2. Photomicrograph of the fabricated 2 x 2 OSLM array fabricated on silicon on PLZT.

Fig. 3. Typical I-V characteristics of Si/PLZT NMOS transistor utilized in OSLM array.

A Spatially Segmented Design Appraoch to Spatial Light Modulators

Ravindra A. Athale, BDM Corp.and Sing H. Lee, Sadik Essner, University of California, San Diego

BACKGROUND

All optically addressed spatial light modulators (SLM) contain the functionalities of detection of input light pattern and corresponding modulation of the readout beam. These two functions are often performed by two physically distinct parts, although in some cases the same material or structure performs these two functions. The isolation between these two functionalities of an SLM is an important feature, which can be achieved using several different approaches: (1) wavelength seperation between read and write signals, (2) seperation along the direction **perpendicular** to the device plane, (3) seperation along a direction **within** the device plane.

The most familiar SLMs based on the wavelength seperation approach are the Pockel's Readout Optical Modulator (PROM) and its variant, PRIZ. Although simple in construction, these devices are not cascadable thus limiting their applicability. The isolation between the detector and readout is also less than perfect, thus imposing limitation on the readout beam intensity. In the second approach, the separation between detection and modulation takes place along the direction perpendicular to the plane and is adopted by most of the familiar SLMs (PhotoTITUS, Hughes LCLV, Hamamatsu MSLM). These devices are readout in reflection and sometimes contain an additional light blocking layer between the detector and the modulator. These devices have primiarily utilized electrooptic materials that operate in a longitudinal geometry (electric field and light propagation colinear). These devices are also mainly fabricated in continuous structures, although discrete arrays of pixels can also be achieved. In this paper we will describe the SLM design approach that uses the third alternative of lateral separation within the plane of the device in order to achieve the desired isolation.

DEVICE DESIGN AND RESULTS

The lateral separation of the detector and modulator in the plane of an SLM necessarily implies that the device consists of a 2-D array of discrete cells and not a continuous structure. The schematic diagram of such an SLM is shown in Figure 1(a). As such, this devices resembles a true three terminal device with a control terminal, an input/power terminal and an output terminal. The single cell of this device contains a detector and a modulator that are electrical coupled. The electrical coupling

between the detector and modulator can be achieved using four distinct geometries shown in Figure 1(b). These configurations are created by arranging the electric field in the detector/modulator colinear/perpendicular to the direction of light propagation. The first two configurations (L-L and T-L) are similar to most of the conventional SLMs in that they use longitudinal electrooptic effect. The planar geometry of the electrodes associated with the detectors in the T-L configuration makes the fabrication easier using standard semiconductor processing techniques. The remaining two configurations (L-T and T-T) on the other hand utilize a transverse electrooptic effect and hence are unique. In the spatially segmented approach to SLM design, the transverse electrooptic effects can be used just as easily as longitudinal effects thus opening up a much wider selection of materials (e.g. PLZT electrooptic ceramic) that can be used.

Three out of these four structures have so far been experimentally demonstrated. The L-L and L-T gemoetries used the twisted nematic liquid crystal as the modulator and sputter deposited CdS thin film photoconductor as the detector. These devices were designed and fabricated for performing logic operations on binary images and were assembled in simple circuits as well as with optical feedback to demonstrate cascadability [1-3]. The T-T gemoetry has been fabricated with PLZT electrooptic ceramic as the modulator and a Si phototransistor as the detector [4].

SPECIAL FEATURES

In a simple photoconductor-liquid crystal SLM the electrical impedance match between the two parts is critical to obtaining good depth of modulation. The segmented design allows electrode geometry manipulation for better impedance matching. For example, the electrode gap in the L-T design or the transfer electrode shape in the L-L design can be adjusted for optimum voltage transfer to the liquid crystal as a function of the control light intensity. This can allow the operating region to shift over different parts of the electrooptic response of the modulator.

The potential role of SLMs in optical processing has evolved considerably in the past decade. Although the original function of incoherent-to-coherent conversion and real-time input transduction still plays a major role, increasing attention is being paid to SLMs as active components an optical computing architecture. Towards this, "smart" SLMs are being developed for performing linear and nonlinear, point and neighborhood operations on the input images. The segmented design described in this paper offers the flexibility needed for this role.

The plane of the segmented SLM can be utilized for connections between different pixels. It has been proposed to perform summation of light intensities along a column with detector interconnections and broadcasting along a column with modulator interconnections for a compact electrooptic neural net architecture [5]. A more complex interconnection shown in Figure 2 can implement a cyclic shift of input elements that could find use in digital optical architectures.

One proposed optical architecture for adaptive, multilayer neural net model requires a bidirectional SLM with different transfer characteristics for the two directions [6]. Such an SLM can be easily designed with the segmented approach by coupling two modulator cells to a single detector cell as shown in Figure 3.

SUMMARY

A segmented approach to SLM design is shown to provide flexibility in the selection of the electrooptic material and electrode geometries. This flexibility, which comes at the expense of more involved fabrication, can be exploited in achieving a widre variety of point and neighborhood, linear and nonlinear operations on input images.

REFERENCES

1. R.A.Athale, "Studies in Digital Optical Processing", Ph.D Thesis, University of Californiz, San Diego, 1980.
2. R.A.Athale and S.H.Lee, Opt. Eng., Vol.18, p.515, 1979
3. R.A.Athale and S.H.Lee, Appl. Opt., Vol.20, p.1242, 1981.
4. S.H.Lee, S.C.Essner, M.A.Title, and T.J.Drabik, Opt. Eng., Vol.25, p.250, 1986.
5. R.A.Athale, H.H.Szu, and C.B.Friedlander, Opt. Lett., Vol.11, p.482, 1986.
6. D.Psaltis, K.Wagner, and D.Brady, Proceedings of IEEE First International Conference on Neural Networks, Vol.III, p.549, (IEEE Catalogue No. 87TH0191-7), 1987.

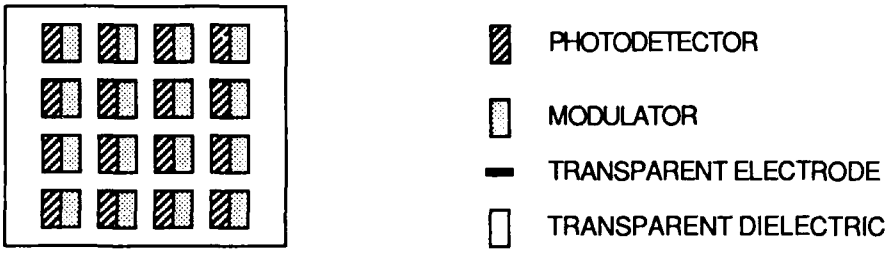

Figure 1(a): Schematic diagram of a spatially segmented SLM

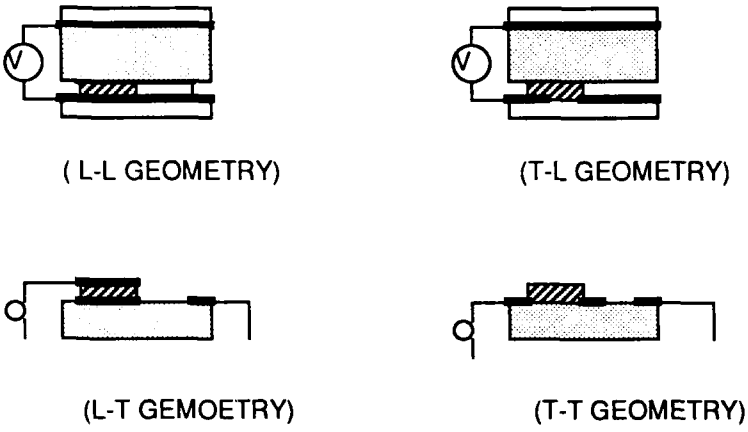

Figure 1(b): The four electrode geometries for a segmented SLM

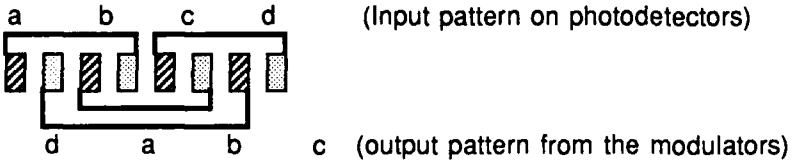

Figure 2: The electrode pattern implementing a 4-pixel cyclic shift within the segmented SLM.

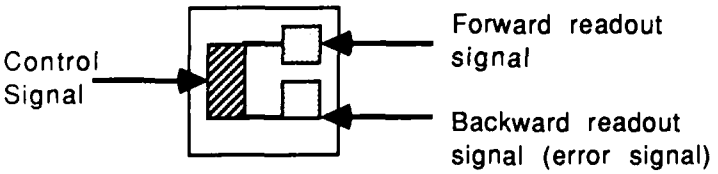

Figure 3: The schematic diagram of a single pixel of a segmented SLM to be used in an optical Backpropagation Neural net. The forward and backward propagating signals have seperate modulator sections having appropriate transfer functions

THURSDAY, JUNE 16, 1988

EMERALD BAY BALLROOM

3:10 PM–5:00 PM

ThD1–5

LIQUID CRYSTAL DEVICES: 3

Jeffrey Davis, San Diego State University, *Presider*

On the Progress of the Liquid Crystal Television Spatial Light Modulator

Hua-Kuang Liu and Tien-Hsin Chao
Jet Propulsion Laboratory
California Institute of Technology
Pasadena, California 91109

The pocket-sized liquid crystal televisions recently marketed by several Japanese companies have been welcome gifts among friends and found useful in applications such as the view-finders in video cameras. Many optical processing researchers have also begun to use these devices as a spatial light modulators (SLM's) in a variety of ways. It has been demonstrated that LCTV's can be used as optical input devices, logic elements, computer generated hologram recordings, and 2-D phase image representations. The LCTV may be used for these processing applications because it has several attractive features. For example, it is electronically addressable through a micro-computer, and since it is a TV by design, it is naturally addressable by a TV camera and it can be refreshed at a speed of 30 Hz. By definition, when the LCTV is used as a SLM, it can be controlled remotely by an emitting antenna anywhere in the world. So one can imagine that a joint experiment on optical processing could be performed by researchers from Asia, Europe, and the United States through the TV transmitter and receiver linkage. The speed of 30 frames/sec. is sufficient for the present usage because the inputting of image signals from a computer can hardly exceed this speed.

The purpose of this paper is to give a review of the principle of operation of the LCTV SLM, to present the recent findings of the spatial light modulation properties of a high-resolution research module LCTV, and to make a comparison of this module and the Radio Shack, and the Epson modules.

The basic structure of a twisted nematic cell is shown in Figure 1. The liquid crystal molecules are sandwiched between two layers of transparent electrodes[1]. An electric field can be applied between these electrodes. In Figure 1(a), it is shown that when the two polarizers are in parallel, due to the rotation of the polarization of the light through the cell, the output is dark when the addressing voltage is off. The output is bright when the addressing voltage is on. The opposite is true when the polarizers are orthogonal as shown in Figure 1(b). In the TV operation, to gain speed, the rotation is much less than 90 degrees and therefore the contrast is reduced. Recently, thin film transistors(TFT) have been built into the LC cells as shown in Figure 2. The function of these TFT's is to hold the addressing voltage and thus to prevent the loss of contrast due to the voltage relaxation effect[2]. The Epson LCTV has TFT's in the cells.

Ordinary LCTV's that are commercially available have a total number of pixels of not over 20,000 and a pixel size of not less than 300 by 300 square micrometers. The characteristics of these types of LCTV SLM have been reported during the past couple of years in the literature. Recently, we have experimented with a research-type LCTV SLM that is not yet commercially available. This LCTV has a screen dimension of 21.56mm x 28.512mm having 220 x 648 total pixels. However, since it is designed for color TV, the number of effective pixels equals one third of the total to account for the three primary colors. For our test, the color filters in the screen have been removed to achieve black-and-white transmission. Under this condition, the LCTV still has a spatial resolution that is about an order of magnitude higher than the existing models on the market.

After proper correction of the non-uniformity of the aperture, due to the uneven structure of the multiple-layer TV screen, we measured the Fourier transform of the high-resolution LCTV and recorded the result which is shown in Figure 3(a). For comparison, a similar result of that of a previous Radio Shack LCTV SLM is shown in Figure 3(b).

To see the other characteristics of this high-resolution LCTV, we have also measured the angular rotation of the liquid crystal molecules as well as the corresponding light transmission and contrast ratios as a function of the bias voltage of the TV. The contrast versus bias voltage is shown in Figure 4. As it can be seen, when the bias voltage is 14 volts, the maximum contrast ratio is only about 6:1. The poor contrast is probably due to two reasons. One is that in order to maintain the 30 Hz TV frame rate, the maximum angle of rotation of the nematic liquid crystals must be relatively reduced to cover the increased number of pixels. In addition, we have found that the laser beam becomes elliptically polarized after it passes through the liquid crystal with a biased voltage as high as 14 volts. This could cause a reduction of the contrast.

To those who question the value of this device because of its low cost, we would respond as follows: If we counted all the development cost that the display community has invested in this device, the cost of each unit of the LCTV would probably be much higher than any of the other existing SLM's on the market today. An example is the research module under test in our laboratory; it was extremely expensive to develop. Furthermore, a significant improvement can be made on this device with regard to both contrast and speed. An LCTV with contrast ratio of over 100, operating at TV frame rate and of high resolution is being developed in Japan. However, if we hope that the LCTV's will serve as SLM's operating according to optical processing specifications, intensive research work in this area should be encouraged. For example, the following additional specifications are desired: light throughput of more than 25%; operating wavelength of 0.6 to 1.3 micrometers; and an overall flatness of within 0.1 wavelength over the aperture and writing speed of 100 sec^{-1}. These goals seem within reach if reasonable development

efforts can be devoted to them.

To present an overview of the latest progress on the LCTV SLM's, we have summarized the characteristics of the Radio Shack, the Epson, and the high-resolution module LCTV SLM and listed the data in a Table of Comparison. This Table will be presented in the meeting.

The authors would like to thank Shigeru Morokawa for providing JPL with the experimental LCTV modules and for many helpful discussions. The research reported in this paper was performed at the Jet Propulsion Laboratory, California Institute of Technology, as part of its Innovative Space Technology Center, which is sponsored by the Strategic Defense Initiative Organization/Innovative Science and Technology through an agreement with the National Aeronautics and Space Administration (NASA). The work described was also co-sponsored by NASA OAST and the Physics Division of the Army Research Office.

References

1. W. E. Haas, "Liquid Crystal Display Research: The First Fifteen Years", Mol. Cryst. Liq. Cryst., Gordon and Breach Publishers, Inc. 94, 1(1983).

2. S. Morozumi, "Application to the Pocket Color T.V. - TFT array -", Electronic Magazine, Ohmsha, Ltd., Tokyo, Japan, 30, No. 6, 39(1985).

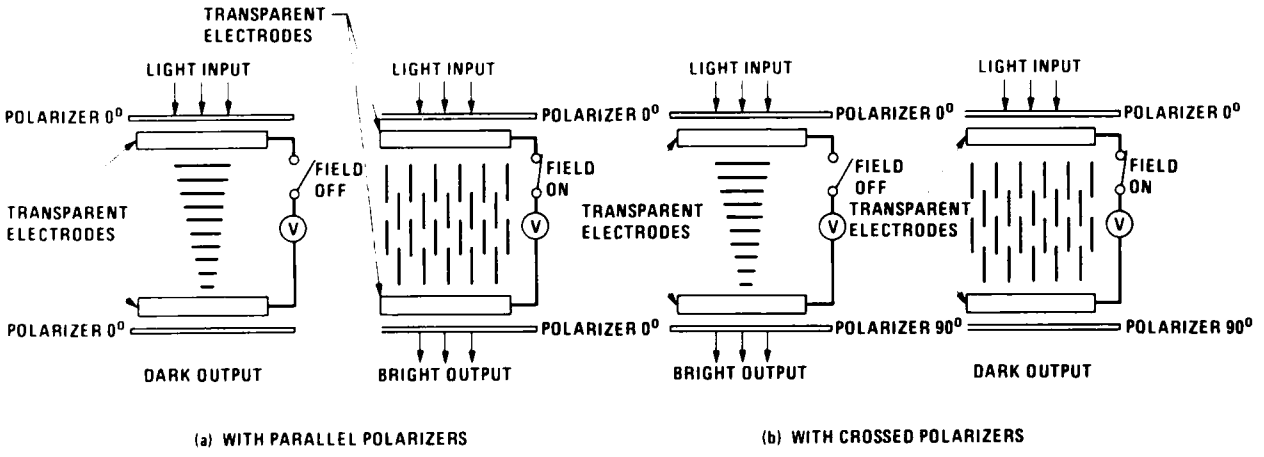

Figure 1. The basic structure and operating conditions of a twisted nematic liquid crystal cell.

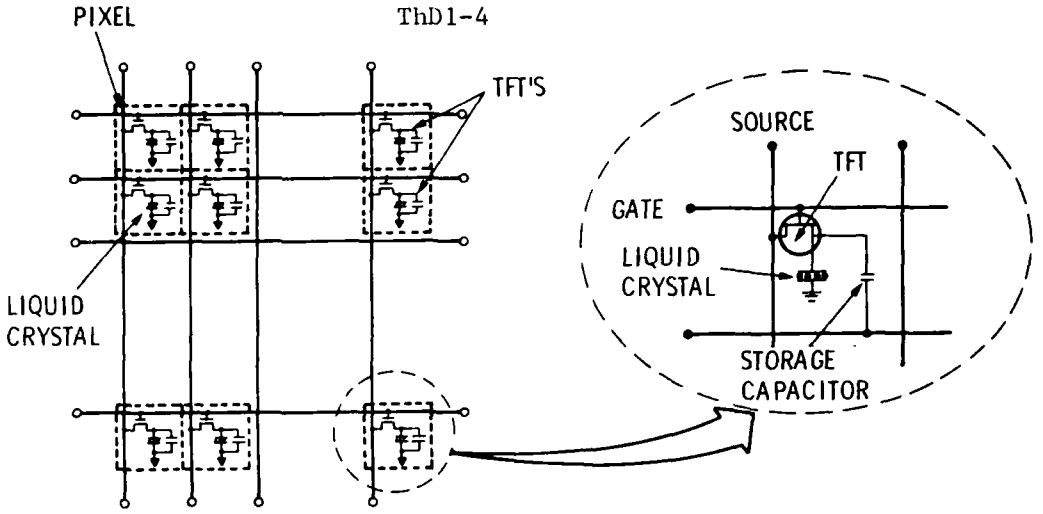

Figure 2. Thin film transistor (TFT) controlled twisted nematic crystal arrays.

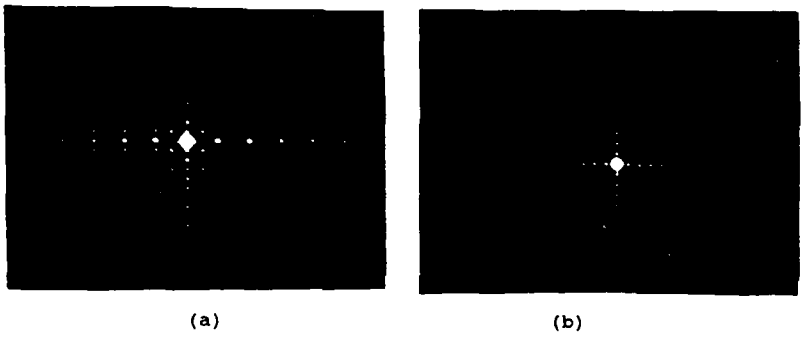

Figure 3. (a) Fourier spectrum of a research-module high resolution LCTV. (b) Fourier spectrum of a Radio Shack LCTV.

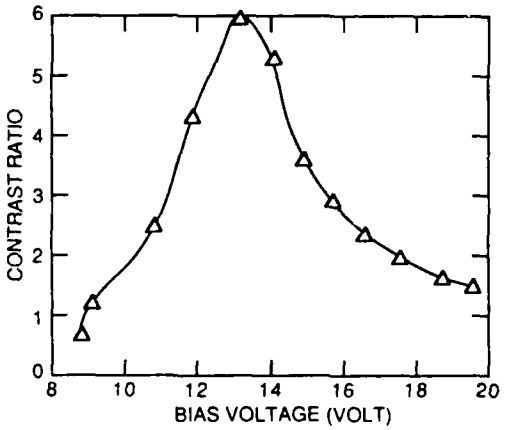

Figure 4. Contrast ratio versus bias voltage of a research-module high-resolution LCTV

EVOLUTIONARY DEVELOPMENT OF ADVANCED LIQUID CRYSTAL SPATIAL LIGHT MODULATORS

N. Collings, W. A. Crossland
STC Technology Ltd, London Road, Harlow, Essex, CM17 9NA
and
D. G. Vass
Dept. of Physics, Edinburgh University, Mayfield Road, Edinburgh, Scotland, EH9 3JZ

INTRODUCTION

One of the future goals for computing will be the ability to transform data arrays at high speed. Where the transformation is regular across the array, such as symbolic substitution, or can be realized with simple optical components, such as the Fourier transform, then it is a natural solution to spatially multiplex the data across a coherent light beam. This entails the need for developing SLM's of high space-bandwidth product. In order to reduce thermal dissipation an ideal electro-optic effect should operate at low applied voltages and use a material of low dielectric constant. Liquid crystal devices fulfil some of these requirements. Here we describe the properties of multiplexed ferroelectric liquid crystal (FLC) spatial light modulators that run at faster than video frame rates. We suggest that for reasons of addressing speed, compactness, and integrability with silicon circuitry, then silicon active backplane FLC SLMs offer significant advantages. The design and potential performance of such devices is briefly discussed, as is the possible impact of a more recent fast, analogue electro-optic effect in chiral smectic liquid crystals.

FERROELECTRIC LIQUID CRYSTALS

In order to demonstrate the applicability of ferroelectric liquid crystals (1) to SLM technology, we have developed a 64 x 64 display device which operates at video line address times (2), and have proven its applicability to the optical correlator system (3).

The characteristics of this SLM were: size of pixellated area 1 sq. in; contrast ratio of 35:1 (pixel) and 20:1 (character); and transmission of 50%. The power required to drive this device is 4mW. A photo of the packaged experimental device is shown as Fig. 1.

These devices operate in a multiplexed manner, and very large arrays of pixels can in principle be addressed due to the electro-optic bistability. Multiplexed in this context refers to the address mode; the data is loaded into the display a row at a time and the pixel voltages on each row are submitted to error voltages when subsequent rows are being addressed. The bistability of the electro-optic effect is sufficiently strong, so that the state of the liquid crystal is not altered by these error voltages. However, the contrast ratio is poorer than it would be at a pixel which is not subject to these error voltages, since the optical condition of the pixel is modulated by them, though without inducing them to change to the other bistable state. Under conditions of continual electronic refresh (such as might be used in a visual display device), then these devices achieve a contrast ratio of >20:1. Methods of increasing this value in SLMs by modifying the electronic addressing mode, or by changes on the construction of the device will be discussed. (Values of >1000:1 are achieved in directly addressed pixels.) With advances in materials, we have been able to reduce the frame speed at room temperature to 2.5 msec. Currently, we are developing a 128 x 128 version (4).

ACTIVE BACK PLANE SLMs

The active back plane approach incorporates one or more transistors at each pixel (5, 6). The transistor allows the pixel voltage to be established and then isolated at a speed determined by the transistor circuitry, and independent of the response time of the liquid crystal. Therefore, this approach has considerable advantages over the multiplexed mode of operation. In terms of speed, a number of rows can be addressed within the liquid crystal response time, rather than one in the multiplexed case. In terms of contrast, the drive voltage can be sustained at the pixel and error voltages will not appear; consequently, higher contrast can be expected. In terms of size, the ability to fabricate transistor circuitry around the periphery of the array allows a more compact design than one in which every row and column electrode

must be separately connected to external wiring. In addition, if single crystal silicon is processed to produce the active back plane then it is not difficult to conceive of a more intimate connection between the SLM and memory blocks on the same wafer, which would allow faster access times. The disadvantages of this approach are lower yield; undesirable surface topography on the processed silicon; and smaller pixel real estate as a proportion of the repeat spacing of the pixels. Devices using single crystal silicon as the active backplane must also operation in reflection.

A device using a static RAM active backplane design with nine transistors per pixel, and a 16 x 16 pixel array has been developed at Edinburgh University (6). At present it employs a nematic liquid crystal, which is much slower than can be achieved with ferroelectric materials. It is also low resolution, but it represents an important step in the evolution of single crystal silicon active backplanes. Present collaborative work between STC Technology and Edinburgh centres on fast dynamic RAM single crystal SLMs with large arrays of pixels and using ferroelectric liquid crystals. Trade offs between matrix size, semiconductor technology and minimum feature size, drive voltage and speed will be briefly discussed. Meanwhile, development of static RAM devices of higher complexity continues.

FUTURE GENERATIONS OF LIQUID CRYSTAL SPATIAL LIGHT MODULATORS

A successful active back plane technology can be brought together with other fast liquid crystal effects. Although the switch time of the present ferroelectric materials can be fast, their settling time is much longer and limits the frame speed of the device. We will be exploring the use of ferroelectrics with higher spontaneous polarization than those used in display devices, and materials specifically designed for active matrix addressing.

Response times of 350 nanosecs have recently been observed using the electroclinic effect in chiral smectic A systems (7, 8). This appears to be faster than comparable measurements on ferroelectric liquid crystal devices. In addition, the electro-optic response is accurately linear. Problems requiring critical evaluation include the available contrast range, requirements in terms of temperature stability, and electronic addressing methods. Recent measurements on single pixel test devices of this kind, based on novel materials, are presented and their applications to SLMs discussed.

To utilise the wide grey scale response available from the electroclinic effect requires the generation of analogue voltages at each pixel. In electrically addressed active matrix devices this is conceivable, but necessitates more complex circuitry. However, this would also find applications for the fine tuning of the phase modulation at each pixel of the SLM, which would allow more sophisticated application of these devices.

ACKNOWLEDGEMENTS

The support of two programmes which are sponsored by the UK Department of Trade and Industry and the Science and Engineering Research Council, is acknowledged. These programmes are the JOERS/Alvey LM8/11/5, under which most of the ferroelectric liquid crystal materials have been developed, and the JOERS/Alvey LM8/03/132, which is funding the active back plane development.

REFERENCES

1. Clark, N.A. and Lagerwall, S.T., Appl. Phys. Lett., 36 (1980), 899.

2. Bone, M.F., Coates, D., Crossland, W.A., Gunn, P., and Ross, P.W. 1987 "Ferroelectric liquid crystal display capable of video line address times". Displays (July), pp 115-8.

3. Collings, N., Chittick, R.C., Cooper, I.R., and Waite, P. 1987 "A hybrid optical/electronic image correlator" in Laser/Optoelectronics in Engineering, ed W. Waidelich (Springer-Verlag, 1987).

4. Sparks, A., Chittick, R.C., Brocklehurst, J.R., Crossland, W.A., "A 128 x 128 Multiplexed Ferroelectric SLM". To be published.

5. Crossland, W.A., Needham, B., and Ross, P.W. 1985 "Single-crystal silicon active-matrix displays". Proc. SID, 26 (3), pp 175-81.

6. Underwood, I., Sillitto, R.M., and Vass, D.G. 1985 "Evaluation of an nMOS VLSI array for an adaptive liquid-crystal spatial light modulator". IEE Proc. Part J : Opto-electronics, 133, pp 77-82.

7. Bahr, Ch. and Heppke, G. 1987 "Optical and dielectric investigations on the electroclinic effect exhibited by a ferroelectric liquid crystal with high spontaneous polarization". Liquid Crystals, 2(6), pp 825-31.

8. Bone, M.F., and Coates, D.C. "The electroclinic effect in some novel chiral smectic A mixtures". Paper submitted to the 12th International Liquid Crystal Conference in Freiburg (Autumn, 1987).

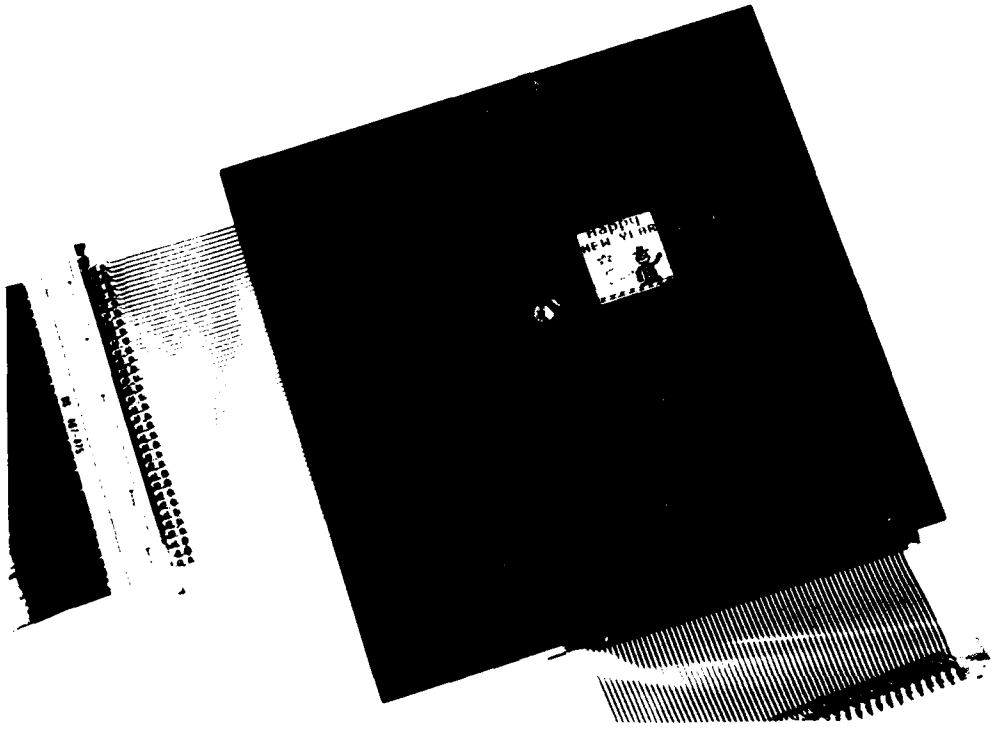

Fig. 1 64 x 64 Multiplexed Ferroelectric SLM

Ferroelectric Liquid Crystal Spatial Light Modulator: Materials and Addressing

L.A. Pagano-Stauffer M.A. Handschy N.A. Clark

Displaytech, Inc.
2200 Central Ave., Suite A
Boulder, Colorado 80301

1 Introduction

Ferroelectric liquid crystal (FLC) technology is ideally suited for the making of spatial light modulators (SLMs) because of its fast, low-voltage, low-power electrooptic effect. Its bistabilty and sharp dynamic threshold further make multiplexed addressing schemes attractive, promising SLMs with a large number of elements yet with an economical number of electronic drivers. We report here results of several implementations of the most common multiplexing scheme, "matrix addressing," and point out several properties of the FLC materials that are likely to influence the performance of matrix-addressed SLMs.

2 Electrical Matrix-Addressing

The matrix-addressed ferroelectric liquid crystal SLM is made by filling the gap between closely spaced transparent electrode plates with FLC. The electrode layer on one plate is patterned into rows, on the other it is patterned into columns. A pixel is defined by every overlap of a row and column electrode. One can then switch a selected pixel by applying voltages to its row and column electrodes; this inevitably puts voltages on the unselected pixels in the same row and column. The challenge of matrix addressing is then to develop voltage waveforms that produce the minimum optical response in the unselected pixels while producing the maximum response in the selected ones.

FLC electrooptics. Applying a moderate voltage to a simple FLC device produces a state with its optic axis nearly uniform along the direction perpendicular to the electrode plates. In this "voltage-preferred" state the optic axis is nearly parallel to the plates. Applying the opposite sign of voltage rotates the optic axis aroung the "tilt cone" of angle ψ, switching the device to another similar state, with the optic still nearly uniform and parallel to the plates, but now at an angle 2ψ to the first voltage-preferred state. Between crossed polarizers these voltage-preferred states have maximum optical contrast. The states obtained after removing the voltage from the voltage-preferred states, while not necessarily of maximum contrast, are optically distinct—that is the FLC device is bistable. Furthermore, switching from one voltage-preferred state to the other in a given amount of time requires the applied voltage magnitude be above a certain sharply-defined threshold value. These characteristics of the FLC device's optical response are important advantages for matrix-addressing. They imply that a waveform whose average over long times is zero and whose average over short times is small enough will have negligible optical effect. The fact that the FLC is average responding rather than r.m.s. responding allows matrix addressing waveforms to be equally effective on a device of any number of lines.

Bistability. In practice, two effects are responsible for the above-mentioned bistability: surface interactions and dielectric anisotropy. A surface is formed in the center of the device by a kink in the smectic

layers that is produced by their shrinkage accompaning the transition from the orthogonal, paraelectric smectic A* phase to the ferroelectric, tilted smectic C* phase.[1,2] When the layer tilt δ is less than the molecular tilt ψ two molecular orientations (those having the optic axis parallel to the electrode plates) have zero strain across the center kink surface. The surface stress of states intermediate to these two states destabilizes them, producing bistability with an energy barrier of about 0.1 erg/cm between the two stable states. Both the ferroelectric torques and surface torques favor states with the optic axis parallel to the plates, with the surface torques favoring the two states equally, producing bistability, and the ferroelectric torques favoring one state over the other, producing switching between the states when they are strong enough. However, another electrostatic torque, arising from the dielectric anisotropy of the material can be helpful. When the dielectric anisotropy $\Delta\epsilon$ is negative, another torque equally favoring the two states parallel to the plates is produced. Since the dielectric torque is quadratic in the applied field ($\Gamma = (\Delta\epsilon/4\pi)E^2 \sin^2\psi$), while the ferroelectric torque is linear ($\Gamma = PE$), these dielectric torques will significantly enhance bistability when the applied field E is comparable to $4\pi P/(\Delta\epsilon \sin^2\psi)$, producing "dielectric stabilization."

We have investigated several matrix-addressing schemes for use with FLC arrays. In a matrix-addressed SLM the voltage across a pixel is the difference between the intersecting row and column potentials. Driving waveforms are organized to allow switching of only the element defined by the intersection of the selected row and column electrodes. Several different addressing schemes using row (or line)-at-a-time addressing have been successfully demonstrated with different FLC compounds (see ref. [3,4,5,6,7]). These matrix-addressing schemes rely on the bistability and threshold of the FLC material. The critical threshold value is seen in the pulse height (V), pulse width (τ) product, creating a critical ($V \cdot \tau$) area. Thus, if the peak voltage V is just sufficient to switch from one state to the other if applied for a time τ, then a ***subthreshold*** pulse of height $V/3$ will not cause switching when applied for the same time τ. The same is true for a pulse of peak height V applied for a time of $\tau/2$. The select waveform sequence, usually consisting of 2-8 pulses, is the amount of time used to switch an individual row. Since the addressing is done a row-at-a-time, the rows which are not being addressed receive non-select waveform sequences consisting of ***disturb*** pulses. The critical ($V \cdot \tau$) product of an FLC device varies gratly with the material, temperature, surface conditions, and cell thickness.

A recently developed matrix-addressing scheme uses varying pulse widths for the pixel select and pixel non-select waveforms.[8] Generation of these waveforms for different pixels is shown in Figure 1. During the select waveform sequence, the select pulse is applied and has a peak voltage V and a pulse width τ. This pulse switches the FLC element into its desired state. During the successive non-select waveform sequences, the disturb pulses vary in amplitude between 0, $V/3$, and $2V/3$ while the pulse width is reduced to $\tau/2$. By shifting the nonswitching parts of the waveform to higher frequences, this scheme exploits the dielectric stabilization described above.

3 SLM Device Development and Results

The prototype FLC SLM which we are using is a 4 × 4 array with each pixel approximately 1.8 mm on a side with 0.6 mm spacing between pixels. Custom driver electronics have been designed and built to provide maximum flexibility in generating various waveforms. The user can select up to 16 pulses per select sequence and up to eight different voltage levels for each pulse. The pulse width is independently controlled by a timer circuit and can be adjusted from 1 μs to 100 ms.

We have investigated several different commercially available FLC compounds, surface alignment treatments, and matrix-addressing waveforms to develop a fast, low-power, high contrast FLC SLM. Material studies include SCE3 and SCE4 from British Drug House, and ZLI-3654 from E. Merck. The surface alignment material used is polyvinylalcohol (PVA).

Characteristic parameters including rise time, fall time, delay time, and contrast ratio of each device were measured with the device in direct-drive and ±12 volts applied to each pixel. The compound proven most desirable for matrix-addressing was the ZLI-3654 material. The measured rise time of the material

is 22 μs and the contrast is ~105:1 using HeNe (633 nm) laser light in direct-drive operation.

We used the dielectric stabilization matrix-addressing scheme shown in Figure 1 with a select pulse width of 22 μs and a peak voltage of 27 volts. Averaging the optical response over time, a contrast ratio of 8.5 : 1 was obtained for an individula pel switching between its bright and dark state when placed between crossed polarizers. A contrast ratio of ~7:1 was obtained for two adjacent pixels in opposite states.

This matrix-addressing scheme requires six pulses for a select waveform sequence. With a pulse width of 22 μs, the entire 4 × 4 array is addressed in 528 μs. Using the same material and the same addressing scheme, it is possible to address an array of nearly 230 × 230 at a frame update rate of 30 ms.

4 Future Work

With the advancement of faster compounds, successfully addressing a 1000 × 1000 array is quite realistic. For example, a material having a switching time of just 5 μs (obtainable today at 60°C with $V < 30$ volts), could have a multiplexing ratio greater than 1000:1 for a frame update time of 30 ms, yielding an optical processing rate of 33 Mbits/sec. Molecular engineering of FLC compounds optimized for high selection in matrix-addressed devices is possible, but would benefit from a more detailed understanding of the mechanisms controlling the ratio of layer tilt to molecular tilt, which in turn controls the bistability. Detailed models of the switching dynamics of FLC devices would allow effective waveforms to be designed rather than developed by trial and error.

References

[1] T. P. Rieker, N. A. Clark, G. S. Smith, D. S. Parmar, E. B. Sirota, and C. R. Safinya. *Phys. Rev. Lett.*, 59:2658, 1987.

[2] N. A. Clark and T. P. Rieker. *Phys. Rev.*, A37:1053, 1988.

[3] Y. Sato, T. Tanaka, M. Nagata, H. Takeshita, and S. Morozumi. In *Proceedings of SID*, page 348, 1986.

[4] T. Umeda, T. Nagata, A. Mukoh, and Y. Hori. In *Proceedings of SID*, page 352, 1987.

[5] J. Wahl, T. Matuszczyk, and S. T. Lagerwall. *Mol. Cryst. Liq. Cryst.*, 146:143, 1987.

[6] L. A. Pagano-Stauffer. *Optical Logic Gates Using Ferroelectric Liquid Crystals*. 1987.

[7] M. F. Bone, D. Coates, W. A. Crossland, P. Gunn, and P. W. Ross. *Displays*, 3:115, 1987.

[8] S. T. Lagerwall. Electronic addressing of ferroelectric and flexoelectric liquid crystal devices. International Patent Application No. PCT/SC86/00476, 1987.

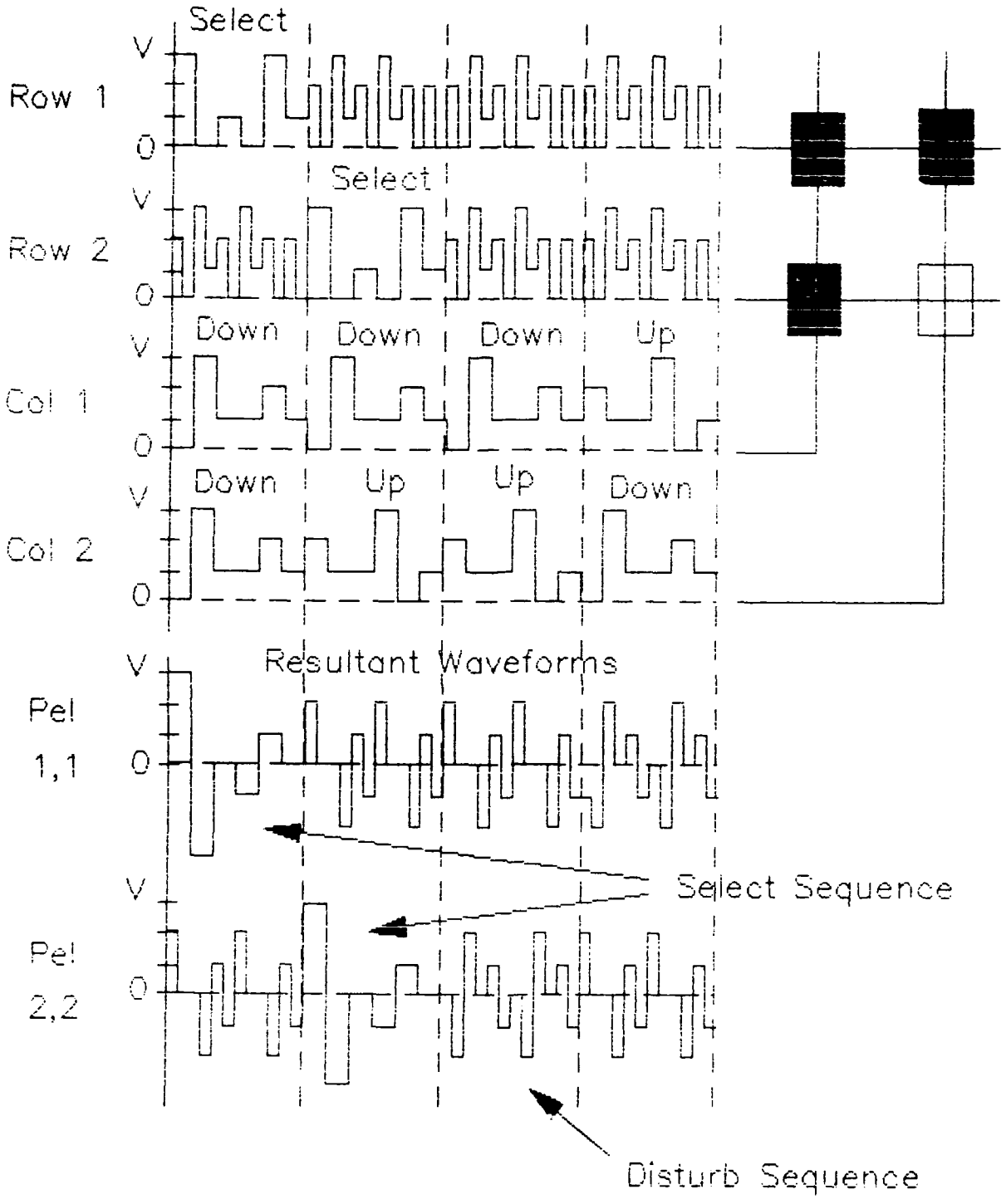

Figure 1 Multiplex drive waveforms using dielectric stabilization. (After ref. [8]).

Development of a spatial light modulator - a randomly addressed liquid-crystal-over-nMOS array.

D.J. McKnight, D.G. Vass and R.M. Sillitto

Department of Physics, University of Edinburgh,

Mayfield Road, Edinburgh. EH9 3JZ. U.K.

Introduction

Following the successful fabrication of a prototype liquid crystal over silicon spatial light modulator [1,2], a more advanced version having a larger number of pixels with smaller dimensions is being developed. To provide an indication of the progress being made towards the realisation of higher performance devices, details relating to the prototype are included in parentheses in the description of the new active silicon backplane. As described below the prototype has also been used as a test-bed for optimising the performance of the light modulating layer for the new device.

The nMOS active backplane

An nMOS array having 50 x 50 [16 x 16] pixels has been designed using the VLSI packages available on computers at Edinburgh University and at the Rutherford Appleton Laboratory. Test wafers have been processed using the 1.5 [6.0] μm nMOS process being developed at the Edinburgh Microfabrication Facility. A photograph of a fully processed silicon backplane is shown in figure 1. Every pixel contains a metal pad 45 x 44 [110 x 110] μm^2 formed by evaporating an Aℓ-alloy on to the optically flat surface of the wafer to form a good quality mirror. The metal pad also acts as an electrode for transmitting the signals from the output of the pixel circuitry to the element of the overlying liquid crystal layer immediately above it. Adjacent rows and columns of the array are spaced 74 [200] μm apart.

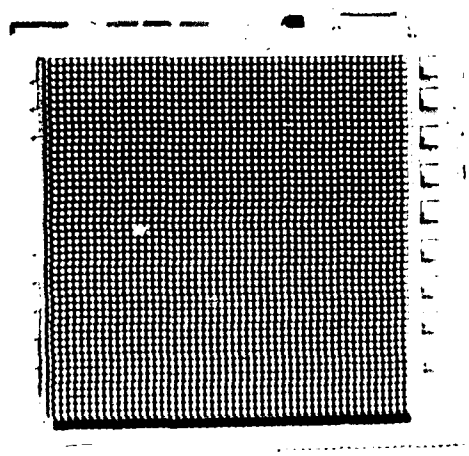

Figure 1

A photograph of the nMOS array covering an area of 3.7 x 3.7 mm^2 on the silicon chip. [The prototype array has an active area of 3.2 x 3.2 mm^2.]

The circuitry associated with each pixel incorporates a static memory cell whose output signal controls through a XNOR arrangement the phase of the voltage drive signal applied to the mirror electrode, as illustrated in figure 2. A universal clock signal CK of nominal amplitude 5V peak-to-peak is broadcast to all pixels. Also the complement $\overline{CK}$ of the clock signal is applied to the common counter electrode of the liquid crystal cell formed over the surface of the array. As indicated by the truth table, the voltage difference between the counter electrode and the mirror electrode of an individual pixel is negligible when the memory cell output has a logic value '0', but oscillates at the clock frequency with a RMS value of 5V when the memory cell output has the logic value '1'. In this way the modulation of the reflected light passing through the liquid crystal is controlled by the stored logic value; indeed by adjusting the precise value of the voltage supply to the chip and the amplitude of the clock signal, the drive voltage across the liquid crystal layer may be tuned within the range 4-7 V to optimise the optical performance of the device.

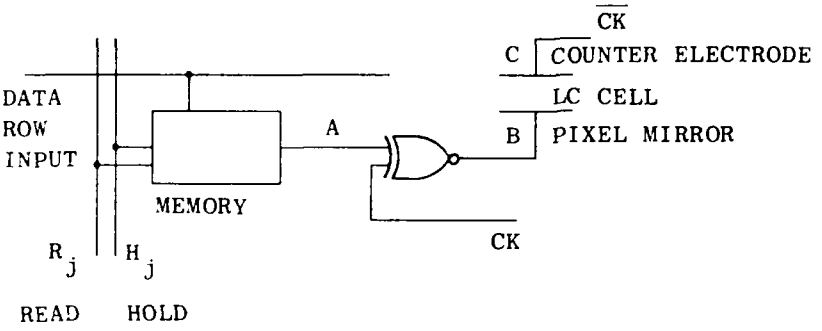

Input				Liquid crystal
A	CK	B	C	State
0	0	1	1	OFF
0	1	0	0	OFF
1	0	0	1	ON
1	1	1	0	ON

Figure 2. Functional diagram and truth table for pixel operation.

The circuit diagram of the 9 transistor cell is presented in figure 3(a) with in 3(b) a micrograph of the corresponding section on a processed wafer showing the physical layout of the circuitry around a pixel mirror.

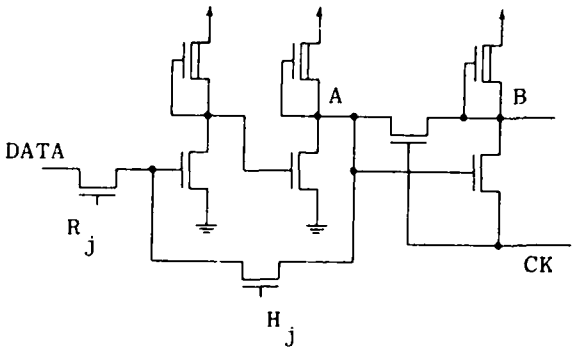

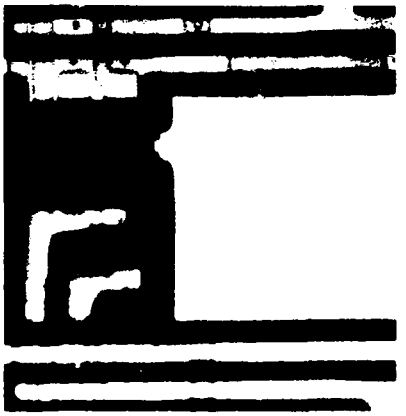

Figure 3.
(a) Diagram of pixel circuit. (b) Micrograph of pixel (74 x 74 μm^2).

To store a pattern within the memory array, a 50-bit binary word is loaded serially into a shift register to appear in parallel at the inputs to the rows. Simultaneously another 50-bit word is loaded into a "column enable" shift register to select the column(s) being addressed; this allows the READ and HOLD lines of the column(s) to be controlled externally. The former 50-bit word is then transferred into the memory cells of the j^{th} column by addressing in the correct sequence the READ and HOLD lines, R_j and H_j respectively, figures 2 and 3. The same word may be loaded at the same time into the other selected columns, if any.

Sample structures have been fabricated on wafers to investigate and characterise the performance of single transistors, single pixels, sections of shift registers etc. for the 1.5 μm process. Electrical tests have shown that these components function correctly and assessment of the array itself is continuing. It is expected that the full 50 x 50 array will operate with frame frequencies up to 1 KHz and universal clock frequencies up to at least 100 KHz.

The light modulating layer

Several reflecting liquid crystal cells have been constructed to simulate the behaviour of the pixels of a SLM, using an aluminised silicon wafer as the reflecting back electrode and an ITO coated glass plate as the transparent front electrode. Using a nematic liquid crystal, BDH type E7, and PVA alignment layers on the electrodes, the cells were assembled to create a conventional 45° twisted nematic arrangement [3].

The reflectivities of sample cells, 5 x 5 mm^2, were measured. A beam of coherent light from a He-Ne laser was polarised and shone normally on a cell, with the polarisation vector parallel to the director of the liquid crystal at the front surface. The reflected light was steered by a beam splitter through an analyser and then focussed by a lens onto a photodiode, Centronic OSI5. The liquid crystal cell was driven by a 1 KHz square wave voltage signal and the intensity of the light transmitted through the system was measured as a function of the amplitude of the drive signal. With crossed polaroids, typical variations in intensity for a 12 μm thick cell are shown in figure 4.

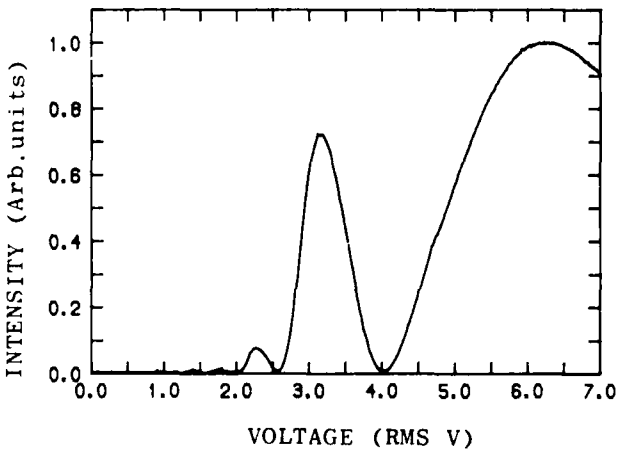

Figure 4.
Variation of reflected light intensity from test cell.

The switching characteristics of the cells were also investigated. It was found that the optical switch-ON and switch-OFF processes were completed withIN 100 ms of the electrical signals being applied.

Optical performance of a prototype SLM

Finally a SLM was assembled using the prototype array and a 45° liquid-crystal configuration, but with obliquely evaporated magnesium fluoride instead of rubbed PVA as the alignment layers. Photographs of the SLM imaged in coherent He Ne laser light are shown in figure 5.

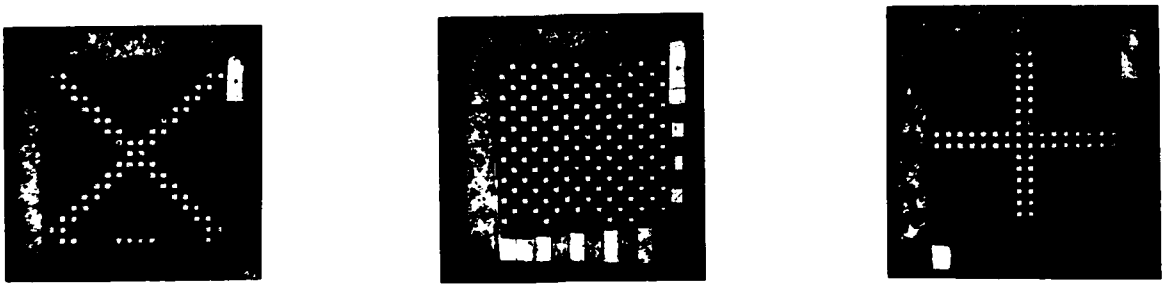

Figure 5. Patterns displayed on the SLM imaged in coherent light.

Acknowledgements

We wish to acknowledge the assistance and facilities provided by Mr. A. Kurzfeld, R.A.L. (VLSI design and mask making), Professor J.M. Robertson, Dr. R.J. Holwill and Mr. Z Chen, E.M.F. (silicon fabrication), Professor R.A. Cowley, E.U. Physics Department and the many staff who helped us in these organisations. We appreciate the stimulating support from Mr. W.A. Crossland and colleagues at, S.T.C. Technology Ltd., and from the other members of our Applied Optics Group.

A grant from the U.K. Science and Engineering Research Council to support this work is gratefully acknowledged.

References

1. Underwood, I., Vass, D.G. and Sillitto, R.M., IEE Proc. J.: Opto-electronics 133, 77-82, 1986.
2. Underwood, I., Willson, P.H., Sillitto, R.M. and Vass, D.G., Proc. SPIE 860 (paper 201-01), 1987.
3. Jacobsen, A., Grinberg, J., Bleha, W.,Miller, L., Fraas, L., Meyer, G., and Boswell, D., Info. Disp., 12, 17-22, 1975.

Nonlinear Optics of Liquid Crystals for Image Processing, Professor Iam Choon Khoo, Department of Electrical Engineering, The Pennsylvania State University, University Park, PA 16802

Summary

Current research and development in optical imaging, computing, communication and signal processing and switching have focused considerable efforts on highly efficient nonlinear optical and electro-optical materials. In combination with novel nonlinear optical processes and cw or pulsed lasers covering a wide spectral range, several useful practical devices have been developed. In particular, optical switching elements and logic gates[1,2], infrared-to-visible image converter, real time image correlators, image or beam amplifiers[3], nonlinear guided wave structures, optical memory devices (e.g., associative memory by phase conjugation[4]) and various beam steering and beam combining devices[5] have been proposed and demonstrated. Concommitant to these device developments, optimization procedures and system requirement considerations have narrowed the "ideal" nonlinear optical materials to a few classes, such as semiconductors, photorefractive crystals and organic materials[6]. Several of these materials are still in the research phase, although they have been shown to possess many desirable characteristics (such as high speed and low energy requirements).

The other components of an all-optical multiprocessor architecture, for example, the spatial light modulators, beam steering arrays, memory devices also employ a variety of semiconductors, photorefractive and electro-optical crystals.

In this paper, we will focus on the unique characteristics of nematic liquid crystals, and newly developed/observed nonlinear processes, for applications in some of these optical switching and beam amplification devices. In particular, liquid crystals possess very broad bandwidth response (visible through infrared), can operate fairly fast (to nanosecond response times) with low energy requirement (estimated to be on the order of <nanojoule for bistable elements), possess high damage threshold (>500

Megawatt/cm^2), well known low-cost fabrication techniques and stability, integrated circuit compatibility (eg. thin film configuration) and room-temperature operation capability[7].

In the last few years various nonlinear optical processes have been demonstrated, including optical bistability, AND and NOR type logic gates, transistor action, wavefront conjugation, beam applications and image reconstruction, etc., but they are based on the much slower, though extremely large reorientational nonlinearities. Recently, the much faster response of thermal nonlinearity is recognized in several studies which point to the possibility of many of the aforementioned devices. Furthermore, the thermal nonlinearity can also be utilized for beam amplifications, image reconstruction, correlation, and conversion devices, operating from the visible through the infrared regime[8]. Correspondingly, we have developed theories (with successful preliminary experimental demonstrations) regarding these new aspects of nonlinear optical wave mixing processes (for a general Kerr medium[9], and for thermal nonlinearity[8]). Equally significant are the recent demonstration of optical image conversion[10], optical wavefront conjugation with gain by our group and the French Thomson CSF group, and image correlation[12], using the faster thermal nonlinearity. We have also formulated a detailed theory of transverse optical bistability switching[13a]--the basic mechanism, conditions for switching, switching intensities and characteristics--following our first successful experimental demonstrations[13b]. The theory explicitly outlines the conditions for switching for both positive and negative nonlinearities (both naturally exist in nematic liquid crystal films) in conjunction with the laser beam

curvature and distances between optical elements. Transverse diffusion, saturation and their roles in the optical bistability switching characteristics and intensity are also theoretically investigated[13a].

Using the newly developed two and four-wave couplings, we have also pursued experimental studies of the various predicted opticmal configurations for amplification of laser beams, or image or message-bearing beam, and the related self- and ring-oscillation adaptive optics devices. Ultimately, these wave-mixing effects, which have led to successful demonstration of phase conjugation with gain and self-oscillation, may also be configured, in conjunction with holographic elements, for associative image reconstruction and two-dimensional beam deflection and steering operations[14]. In view of the transparency of liquid crystal throughout the visible--infrared region, various image conversions (visible to infrared, near to far infrared, etc.) can obviously be achieved using the Bragg-type diffraction geometry used in a previous preliminary study[10].

References:

1. See, for example, M.T. Tsao, L. Wang, R. Jin, R.W. Sprague, G. Gigioli, H.M. Kulcke, Y.D. Li, H.M. Chou, H.M. Gibbs and N. Peyghambarian, "Symbolic substitution using ZnS interference filters," Opt. Eng. 26, 41 (1987) and numerous references therein in optical logic gates. See also, K.H. Brenner, A. Huang, and N. Streible, "Digital optical computing with symbolic substitution," Appl. Opt. 25, 3054 (1986).

2. See, for example, S.D. Smith, A.C. Walker, B.S. Wherrett, F.A.P. Tooley, N. Craft, J.G.H. Mathew, M.R. Taghizadeh, I. Redmond and R.J. Campbell, "Restoring optical logic: demonstration of extensible all-optical digital systems," Opt. Eng. 26, 45 (1987) and references therein.

3. See, for example, most of the articles in the special issue on, "Materials and devices for optical information processing," Opt. Eng. 25, 1986 and also in the special issue on "Nonlinear optical materials, devices and applications," Opt. Eng. 24, (1985).

4. Amnon Yariv and Sze-Keung Kwong, Opt. Letts. 11, 186 (1986); B.H. Soffer, G.J. Dunning, Y. Owechko and E. Marom, Opt. Letts. 11, 118 (1986).

5. J.P. Huignard, H. Rajbenbach, Ph. Refregier and L. Solymar, "Wave mixing in photorefractive bismuth silicon oxide crystal and its applications," Opt. Eng. 24, 586 (1985). See also various articles by J. Feinberg, M.B. Klein, A.R. Tanguay, C. Warde, U. Efron, A.M. Glass and others in the special issue on "Materials for optical processing" in JOSA B3, (1986).

6. D.A.B. Miller et al., Opt. Letts. 9, 567, (1984); M. Dagenais and W.F. Sharfin, Appl. Phys. Lett. 46, 230 (1985); T. Venkatesan et al., Opt. Letts. 9, 297 (1984); Williams, D., ed. "Nonlinear optical properties of organic and polymeric materials," (Plenum, N.Y. 1983).

7. I.C. Khoo, "Nonlinear optical properties of liquid crystals for optical imaging processes," Opt. Eng. 25, 198 (1986); I.C. Khoo, IEEE J. Quant. Electronics QE-22, 1268 (1986), and references therein.

8. I.C. Khoo et al., "Low power laser beam amplification via thermal grating mediated degenerate four wave mixings in a nematic liquid crystal film," J.Op.Soc.Am.B Feb. (1988).

9. T.H. Liu and I.C. Khoo, "Probe beam amplification via degenerate optical wave-mixing in a Kerr medium." IEEE J. Quant. Electron QE 23,2020 (1987).

10. I.C. Khoo and R. Normandin, Appl. Phys. Lett. 47, 350 (1985).

11. I.C. Khoo, Appl. Phys Lett. 47, 908 (1985); L. Richard, J. Maurin, and J.P. Huignard, Opt. Comm. 57, 365 (1986).

12. S. Puang-Ngern and S.P. Almeida, Technical Digest, 1986 OSA Annual Meeting, p. 34.

13. (a) I.C. Khoo et al., "Transverse self-phase modulation and bistability in the transmission of a laser beam through a nonlinear thin film." J.Op.Soc.Am.B4,886(1987)
(b) I.C. Khoo et al., Phys. Rev. A29, 2756 (1984).

14. G. Pauliat, J.P. Herriau, A. Delboulbé, G. Roosen and J.P. Huignard, "Dynamic beam deflection using photorefractive gratings in BSO crystals," JOSA B, 3, 306 (1986).

THURSDAY, JUNE 16, 1988

EMERALD BAY ROOMS

6:00 PM–9:30 PM

ThE1–15

POSTER SESSION

Hua-Kuang Liu, Jet Propulsion Laboratory, *Presider*

An Optical Intensity and Polarization Coded Ternary Number System

Shing-Hong Lin
Physical Optics Corporation
2545 W. 237th St.
Torrance, CA 90505

1. INTRODUCTION

The lack of practical multiple-valued logic devices has in the past discouraged extensive investigation into multiple-valued logic. Recently, however, a number of optical processors have been presented to perform either multiple-valued logic functions[1,2], modified signed-digit arithmetic[3], or residue arithmetic[4]. Most of these implementations utilize position coding for the representation of residue numbers or multiple-valued numbers. For example, 9 pixels are needed to represent the combinations of two ternary inputs, and only one of the pixels will be turned ON at a time. As a result, the spatial utilization of input SLM (spatial light modulator) plane is quite low. In this paper, a new ternary number representation, which make use of both intensity and polarization codings, is proposed to perform both ternary logic operations and modified signed-digit arithmetic. The advantages of this system are that only one pixel is used to carry 1-bit information, and the conventional optical logic array[5] and SLMs, which are designed for binary system implementation, can be used in the proposed ternary system.

2. TERNARY NUMBER REPRESENTATION

The ternary number representation utilized in this paper is a fixed radix 2 and a digital set [$\underline{1}$, 0, 1], where $\underline{1}$ denotes -1. An n-digit ternary integer $Y = [y_{n-1}...y_0]$ ($y_i \in \{\underline{1}, 0, 1\}$) has the value

$$\sum_{i=0}^{n-1} y_i \cdot 2^i \qquad (1)$$

For example, [0101], [011$\underline{1}$], and [1$\underline{1}$1$\underline{1}$] will represent "5". In optical implementation, It requires three different states to represent the three possible values of a ternary digit. Thus, the 1 can be represented by a horizontally polarized light with intensity 1, $\underline{1}$ by a vertically polarized light with intensity 1, and 0 by a light with intensity 0. The representation based on the intensity and polarization codings is shown in Figure 1.

The input stage of an optical ternary system can be simply realized by cascading a binary-intensity SLM (which represents 0 and 1 intensity)[6] with a polarizing SLM (which represents vertical and horizontal polarization)[7]. If we add two ternary inputs optically, 6 possible states, i.e., {00}, {01}, {0$\underline{1}$}, {1$\underline{1}$}, {11}, and {$\underline{1}$ $\underline{1}$}, can occur. These states are shown in a phasor diagram in Figure 2. Various ternary logic operations and ternary arithmetic are, hence, realized by separating the six input states into three output states (i.e., $\underline{1}$, 0, 1). Examples will be provided for ternary combinatorial logic functions in the next section; the realization can be generalized to ternary arithmetic.

3. OPTICAL TERNARY COMBINATORIAL LOGIC

The availability of MAX, MIN, and appropriate unary operators enable any multiple-valued combinatorial function to be synthesized in a sum-of-products form as shown in Figure 3 [8]. As their name implies, the MAX and MIN operators give outputs that take the value of the maximum or the minimum of the input signals, respectively (as indicated in Figure 4 for the ternary system). As shown in Figure 5, the optical implementation of MAX and MIN operators is to separate the phasor diagram into 3 output regions, each of which corresponds to an output value (i.e., $\underline{1}$, 0, or 1). If P_H and P_V represent the polarization directions of a polarizer in the horizontal and vertical axes, respectively, then the optical implementations of MAX and MIN operators are shown in Figure 6. For example, in MAX realization, a P_V polarizer will discriminate {(00), (01), (11)}, {(1$\underline{1}$), (0$\underline{1}$)} and {($\underline{1}$ $\underline{1}$)}, by 0-, 1-, and 2- intensity values, respectively; an LCLV (liquid crystal light valve), which acts as an AND array, will separate { (00), (01), (11), (1$\underline{1}$), (0$\underline{1}$)} and {($\underline{1}$ $\underline{1}$) } into 0 and 1 output intensity value, respectively; finally, an output polarizer with vertical polarization will turn all the 1-intensity pixels from the AND array into vertical polarization which represents $\underline{1}$ in the ternary system. Similarly, {(01), (1$\underline{1}$), (11)} can be discriminated from others by a P_H polarizer and an OR array for ternary output 1 (i.e., horizontally polarized light). Since the input set {(00), (0$\underline{1}$)} corresponds to the output value of 0, the discrimination of {(00), (0$\underline{1}$)} from others is not necessary. Therefore, the realization of MAX only requires two parallel stage as shown in Figure 6. For providing functional completeness, the unary operator can be simply implemented in the polarizing SLM[7].

4. CONCLUSIONS

In this paper, we have introduced a new representation for ternary logic and arithmetical operations that are more powerful than our familiar binary operations. The new representation is based on intensity and polarization coding, and has very simple optical implementation with the aid of several polarizers and conventional optical logical arrays (designed for binary systems), the architectural realization of a complete ternary combinatorial function has been demonstrated and the extension to the ternary arithmetical operations is straightforward.

REFERENCES

1. R. Arrathoon and S. Kozaitis, "Shadow casting for multiple-valued association logic," Opt. Engr. 25, 29 (1986)
2. T.K. Gaylord and N.M. Mirsalehi, "Truth-table look-up parallel data processing using an optical content-addressable memory." Appl. Opt. 25, 2277 (1986).
3. B.L. Drake, et al, "Photonic computing using the modified signed-digit number representation," Opt. Engr. 25, 38 (1986)
4. S.F. Habiby and S.A. Collins, Jr., "Implementation of a fast digital optical matrix-vector multiplier using a holographic look-up table and residue arithmetic," Appl. Opt. 26, 4639 (1987)
5. T. Venkatesan, et al, "Fabrication of arrays of GaAs optical bistable devices," Appl. Phys. Lett. 48, 145 (1986)
6. W.E. Ross, et al, "Two-dimensional magneto-optic spatial light modulator for signal processing," Opt. Engr. 22, 485 (1983)
7. K.M. Johnson, et al, "Polarization-based optical logic gate utilizing ferroelectric liquid crystals," Opt. Lett 12, 611 (1987)
8. S.L. Hurst, "Multiple-valued threshold logic: Its status and its realization," Opt. Engr. 25, 44 (1986)

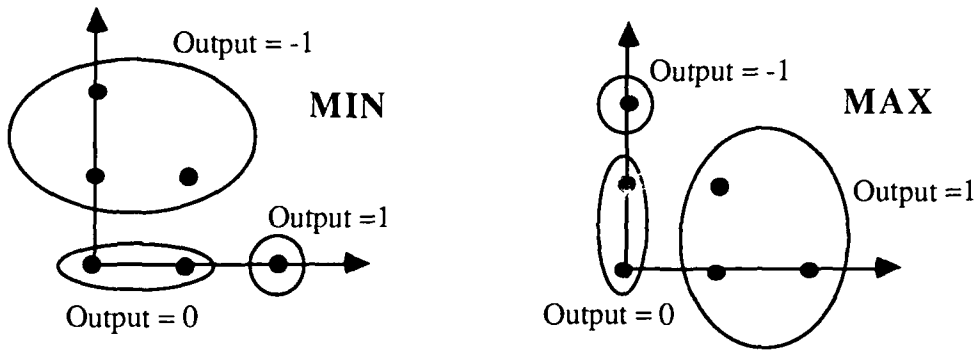

Figure 5. Phasor diagrams for MAX and MIN operations

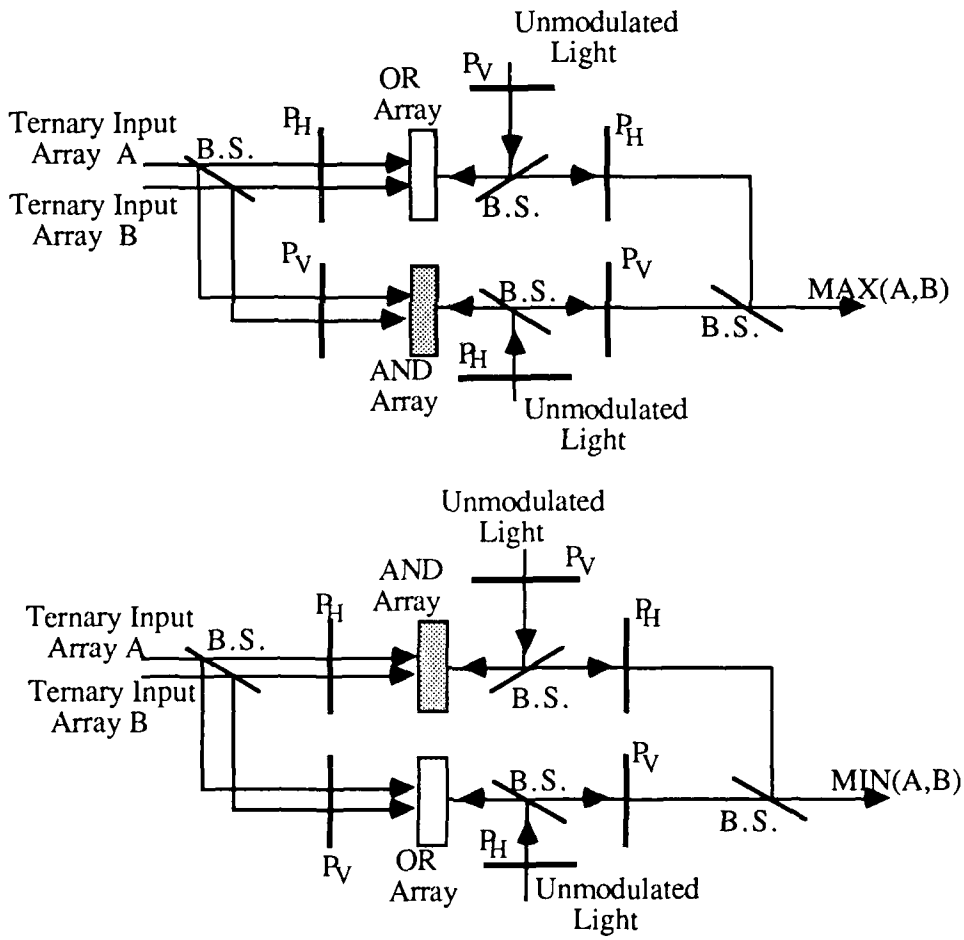

Figure 6. Optical implementations for MAX and MIN operations

	Intensity	Polarization
- 1	1	Vertical
0	0	Don't Care
1	1	Horizontal

Figure 1. Ternary number representation based on intensity and polarization codings

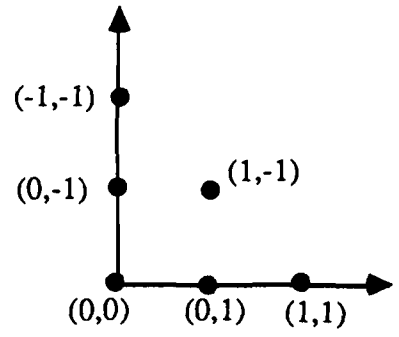

Figure 2. Phasor diagram for two ternary inputs

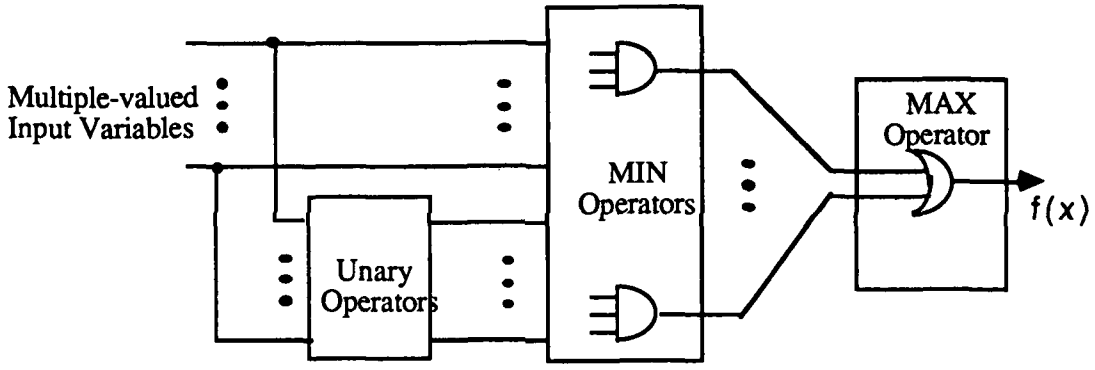

Figure 3. General realization for any multiple-valued combinatorial function, using MAX, MIN, and unary operators

Ternary MAX(A,B)

B \ A	- 1	0	1
- 1	- 1	0	1
0	0	0	1
1	1	1	1

Ternary MIN(A,B)

B \ A	- 1	0	1
- 1	- 1	- 1	- 1
0	- 1	0	0
1	- 1	0	1

Figure 4. Two ternary-input MAX and MIN operators

Active-Matrix-Addressed Viscoelastic Spatial Light Modulator

R.Gerhard-Multhaupt, R.Tepe, W.Brinker, and W.-D.Molzow

Heinrich-Hertz-Institut Berlin GmbH, Einsteinufer 37,
D-1000 Berlin 10, Federal Republic of Germany

Introduction

Thin metallized viscoelastic layers with active-matrix addressing are proposed as spatial light modulators (SLM's) for eventual use in a reflective Schlieren light valve or in other electro-optical devices. A periodic deformation of the mirror electrode covering the viscoelastic layer leads to diffraction of the incoming light; the relative light intensities in the diffraction orders are determined by the deformation amplitude and can thus be controlled by means of the applied voltages. In order to obtain an almost linear deformation response with relatively small video signals V_S, a constant bias voltage V_0 is applied between the top (mirror) electrode and the interdigital-electrode grid. Further details of the suggested viscoelastic SLM and a theoretical analysis of its deformation behavior are found in previous articles [1,2].

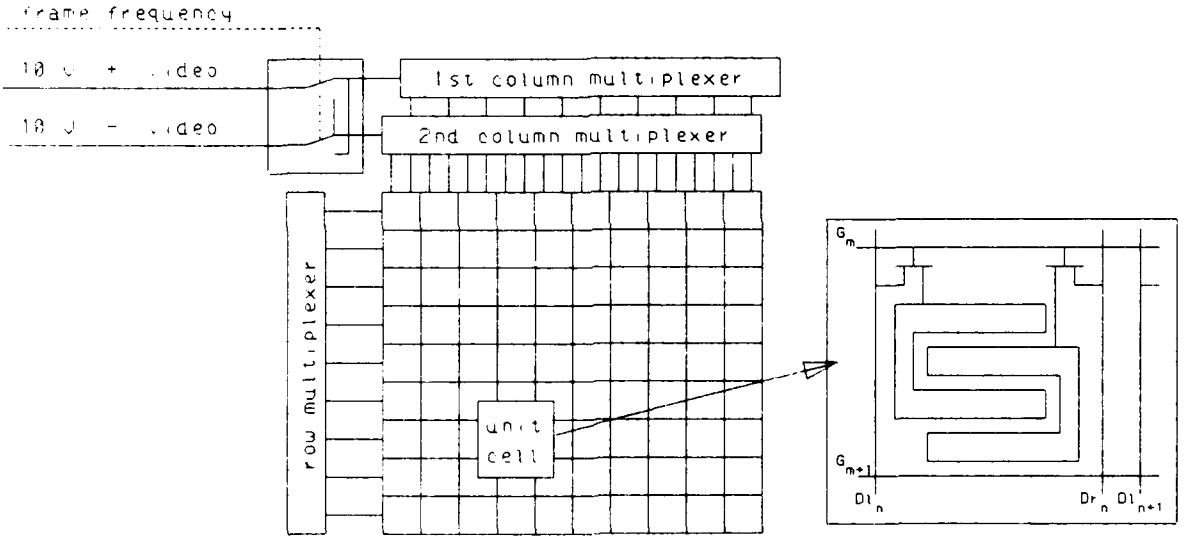

Fig.1. Schematic drawing of the proposed active matrix with two metal-oxide-semiconductor (MOS) silicon transistors and two electrode pairs per picture element; the insert shows the circuitry of a unit cell (one picture element).

Active-Matrix Design

The proposed active matrix consists of a two-dimensional array of MOS silicon transistors which allow for an independent addressing of all picture elements as schematically depicted in Fig.1. Each picture element carries one pair of interdigital signal electrodes as shown in the enlarged insert of Fig.1. These electrodes define two periods of the potential distribution effecting the required sinusoidal surface deformation of the viscoelastic SLM. At the periphery of the chip, the incoming serial video signals are paralleled by means of two column multiplexers and applied to the drain lines Dl_n and Dr_n (metal column electrodes). After completion of the actual image line, the next gate line (poly-silicon) is selected by the line (or row) multiplexer. The floating source contacts of all MOS transistors in this line and thus also the

directly connected diffraction-electrode pairs are charged to the same voltages as the respective drains. Subsequently, the gate line is switched off. Now, the following line of video information is transferred to the drain lines, the appropriate gate line is selected, and the sequence is repeated.

Apart from providing for some redundancy, the two transistors found in each picture element can be employed to shift the deformation grating periodically by half a period in order to avoid irreversible long-term deformations of the SLM. Two switches operating at the video-frame rate lead to the required alternation of the drain voltages. However, since the transistors operate with one polarity only, a constant offset voltage equal to the maximum video signal (typically about 10V) has to be added to the two symmetric video signals.

Theoretical Analysis of the Deformation Behavior

Since a sinusoidal deformation of the mirror electrode is desired for optimal diffraction properties, the electric potential at the interface between active matrix and viscoelastic layer is assumed as $V(x)=V_0+V_S\cos(2\pi f_r x)$, where V_0 and V_S are the bias and signal voltages, respectively, f_r is the spatial frequency of the periodically varying potential, and x is the spatial coordinate perpendicular to the length direction of the picture-element electrodes. With respect to the available transistor voltages and the required linearity, the signal voltages should be much smaller than the bias voltage: $V_S/V_0 \ll 1$. Using these assumptions together with the proper boundary conditions, the electric field in the viscoelastic layer can be analytically determined from Laplace's equation for the potential $\Delta V=0$ (for details see Refs. [1] and [2]).

In order to calculate the deformation of the viscoelastic layer under the influence of the electric field, the theory of linear viscoelasticity [3] is employed: The layer is modelled with an elastic element ("spring") characterized by the shear modulus G and a dissipative element ("dashpot") representing the dynamic viscosity η. According to the so-called Voigt model, whose electrical analogue is the Maxwell model, the two elements are connected in parallel. Consequently, since the viscoelastic layer is isotropic and incompressible, its mechanical behavior is governed by Laplace's equation for the pressure $\Delta p=0$ together with suitable boundary conditions (no deformation at the interface to the active matrix) [2].

In addition to the viscoelastic properties of the layer itself, the mechanical behavior of the mirror electrode has to be taken into account. Here, the theory of plates [4] is used to determine the bending resistance of the thin metal layer as a function of its thickness δ, Young's modulus E, and the bending radius depending on the respective deformation. Altogether, the time behavior as well as the spatial-frequency response of the SLM deformation were calculated for realistic sets of the parameters mentioned above [5].

An example is given in Fig.2 which shows the theoretical spatial-frequency responses of three metallized viscoelastic layers with different thicknesses. Different bias voltages were assumed in agreement with experimental values (see below). The responses exhibit a band-pass characteristic whose low-frequency part is caused by the incompressibility of the layers, whereas the steep high-frequency decrease is determined by the thickness of the SLM and the bending resistance of the mirror electrode. Because only final deformation amplitudes are depicted in Fig.2, the results do not depend on the viscosity η of the viscoelastic material.

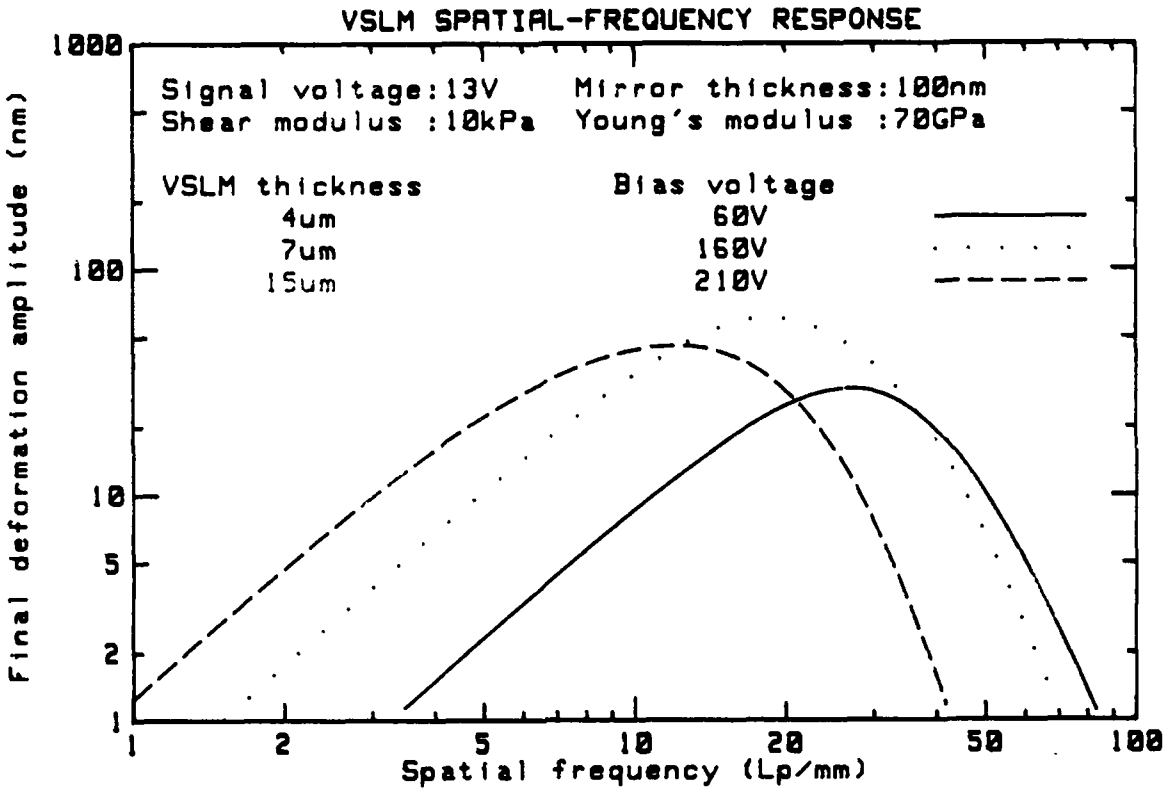

Fig.2. Theoretical spatial-frequency responses of metallized viscoelastic spatial light modulators (VSLM's) with different thicknesses; the assumed values of the relevant parameters are given in the Figure.

Deformation Measurements

For the experimental investigation of the deformation behavior, interdigital-electrode patterns with several different grating periods were employed instead of the active matrix which will be available only later. The temporal performance of the viscoelastic layers was determined by means of diffraction measurements; some results are given elsewhere [1]. An example of measured spatial-frequency responses is presented in Fig.3 where the same layer thicknesses (4, 7, and 15μm) and bias voltages (60, 160, and 210V) as in the theoretical result of Fig.2 were used.

Fig.3 contains values of the quasi-steady-state deformation amplitudes which were obtained by manually evaluating interference images taken with a Zeiss photomicroscope equipped with a Mirau interference attachment [1]. Especially for small deformations, large error bars have to be taken into account because of the uncertainties of the visual evaluation. At lower spatial frequencies, the electrode stripes generate deformations which are not sinusoidal, since the approximately trapezoidal potential distribution in the electrode plane contains prominent higher spatial harmonics [2]. Therefore, values in this range represent only estimates; computer evaluation of the Mirau interferograms is planned in order to remedy the problem. However, in view of these difficulties and the fact that the viscoelastic and mechanical parameters of the experimental SLM devices are not known, the qualitative agreement between the analytical results of Fig.2 and the experimental values of Fig.3 is quite satisfactory, at least for the higher spatial frequencies.

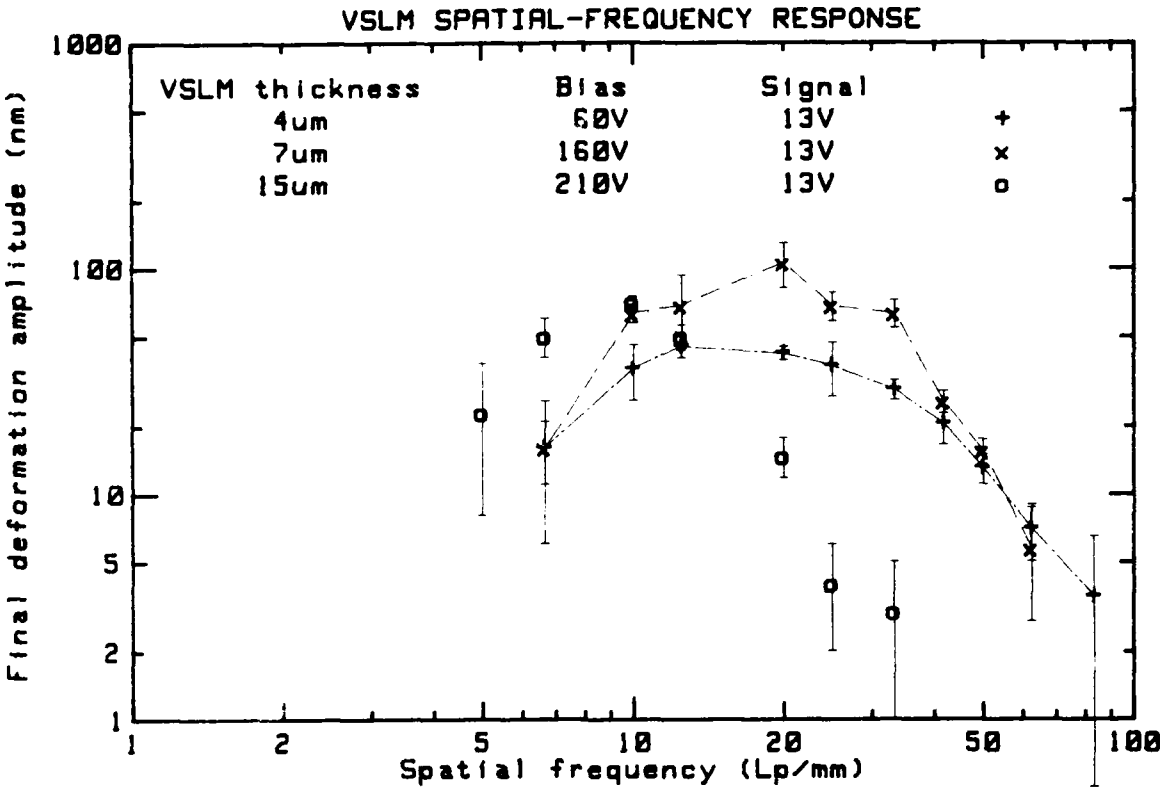

Fig.3. Experimental spatial-frequency responses of viscoelastic spatial light modulators (VSLM's); details are given in the Figure and in the text.

Conclusions

From our analytical and experimental results, the time behavior and the spatial-frequency response of viscoelastic SLM's seem to be sufficient for full modulation of high-resolution images at video frame rates. Open questions concern the long-term stabilities of mirror electrode and viscoelastic layer, the avoidance of defects in these layers and in the transistor array, and the optimization of the necessary reflective Schlieren-optical system. Work on these problems is under way.

Acknowledgements

The authors are indebted to Prof.Dr.G.Mahler, Dr.H.-L.Fiedler, and D.Stuch for stimulating discussions, to Dr.W.E.Glenn for providing the metallized viscoelastic layers and to L.Emich for valuable support with the numerical evaluation of the theoretical and experimental results. Thanks are also due to the German Federal Minister for Research and Technology (BMFT) who supported this work under research contract No. TK 429/2; the responsibility for the contents of this Summary rests, however, solely with the authors.

References

1. R.Tepe, R.Gerhard-Multhaupt, and W.Brinker, Proc.SPIE **684**, 20-31 (1986).
2. R.Tepe, J.Opt.Soc.Am.A **4**, 1273-1282 (1987).
3. T.Alfrey, *Mechanical Behavior of High Polymers* (Interscience, N.Y. 1948).
4. L.D.Landau, E.M.Lifschitz, *Elastizitätstheorie* (Akademie-Verlag, Berlin).
5. R.Tepe, to be published (1988).

"PATTERN RECOGNITION UTILIZING BINARY LIGHT MODULATORS"

Robert E. Hill
Department of Electrical Engr
Louisiana Tech University

Donald K. Fronek
Department of Electrical Engr
Louisiana Tech University

Calton S. Faller
Department of Electrical Engr
Louisiana Tech University

Richard A. Lane
U.S. Army Missile Command
Army Misile Laboratories

ABSTRACT:

The Optics Laboratory at Louisiana Tech University is developing application capability for high speed image processing and pattern recogition using a three-plane Vander Lugt optical correlator.

INTRODUCTION:

The recognition of "targets" in real time is currently of tremendous concern to the Federal Government for navigation and military operations. Computing the spatial position and type of incoming target has been a time consuming exercise because of the large amount of data to be processed. A combination of optical and image processing has been used by several notable industrial and academic institutions[2,4,5,7,9] in an attempt to solve existing speed problems. SEMETEX, a manufacturer of high speed magneto optic spatial light modulators, has recently produced a 128 x 128 pixel binary modulator capable of "switching" frames at above 2000 frames per second. This technology breakthrough has inspired researchers to generate several "filter masks" for each target type and to correlate various prototype signatures with actual real-time image data input. Optical processing in the form of Fourier Transform Correlation is handled in a Vander Lugt optical correlator. Input images and filter "masks", called Binary Phase Only Filters, are generated by computer in real-time. The high-speed spatial light modulators allows the filter mask to "keep up" with commerical raster rates. Image enhancement and real-time processing follows at the "detection plane" under control of another special purpose digital computer. The optics laboratory in the Department of Electrical Engineering at Louisiana Tech University has recently procured the necessary equipment and processing software to investigate basic and advanced topics using the new Binary Light Modulators. Work is continuing and several applications have already been identified that are quite attractive to Federal agencies for future funding.

Optical computing has been extremely attractive from the point of view of handling very large amounts of data in a very short period of time. It is the ultimate system for parallel processing and transfer of information. Image processing and pattern recognition is currently a "hot" topic, nationally, and is at the "top" of military interest with respect to missile guidance and navigation. Although optical computing has been done in the laboratory at many research facilities, applications have largely gone aside for lack of compactness, unit cost, and "second sourcing". In the last ten years, several manufacturers have produced a device capable of "switching" light on and off thereby providing a "binary" logic and arithmetic processing capability. The "switch time", so far, has been very slow and limits further development for military use.

The use of spatial light modulators in the area of pattern recognition is especially significant due to the parallel nature of the processing and the real time target identification that is so attractive for military applications. The input SLM acts as a binary transparency of the image when illuminated by linearly polarized plane waves from a laser (such waves are already routinely generated in the optics laboratory utilizing a HeNe laser, spatial filter and lens doublet collimator).

The second plane is the Fourier plane in which the light amplitude distribution is the Fourier transform of the input image due to the transforming properties of the Lens, L1. By inserting a filter or "pupil mask" with an amplitude transmittance proportional to the conjugate of the image transform, an optical matched filter is implemented which maximizes the signal-to-noise ratio. This is also equivalent to correlating the input signal with the "point response" of the filter. The second lens, L2, again transforms the output signal of the filter and the resulting correlation is projected to the third plane.

The third plane consists of a raster scanned television camera to record autocorrelation peaks in the light distribution. Although commercial raster rates are adequate for current state-of-the-art throughput, this will eventually be replaced with a faster responding CCD array when SLM frame rates improve. The third plane camera monitor will interface with an IBM-AT class computer for further analysis of the correlation output---i.e. thresholding, filtering, spatial position, etc.

Several techniques are being implemented to improve the signal-to-noise ratio and hence target identification. Advanced edge detection hardware (supplied by Image Technology) will be utilized to maximize input target definition and proper scaling of target objects. This is expected to limit the required filter search and greatly increase system throughput. It has also been shown (Casasent and Furman) that cross-correlation peaks with noise (objects with similar spatial spectral content) can be minimized by emphasizing spatial frequencies identified with dominant features of the target. Algorithms will be developed to filter the computer generated hologram in an attempt to minimize these cross-correlation peaks.

The research thrust at the output plane is centered around the development of signal processing techniques to identify true correlation peaks and track their movement. Introducing a CCD array detector in the output plane will require the design of a high speed interface to store array data in memory. It is recognized that the initial physical size of the correlator limits it applicability to certain military operations (although this is not necessarily the case for automated manufacturing applications). An extensive effort is being made to miniaturize the correlator(Litton, US Army Missile Command, others). This is being accomplished by using semiconductor lasers, short focal length collimator lenses, a CCD detector array vs a television vidicon, and geometries designed to shorten the distance between L1 and L2 without vignetting edge rays. Techniques discussed involving computer generated binary filter masks, image enhancement and edge detection, as well as the general application of optical correlation to pattern recognition are all on the current edge of signal processing technology.

BACKGROUND:

The fundamental theory of optical spatial filtering was done in the mid-1950's by Cheatham, Kohlenberg, and O'Neill. Since that time, significant extension and progress has been made in optical data processing and spatial filtering. Author Vander Lugt [10], in 1964, presented a method for a "practical" realization of a general complex optical filter. Up to this point in time, only photographic film had been used successfully as a correlating "filter" for the optical processing. Furthermore, Vander Lugt's work showed that his filter could be implemented by binary values in two dimensions using a "phase" principle and coherent light. Since a spherical lens can take the Fourier transform of a complex distribution of light, one can construct an optical system by arranging a sequence of lenses which forms a succession of Fourier transform planes. An image at the inputs plane can be effected by placing a lens behind plane P2 as shown in the figure below. A positive spherical lens always introduces a positive kernel in the transform relationship.

Vander Lugt assumed that the system has unity magnification and sufficient "bandwidth" to pass the highest spatial frequency of the input function (This concept requires that a very high quality "matched" set of Fourier transform lenses be used in the correlator such as the SORL 15/5F used in this research). When a "filter" is placed at P2, the output of the system essentially represents the probability that a correlated signal has occurred. A bright spot at the output plane, P3, indicates a high degree of correlation and low-light level indicates a low degree of correlation. However, the system is sensitive to the "orientation" of the input signal but a rotation of the filter at P2 relative to the input provides a sequential search of all orientations (To accomplish this task in real-time a high speed computer is required to generate a sequence of images that represents various filter orientations).

Ten years later (1974), coherent optical processing had been "refined" to the extent that major attention was being focused on spatial filter technology and much research was devoted to the fabrication of arbitrary phase and amplitude filters. Much interest was spent in identifying materials that could change the angle of polarized coherent light. Magnetooptic effects in materials such as MnBi, NiFe, and others were quite attractive for realization. Other techniques, such as liquid crystal, thermoplastics, acoustooptics, also received considerable interest. In 1979, Lee developed the methodology to generate binary holograms. In 1977, Litton Data Systems of Van Nuys, California, under the direction of Dr. William Ross, invented the LIGHT MOD (Litton Iron Garnet H-Magnetically Triggered Magneto Optic Device) in conjunction with SEMETEX and Airtron. SEMETEX is currently manufacturing several "array" type of devices.

The original SEMETEX 48 x 48 array was called the SIGHT MOD (SEMETEX being substituted for LITTON) 48. Much of the research up to 1985 was done with a 48 x 48 sized array at the input and Fourier planes. Currently the SIGHT MOD arrays produce (or have the potential to produce) the highest "frame" rate of any spatial light modulator, SLM. The liquid crystal form of spatial light modulator is quite popular because of its availability and low cost, but suffers in frame rate by a factor of 100 to 1000. It was only in about 1982 when Ross,

Psaltis and Anderson presented the results of the current fabrication techniques. Quickly, Horner, Yu, Psaltis, Flannery, Davis, Mills, and many other researchers began setting up Vander Lugt correlators with 48 x 48 array SIGHT-MOD's used as the generator of binary filters and as an input image generator. Both devices are controlled by an IBM-AT class of computer and can operate at commercial television raster rates. The switching time for "frame" rates is currently very low owing to the fact of using "serial data transmission" to the SIGHT MOD units. It is anticipated that 10,000 frames per second could be obtained if frame rate switching was done "in parallel" rather than serial as it typically is being done now. Just developing a "driver" for the SIGHT-MOD to switch at high-speeds would justify a small research project. Dr. Charles Higgins (Ph. D. May 1987, New Mexico State University at Las Cruces), has provided an insight to this problem.

Currently, the researchers mentioned above are "just" receiving the newer 128 x 128 SIGHT MOD's to continue their research efforts. SEMETEX predicts that 256 x 256 SIGHT-MOD's will be available during the first quarter of 1988 but the cost will be in excess of $40,000 per unit.

EARLY EXPERIMENTS:

As of this date, the research team has obtained all of the hardware necessary to begin a series of correlation experiments. Software to drive the SEMETEX SLM's and the ability to produce a BPOF mask is missing. Currently, a series of experiments is being performed to determine the "optimal" input target size within the image scene to produce a reasonably large transform pattern. Several schemes of observing data at all planes are being employed. The SEMETEX device is being studied to determine the "best" approach to increase the "write" speed. By the time of the conference presentation, we expect to have preliminary data on transform verification, correlated "spot" image pre-processing algorithms, and input image enhancement. Several graduate students have already indicated a serious interest in this emerging and exciting area of optical/image processing.

SUMMARY:

The Optics and Image Processing Laboratory at Louisiana Tech University is currently involved in the development of applications for optical processing using the Vander Lugt correlator and real-time image processing techniques. This research is in progress and presently employs only a single SEMETEX SIGHT MOD placed at the Fourier Plane. Plans are being made to acquire a second SIGHT MOD at the time of this presentation. The research team is developing expertise in:

1. Correlator Input Image Enhancement
2. Generation of BPOF Masks
3. Correlator Output Image Enhancement
4. Target Acquisition and Tracking
5. Real-Time Image Processing Algorithms
6. High-speed SIGHT MOD display rates
7. System Software
8. Signal Measurement Techniques

Bibliography and Cited Literature

1. Alastair D. McAulay, "Spatial light Modulator Interconnected Computers", IEEE COMPUTER, October 1987, p-45.

2. Davis, Dav, Lilly, Taber, H.K. Liu, "Grav Scale Operation of a Multichannel Optical Convolver Using the SEMETEX Magnetooptic Spatial Light Modulator", San Diego State University, Dept of Physics. SPIE 825-26, Aug 87.

3. S.A. Mills, and W.E. Ross, "Dynamic Magnetooptic Correlator Real Time Operation", Litton Data Systems, Van Nuys, California, SPIE 753-09, p-1-10

4. Flannery, Keller, Cartwright, Loomis, "Binary Phase Only Correlation For Machine Vision Applications", University of Dayton Research Institute, Optical Engineering April 1987-7-51.

5. R.P. Kallman, "Optical Low Noise Phase Only and Binary Phase Only Correlation Filters For Threshold Detectors", North Texas State University, Denton. Applied Optics, 1 Dec 1986, Vol 25-23, p-4216.

6. Robert Anderson, "Edge Enhancement of Coherent Magnetooptic Images", Litton Data Systems, Van Nuys, Applied Optics, 15 March 1986 Vol-25-6, p-976.

7. Flannery, Biemacki, Loomis, Cartwright, Caulfield, "Real Time Coherent Correlator Using Binary Magnetooptic Spatial Light Modulators at Input and Fourier Planes", University of Dayton Research Institute, Applied Optics, Vol 25-4, 15 February 1986, p-466.

8. Miller, Ross, Anderson, Mills, Cox, "NCTR: High-Speed Optical Correlation Comes Of Age", Proprietary Report of Litton Data Systems, Van Nuys, California August 1985

9. Psaltis, Paek, Venkatesh, "Optical Image Correlation With A Binary Spatial Light Modulator", California Institute of Technology, Department of Electrical Engineering, Pasadena. Optical Engineering December 1984, Vol 23-6, p-698.

10. Anthony Vander Lugt, "Optical Pattern Recognition: An Overview" Harris Government Systems, Melborne. Optical Engineering Dec 84, Vol-23-6, p-688

11. Ross, Snapp, Anderson, "Fundamental Characteristics Of The Litton Iron Garnet Magneto-optic Spatial Light Modulator", Litton Data Systems, Van Nuys, California. SPIE 388-08, 1984.

12. Ross, Psaltis, Anderson, "Two Dimensional Magneto Optic Spatial Light Modulator For Signal Processing", Litton Data Systems, SPIE 341, 1982. p-191.

13. A. Vander Lugt, "Coherent Optical Processing", Electronics Systems Division Harris Corporation. IEEE Proceedings, October 1974, Vol 62-10, p-1300.

14. A. Vander Lugt, "Signal Detection By Complex Spatial Filter", IEEE Trans on Information Theory, April 1964, IT-10, p-139.

General Thin-Lens Action on Spatial Intensity Distribution Behaves as Non-Integer Powers of Fourier Transform

Lester F. Ludwig

Bell Communications Research
331 Newman Springs Road, 1A-221
Red Bank, New Jersey 07701
201-758-4018

This paper shows that the classical equations for the action of a thin-lens on the spatial intensity distribution of light [3] behave generally as *non-integer powers of the Fourier transform* [1,2] for separation distances within the lens-law boundary.

This very general result includes traditional *Fourier Transforming* and *Lens-Law* properties as special cases (corresponding to the Fourier Transform raised to powers of 1 and 2, respectively). Between these special classes of separation distances, the lens action on the spatial intensity distribution of light behaves as the Fourier transform raised to powers between 0 and 2 (for example, 1.3, etc.), varying as a continous function of the separation distances. These non-integer powers of the Fourier transform form an algebraic group of unitary operators which are diagonalized by the Hermite functions [1], making the representation potentially useful in engineering applications.

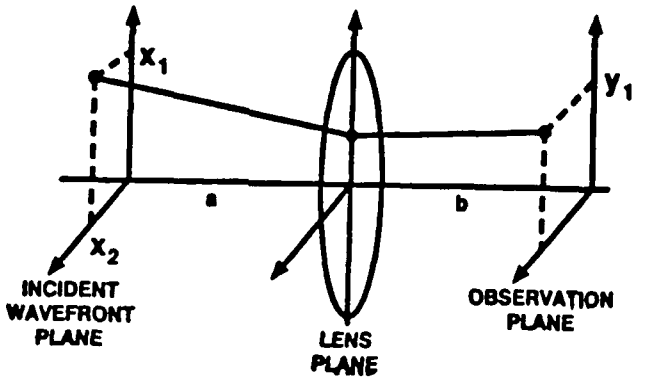

Figure 1. *A thin-lens and definition of associated geometric quantities.*

Levi [3] gives the equation for the action of a thin-lens with focal length f as (in terms of the geometry and definitions of Figure 1):

$$\mathcal{L}_{(a,b,f)}[u(x_1,x_2)](y_1,y_2) = \frac{\lambda i C}{c} e^{\frac{2\pi i(a+b+c/2)}{\lambda}} \int_{-\infty}^{\infty}\int_{-\infty}^{\infty} e^{\left[\frac{2\pi i(ca-1)}{2ca^2\lambda}(x_1^2+x_2^2)\right]} e^{\left[\frac{2\pi i(cb-1)}{2cb^2\lambda}(y_1^2+y_2^2)\right]} e^{\left[\frac{-2\pi i}{\lambda abc}(x_1y_1+x_2y_2)\right]} u(x_1,x_2)\,dx_1dx_2$$

where

$$c = \frac{1}{a} + \frac{1}{b} - \frac{1}{f}$$

In this paper a construction is given for non-integer powers of the Fourier transform and is identified as the spatial distribution component of this equation for thin-lens action:

$$L_{(a,b;f)}[u_{(x_1,x_2)}] \;=\; p\; F^{\alpha}[u_{(s_x x_1, s_x x_2)}]\left[\frac{y_1}{s_y}, \frac{y_2}{s_y}\right]$$

where p, α, s_x, and s_y are functions of only a, b, and λ. Special cases are briefly considered, and additional related results are categorically listed.

1. NON-INTEGER POWERS OF THE FOURIER TRANSFORM

This paper will used the normalized definitions of the Fourier transform (denoted "F") and its inverse (denoted "F^{-1}"), i.e.:

$$F[f(x)](y) = \int_{-\infty}^{\infty} f(x) e^{-2\pi i x y}\, dx,$$

$$F^{-1}[f(y)](x) = \int_{-\infty}^{\infty} f(y) e^{2\pi i x y}\, dy.$$

for the one-dimensional case. By change of variables arguments the Fourier transform is seen to be a unitary operator that is of period 4 in its exponent, i.e., obeying the composition rule as shown in Figure 2.

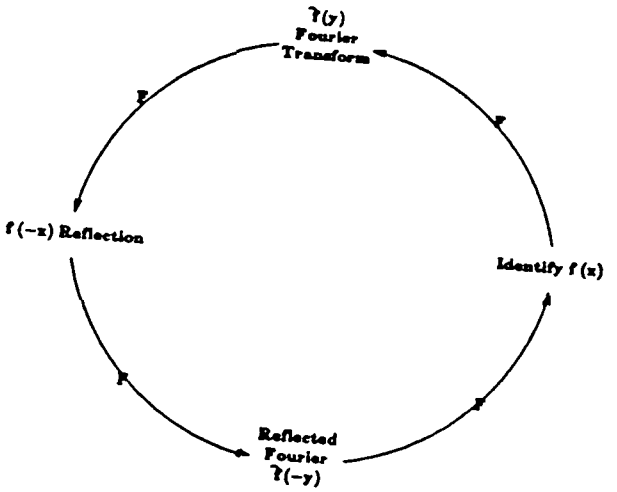

Figure 2. *Composition behavior of the Fourier transform showing integer powers are periodic in the exponent with period 4.*

It is possible to generalize this behavior to non-integer values of the exponent by constructing an algebraic group of operators embedding the Fourier transform and its integer powers [1,2]; henceforth this constructed operator will be called the "Fractional Fourier Transform". Condon [2], with the assistance of Von Neumann, tried this 50 years ago by solving integral equations but was only able to obtain a partial result. The author [1] has produced a complete construction using eigenfunctions which is breifly outlined here.

Wiener showed that the Fourier transform is diagonalized by the Hermite functions h_n which act as orthonormal eigenfunctions with associated eigenvalues $(-i)^n$ [4]

$$F[h_n(\cdot)](x) = (-i)^n h_n(x).$$

Thus, in a space of functions closed under the Fourier transform (such as L^2), it is possible to represent functions in terms of their Hermite function expansion

$$f(x) = \sum_{n=0}^{\infty} c_n\, h_n(x)$$

where each c_n are simply the projections of f against each h_n:

$$c_n = \left[\int_{-\infty}^{\infty} f(\tau) h_n(\tau) d\tau \right]$$

and hence represent their Fourier transform as

$$F[f(x)](y) = \sum_{n=0}^{\infty} c_n (-i) h_n(y).$$

Since the $\{h_n\}$ are orthonormal, an integer k power of the Fourier transform may be represented as

$$F^k(f) = F^k \left[\sum_{n=0}^{\infty} c_n h_n \right] = \sum_{n=0}^{\infty} c_n F^k(h_n) = \sum_{n=0}^{\infty} c_n (-i)^k h_n.$$

(This is comparable to taking powers of a diagonalizable matrix.) The value of k can then be extended by limit arguments to non-integer values. By carefully combining slightly expanded versions of these ideas non-integer powers of the Fourier transform can be given as

$$F^{\alpha}(f)(y) = \int_{-\infty}^{\infty} \left[\sum_{n=0}^{\infty} e^{-in\alpha\pi/2} h_n(y) h_n(x) \right] f(x) dx.$$

The infinite series can be summed in closed form, resulting in

$$F^{\alpha}[u(x)](y) = \sqrt{\frac{e^{-i\pi\alpha/2}}{\sin(\pi\alpha/2)}} \int_{-\infty}^{\infty} u(x) \quad e^{2\pi i \left[\frac{1}{2}(x^2+y^2)\cot(\frac{\pi\alpha}{2}) - xy \csc(\frac{\pi\alpha}{2}) \right]} dx$$

a which may be shown to be very interesting algebraic group of unitary operators that are diagonalized by the Hermite functions. In two dimensions, the form is simply:

$$F^{\alpha}[u(x_1,x_2)](y_1,y_2) = \frac{e^{-i\pi\alpha/2}}{\sin(\pi\alpha/2)} \int_{-\infty}^{\infty}\int_{-\infty}^{\infty} u(x_1,x_2) \quad e^{2\pi i \left[\frac{1}{2}(x_1^2+x_2^2+y_1^2+y_2^2)\cot(\frac{\pi\alpha}{2}) - (x_1y_1+x_2y_2)\csc(\frac{\pi\alpha}{2}) \right]} dx_1 dx_2$$

2. IDENTIFICATIONS WITH LENS EQUATION

The quadractic form of the kernel above and in the lens equation now appear equivalent within a factor and change of variables. Define new variables scaled by positive scalings s_x and s_y:

$$s_x \tilde{x}_j = x_j$$
$$s_y \tilde{y}_j = y_j$$

and relate to the two-dimension Fractional Fourier Transform in variables $\tilde{x}_j$, $\tilde{y}_j$ where $j \in \{1,2\}$:

$$L_{(a,b;f)}[u(x_1,x_2)](y_1,y_2) =$$

$$\frac{\lambda i C}{c} e^{\frac{2\pi i(a+b+c/2)}{\lambda}} \int_{-\infty}^{\infty}\int_{-\infty}^{\infty} e^{\left[\frac{2\pi i(ca-1)s_x^2}{2ca^2\lambda}(\tilde{x}_1^2+\tilde{x}_2^2) \right]} e^{\left[\frac{2\pi i(cb-1)s_y^2}{2cb^2\lambda}(\tilde{y}_1^2+\tilde{y}_2^2) \right]} e^{\left[\frac{-2\pi i s_x s_y}{\lambda abc}(\tilde{x}_1\tilde{y}_1+\tilde{x}_2\tilde{y}_2) \right]} u(s_x\tilde{x}_1, s_x\tilde{x}_2)\, s_x s_y d\tilde{x}_1 d\tilde{x}_2$$

From this one may identify:

$$2\pi i \cdot \frac{1}{2}\cot(\frac{\pi\alpha}{2}) = \frac{2\pi i(ca-1)s_x^2}{2\lambda ca^2} = \frac{2\pi i(cb-1)s_y^2}{2\lambda cb^2}$$

$$2\pi i \csc(\frac{\pi\alpha}{2}) = \frac{2\pi i s_x s_y}{\lambda abc}$$

Solving one obtains

$$\alpha = \frac{2}{\pi} arccos\left[sgn(f-a) \frac{\sqrt{(f-a)(f-b)}}{f} \right]$$

$$s_x = \sqrt{\lambda \sqrt{af+bf-ab}} \sqrt{\frac{f-a}{f-b}}$$

$$s_y = \sqrt{\lambda \sqrt{af+bf-ab}} \sqrt{\frac{f-b}{f-a}}$$

This gives the final representation

$$L_{(a,b;f)}[u(x_1,x_2)](y_1,y_2)$$

$$= \lambda^2 Cab \; e^{\frac{2\pi i(a+b+c/2)}{\lambda}} \; ie^{(-\alpha\pi i/2)} F^{A(f,a,b)}[\, u(s_x x_1, s_x x_2)\,](\frac{y_1}{s_y}, \frac{y_2}{s_y})$$

where

$$A(f,a,b) = \frac{2}{\pi} arccos\left[sgn(f-a) \frac{\sqrt{(f-a)(f-b)}}{f} \right].$$

3. SPECIAL CASES

The general results above are consistant with special cases of classical optics:

1. *Lens-Law Case* ($\frac{1}{a} + \frac{1}{b} = \frac{1}{f}$). Here $\alpha = 2$, giving the spatial inversion of the image, and $s_y/s_x = b/a$, giving the magnification law.
2. *Fourier Transform Case* ($a = b = f$). Here $\alpha = 1$, giving the spatial Fourier transform of the image, and $s_y/s_x = 1$, giving the frequency scaling by λ after change of variables to the non-normalized representation of the Fourier transform.

The case of $a = b$ and cases where either $a = f$ or $b = f$ also have interesting simplications.

4. ADDITIONAL TOPICS

Results can also be derived for multiple lens systems, Huygen-Fresnel apertures, lens transfer functions, and interpretations outside the lens-law boundary.

5. ACKNOWLEDGEMENTS

The author wishes to thank C. Robin Graham of the University of Washington for mathematical assistance and Myra Boenke of U.C. Berkeley for suggesting optics applications.

6. REFERENCES

[1] Lester F. Ludwig, *Non-Integer Powers of the Fourier Transform Operator,* Bellcore Internal Publication (under revision for public release).

[2] E. U. Condon, "Immersion of the Fourier Transform in a Continuous Group of Operators," *Proc. Nat. Acad. Sci. USA,* Vol 23, 1937, pp. 158-164.

[3] Levi, *Applied Optics, Vol. II,* section 19.2.

[4] Wiener, *The Fourier Integral and Certain of Its Applications,* Dover, 1958.

Paper Withdrawn

Paper Withdrawn

Experimental Investigation of Photoemitter Membrane Spatial Light Modulator Performance Limit

Peter B. Rolsma and John N. Lee
Optical Sciences Division, Naval Research Laboratory
Washington, D.C. 20375-5000

Tae-Kwan Oh
Sachs/Freeman Associates, Inc.
1401 MacCormick Drive, Landover, MD 20785

A photoemitter membrane light modulator(PEMLM) is enhanced by adding a visible light photocathode to the basic structure[1]. The basic structure consists of four parts; a microchannel plate(MCP), a grid, a deformable membrane, and a transparent electrode as shown in Figure 1. Previously the input of the MCP was used as a photocathode to convert an ultraviolet(uv) image into an electron distribution. The MCP then amplifies this distribution by secondary emission, similar to a photomultiplier tube. At the output of the MCP the electron energies are low. The purpose of the grid that is added to the MCP output, is to control the electron energy. If the energy is low the electrons will be deposited onto the membrane. If they are high, excess secondary emission at the membrane will occur and electrons will be removed from the membrane. Thus, images are added or subtracted by changing the grid voltage. The rate at which these functions and other possible functions occur, is dependent upon the rate of electron generation by the MCP, up to the point of MCP saturation. This electron generation is the product of the light intensity and photocathode quantum efficiency. Using the MCP input as a photocathode requires a strong uv light because of a low quamtum efficiency($\simeq 10^{-7}$), even at short wavelengths. To avoid the problems of working with uv, a cesium-antimony(Cs_3Sb) photocathode for the PEMLM is being fabricated. This will allow the use of red light for a write beam. Previously, high frame rates were not achieved because of the limits of the light source. With the Cs_3Sb photocathode frame rates should be increased to the MCP strip current limit.

The fabrication of the photocathode results in two complications for the PEMLM. The first complication is the vacuum system must be divided into two regions. The photocathode is fabricated in the first region and then moved to the PEMLM in the second region. To construct the photocathode three layers are evaporated on the glass substrate: chromium, antimony, and cesium. The chromium is evaporated first, making a transparent conducting layer. Next the antimony is evaporated, followed by the cesium. This last layer creates a Cs_3Sb compound that has a low work function. This low work function gives the desired response in the visible light range but also demands a very clean environment. To avoid contamination of the photocathode, it is fabricated in and never leaves a ultrahigh vacuum of 10^{-9} torr. This forces the PEMLM to be placed in the vacuum system but it has to be shielded from the evaporation. The Cs_3Sb compound is highly resistive but each element alone is conductive and could

damage the MCP properties. The cesium in particular is very reactive and has a low vapor pressure that allows the possibility of it contaminating the PEMLM. The second complication is, to achieve a long-term ultrahigh vacuum, a high temperature bake is required. This requires the PEMLM to survive the elevated temperature.

An ultrahigh vacuum transfer system was built with two separate regions. It has the glass substrate mounted on a thrust tube at the top of the system. The thrust tube can be pushed down transfering the substrate to the bottom of the system. The top and bottom regions are separated by a gate valve. The valve is closed during any evaporation. The evaporation sources are attached to a bellows that moves perpendicular to the axis of the trust tube. This allows the sources to be moved between the glass substrate and gate valve for the evaporations. After the evaporations are completed the sources are retracted, the valve is opened, and the thrust tube moves the photocathode down against the MCP input face. The substrate has a lip, that seats against an indium gasket, when it contacts the MCP. The gasket seals the lower region from the top of the transfer system. The photocathode and PEMLM can then be demounted from the larger part of the system. Figure 2 shows the spatial responsivity of a photocathode fabricated in the transfer system.

The properties of the membrane must withstand the high temperature bake and be tailored to optimize the speed of the device. It is commom to bake the system above 250 °C to remove any possible source of photocathode poisoning. We have found reasonable results with a longer bake at 150 °C. This lower temperature is still too high for the traditionally used nitrocellulose membrane. Nitrocellulose has been used because the process of making the film on water, produced a membrane with a preset tension. This tension plays a central role in the membrane dynamics[3]. The behavior of the membrane can be modeled by the differntial equation,

$$M \frac{\partial^2 z}{\partial t^2} + M\gamma \frac{\partial z}{\partial t} - T \left[\frac{\partial^2 z}{\partial r^2} + \frac{\partial z}{r\,\partial r} \right] = P(t) \qquad (1)$$

where, Z is the membrane deflection. M is the mass density, γ is the damping coefficient, P(t) is the spatially uniform pressure on the membrane, and T is the preset membrane tension. For a parabolic shape membrane of radius R, equation (1) reduces to

$$\frac{\partial^2 z}{\partial t^2} + \gamma \frac{\partial z}{\partial t} + \omega_0^2 z = \frac{P(t)}{M} \qquad (2)$$

with $\omega_0 = (4T/MR^2)^{1/2}$. This is the equation for a damped oscillator. Both the membrane's deflection amplitude and resonant frequency, ω_0, are functions of T. The constants, ω_0 and γ, can be determined experimentally by ploting driving frequency vs the membrane's amplitude (Fig.4). The curve peaks at ω_0 and the full width at half the maximum is γ. When an image is impressed on the device the output is valid when the membrane has settled to a new equilibrium. For this

system equilibrium is reached in about $20\pi/\omega_0$. This is one speed constraint. The second is the rate of electron deposition on the membrane. The charge in an electric field produces the force P(t). The time it takes a MCP with a current density J to deform the membrane a quarter wave is

$$t_w = T\, d\, \lambda / R^2 V_b J, \qquad (3)$$

where V_b/d is the electric field at the membrane, which is limited by vacuum breakdown, and λ is the read light wavelength. The tension of the membrane is in both equations and within the limits of the material can be adjusted to maximize the frame rate of a given MCP strip current. The optimized tension is when $t_w = 20\pi/\omega_0$ and this is

$$T = [\, 30\pi (M)^{1/2} J V_b R^3 / 4d\lambda \,]^{2/3}. \qquad (4)$$

To obtain the above performance parylene membranes are being used [4]. Figure 3 is a SEM picture of parylene after one week at 160 °C in a vacuum. Other membranes that have been investigated include an inorganic polymer membrane material (2,2,2,-trifluoroethoxy phosphazene[5]) and SiO_2, but both have exhibited stability problems. System bakes at 220 °C can be done with parylene[4]. The thin film (44 nm) is grown on the glass plate by a CVD process. The film is floated off glass and streched to the desired tension before applying it to the MCP.

The combination of the new membrane materials and photocathode leads to a more useful device. The high photocathode's quantum efficiency should allow a HeNe laser to saturate the MCP. This is close to the maximum current that can be used continuously. The new membrane tension will be adjusted to match the current. Faster PEMLM frame rates will be possible as MCP technology provides increased strip current.

REFERENCES

1. A. D. Fisher, L.-C. Ling, J. N. Lee, and R. C. Fukuda, Opt. Eng. 25, 261(1985).

2. R. Dillon, "A Vacuum Transfer Technique for Photocathode Creation," B.S. Thesis, M.I.T.(1982).

3. Lai-Chang Ling, "Photoemitter Membrane Spatial Light Modulator," Ph.D. Thesis, Optical Science Center, Univ. of Arizona(1986).

4. M. A. Spivack, Rev. Sci. Instrum. 41, 1614(1972).

5. R. R. McCaffrey et al., J. Membrane Sci. 28, 47(1986).

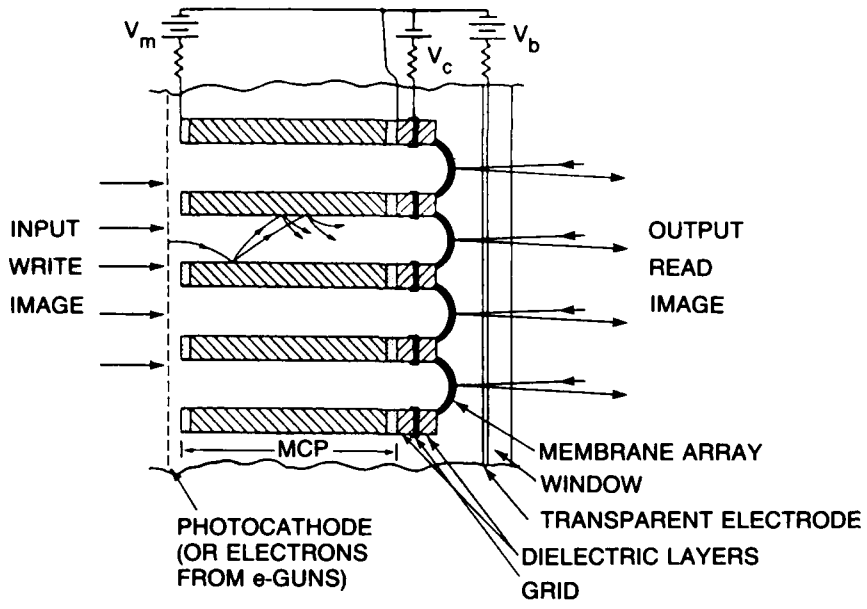

Fig. 1

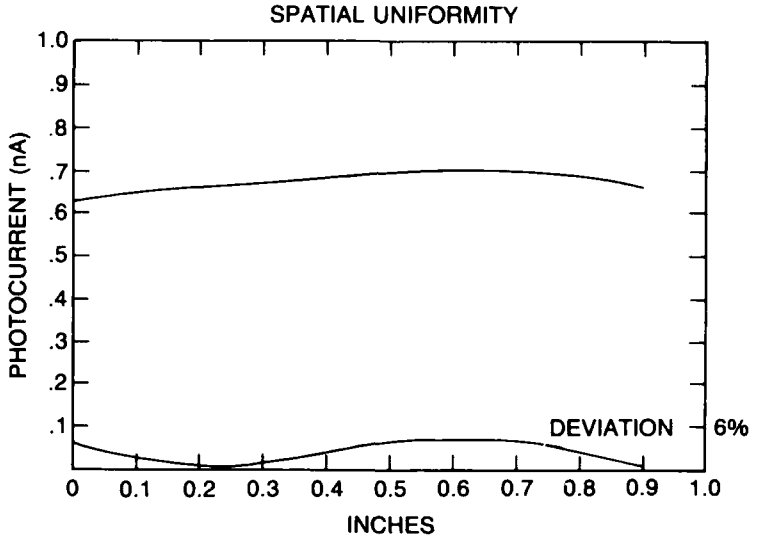

Fig. 2

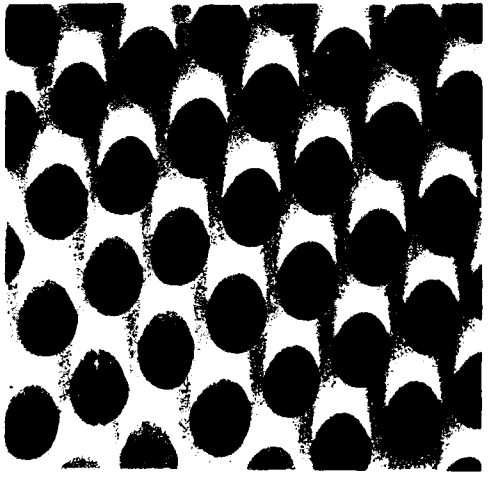

Fig. 3

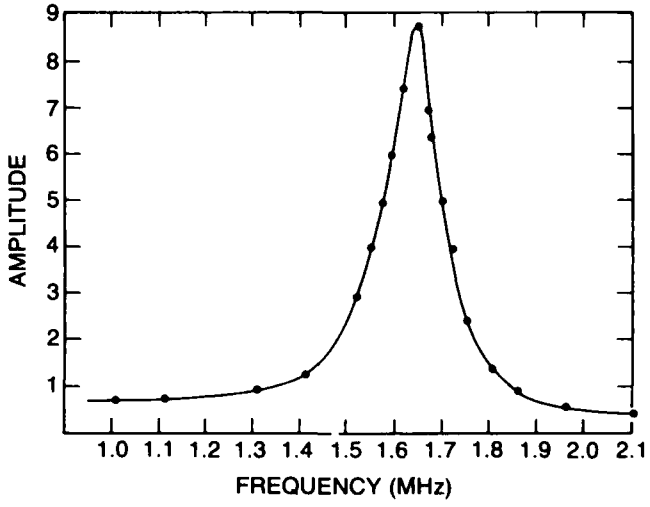

Fig. 4

AN APPLICATION OF OPTICAL LOGIC ON FERROELECTRIC LIQUID CRYSTAL SPATIAL LIGHT MODULATORS TO NEURAL NETWORK PROCESSING

Mark A. A. Neil and Ian H. White,
Cambridge University Engineering Department.
Trumpington Street, Cambridge CB2 1PZ, England.

Abstract

We discuss the use of ferroelectric liquid crystal spatial light modulators as optical polarisation rotating logic elements in a direct storage implementation of the Hopfield model.

Introduction

The development of spatial light modulators as inputs to parallel optical array processing systems has reached a stage where many forms of device are available. In particular ferroelectric liquid crystal spatial light modulators (FLCSLMs) have been shown to have the advantage that they are adiabatic devices which allows good fanout and cascadability [1]. We describe a combinatorial logic scheme based on optical polarisation rotation and show how it may be used in a direct storage implementation of the Hopfield model [2] to overcome problems of encoding bipolar entities on spatial light modulators.

Logical encoding on FLCSLMs

FLCSLMs based on the surface stabilised electro-optic effect may be considered as an array of half wave plates whose axes can be switched electrically between two stable orientations separated by an angle θ (ideally $\pi/4$). A logic scheme can be envisaged where logical **TRUE** and **FALSE** values are encoded as light signals of orthogonal linear polarisation. Figure 1 shows the effect of the two pixel states on each of these logic states.

It has been shown that by appropriate positioning of polarisation filters, various logical combinations can be realised [1]. In particular the placing of a horizontal polarisation blocking filter after the device allows the detection of the function **(A AND B) OR ($\overline{\text{A}}$ AND $\overline{\text{B}}$) ≡ A XNOR B.** Moreover without the filter both **TRUE ≡ A XNOR B** and **FALSE ≡ $\overline{\text{A XNOR B}}$** outputs are present and so may be cascaded into further devices. The **XNOR** function is

equivalent to multiplication within the number set {+1,-1}, hence the applicability to the Hopfield model which relies on such a process.

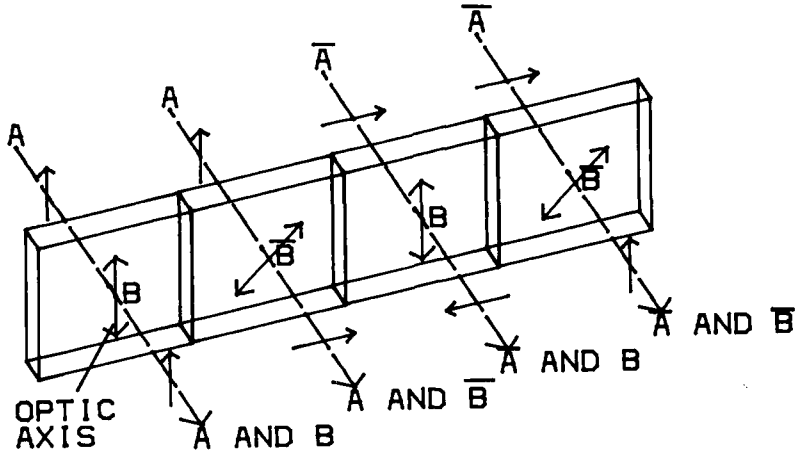

Figure 1 A diagram showing the effect of the two pixel states of a FLCSLM on orthogonal linearly polarised light inputs.

Direct storage scheme and logical representation

The Hopfield model is usually described by a sum of outer products of the stored vectors to give a multivalued synaptic weights matrix, T_{ij}. Memory retrieval then occurs by thresholding the product of this matrix and an input test vector, to give a better approximation to the nearest stored vector.

The mathematically equivalent direct storage method [3] involves bypassing the synaptic matrix setup and performing all calculations directly on the stored vectors. This can be expressed mathematically by the equation;

$$v_i'^{(mo)} = \mathrm{sgn}\left[\sum_{m=1}^{M} \sum_{j=1}^{N} v_j'^{(mo)} v_j^{(m)} v_i^{(m)} \right] \qquad (1)$$

where $v_i'^{(mo)}$ is a better approximation of $v_j'^{(mo)}$, the input test vector, to its nearest stored vector $v_i^{(mo)}$ and sgn[x] is the sign (+1 or -1) of x (i.e. the threshold function). Vector elements are encoded with bipolar values of +1 or -1 for maximum accuracy. Multiplication under such a number set, as mentioned above, is however equivalent to the logical function **XNOR** and so equation (1) can be modified to give;

$$v_i'^{(mo)} = \mathrm{sgn}\left[\sum_{j=1}^{N} \sum_{m=1}^{M} \left[v_j'^{(mo)} \ \mathbf{XNOR}\ v_j^{(m)} \ \mathbf{XNOR}\ v_i^{(m)} \right] - M \times N/2 \right] \qquad (2)$$

The synaptic matrix, T_{ij}, and its multivalued elements no longer appear

in the equations and thus the required processing is simplified. The logical formulation can be implemented with FLCSLMs thus retaining the increased accuracy of bipolar calculations.

Physical realisation of the processor

The logic terms in equation (4) of the form **A XNOR B XNOR C** are realised by passing linearly polarised light into a series of three FLCSLM elements holding the required vectors. The truth table obtained using such devices for each of A, B and C is shown below.

A	B	C	A XNOR B XNOR C	Output polarisation state
0	0	0	0	0
0	0	1	1	$+2\theta$ $(\pi/2)$
0	1	0	1	-2θ $(-\pi/2)$
0	1	1	0	0
1	0	0	1	$+2\theta$ $(\pi/2)$
1	0	1	0	-4θ $(-\pi)$
1	1	0	0	0
1	1	1	1	$+2\theta$ $(\pi/2)$

Again a polarisation filter may be used to distinguish between the **TRUE** and **FALSE** output states when $\theta = \pi/4$. The devices used in the processor are of the type described in ref [4] with values for θ of around 48 degrees. Computer simulations of the effect of such deviations indicate no degradation of the overall performance of the processor; in fact it may even be improved.

Figure 1 shows a schematic layout of a processor based on anamorphic lensing systems (not shown). The operations performed are an inner product of v'_j and each v_j, followed by an outer product of the result with v_i. Parallel processing over the M stored vectors is achieved by arranging them end to end on one line. The cross terms in the outer product are masked out in a projected plane, the effective T_{ij} plane, where any other desired masking may be performed e.g. to partition the net.

The output of the processor, after analysis with a polarisation filter and detection on the photodiode array, is thresholded electronically to give v''_i. Feedback and control of the FLCSLMs are managed by an overseeing microcomputer. With such an optical arrangement, using 64×64 element FLCSLMs, it is possible to process 3 stored vectors of length 20 elements simultaneously in a processing cycle time limited by the write time of the devices to about 100 μsecs. We are currently developing an alternative arrangement whereby the stored vectors are processed in a more compact system giving more efficient use of SLM space.

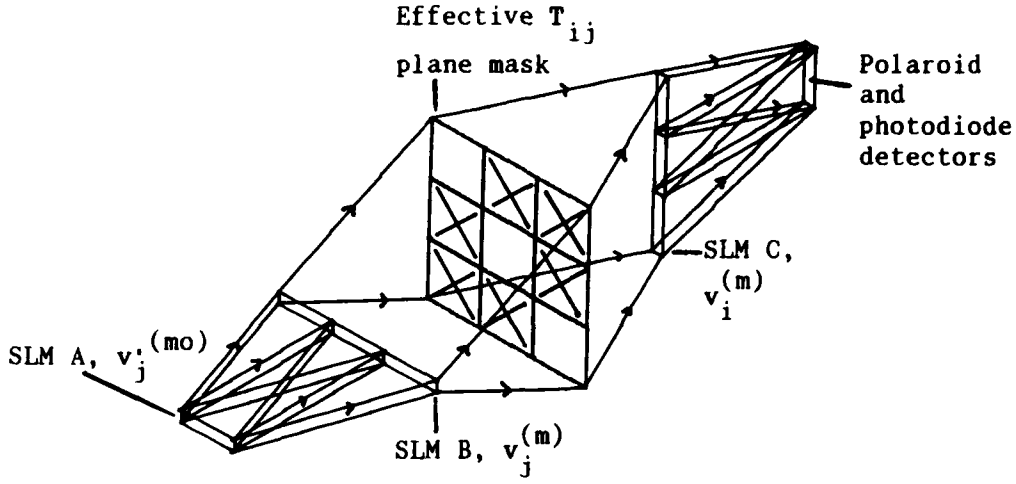

Figure 2 A schematic diagram of the optical vector processor. Lenses are omitted for clarity

Conclusion

We have described the application of a logic scheme on ferroelectric liquid crystal SLMs to a neural network algorithm. We hope to present at the conference results of a working optoelectronic neural processor.

Acknowledgements

This project is supported under the UK Joint Optoelectronic Research Scheme. In particular we thank STC Technology Ltd for the supply of spatial light modulators and GEC Research Ltd for driver circuitry. M.A.A.N would also like to thank the UK Science and Engineering Research Council for a maintenance grant.

References

1. Johnson K M et al. Opt. Eng., Vol 26, no 5 (1987), pg 385.
2. Hopfield J J. Proc. Nat. Acad. Sci. USA, Vol 79 (1982), pg 2554.
3. Fahrat N. Appl. Opt., Vol 26, no 23 (1987), pg 5093.
4. Bone M F et al. Displays July 1987, pg 115.

Paper Withdrawn

Paper Withdrawn

Rotatioanlly Invariant Joint Transform Correlation

F.T.S.Yu, S.Jutamulia, X.Li and E.Tam

Department of Electrical Engineering, The Pennsylvania State University,

University Park, Pennsylvania 16802

Don.A.Gregory

U.S.Army Missile Command, Research, Development and Engineering Center,

Research Directorate, Redstone Arsenal, Alabama 35898-5248

1. Introduction

Many problems in pattern recognition require the identification of an object that has an unknown rotational orientation, and many rotationally invariant correlation techniques have been proposed.[1] This paper describes two rotational-invariant methods utilizing a joint transform correlator that can be implemented with liquid crystal televisions (LCTVs).[2]

2. Information Reduction Joint Transform Correlator

The basic idea of this method is to apply multiple references in a single joint transform corelator. In principle, the tolerance of a correlator can be adjusted by limiting the correlated spatial frequency bandwidth. To gain larger tolerances, the low frequency components must become dominant. Ideally, the zero frequency component will have the largest tolerance, i.e., rotational invariance. However, different objects cannot be distinguished because all images have a common zero frequency component.

If a reference has a rotational tolerance of 30°, then only 12 references are needed to achieve 360° rotational-invariance. It must be considered that only a limited space-bandwidth product (SBP) is available and that a large number of references will saturate the reference space. Therefore, to implement multiple references in the same plane, the information content of each reference image must be reduced. This reduction is done by using only the edge information in the reference image. In general, an edge-enhanced image provides the accuracy of detection, thus reducing the ambiguity of the spatial content. Figure 1a shows the edge enhanced multiple references of the letter "R". Individual references are equally distributed in a circle with an angular spacing of 30°. The total SBP

(number of pixels) in the circle of reference is approximately 4665, while 1612 pixels are occupied by the references themselves. Obviously if the solid letter "R"s are used, the circle of reference will be saturated. A computer simulation was performed to generate the correlation peak and SNR of the reference with the rotated letters "R" and "X" as shown in Fig. 1b. Figures 2 and 3 show that the tolerance is about 15°, thus 24 references will cover the entire 360° rotational space.

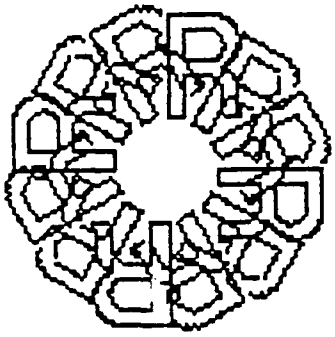

Figure 1a. Reference used in the computer simulation.

Figure 1b. The edge-enhanced letters "R" and "X"

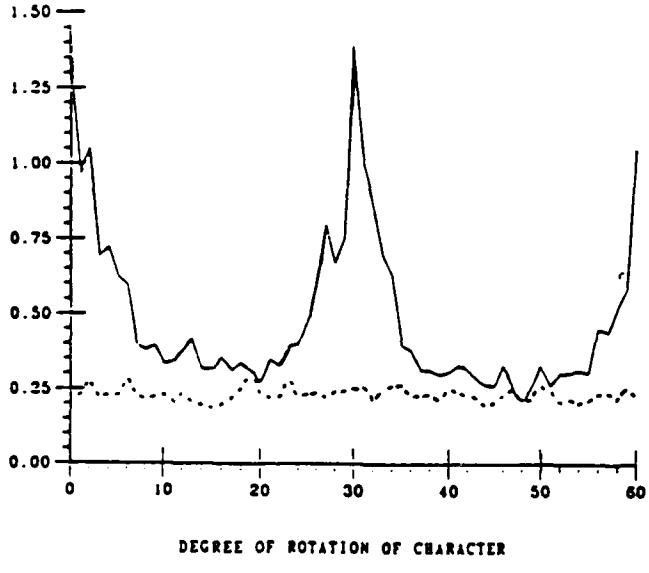

Figure 2. The peak value (arbitrary units) of the correlation spot as a function of the degree of rotation of the letter "R" (solid line) and the letter "X" (dotted line).

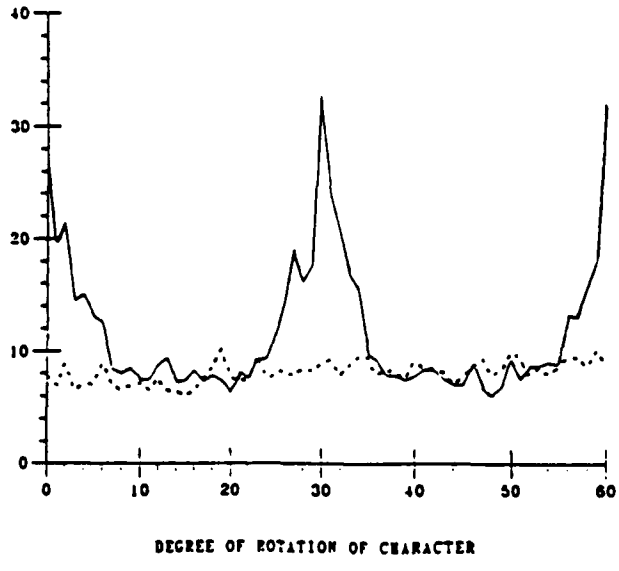

Figure 3. The SNR of the correlation spot as a function of the degree of rotation of the letter "R" (solid line) and the letter "X" (dotted line).

3. Circular Harmonic Phase Only Joint Transform Correlator

It is possible that circular harmonic filters[3] may be implemented in a joint transform correlator. A reference image expressed in polar coordiante $f(r,\theta)$ can be decomposed into circular harmonics :

$$f(r,\theta) = \sum_{M=-\infty}^{+\infty} f_M(r) e^{jM\theta}, \tag{1}$$

where

$$f_M(r) = \frac{1}{2\pi} \int_0^{2\pi} f(r,\theta) e^{-jM\theta} d\theta. \tag{2}$$

If we select only a single harmonic reference

$$f_r(r,\theta) = f_M(r) e^{jM\theta}, \tag{3}$$

rotational-invariant correlation can be obtained. The binarized phase factor of Eq. (3) may be constructed as a binary phase only filter using a LCTV.

4. Concluding Remarks

We have proposed two rotationally invariant joint transform correlation techniques in this paper. We note that the joint transform correlator has advantages such as : simplicity in reference generation and lower resolution requirements, which are very suitable for electronically-addressed low resolution spatial light modulators such as LCTVs.

Acknowledgment

This research is partially supported by the U.S.Army Missile Command through the U.S.Army Research Office, contract number DAAL03-87-0147.

References

1. See, for example, G. F. Schils and D. W. Sweeney, "Rotationally invariant correlation filtering," *J. Opt. Soc. Am. A.* **2**, 1411 (1985), and references therein.
2. F. T. S. Yu, S. Jutamulia, T. W. Lin and D. A. Gregory, "Adaptive real-time pattern recognition using a liquid crystal TV based joint transform correlator," *Appl. Opt.* **26**, 1370 (1987).
3. Y. N .Hsu and H. H. Arsenault, "Optical pattern recognition using circular harmonic expansion," *Appl. Opt.* **21**, 4016 (1982).

DYNAMIC INTERCONNECTIONS WITH A LENSLET ARRAY AND AN SLM

I. Glaser and A. A. Sawchuk

Signal and Image Processing Institute
University of Southern California
University Park, Mail code 0272
Los Angeles, CA 90089-0272

INTRODUCTION

A digital circuit can be implemented with a global linear transformation and a point non-linearity. Several suggestions, and a few experimental demonstrations, have shown that, by using optics to implement the global transformation part, hybrid opto-electronic digital processors can be built **(1,2)**. Though such hybrid systems are still limited by the switching time of the electro-optical or electronic point-non-linear part of the system, their overall throughput can benefit from the inherent parallelism of lightwave communication, particularily when a free-space, three dimentional, optical configuration is being used; unlike conventional electronic gate-arrays, these hybrid opto-electronic ones have no "design rules" that limit the complexity and generality of their interconnections.

Another type of system that can be described in terms of a linear-transform/point-non-linearity cascade (or several such stages) is an artificial neural network **(3)**. Again, all-electronic implementations of neural networks have been demonstrated; however as the number of the "neurons" increases it becomes more and more difficult to use electronic communications; optical (or an opto-electronic hybrid) neural network becomes the prefered solution.

For both the gate array system and (a single stage of) an artificial neural network, the relation between the inputs $f_{j,k}$ and outputs $F_{l,n}$ of the system is given by

$$F_{l,m} = P\left\{\sum_{j,k} f_{j,k}\, K(j,k;\, l,m)\right\} \tag{1}$$

where $P\{...\}$ is a point-non-linearity and $K(j,k;\, l,m)$ is a linear transformation kernel **(1,3)**.

For gate arrays, $P\{...\}$ can be a simple step function. For example, to implement an array of NOR gates, $P\{a\} = 1$ if $a < 0.5$ and equals 0 otherwise. Here, the kernel K is a list of interconnections; $K(j,k;\, l,m)$ is set to one if the output of the (j,k)-th gate is to be connected to the input of the (l,m)-th gate; all non-connected terms of K are set to zero.

For a neural network, $P\{...\}$ is the neuron threshold function, and the terms of $K(j,k;\, l,m)$ are the network interconnection weights.

It is clear from the form of the kernel K in Eq. (1) that any general optical implementation that has 2-D input and output arrays must provide a four-dimentional transform kernel. Since real space is limited to three dimensions, this kernel must be implemented by some form of multiplexing **(4)**. Multiplexing can be done by holography; one may use, for example, multi-facet holograms or volume holograms. However, changing and re-writing complex holgrams dynamically is very difficult. In this work we discuss an

alternative tool: the lenslet array.

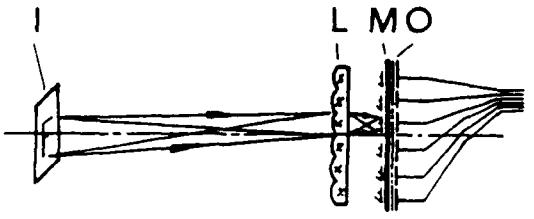

Figure 1: A lenslet array processor. I is the input plane, L is the lenslet array, M is the mask and O is the output plane. From ref. (5).

LENSLET ARRAYS

The use of a lenslet array for (analog) 2-D linear transformations is depicted in Figure 1. The lenslet array *(L* in Figure 1*)* forms multiple images of the input *(I)* spatial signal. Each of these images is precisely indexed with the appropriate transparency of one base function of the transformation kernel on the mask *(M)*. Thus, the total amount of light that gets through the mask from a lenslet located at coordinates (l,m) is proportional to the transformed term $\sum_{j,k} f_{j,k} K(j,k; l,m)$.

When this lenslet array processor is combined with some electro-optical device that provides point-non-linearity, and, possibly, with mirrors and beam-splitters that allow feed-back and convenient I/O, we can obtain a sequential-logic circuit (2) or an iterative artificial neural network.

It is useful to have such systems with *dynamic* reconfigurability. Conventional digital processors can be adapted to new tasks by programming, breaking the desired operation into many small operations which are then performed sequentially. We can envision, however, a different type of processing circuit whose function can be changed by changing its own geometry: reconfiguring the interconnections so that the specific problem is solved in few processing cycles. This reconfigurable circuit combines the flexibility of programmable CPUs with the speed of hard-wired logic.

For neural networks, the desirability of flexible interconnections, or weights, is widely recognized. It is a basic building block for *learning* artificial neural networks.

To obtain dynamic reconfigurability we use a spatial light modulator (SLM) as the mask. If a transmitting SLM is available, the configuration of Figure 1 can be used. However, most light-addressed SLMs are reflective; for these we must use an alternative configuration. In the example shown in Figure 2 light from the output, right, surface of the *non-linear device* is imaged by the *lenslet array* onto the surface of the *spatial light modulator* that serves as a mask. Light that hits "on" points at the SLM is reflected; it is imaged, through the *beam splitter*, *mirrors* and the *imaging lens* to the input, left, side of the *non-*

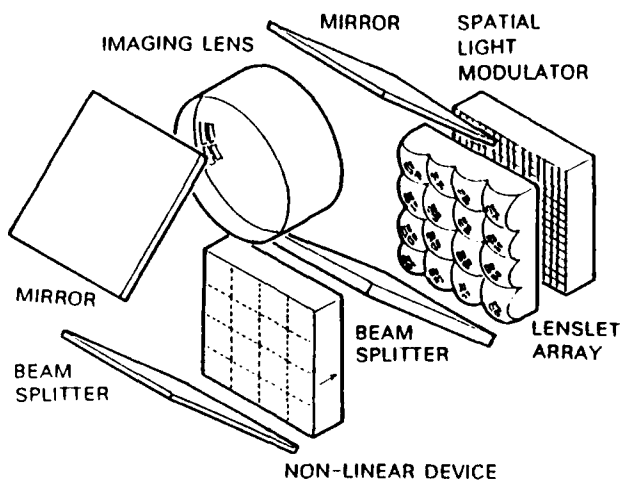

Figure 2: A lenslet array based processor with a reflective SLM mask

linear device. After going through a point-non-linear transformation, light reenters the optical system. The system input and output can be done optically throgh the *beam splitters*. For the non-linear device we may use any device that provides the desired point non-linearity, such as a second SLM or an array of LEDs on one side, photo-diodes on the other and drive (and usually invert) circuits in between.

Performance considerations

The potential performance of lenslet array processors have been discussed at length elsewhere **(6,7)**. Limiting factors include optical aberrations and diffraction, mechanical error in the mask/lenslet-array alignment and errors in the mask. Only the last item is affected by the use of an SLM as the mask. As seen in Figure 2, if we allow interconnection of each gate to any other (or the same) gate, each lenslet must image the entire array. Thus, if our array (the non-linear device *and* the lenslet array) is of size $N \times N$, the SLM mask must resolve at least $N^2 \times N^2$ points. This poses rather severe demands on the spatial resolution f_{SLM} of the SLM

$$f_{SLM} > \frac{N}{q} \tag{2}$$

where N is the number of lenslets in the array in each dimension and q is the pitch of the lenslet array, Also, the linear space bandwidth product must be higher than N.[2]

Another problem, is that of undesired light in the system. If an "off" pixel at the SLM is $1/r$ times as bright as an "on" pixel, it is possible that enough light will be accumulated from r "off" pixels to confuse the system to "think" that there are one or more extra "on" pixels, resulting in an erronous output. The number of SLM pixels that each lenslet sees, which equals the number of gates in the system, N.[2] This number must be lower than r, hence

$$N < \sqrt{r} \tag{3}$$

CONCLUDING REMARKS

We saw how the combination of a spatial light modulater and a lenslet array can produce a dynamically reconfigurable, hence programmable, optical processor that can be used as a logic gate array or an artificial neural network. No alternative optical system offers similar ease in converting new specifications for interconnections into physical interconnections in real time. Though the demands on the SLM in this system are rather high, and can be satisfied with available SLMs only for a modest number of gates or neurons, we expect that with the coming new generation of SLMs, larger space bandwidth product and better extinction ratio (dynamic range) would allow large reconfigurable lenslet array processors which would become valuable as optical processing tools.

REFERENCES

(1) Chavel, P. H., Forchheimer, R., Jenkins, B. K., Strand, T. C. and Sawchuk, A. A., "Architectures for a Sequential Optical Logic Processor," pp. 6-12 in *Proceedings of the 10th International Optical Computing Conference*, ed. Caulfield, H. J., (IEEE Computer Society Press, Silver Spring MD, 1983).

(2) Glaser I. and Perelmutter L., "Optical Interconnections for Digital Processing: A NonCoherent Method," Optics Letters **11**, 53-55 (1986).

(3) Farhat, N. H., Psaltis, D., Prata, A. and Paek, E., "Optical Implementation of the Hopfield Model," Applied Optics **24**, 1469-1475 (1985).

(4) Glaser, I., "Lenslet-Mask-Array Devices: A Noncoherent Alternative to Computer-Generated Holograms?," in: *Optical Society of America Annual Meeting* Tucson, Az., USA, October 1982; abstract: Journal of the Optical Society of America **72**, pp. 1751a (1982).

(5) Glaser, I., "Non-Coherent Parallel Optical Processor for Discrete 2-D LinearTransformations," Optics Letters **5**, 449-451 (1980).

(6) Glaser, I., "Information Processing with Spatially Incoherent Light," pp. 389-509 in *Progress in Optics* **XXIV**, ed. Wolf, E. (North Holland, Amsterdam, 1987).

(7) Perelmutter, L. and Glaser, I., "Digital Incoherent Optical Interconnections," pp. 215-220 in *Proceedings of the 1986 International Optical Computing Conference*, Proc. SPIE **700** Ed. Shamir, J. (SPIE, Bellingham Wa., 1986).

Real-time Object Recognition and Classification by Code Division Multiplexed Phase-only Encoded Filters, B. Javidi and S. F. Odeh, Michigan State University, Department of Electrical Engineering, East Lansing, Michigan, 48824

Abstract.

A multiobject shift invariant pattern recognition system that uses Code division multiplexed binary phase-only filters is presented. The system computes the binary correlation between an input pattern with a generalized set of pattern functions. This technique uses a filter which consists of a set of binary phase-only code division multiplexed reference pattern functions. The functions in the reference set may correspond to either different objects or different variations of the object under study. In the proposed architecture, the position of the output binary correlation peaks represent the locations of the objects in the input plane. This is different from phase coded pattern recognition systems in which the location of the output peak determines the class of the input object[+]. Here, the system is shift invariant and multiple objects can be present at the input plane. The pattern recognition is performed without increasing the space-bandwidth product requirements of the system. Computer simulations of the architecture are also used to study the performance of the pattern recognition architecture. The signal-to-noise ratio (SNR), and the peak to the maximum correlation sidelobe ratio (P/SL) are evaluated as the criteria for the system performance.

Here, we intend to store a number of binary phase-only filters by using multiplexing techniques. Each binary phase-only filter is multiplexed by a corresponding m-sequence binary code. The matched filter is the superposition of the m-sequence code multiplexed submatched filters. This is similar to code division multiplexing in multiple-access spread spectrum communications systems where a number of different signals are supposed to use the same bandwidth simultaneously. These systems usually employ quasi-orthogonal functions such as m-sequence binary codes for multiplexing. For example, if two codes, which are assigned to two different channels, are added and sent over the same bandwidth, the receiver can accept one code and reject the other by correlation techniques.

[+] J.R. Leger and S.H. Lee, *Applied Optics*, Vol. 21, 274 (1982).

The pattern recognition system employing multiplexed binary phase-only filters is shown in Fig. 1. The system L is an optical processor where the inputs to the system are the objects under investigation $f_i(x,y)$ and the outputs of the system are the convolution between the input signals $f_i(x,y)$ and the m-sequence codes $m_i(x,y)$ assigned to the i^{th} input signal. The output signals are Fourier transformed which yield the Fourier transform of the input signal modulated by the Fourier transform of the corresponding m-sequence code. Mathematically, this can be written as:

$$f_i(x,y) * m_i(x,y) \xrightarrow{F.T.} F_i(\alpha,\beta)\, M_i(\alpha,\beta), \qquad (1)$$

where (α,β) are the spatial frequency coordinates, * denotes convolution, and $F_i(\alpha,\beta)$ and $M_i(\alpha,\beta)$ correspond to the Fourier transforms of $f_i(x,y)$ and $m_i(x,y)$, respectively.

The code modulated Fourier transform of the input signal is applied to a code division multiplexed binary phase-only filter located at plane P_2. This filter is synthesized by evaluating the binary phase-only filter for the reference objects when modulated by the corresponding spread spectrum code. The process is repeated for each input signal and the submatched filters are added linearly to produce the filter. This can be expressed mathematically for the input signals as:

$$H_{BPOF}(\alpha,\beta) = \begin{cases} +1\,; & \text{if } \mathrm{Re}\sum_{i=1}^{N} H_i(\alpha,\beta) \geq 0 \\ -1\,; & \text{otherwise,} \end{cases} \qquad (2)$$

where $H_i(\alpha,\beta)$ is the submatched filter for each multiplexed reference signal defined as:

$$H_i(\alpha,\beta) = F_i^*(\alpha,\beta)\, M_i^*(\alpha,\beta). \qquad (3)$$

The operation of the proposed system can be understood by applying an input signal convolved with the corresponding code to the above filter. The resultant light field leaving the filter plane is given by:

$$T(\alpha,\beta) = F_i(\alpha,\beta)\, M_i(\alpha,\beta)\, H_{BPOF}(\alpha,\beta), \qquad (4)$$

where $T(\alpha,\beta)$ represents the light field leaving the filter plane. The output correlation distribution at plane P_3 is the inverse Fourier transform of $T(\alpha,\beta)$ taken by lens L_2.

Computer simulations of the multiple image correlator described above are presented. The simulations are carried out using a 128x128 point 2-D fast Fourier transform (FFT), and the results are plotted by a 3-D plotting subroutine. The correlation tests are performed for the letters A, F, J, N, Z, β, γ, λ, π, and ψ as reference objects. The code division multiplexed binary phase-only filter is synthesized to detect the above reference objects using a set of ten quasi-orthogonal spread spectrum codes. The results of the computer simulations are shown in Table I. Figure 2 shows the output correlation intensity for 128x128 bit code division multiplexed binary phase-only filter when the input signal β is used.

TABLE1*. Results of Computer Simulations.

	Code Division Multiplexed Classical Matched Filter		Code Division Multiplexed Phase-only Filter		Code Division Multiplexed Binary Phase-only Filter	
Input	SNR	P/SL	SNR	P/SL	SNR	P/SL
A	5.35	2.90	19.43	17.79	17.96	23.23
F	7.87	4.65	17.70	19.62	16.40	14.39
J	6.72	3.34	15.74	12.47	14.95	11.06
N	7.16	3.92	17.53	13.93	17.44	19.17
Z	4.81	2.12	18.74	13.73	17.03	25.85
β	4.07	2.16	21.77	34.43	21.37	29.58
γ	5.15	2.12	21.85	29.27	21.81	30.44
λ	6.52	4.53	22.14	23.58	21.68	25.88
π	5.30	2.47	23.08	32.94	21.75	20.78
ψ	7.13	4.34	22.88	34.55	23.78	31.82

* SNR is the signal-to-noise ratio. P/SL is the ratio of the correlation peak intensity to the maximum correlation sidelobe intensity.

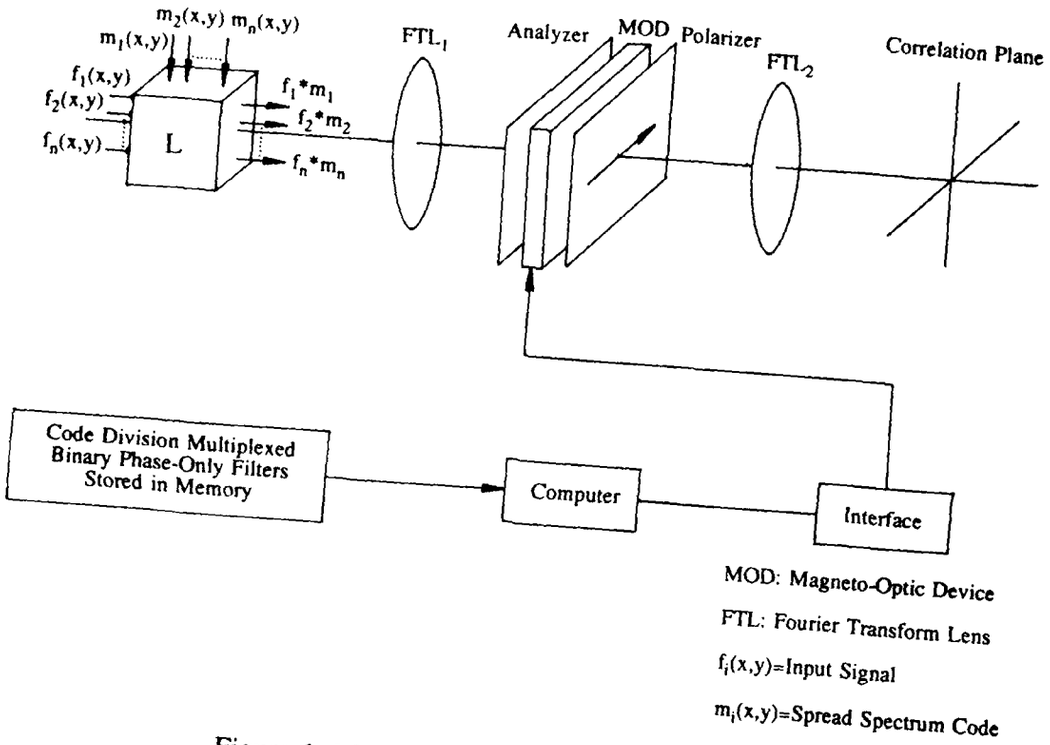

Figure 1. Multiple Image Optical Correlator.

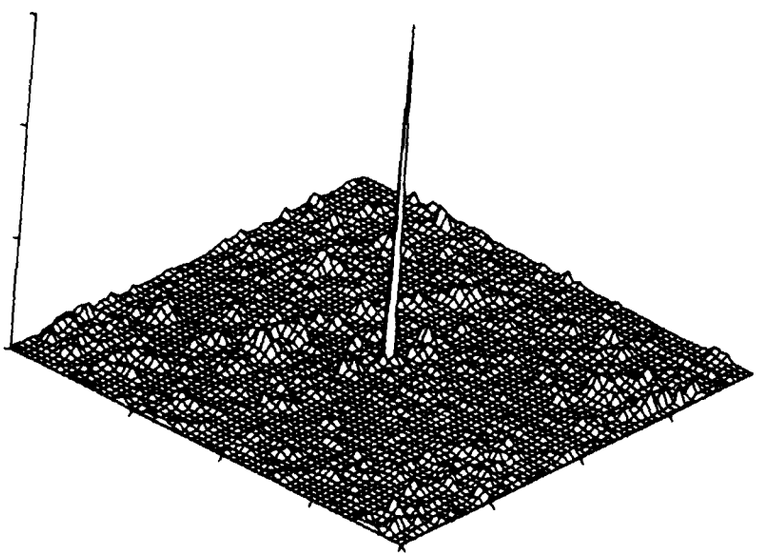

Figure 2. The output correlation intensity for 128x128 bit code division multiplexed binary phase-only filter when the input signal β is used. Ten multiplexed reference signals were used to synthesize the filter.

SPATIAL LIGHT MODULATORS IN MULTIMODE FIBERS

Mahmoud A. El-Sherif
Air Defence College,
Alexandria, Egypt.

ABSTRACT

An external field applied to a **modified multimode fiber** induces modal power redistribution. This technique is examined for **spatial light modulators** , and promising results are obtained.

INTRODUCTION

There has been a growing interest in fiber optic devices fabricated on or arround the fiber. Such devices involve removal of cladding over a small length of the fiber and replacing it with a sensitive medium like electrooptic, magnetooptic, or dye material.[1-3] In this paper, an electrooptic material is used as an active cladding, and the device is employed as spatial light modulator. The principle of this device, shown in fig.1, is explained elsewhere.[3-5] In short, when a field is applied, to the modified cladding, the index of refraction increases, leading to modal coupling, and results in modal power redistribution. This modal coupling has been investigated theoretically and experimentally. The analysis results in a matrix formula which gives the complex amplitudes of the modal fields in terms of the perturbation in the active region. For experimental investigation, the modal power redistribution, i.e. the spatial modulation, is examined by a very fine scanning of the far-field pattern at the output end of the fiber.

THEORETICAL ANALYSIS

In this analysis, the wave theory approach and the continuity equations are used at the input and output of the active region (at z=-d and z=0) for the evaluation of the modal fields, shown in Fig.2, and the results are,

at z=-d

$$\sum_{n=1}^{N} \left[b_n e^{+j\beta_n d} - c_n e^{-j\beta_n d} \right] e_n = \sum_{s=1}^{S} \left[f_s(\Delta n)\, e^{+j\beta'_s(\Delta n)d} - g_s(\Delta n)\, e^{-j\beta'_s(\Delta n)d} \right] E_s(\Delta n) \qquad (1)$$

and at z=0

$$\sum_{n=1}^{N} a_n e_n = \sum_{s=1}^{S} [f_s(\Delta n) - g_s(\Delta n)] E_s(\Delta n) \qquad (2)$$

where b_n and c_n are the complex amplitudes of the n-th forward and backward modes, respectively, and N is the total number of modes in region I. β_n is the eigenvalue of the n-th mode and e_n and h_n are the orthonormal eigenfunctions representing the various modes in Region I. Furthermore, S is the total number of propagating modes in the active region, $f_s(\Delta n)$ and $g_s(\Delta n)$ are the complex amplitudes of the S-th forward and backward modes, respectively, and are a function of the electrooptic effect, i.e. Δn, of the active material. $E_s(\Delta n)$ and $H_s(\Delta n)$ are the transverse fields of the S-th mode for a complete set of orthonormal functions. $\beta'_s(\Delta n)$ is the complex propagation constant of the S-th mode. This propagation constant is a function of the electrooptic effect in the acttive region. a_n is the complex amplitude of the n-th mode in region III. The expressions for the magnetic fields are similar to equations 1 and 2. A complete analysis concerning the complex propagation constants for guided and radiative modes is discussed in a different paper.[6] Using these field equations, the output modal amplitude a_n is derived in terms of the input modal amplitudes and the electrooptic effect of the active material, this results in a general matrix form, as

$$[a]_{nx1} = [B(\Delta n,d)]_{nn} [b]_{nx1} + [C(\Delta n,d)]_{nn} [c]_{nx1} \qquad (3)$$

where, n=1,2,...,N, $[a]_{nx1}$ are the output modal amplitudes in region III at z=0, and $[b]_{nx1}$ and $[c]_{nx1}$ are the input modal amplitudes for the incident and reflected waves at z=-d, respectively. $[B(\Delta n,d)]_{nn}$ and $[C(\Delta n,d)]_{nn}$ are the coupling coefficients of the input forward and backward modal amplitudes to the output modal amplitudes, respectively. These coefficients are functions of the perturbation of refractive index. The theoretical analysis shows the redistribution of the output modal fields, i.e. the spatial modulation of interference pattern at the end of the fiber. This spatial modulation will depend on the external applied field.

EXPERIMENTAL INVESTIGATION

A He-Ne laser is used to fill a limited number of modes of a multimode fiber. The nominal indices of this fiber are n_{co}=1.6 and n_{cl}=1.48. A nematic liquid crystal (NLC), having n_o=1.4962 and n_e=1.617, is used as a modified cladding. To scan and display the far-field radiation pattern, a computer-controlled, three-dimensional micro-positioner is used, as shown in Fig.3. The detected far-field pattern in the absence and presence of an external dc field is shown in Fig.4. The applied field redistributes the modal power, causing a significant coupled-mode-power. Consequently, the shape of the interference pattern in the far-field is changed.

The results are qualitatively in agreement with the theoretical analysis. In addition, because the electrooptic effect of the NLC is the result of the anisotropic polarizability of its molecules, the polarization sensitivity of the device is being investigated. Further more, the experiment was repeated several times and the consistency of the stability of the far-field pattern was verified. Therefore, this technique can be employed for sensitive applications. For real time informations, the interference pattern can be detected by using a CCD (video) camera, or two dimensional array of sensors.

CONCLUSION

A new technique that turns part of a **multimode fiber** into a **spatail light modulator** is presented. Additional work is needed to optimize the results and investigation for possible future uses.

REFERENCES

1. M. El-Sherif and J. N. Zemel, "Twisted Pair Optical Fiber pH Sensors," IEEE, Third Int. Conf. on Solid-State Sensors and Actuators, Philadelphia, Pennsylvania, 1985, Tech. Digest, pp.434-437.
2. M. El-Sherif, P.M. Shankar, P.R. Herczfeld, L. Bobb and H. Krumboltz, "On-Fiber Electrooptic Modulator/Switch," Appl. Opt., Vol. 25, No. 15,1 August 1986.
3. Mahmoud A. EL-Sherif, "On-Fiber Sensor and Modulator," CPEM'88 Conf., Japan, June 1988, will be presented.
4. M. El-Sherif, P.M. Shankar, P.R. Herczfeld, L. Bobb and H. Krumboltz, "An Optical Fiber Electro-Optic Modulator," Fiber/LASE 86, SPIE Conference, September 1986.
5. M. El-Sherif, P.M. Shankar, P.R. Herczfeld, L. Bobb and H. Krumboltz, "An On-Fiber Active Transducer," IEEE, Fourth Int. Conf. on Solid-State Sensors and Actuators, Tokyo, Japan, 1987, Tech. Digest, pp.200-203.
6. M. El-Sherif, " Multimode Fibers For Spatial Modulation ," in process.

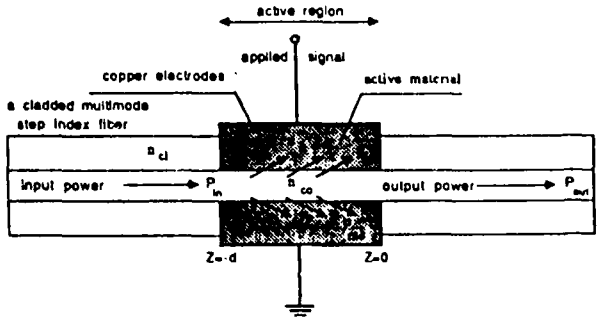

Fig.1. The principle of SLM in optical fiber.

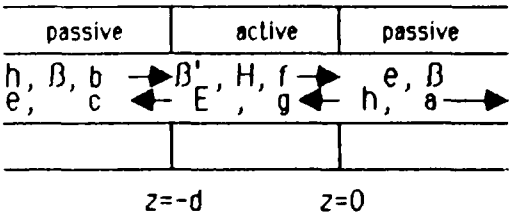

Fig.2. The multimode device geometry.

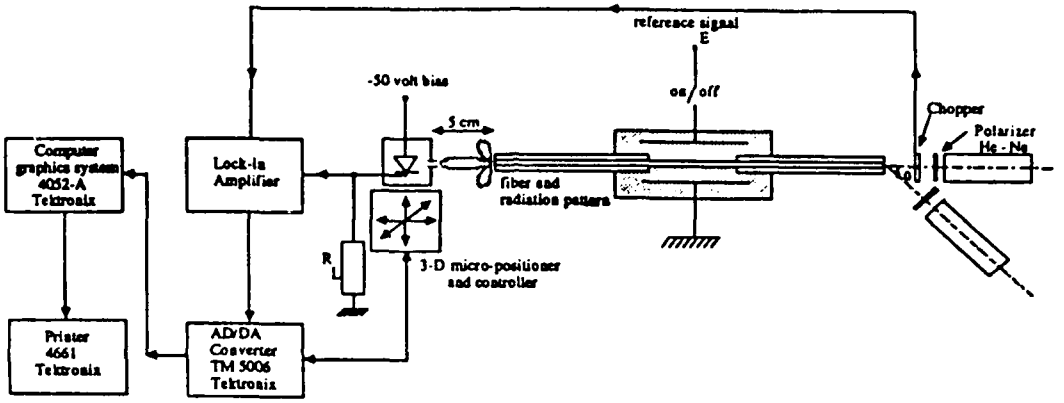

Fig.3. The experimental setup used for scanning the spatial redistribution of the far-field pattern.

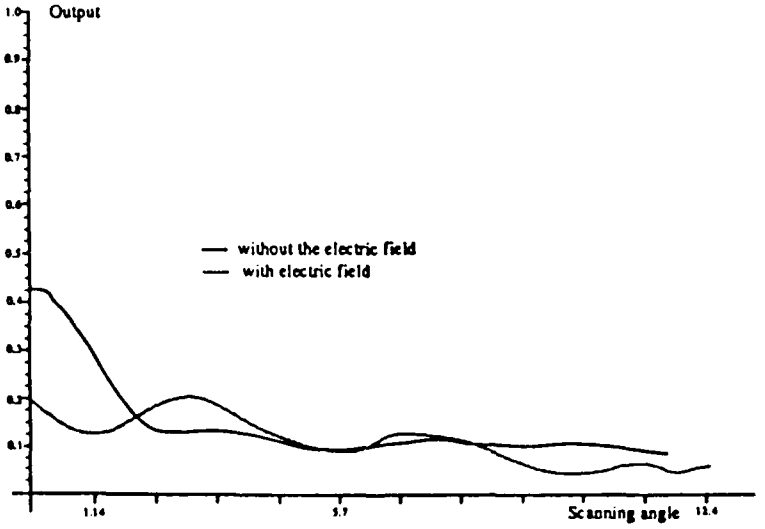

Fig.4. The spatial modulation of the far-field pattern as a result of the applied field.

Optical Pattern Recognition using an Optically Addressed Spatial Light Modulator.

Janine M. Vaerewyck
Department of Physics
University of Alabama in Huntsville

H. John Caulfield
Center for Applied Optics
University of Alabama in Huntsville
Huntsville, AL 35899

Introduction

The purpose of this paper is to discuss the first results of a continuing study on the use of a Spatial Light Modulator in a pattern recognition system. The specific SLM that is being studied was built by Lockheed Missiles and Space Company Inc. of Palo Alto Ca.[1] and is on loan to the University of Alabama in Huntsville. This SLM, an optically addressed device, is being used as a spatial filter in a pattern recognition system. The results of a computer study into the most advantageous use of the SLM will be presented as well as the experimental test plan that has been devised from these results.

Theory

The experimental system is shown in Figure 1. Parallel light will enter the system from the right. L1 will focus this light at the SLM. An object transparency will be placed between L1 and the SLM to enable the size of the fourier transform to be easily controlled. The SLM will be optically addressed from the opposite side using a page oriented hologram on which the fourier transforms of the input objects will be stored. In this configuration all phase information will be lost and the SLM will act as an addressable soatial filter. After reflecting off the SLM, the input beam will retrace its path to a beam splitter. The beam will then pass through L2 and be reconstructed in the output plane. One should note that this system is much like a basic spatial filter system such as that discussed by Goodman[2].

If an object is input to this system and the fourier transform of that object is used to optically address the SLM, an unaltered image of the object will be seen in the output plane. If the same object is input to the system and a different fourier transform is used to address the SLM, a distorted image of the input object will be observed in the output plane. In this way this system can be used as a pattern recognition system.

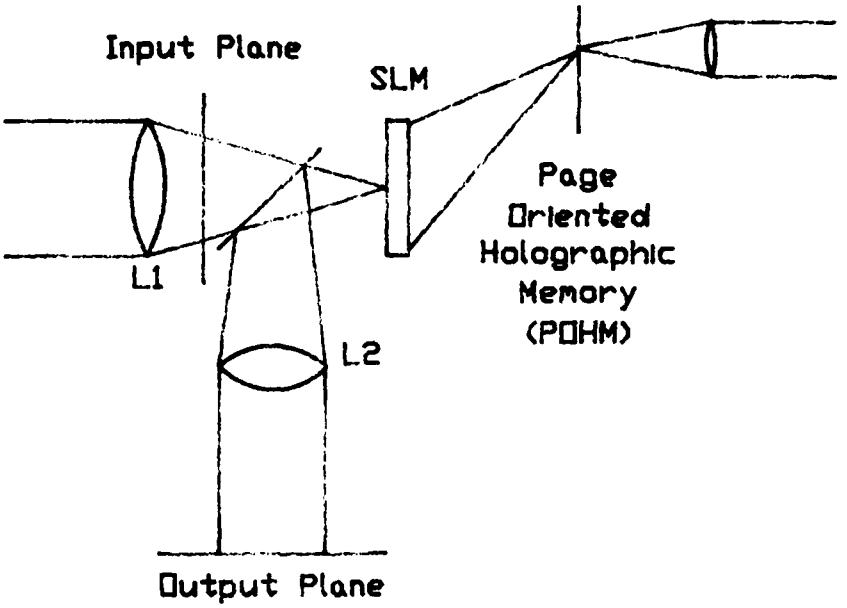

Figure 1.

The concern of this study is to determine the best use of the SLM in this system. Three main areas are being explored. First the positioning of the input fourier transform on the SLM. There is expected to be a best orientation of the input transform. This orientation depends not only on the SLM but on the input object itself. Second the size of the input transform is being considered. Once again both the SLM and the image are taken into account. As stated above, the variation of the size of the transform is simply performed in this system. Lastly, the feasibility of inputting more than one transform of the same object to the system is being explored. This can be accomplished using a grating placed between the input object transparency. This grating will have to be designed for each input object and each SLM.

In order to study this system more efficiently a computer study is being conducted. The SLM is being modeled as a binary phase only filter using the techniques described by Psaltis et al[3]. A Fast Fourier Transform program is being used to perform the required transformations. The effect of having a SLM that is not continuous has been studied to allow comparison of continuous and noncontinuous SLMs. As expected noncontinuous modeled SLMs give much more distorted results than continuous modeled SLMs. Arsenault and Bergeron[4] described a method of recording the complex phase and amplitude of the fourier transforms in computer generated holograms. Using superpixels, consisting of many individual pixels, a computer generated hologram can be written that they report has improved quality and has phase accuracy of better than $\pi/4$. This technique may be used to construct the page oriented hologram that will be used to optically address the SLM.

Conclusions

From the results of this study a test plan will be devised that will thoroughly explore the capabilities of the SLM in the system. The results of this study will also be used to begin the initial design of the page oriented hologram that will be used to address the SLM. Initial lab experiments will be conducted using a much simpler version of this device.

Acknowledgement

This work is being done with support from Lockheed Missiles and Space Company Inc. Reaserch and Development division under the contract titled Fast Spatial Light Modulators(SD-PA-D 6730F).

References

1. D. Armitage, W. W. Anderson, and T. J. Karr, "High-Speed Spatial Light Modulator," IEEE J. Q. E. QE-21, 1241-1248 (1985).

2. J. W. Goodman, *Introduction to Fourier Optics* (McGraw-Hill Co., New York, 1986)

3. D. Psaltis, E. G. Paek, and S. S. Venkatesh, "Optical Image Correlation with a Binary Spatial Light Modulator," Opt. Eng. **23**, 698 (1984).

4. H. H. Arsenault, and A. Bergeron, "Recording Binary Holograms on Small Supports for Pattern Recognition," O-E Lase 88,Los Angeles, 10-15 January 1988, paper21 SPIE Proceedings **884** (in press).

FRIDAY, JUNE 17, 1988

EMERALD BAY BALLROOM

8:30 AM–9:50 AM

FA1–4

APPLICATIONS: 1

Uzi Efron, Hughes Research Laboratory, *Presider*

Optical Matrix-Vector Multiplication Using a Spatial Light Modulator and a Phase Conjugator

Arthur E. Chiou, Pochi Yeh, and Monte Khoshnevisan
Rockwell International Science Center
1049, Camino Dos Rios
Thousand Oaks, CA 91360
Tel: (805) 373-4464

SUMMARY

A variety of optical matrix processing schemes [1, 2] use two-dimensional spatial modulation of optical intensity to represent a matrix to exploit the inherent parallel nature of optics. Such an approach typically requires the projection of a spatial pattern to match another pattern to perform the element-by-element multiplication. The basic incoherent matrix-vector multiplication scheme [3], for example, requires the use of anamorphic optics to project a linear array of sources (or a one dimensional spatial light modulator) to precisely match a two dimensional matrix masks. In the matrix-vector multiplication scheme using four-wave mixing in nonlinear media [4], simultaneous alignment of all the pixels of the matrix and vector is a major task, particularly for a large number of pixels. Misalignment of the pixels may lead to severe errors. For a given size of matrix mask, the density of elements increases as the dimension (N) of the matrix increases. As a result, the requirement on alignment becomes more and more stringent. In practice, the critical alignment required is likely to impose a practical limit on the optimum dimension of the matrix (N) to be of the order of one hundred or less depending on the specific architecture.

In this paper, we report a new scheme for optical matrix-vector multiplication that uses a phase conjugator (with a finite storage time) in conjunction with a spatial light modulator (SLM) to eliminate the pixel-by-pixel alignment requirement at the cost of some reduction in parallelism ($N^2/2$ instead of N^2). Phase aberration due to imperfection in optics is also self-corrected by the phase conjugation process. The optical system involved is relatively

simple compared with the other approaches. Without any modification, such a scheme can also perform matrix-matrix multiplication with $N^2/2$ parallelism.

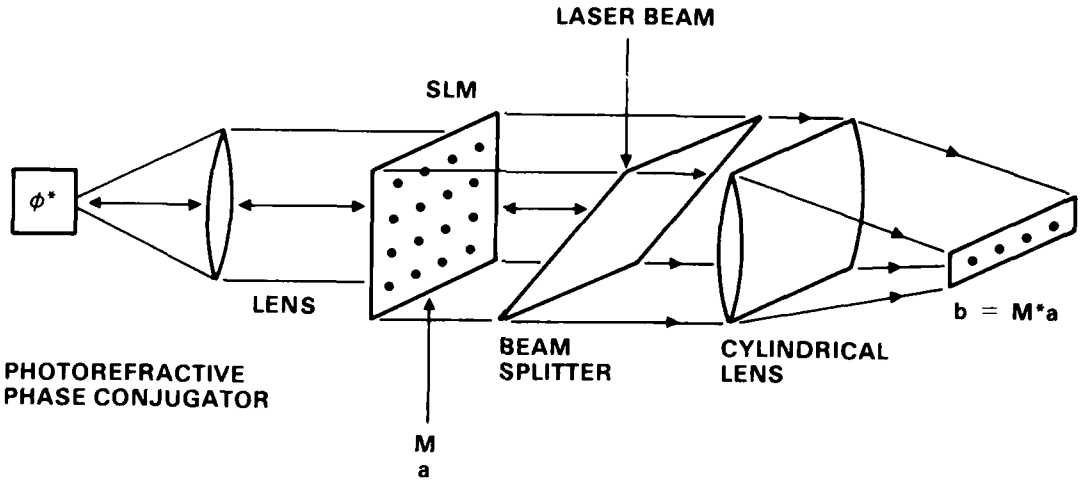

Fig.1 A schematic diagram illustrating the basic concept of optical matrix-vector multiplication using a photorefractive phase conjugator in conjunction with a spatial light modulator.

Referring to Fig.1, we use a SLM to impress the matrix and vector information in sequence to an input laser beam. This beam is directed toward a phase conjugator which has a finite storage time (a photorefractive barium titanate, for example). A cylindrical lens is inserted in the phase conjugate output beam path to perform the summation.

The principle of operation is as follow. the SLM first impresses the matrix information onto the input laser beam. This beam is then incident into a phase conjugator which stores the matrix information after a finite grating formation time. When the matrix information is removed from the SLM, say by turning all the pixels into maximum transmission condition, the phase conjugate beam which contains the reconstruction of the matrix information exists for a finite duration. This finite storage time depends on the strength of the input (read) beam. During this time, if the next frame of the SLM carries the vector information, parallel multiplication is performed as the phase conjugate beam propagates back through the SLM. Here the vector is represented as a two-dimensional array of N identical column vectors, where N is the dimension of the vector. A cylindrical lens in the output port is used to perform the

summation. The dark storage time during which the matrix information can be retrieved is determined by the photorefractive material and the pumping configuration. It ranges from seconds to microseconds.

The system can also perform matrix-matrix multiplication by time multiplexing. In this case, each column vector V_i (i=1 to N) which constitutes the second matrix M_2 is sequentially impressed onto the beam to multiply with the first matrix M_1 according to the matrix-vector multiplication scheme described above. To avoid the degradation of the information of M_1 stored in the photorefractive hologram during the readout, it is necessary to refresh the holographic memory with M_1 to restore its diffraction efficiency. This can be done by re-impressing M_1 onto the beam after each readout cycle. Consequently, a total of 2N clock cycles, consisting of N cycles of write and N cycles of read, will be required to carry out the multiplication of two NxN matrices.

Using a photorefractive barium titanate crystal as a phase conjugator in conjunction with a 48x48 magneto-optic spatial light modulator (SIGHT-MOD SMD48I from Semetex Corp.), we have demonstrated the basic principle described above. Preliminary experimental results will be discussed. Some advantages and disadvantages of this approach will be compared with those of the others.

This work is partially supported by DARPA/AFOSR contract No.F49620-87-C-0015.

REFERENCES:

[1] R. A. Athale, "Optical matrix processors," in Optical and Hybrid Computing, H. H. Szu, Ed., SPIE Vol. 634, 96-111 (1986).

[2] W. T. Rhodes, "Optical matrix-vector processors : basic concepts," in Highly Parallel Signal Processing Architecture, SPIE Vol. 614, 146-152 (1986).

[3] J. W. Goodman, A.R. Dias, and L. M. Woody, "Fully parallel, high-speed incoherent optical method for performing discrete Fourier transforms, " Opt. Lett., **2**, 1-3 (1978).

[4] P. Yeh and A. E. Chiou, "Optical matrix-vector multiplication through four-wave mixing in photorefractive media," Opt. Lett, **12**, 138-140 (1987).

Optical Associative Memory for Word-break Recognition, Eung Gi Paek and A. Von Lehmen, Bell Communications Research, 331 Newman Springs Road, Red Bank, New Jersey 07701

In this paper, we describe a novel associative memory based on a coherent optical correlator which is able to identify individual words in a continuous string of letters. The output is readable text : a series of words with spaces inserted between them. The system is shift invariant and has error correction capability.

The following sentence shows an example of a concatenated word stream, illustrating the word-break problem raised by Tank and Hopfield[1].

TEXTREEDINGWITHAUTWORDBRECKSMAYBEKAMEDIFFICOLT

Without spaces between words, it is difficult to decipher the text. The task becomes even more difficult if the continuous word stream contains errors. The system which can decipher the word stream must be able to recognize words, correct errors in them and insert spaces between them.

Obviously, word-break recognition requires shift invariant pattern recognition. To achieve shift invariant pattern recognition in recent neural network models, all shifted versions must be stored separately. However, coherent optical correlators can perform this task simultaneously and in a parallel fashion due to the shift invariant property of the Fourier spectrum which can be easily obtained by a simple lens.

The principle of optical word-break and error correction system is schematically shown in Figure 1. The system is a modified version of the holographic associative memory originally developed at CALTECH[2]. The memory words are stored in a conventional Fourier transform hologram. All of the memories to be stored are arranged in a column spatially separated along the y direction (perpendicular to the word direction). The Fourier spectrum of all the memories interferes with a single tilted plane wave to simultaneously make a multiple hologram at the focal plane of the lens L_1.

For the word-break recognition, the input word stream is presented at the plane P_1 of an optical VanderLugt correlator. The correlation peaks appear at the corresponding positions of

the correlation plane P_3. These correlation peaks are detected after threshold and are anamorphically imaged so that the separation between the peaks is magnified along the x direction(word direction) only. This can be achieved either by the anamorphic lens system which consists of the two cylindrical lenses or by electronically adjusting the horizontal scale of the video monitor. These bright spots are reflected back to illuminate the hologram again. Light emerging from the hologram reconstructs all memory words at the output plane P_4 which is situated at the symmetric position of the input plane with respect to the beamsplitter. The reconstruction due to light from each bright spot is the entire word memory shifted by the position of the pinhole. At the origin of plane P_4, a window is placed to select only the desired central portion of the reconstructed images, which is the corrected version of the original input with spaces between words.

Figure 2 shows the experimental results. The four words used as the memories in this experiment are shown in Figure 2(a). The correlation output for the concatenated input with errors as in (b) are shown in (c). The sharp autocorrelation peaks appear at the corresponding positions of the filter along the y direction and are shifted according to the positions of the input along the x direction. Also, the sidelobes appear over the whole correlation plane. Figure 2(d) shows the thresholded version of the correlation output shown in 2(c) after peak detection with the spaces between peaks magnified along the x direction. The final output from the system is shown in Fig. 2(e). Compared with the initial input in (b), spaces are inserted between words and all the errors in the input are corrected.

In summary we have described an optical word-break recognition system with error correction capability which outputs readable text. An analytical description of the system discussed has been done, and will be presented along with experimental results. The authors acknowledge E.M. Kirschner for technical assistance in preparing the transparencies.

REFERENCES

1. D. W. Tank and J. J. Hopfield, " Neural computation by concentrating information in

time," Proc. Nat. Acad. Sci., **84,** 1896, 1987.

2. E. G. Paek and D. Psaltis, "Optical associative memory using Fourier transform holograms," Opt. Eng., **26(5),** 428, 1987.

FIGURE CAPTIONS

Fig. 1 Holographic word-break recognition system.

Fig. 2 (a) The four patterns stored in the holographic memory ; (b) The input to be read ; (c) correlation output ; (d) the thresholded version of the correlation output which is anamorphically magnified along the x (word) direction ; and (e) the associative recalled output with spaces between words and error corrections.

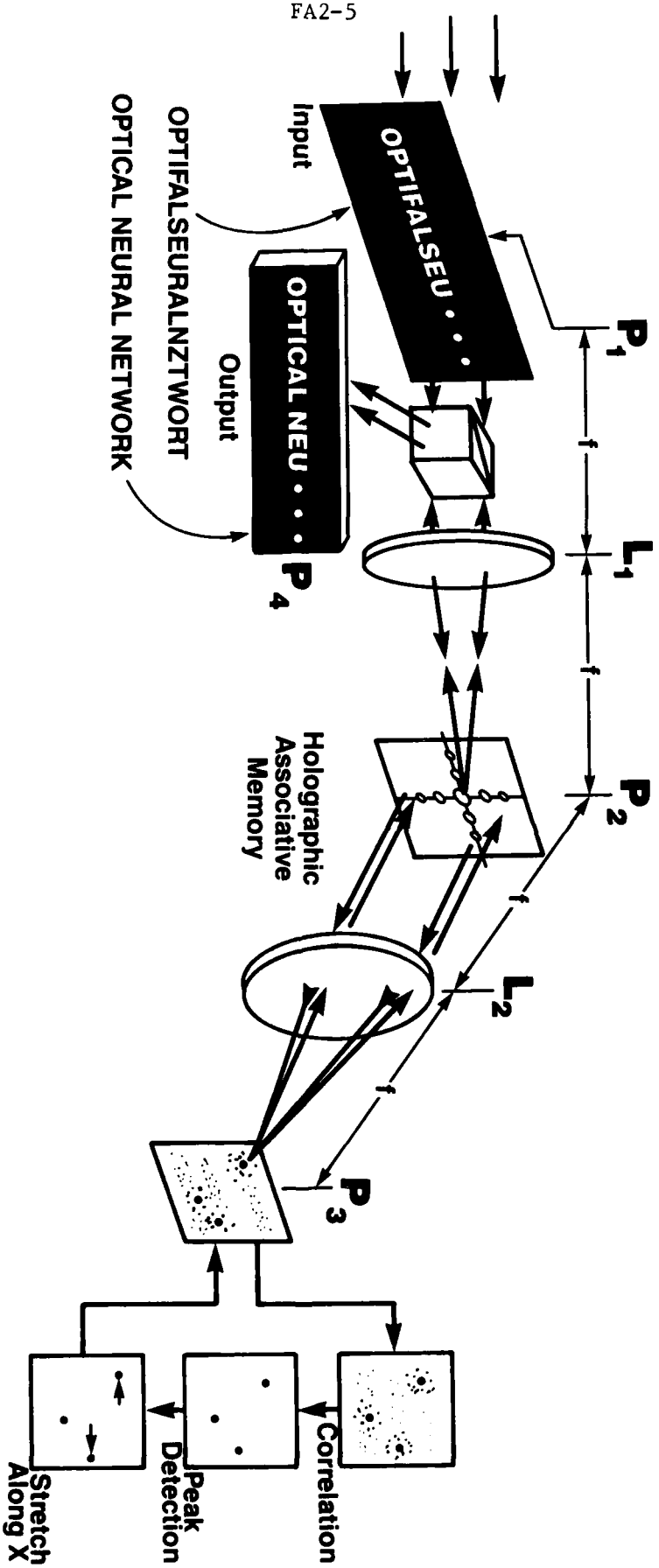
OPTICAL NEURAL NETWORK
OPTIFALSEURALNZTWORT
Input
Output
OPTIFALSEU . . .
OPTICAL NEU . . .
P1
P4
L1
f
f
Holographic Associative Memory
P2
f
L2
f
P3
Stretch Along X
Peak Detection
Correlation

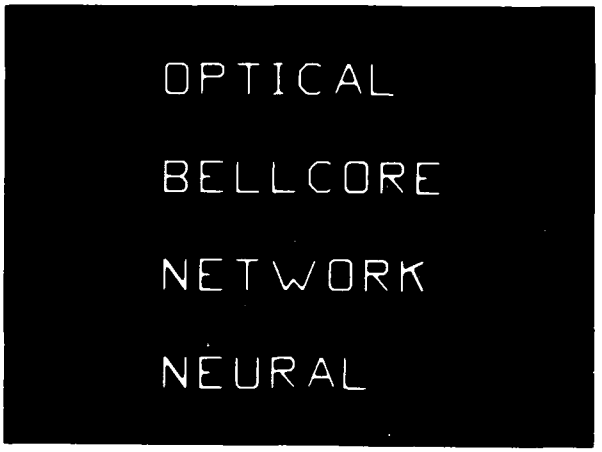
OPTICAL
BELLCORE
NETWORK
NEURAL

a


OPTIFALSEURALNZTWORK

b

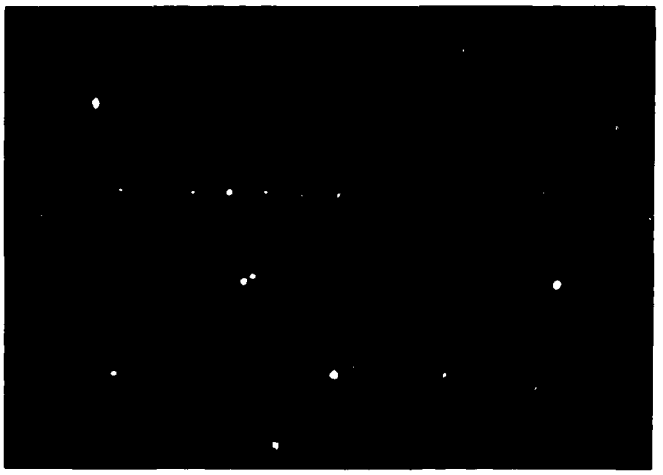

c

d


OPTICAL NEURAL NETWORK

e

ADAPTIVE FRAUNHOFER DIFFRACTION PARTICLE SIZING INSTRUMENT USING A SPATIAL LIGHT MODULATOR

E. Dan Hirleman and Paul A. Dellenback*

Mechanical and Aerospace Engineering Department
Arizona State University, Tempe, Arizona 85287
(602) 965-3895

*Mechanical Engineering Department, Southern Methodist University, Dallas, TX

SUMMARY

Introduction

Electro-optical sensors can measure a variety of properties important in manufacturing and industrial processes such as temperature, species concentrations, particle sizes, flow velocities and rates, surface characteristics and velocities, and part geometry. The performance improvements available from next-generation electro-optical sensors will be due in part to the integration of some forms of artificial intelligence into the system. For example, we are interested in sensors which might autonomously adapt themselves to optimal or near-optimal configurations as dictated by the instantaneous measurement context. Many schemes for adaptive control of sensor systems can utilize spatial light modulator technology whereby the spatial distribution of an optical field can be controlled. We are investigating laser diffraction particle sizing systems where the angular distribution of scattered light is collected at multiple angles for use in an inverse scattering calculation. Spatial light modulators (SLM) can be used to create programmable detector geometries which can be optimized depending on the particular particle size distribution under analysis. In this paper we the discuss the integration of Faraday-effect magneto-optic spatial light modulators into adaptive laser diffraction particle sizing instruments.

Fraunhofer Diffraction Particle Sizing

Fraunhofer diffraction has achieved widespread acceptance as an optical diagnostic for sizing ensembles of particles large compared to the wavelength. There is extensive literature on the topic reviewed by Hirleman [1987], and several commercial instruments for sizing particles based on the method are available. The conventional Fraunhofer diffraction instrument configuration is given in Fig. 1, where the light diffracted by particles along the line-of-sight of the probe laser beam is collected by a lens and sensed in the back focal (Fourier transform) plane. Each particle size produces a distinctive diffraction pattern signature which is mixed with diffraction patterns from the other sizes at the detector plane. The essence of the particle sizing problem is to unravel these signatures by clever sampling of the diffraction pattern and determine the particle size spectrum. In the context of adaptive control of the system the objective is to extract the maximum amount of useful information on the size distribution with a minimum possible number of measurements. The maximum information obtainable is dependent on the noise levels in the measurements, the sampling or detection scheme, the stability or robustness of the inversion method, the actual size distribution, and the allowable level of uncertainty. Ideally, then, a laser diffraction system would have variable detector geometry and size resolution which could both be adjusted at run time depending on the conditions encountered.

One serious challenge is the fact that the scattering intensity across the region of interest in the detector plane covers 3 or 4 orders of magnitude which approaches the capability of most detectors. Researchers have used a number of schemes to compress the dynamic range of the signals by using multiple detectors and increasing the area of the detectors in those regions (large scattering angles) where the intensity is low. A very common method is to use a monolithic photodiode detector array with elements which increase in size with distance from the detector center such as the annular ring-shaped elements shown in Fig. 1. It appears that most if not all Fraunhofer diffraction instruments using ring detectors utilize a geometry very similar to that of Recognition Systems Inc. which is neither designed nor optimized for this application. Unfortunately then, most inverse Fraunhofer schemes in use today have been dictated by the geometry of an existing detector.

The basic equation of Fraunhofer diffraction particle sizing is a Fredholm integral equation of first order and first kind, and following Hirleman [1988] we formulate the problem:

$$i(\theta)\theta^2 = I_{inc}\,\lambda^2/4\pi^2 \int_0^\infty J_1^2(\alpha\theta)\,\alpha^2\,n(\alpha)\,d\alpha \qquad (1)$$

where: $\alpha = \pi d/\lambda$ is the particle size parameter; $n(\alpha)$ is the unknown particle size distribution; and $i(\theta)$ the scattering intensity which can be measured at various scattering angles. Hirleman [1988] has derived an optimal scaling law for the problem, and annular detectors with areas proportional to θ^2 as in Fig. 1 are optimal. Most workers discretize Eq. (1) and solve the resulting linear system for a discrete particle size distribution. However, for a fixed detector geometry as shown in Fig. 1, the the linear system and its inversion properties then become quite dependent on the size distribution and scattering signature. Further, the amount of information concerning $n(\alpha)$ which can ultimately be extracted via Eq. (1) using measured $i(\theta)$ clearly must depend on the level of noise in the measurements. In fact, the maximum amount of information describing $n(\alpha)$ which can be obtained through an inversion of Eq. (1) is dependent on: the noise levels in the measurements; the sampling or detection scheme; the stability or robustness of the inversion method; the actual size distribution; and the allowable level of uncertainty. Ideally, then, a laser diffraction system would have variable detector geometry, inversion scheme, and size resolution which could all be adjusted in real time depending on the conditions encountered. It is toward this end that the integration of an SLM into the optical system is proposed.

Adaptive Fraunhofer Instrument Using SLM

By adaptive instruments we mean those which have either hardware or software degrees of freedom which can be adjusted on-line depending on the instantaneous context of the measurement. For the present application, we first assume that only a finite number of scattering angles at which measurements can be made are available in any practical instrument. It is also clear that the optimal positions of the detectors (i.e. positions which would provide the maximum amount of information about the particle size distribution) in a laser diffraction instrument depend on the size distribution. This is a dilemma since the size distribution is obviously not known before the measurement is made, and instrument designers must place fixed detectors at locations which will be adequate over a large range of particle sizes. However an intelligent, adaptive instrument would ideally configure the optimal detector placements in real time. This might be accomplished by first obtaining a low resolution estimate of the size distribution, then configuring the detectors to focus on the particle size region of immediate interest. This process could be repeated to obtain higher and higher resolution estimates of the size distribution until the signal/noise considerations do not permit further information to be extracted from the scattering inversion.

The optical system we have developed to introduce adaptive control into the laser diffraction method is shown in Fig. 2. Instead of placing a detector array at the back focal plane of the transform lens, we insert a Faraday-effect SLM discussed by Ross et al [1983] and marketed by Semetex. A large area detector is then placed behind the SLM which is operated in a binary transmit/absorb mode. Pixels are opened in groups which form rings concentric about the optical axis as also shown in Fig. 2. The optimal number and positions of the detectors is determined by condition number or eigenfunction analysis of the inverse scattering problem reported elsewhere by Hirleman [1988]. To summarize briefly that approach, the second moment of the size distribution $n(\alpha)\alpha^2$ is expanded in terms of the eigenfunctions of the kernel $J_1^2(\alpha\theta)$ of the integral equation Eq. (1). The eigenfunctions retain their identity even after passing through the integral operator, but are scaled by a constant which is the associated eigenvalue. Now in general the eigenfunction expansion has an infinite number of terms, but a real measurement can only extract a finite amount of information about $n(\alpha)\alpha^2$; i.e. only the coefficients from a finite number of terms in the $n(\alpha)\alpha^2$ expansion can be determined. The error in neglecting higher order terms in the expansion can be minimized by locating the detectors (i.e. the angles θ at which the $i(\theta)\theta^2$ are measured) at the *zeros* of the eigenfunction term just beyond the highest order eigenfunction which is retained. The number of terms which should be kept depends on the measurement context, and one approach we are investigating involves keeping only those terms for which the eigenvalue is greater than the noise-to-signal ratio in the measurements (the eigenvalues monotonically decrease with increasing order). The number of ring aperture detectors configured in the SLM of Fig. 2 is then equal to the number of terms kept in the eigenfunction expansion, and the detectors are placed at the zeros of the first eigenfunction dropped from the expansion. As the particle sample changes, the system autonomously monitors the stability of the scattering inversion and adjusts the rings accordingly.

The selection of a particular SLM for this application involved several criteria. Typical maximum frequencies of interest are in the 10 kHz range, and spatial frequency dynamic ranges of the order of 100 and greater are required. The magneto-optic device used here is based on the Faraday effect which selectively alters the polarization vector of incident light transmitted through the modulator material. One ramification of adopting a birefringence approach for the SLM is that the original optical field to be modulated must be linearly polarized. Therefore in some applications it is necessary to place a polarizing filter in the optical beam in front of the SLM in Figure 2 such that linearly polarized light is incident on the modulator. In the present application, near forward scattering by particles, the energy is already polarized.

References

Ross, W.E., Psaltis, D. and Anderson, R.H. (July, 1983). "Two-dimensional Magnetooptic Spatial Light Modulator for Signal Processing", *Optical Engineering*, Vol. 22, pp. 485-490.

Hirleman, E. D. (1987). "Laser Diffraction Particle Sizing Techniques", in Flow and Particle Diagnostics, Vol. 58, ICALEO'86 Proceedings, Laser Institute of America, Toledo, Ohio, 168-175.

Hirleman, E. D. (1988). "Optimal Scaling for Fraunhofer Diffraction Particle Sizing Instruments," in Optical Particle Sizing, G. Gouesbet and G. Grehan, eds., Plenum Publishing, London, in press.

Acknowledgements

This research was sponsored by the Air Force Office of Scientific Research, Air Force Systems Command, USAF, under Grant Number AFOSR-84-0187, Dr. Julian Tishkoff, program manager. The U.S. Government is authorized to reproduce and distribute reprints for Governmental purposes notwithstanding any copyright notation thereon.

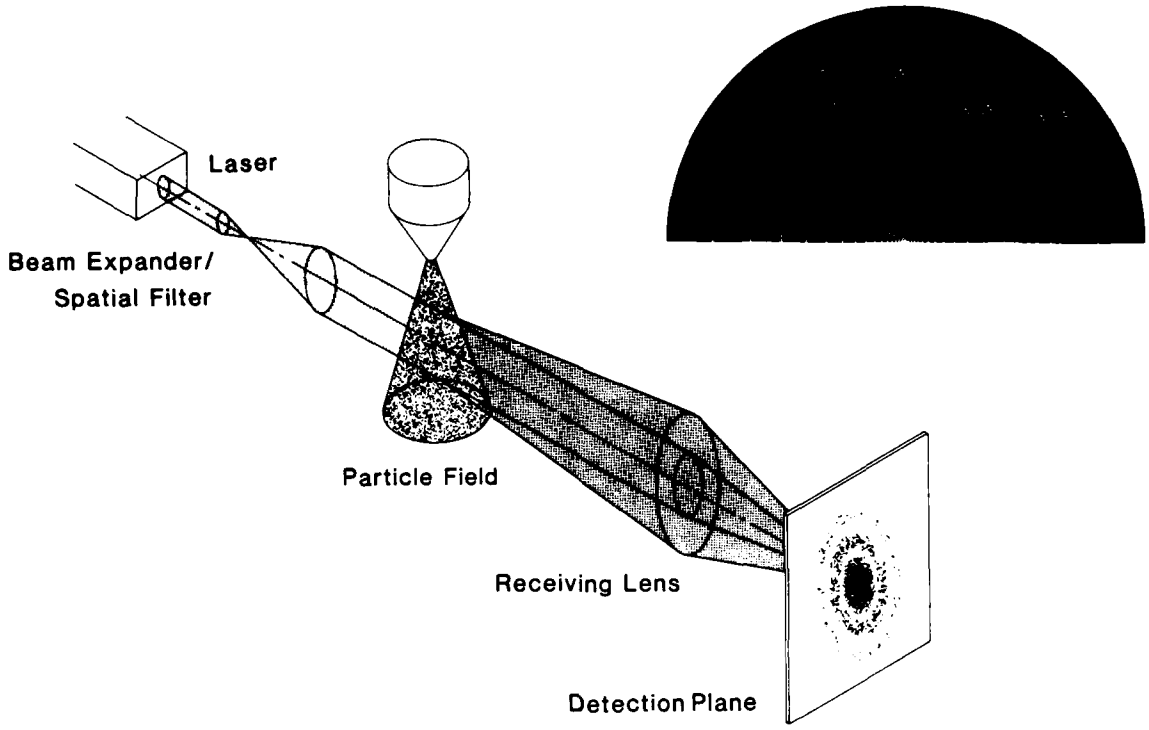

Figure 1. Schematic of a conventional laser diffraction particle sizing instrument. An annular ring detector array is shown.

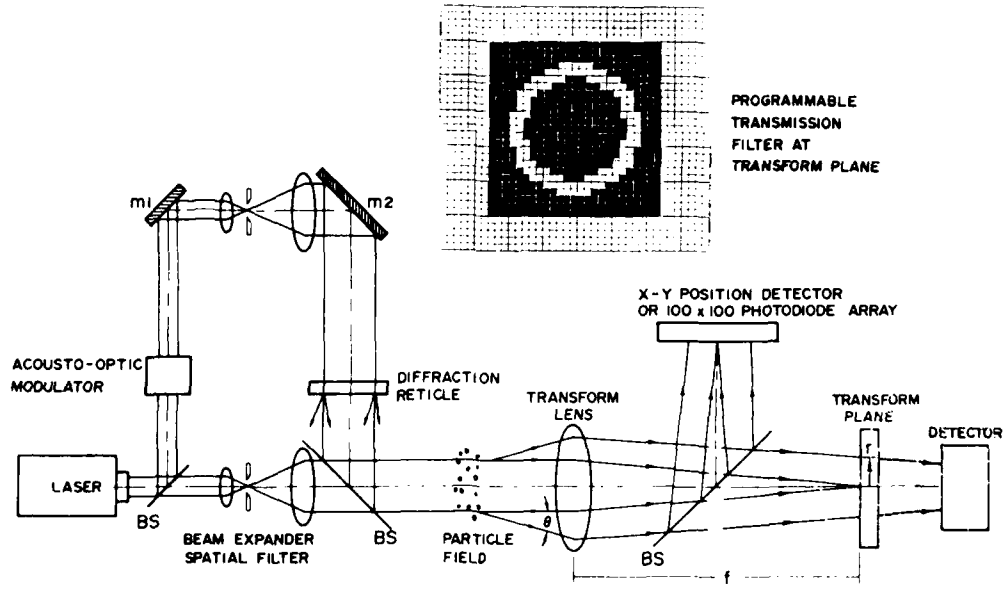

Figure 2. Schematic of laser diffraction particle sizing instrument where a spatial light modulator has been included to provide for on-line, adaptive configuration of the detector collection apertures. Annular ring openings are created in the SLM at the transform plane by setting the pixels to transmit or block the incident polarized light. The field detector collects all light passing through the SLM, and the system is sequenced through a set of rings.

The Use of Binary Magneto-optic Spatial Light Modulators in Pattern Recognition Processors

David Flannery, John Loomis, and Mary Milkovitch
The University of Dayton Research Institute
Dayton, Ohio 45469

1. INTRODUCTION

Binary magneto-optic spatial light modulators (SLM) [1] have been used successfully in several optical computing architectures. Here we concentrate on their use to implement binary phase-only filters [2-6] in coherent optical correlators including general characteristics, correlation performance, smart filters, and the potential for ternary filter encoding.

2. BINARY MAGNETO-OPTIC SPATIAL LIGHT MODULATORS

Magneto-optic SLMs (MOSLMs) are being developed and commercially sold by Litton Data Systems and Semetex Corporation. Currently 48-by-48 and 128-by-128 element models are available and a 256-by-256 lab unit has been made. The construction and operating characteristics have been reported [1], and are only reviewed here.

The MOSLM is an electrically addressed discrete element SLM. The modulation mechanism is Faraday polarization rotation, which with appropriately oriented polarizers provides either binary amplitude or binary phase modulation. Element spacing in the 128-by-128 devices is 0.003 in.

Once set, an element remembers its state essentially forever. This and good uniformity of modulation both intra- and inter-element are advantages of the device. Bulk absorption of around 70% and polarization rotation of about 10 degrees combine with area utilization factors of 60-70% to yield modulation efficiencies of only several percent, a disadvantage. (These factors vary significantly with wavelength over the visible operating range.)

With appropriate drive circuitry the MOSLMs can be addressed very rapidly. Thermal dissipation in the addressing conductors usually limits speed for continuous operation. Litton has reported [7] continuous operation of 128-by-128 MOSLMs at 1100 fps, changing 50% of the elements each frame, which is enabled by drive circuitry designed to provide the minimum addressing pulse length consistent with reliable switching, e.g., 20-30 ns. The device was not specially cooled and the on-chip dissipation of about 0.5 W may result in thermal-optic phase distortions. Although operation was verified optically, the device was not being used in a coherent optical system which would be sensitive to phase distortions. It is anticipated that proper attention to air flow geometry would reduce thermal-optic distortion effects to a level supporting coherent optical processing. Passive optical quality has varied in the past depending on substrate wafer polishing specifications but no fundamental or cost issue precludes peak-to-peak phase distortion of a quarter wavelength.

3. CORRELATION USING MAGNETO-OPTIC BINARY PHASE-ONLY FILTERS

The binary phase-only filter (BPOF) [2,3] encodes only two phase values (0 and 180 degrees), obtained by thresholding a reference function transform, as opposed to the continuous-valued phase and amplitude variations required in a matched spatial filter. Simulations of correlation using the BPOF [3] indicate good performance, including two characteristics associated with any phase-only filter [3]: sharp correlation peaks and high Horner efficiency. Other characteristics and design aspects of the BPOF have been studied [2,8-10].

The MOSLM is well suited for implementing this type filter; it can provide the required binary phase-only encoding and it also implements spatial-carrier-free direct phase encoding with attendant efficiency in space-bandwidth utilization.

We have conducted hundreds of experimental-theoretical comparisons using our real-time MOSLM BPOF correlator and a computer model of the correlator [4,5,11]. The correlator uses two 48-by-48 MOSLMs, one for binary pattern input and the other to implement BPOFs. The comparison study addressed issues of machine vision, character recognition, and several simple types of composite filters. Quantitative agreement with theory was typically within 2 dB or better over hundreds of cases [11].

4. BPOF SMART FILTERS

A "smart filter" is herein defined as one which significantly improves the fundamental trade-off between distortion-invariant response and non-target rejection in linear space-invariant correlation. A number of such formulations have been defined and tested (primarily in simulations), all designed to be encoded in full continuous complex-valued filters [12-15]. The BPOF (and the POF) are fundamentally different because their encoding involves a non-linear operation to generate a (binary) phase-only function.

Initial approaches to creating BPOF smart filters involved simply converting an existing continuous-valued filter function (e.g., SDF filter) to BPOF form by conversion using the appropriate nonlinear operation. This Ad Hoc approach yielded good results [16,17]. More recently, SDF formulations specifically tailored for POF and BPOF encoding have been reported and perform well in simulations [11,18,19]. As mentioned we have demonstrated good experimental performance of simple SDF-type BPOFs (involving only three training images) [11].

Thus the availability of effective smart filters for BPOF implementation seems assured. Development of improved smart filter formulations for both discrete level and continuous level encoding continues, and significant future improvements are likely.

5. TERNARY PHASE-AMPLITUDE FILTERS

We are investigating a discrete-level smart filter approach based on three encoded modulation states, -1, 0, and +1, which may be viewed as a combination of binary phase and binary amplitude modulation. The intuitive motivation for this is simple: The zero modulation state can be used to block spatial frequencies which are not found, or are very weak, in the desired target pattern. This should have little deleterious effect on the desired correlation, but any substantial input energy at these spatial frequencies must arise from non-targets, and blocking them should improve the signal-to-noise in the correlation pattern.

The MOSLM devices are prime candidates for implementing the ternary phase-amplitude filter (TPAF) as they are reported [1] to possess a third state of mixed magnetization, intermediate to the two fully magnetized states normally used, and easily accessed by the proper drive sequence. We believe this state, with proper optical system design, will furnish zero-modulation.

Our initial simulations have explored a strategy for choosing TPAF elements to be blocked (set to zero) based on the ratio of spatial power spectra of desired (target) and undesired (non-target) patterns; we call it the "transform-ratio" method. Figure 1 shows the binary target and non-target patterns used in these

(a) (b)

Figure 1: Target (a) and nontarget (b) binary patterns

simulations, performed with 64-by-64 element resolution using FFT algorithms. Random background noise

in varying amounts (not shown in Figure 1) was added to some input scenes and was considered as an additional non-target (with an assumed "white" spatial frequency spectrum) in formulating filters. This first series of simulations addressed only noise and non-target rejection but not the handling of target distortions.

Filter formulation involved computing the Cosine-BPOF [10] for the target pattern and then zeroing some elements based on the transform-ratio concept. At each spatial frequency bin the target transform energy was compared to both the non-target transform energy and the noise spectral energy for an assumed level of background noise. If the target energy did not exceed both references by a certain ratio, the element was zeroed. This ratio and the assumed noise-blocking level comprise two design parameters of the filter.

The discrimination and signal-to-noise performance of these filters is plotted in Figure 2 as a function of input noise level. Binary background noise was added by comparing the output of a psuedo-random

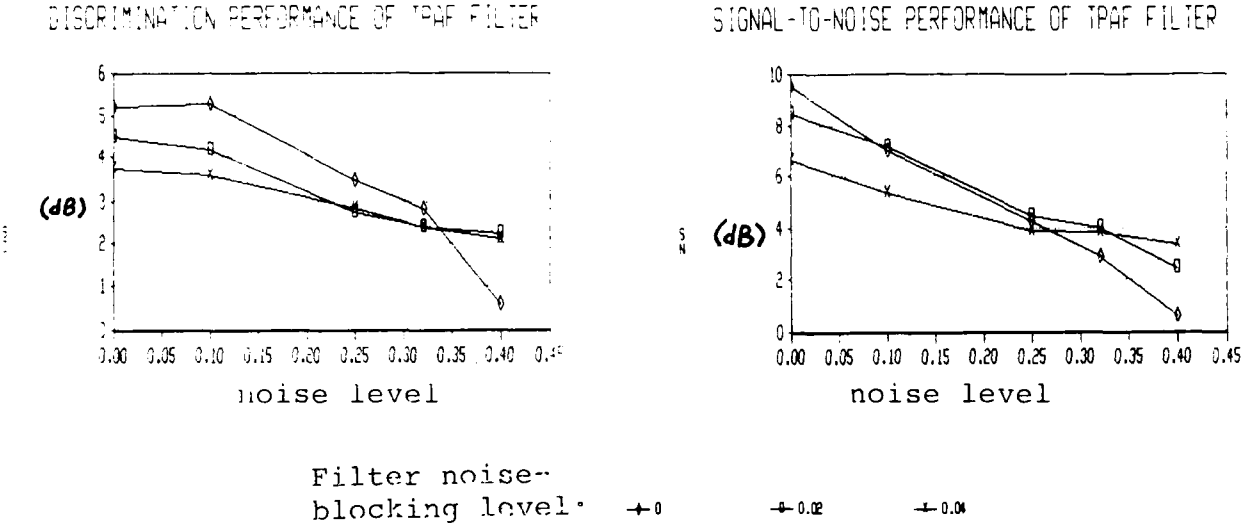

Figure 2: Plots of TPAF filter performance

number generator algorithm with an adjustable threshold and setting input samples when the threshold was exceeded. The noise level indicates the fractional area of noise elements.

All the data in Figure 2 correspond to one transform ratio, 1.21, which was determined to yield good discrimination in the absence of noise. Families are plotted for different choices of the noise-blocking filter parameter. Discrimination and signal-to-noise ratios are based on intensities of the properly located correlation peak and the highest peak located elsewhere, either on the non-target object (discrimination) or in the background region (signal-to-noise) The absolute values of discrimination and signal-to-noise are not so important, as they are subject to arbitrary choices of inputs and resolution. The trends definitely indicate the superior performance of properly designed TPAF filters. Filters using a sufficiently large noise-blocking parameter perform better with large amounts of noise present in the input. As an important point of reference, the Cosine-BPOF for the target object provided 1.14 dB discrimination and 1.98 dB signal-to-noise with an input noise level of 0.4, significantly inferior to the best TPAF.

These simulations indicate the potential for superior performance of ternary smart filters. We are extending our designs to encompass target distortions and plan to implement the filters experimentally.

6. CONCLUSION

Experimental results demonstrate that the binary phase-only correlation filter implemented with magneto-optic SLMs can serve as the basis for powerful real-time correlators applicable to near term civilian and military pattern recognition problems. Discrete level smart filter formulations will enhance their applicability.

MOSLMs have many advantages for optical processing applications. They are commercially available with useful resolution and speed parameters and have demonstrated good performance implementing BPOFs. They have intrinsic memory capability and a well-controlled modulating element response. MOSLMs are also a prime candidate to implement ternary filters with improved smart filter performance.

7. REFERENCES

[1] Ross, W., D. Psaltis, and R. Anderson, SPIE 341, p. 191-198 (August 1982).

[2] Psaltis, D., E. Paek, S. Venkatesh, Optical Engineering, 23, 6, p. 698-704 (Nov./Dec. 1984).

[3] Horner, J. and H. Bartelt, Applied Optics, 24, 18, p. 2889-2893 (15 September 1985).

[4] Flannery, D., A. Biernacki, J. Loomis, and S. Cartwright, Applied Optics, 25, 4, p. 466 (February 15, 1986).

[5] Keller, P., D. Flannery, S. Cartwright, and J. Loomis, Proc. SPIE, 728, p. 257-265 (October 1986).

[6] Mills, S. and W. Ross, SPIE 753, p. 54 (15-16 January 1987).

[7] Maki, T., "High Frame Rate LIGHT MOD Evaluation with the FDS Card Set," Litton Systems internal memo TRM:354:87:148, (26 June 1987).

[8] Kumar, B. and Z. Bahri, "Optimality of phase-only filters," SPIE 884, Computer-Generated Holography II, 12 January 1988 (to be published).

[9] Dickey, F. and T. Stalker, Paper WK3 at Optical Society of America 1987 Annual Meeting, Rochester, NY (21 October 1987).

[10] Cottrell, D., R. Lilly, J. Davis, and T. Day, Applied Optics, 26, 18, p. 3755 (15 September 1987).

[11] Flannery, D., J. Loomis, M. Milkovich, and P. Keller, "Application of Binary Phase-only Correlation to Machine Vision," Optical Engineering, (to be published).

[12] Sharma, V. and D. Casasent, Proc. SPIE, 519, p. 50 (October 1984).

[13] Kallman, R. R., Applied Optics, 25, 7, p. 1032-1033 (1 April 1986).

[14] Schils, G. and D. Sweeney, Optics Letters, 12, 5, p. 307-309 (May 1987).

[15] Mahalanobis, A., B. Kumar and D. Casasent, Applied Optics, 25, 23, p. 4466-4472 (1 Dec 1986).

[16] Horner, J. and P. Gianino, Applied Optics, 24, 6, p. 851-585 (15 Mar 1985).

[17] Kallman, R., Applied Optics, 25, 23, p. 4216-4217 (1 Dec 1986).

[18] Jared, D., D. Ennis, and S. Dreskin, "Evaluation of binary phase-only filters for distortion-invariant pattern recognition," SPIE 884, Computer-Generated Holography II, 12 January 1988 (to be published).

[19] Kallman, R., Applied Optics, 26, 24, p. 5200 (15 December 1987).

FRIDAY, JUNE 17, 1988

EMERALD BAY BALLROOM

10:10 AM–11:30 AM

FB1–4

APPLICATIONS: 2

Martin Sokoloski, National Aeronautics and Space Administration, *Presider*

Real-Time Programmable Joint Transform Correlator with a Threshold Hard-Clipping Microchannel Spatial Light Modulator

F.T.S. Yu, Q.W. Song
Electrical Engineering Department
The Pennsylvania State University, University Park, PA 16802
Y. Suzuki, M. Wu
Hamamatsu Photonics KK. Hamamatsu city, Japan

Abstract

A programmable real-time optical joint transform correlator that generates sharper autocorrelation peaks is presented. In the system, a microchannel spatial light modulator (MSLM) is utilized as the threshold hard-clipping square-law device. A liquid crystal television (LCTV) is used, with a microcomputer, to display input target and reference image at the input plane. By using the feed-back loop, in principle, the system would offer adaptive processing capability. A preliminary experimental result is given.

I. Introduction

Because of the high processing speed and structrural simplicity, various schemes of optical joint transform correlators have been proposed [1] for the application to pattern recognition. Nevertheless, all of the existing techniques have a common drawback, namely, that the correlation peak intensity is only a very small fraction of the illumination intensity. Whenever SNR is low, signal detection becomes increasingly difficult. Using a phase only filter [2] can improve the correlation peak. However, a phase only filter is difficult to realize in practice, with the current state-of-the-art electro-optic devices. In this paper, we will introduce a real-time programmable joint transform correlator utilizing the threshold hard-clipping property of a microchannel spatial light modulator (MSLM) [3]. We will show that this technique is capable of producing sharper and higher autocorrelation peaks than the conventional optical correlator. By combining the advantages of the state-of-the-art electro-optic devices and flexibility of a microcomputer, the system can be built as an adaptive, self-learning correlator.

II. Background

A. Microchannel spatial light modulator

The MSLM is a reflective type electro-optic spatial light modulator. One unique feature of the MSLM is that when the bias voltages are properly controlled, the device can perform quite a number of optical operations in its internal mode processing. Several applications of MSLM to optical information processing and computing have been reported.

B. Joint transform correlator

The principle of the classical joint transform correlator (JTC) is well known. To compare it with the proposed MSLM based system, we shall briefly discuss its operation in a specific example. For simplicity, we suppose both the target and the reference image at the input plane are binary type with square apertures of width w. The main separation between them is assumed l. The amplitude transmittance function of these input objects can be expressed as

$$f(x,y) = [rect(\frac{x-\frac{l}{2}}{w}) + rect(\frac{x+\frac{l}{2}}{w})]rect(\frac{y}{w}). \quad (1)$$

Illuminating the input objects by a collimated coherent light, the power spectrum can be recorded, at the back focal plane of a transform lens, on a square-law convertor. In linear approximation, we would use a linear piecewise model to represent the T-E

(transmittance versus exposure) curve, as shown in Fig.2 (on the next page). Thus the recorded amplitude transmittance can be approximated by

$$t = 1 - \frac{1}{w^4}\left[\frac{sin(\pi w\nu)}{\pi\nu}\frac{sin(\pi w\mu)}{\pi\mu}cos(\pi l\mu)\right]^2. \tag{2}$$

The corresponding autocorrelation functions at the output plane would be

$$f(x,y) = -A\frac{1}{4w^2}[\Lambda(\frac{x-l}{w}) + \Lambda(\frac{x+l}{w})]\Lambda(\frac{y}{w}), \tag{3}$$

where A is the illumination amplitude, and Λ denotes a triangular function defined as

$$\Lambda(\frac{x}{w}) = \begin{cases} 1 - \frac{|x|}{w}, & \text{if} |x| \le w; \\ 0. & \text{otherwise.} \end{cases}$$

In view of Eq.(3), the intensity of the correlation peaks is about $A^2/16w^4$). We shall, in the following, discribe a programmable threshold hard-clipping JTC using a microchannel spatial light modulator (MSLM) to improve correlation peaks.

III. Basic principle

The schematic diagram of the microcomputer based JTC is shown in Fig.1.

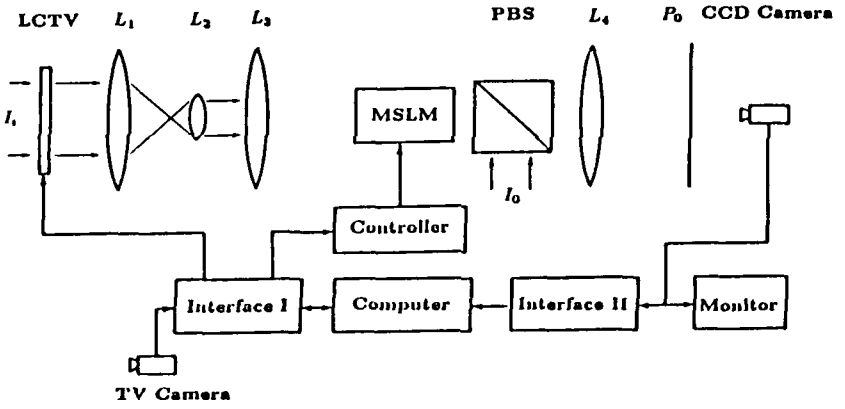

Fig.1 The schematic of a programmable optical joint transform correlator.

The liquid crystal plate of a LCTV is used to display a real-time target and a reference image, at the input plane of an optical processor. The working principle of the LCTV as an optical element is described elsewhere [4]. The major advantage of using LCTV must be that it can be addressed by a microcomputer, for the generation of various reference images. We shall use the MSLM as a threshold hard-clipping device. The output light field is detected by a CCD camera. This detected electrical signal can be sent to a TV monitor for observation, or fed back to the microcomputer for further instruction. Thus an adaptive hybrid electro-optic correlator may be constructed.

Let's assume that the target and reference image be identical. The light intensity distribution at the input window of the MSLM would be

$$I(\nu,\mu) = I_0\left[\frac{sin(\pi w\nu)}{\pi\nu}\frac{sin(\pi w\mu)}{\pi\mu}cos(\pi l\nu)\right]^2. \tag{4}$$

Notice that, the grid structure of the LCTV, which is beyond the resolution limit of the MSLM, is omitted. To obtain a binarized power spectral distribution for joint transform correlation, the bias voltages of the MSLM are adjusted such that those values above the threshold level will be responded. This hard-clipping property of the MSLM converts the input irradiance $I(\nu,\mu)$ into a series of binary phase distribution, between the X and the Y components of the read-out light, as depicted by Fig. 3.

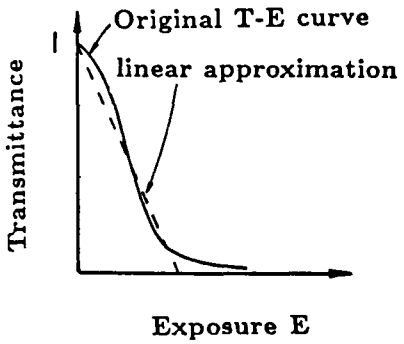

Fig.2 Linear approximation for T-E curve

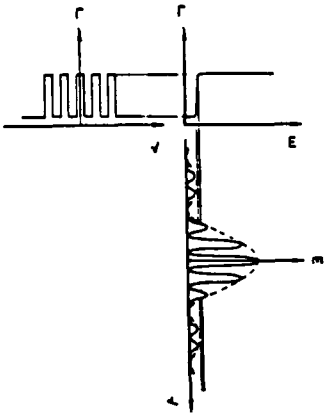

Fig.3 Threshold hard-clipping (from intensity to phase output.)

By binarizing the central lobe of Eq.(4) using the half power criterion, the output phase function can be obtained with first order approximation, as given by

$$\Gamma = \pi rect(\frac{\nu}{1/w}) rect(\frac{\mu}{1/w}) \sum_{-\infty}^{\infty} rect(\frac{\nu}{4l}) \otimes \delta(\nu - \frac{n}{l}), \tag{5}$$

where $\otimes$ denotes the convolution operation. After passing through the polarizing beam splitter (PBS), and transformed by lens 4, the output autocorrelation functions can shown as

$$E = \frac{A}{\pi}\{\frac{sin[\pi(x-l)/w]}{\pi(x-l)} + \frac{sin[\pi(x+l)/w]}{\pi(x+l)}\}\frac{sin(\pi y/w)}{\pi y}. \tag{6}$$

From this equation, we see that the correlation peak intensity of the proposed system is $A^2/\pi^2 w^4$, which is about 1.62 times higher than the conventional one. Moreover, if the bias voltages can be controlled, such that the threshold hard-clipping takes place at a lower intensity level to include the whole main lobe of Eq.(4), as shown in Fig.3, the corresponding output correlation functions can be rewritten as

$$E_1 = \frac{A}{\pi}\{\frac{sin[2\pi(x-l)/w]}{\pi(x-l)} + \frac{sin[2\pi(x+l)/w]}{\pi(x+l)}\}\frac{sin(2\pi y/w)}{\pi y}. \tag{7}$$

The peak intensity of this function is $16/\pi^2 w^4$ (i.e., 26 times higher than the conventional classical JTC). In addition, the width of the correlation intensity (i.e., first zero crossing) is reduced to about one half of that of the conventional JTC. For demonstration, the curves 1,2,3 in Fig.4 show computed normalized correlation intensity distributions for both the conventional and the proposed hard-clipping JTC, as applied to half of the main lobe, the whole main lobe of Eq.(4), respectively. These plots illustrate

ideal hard-clipping offers better correlation peak than the conventional JTC, under the same coherent read-out and noisele.ss condition.

IV. Experimental demonstration

Filgure 5(a) shows a input target and a reference image displaed on the LCTV. The enlarged output irradiance obtained with this technique is shown in Fig.5(b).

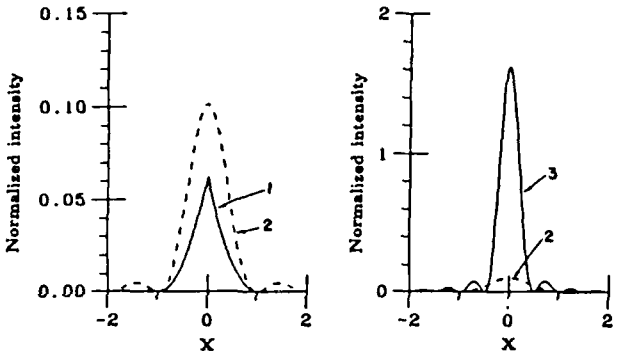

Fig.4 Simulated correlation peaks (normalized).

(a) Input and reference images (on LCTV).

(b) Autocorrelation (enlarged).

Fig.5 Experiment Demonstration

From the result, two distinct autocorrelation peaks can readily be seen. The globel zero-order diffraction is mainly due to the unevenness of the E-O crystal plate within the MSLM. The ratio of the output correlation intensity to illumination intensity, I_{peak}/I_0, is about 1/11. This result corresponds to threshold hard-clipping at the half power level of the main lobe of Eq.(6). This experimental result has not achieved the optimum condition, which is primarily due to the threshold hard-clipping property and the noise behavior of the MSLM. However, the demonstration shows that the technique has certain merit as compare with a conventional JTC, namely shaper and higher correlation peaks.

IV. Concluding Remarks

We have presented a joint transform correlation system utilizing the threshold hard-clipping property of the MSLM, This JTC can produce sharper and higher correlation peaks than the convetional techniques. By combining the flexibility of the microcomputer and the high speed operation of the optical processor, the system would offer the advantages of real-time programmable processing capability, for which an adaptive smart correlator can be developed.

We acknowledge the support of the US Air Force, Rome Air Development Center, Hanscrom Air Force Base, Mass., under contract $F19628-87-C-0086$

Reference

[1] D. Casasent,"Coherent optical pattern recognition: a review," Opt. Eng. **24**, 26(1985).

[2] J.L. Horner and P.D. Gianino,"Phase only matched filtering," Appl. Opt. **23**, 812(1984).

[3] C. Warde, A. Fisher, D. Cocco, and M. Butmswi, "Microchannel Spatial Light Modulator," Opt. Lett. 3, 196(1978).

[4] H.K. Liu, J.A. Davis, and R. A. Lilly,"Optical Data Processing Properties of a Liquid Crystal Television Spatial Light Modulator," Opt. Lett. **10**,635(1985).

Bipolar Joint Transform Image Correlator, B. Javidi, C. J. Kuo, and S. F. Odeh, Michigan State University, Department of Electrical Engineering, East Lansing, Michigan 48824

ABSTRACT

Recently, we have introduced a bipolar joint transform image correlator[+] with substantially superior performance compared to the classical optical correlator. The bipolar image correlator uses nonlinearity at the Fourier plane to binarize the Fourier transforms' interference intensity to only two values, 1 and -1. The performance of the bipolar optical correlator has been compared to the classical optical correlator in the areas of light efficiency, correlation peak to sidelobe ratio, autocorrelation bandwidth, and cross-correlation sensitivity. The correlation signals obtained by the conventional technique suffer from low light efficiency, large correlation sidelobes, large autocorrelation bandwidth, and low discrimination ability. It was shown that compared to the classical correlator, the bipolar joint transform correlator provides significantly higher peak intensity, larger peak to sidelobe ratio, narrower autocorrelation bandwidth, and better cross-correlation sensitivity. The bipolar joint transform correlator produces delta function-like autocorrelation signals, and much narrower and smaller zero order term on the optical axis. Since the autocorrelation functions have delta function features, larger reference images can be used and the restrictions on the locations of the images and their autocorrelation bandwidth, which exists for the classical joint Fourier transform correlator, is eliminated.

In this paper, we present a theoretical investigation of the bipolar joint transform image correlator. Analytical expressions for the output correlation signals of the bipolar joint transform image correlator will be developed. Computer simulations will be used to test the developed analytical expressions of the bipolar correlator. We shall also investigate the performance of the bipolar joint transform correlator when multiple reference objects are stored at the input plane and multiple targets are present at the input scene. Computer simulation of the bipolar correlator is used to study the performance of the system and the results will be compared to the classical joint transform image correlator. We show that the performance of the bipolar correlator is substantially superior to the classical correlator when single or multiple objects are present at the input scene. The bipolar correlator can provide a much higher

[+] B. Javidi and C.J. Kuo, Appl. Opt. Vol.27, No. 4, Feb. 15 (1988).

autocorrelation peak intensity, smaller autocorrelation sidelobes, better discrimination sensi tivity, and narrower DC term. On the other hand, the classical joint transform correlator produces low intensity correlation signals with large sidelobes, wide bandwidth and large DC term.

The bipolar joint transform image correlator using an electrically addressed binary SLM at the Fourier plane is shown in Fig. 1. Plane P_1 is the input plane that contains the multiple reference signals and the multiple input signals displayed on SLM_1. The incoherent images enter the input SLM and are converted to coherent images. Either optically addressed SLM's or electrically addressed SLM's can be used at the input plane. The images are then Fourier transformed by lens FTL_1 and the interfence between the Fourier transforms is produced at plane P_2. The intensity of the Fourier transforms' interference is obtained by a CCD array located at plane P_2 and is binarized using a thresholding network. An electrically addressed SLM operating in the binary mode is located at plane P_3 to read-out the binarized intensity of the Fourier transforms' interference provided by the thresholding network. The correlation functions can be produced at plane P_4 by taking the inverse Fourier transform of the thresholded interference intensity distribution at plane P_3.

A numerical analysis of the bipolar optical correlator is provided to study the performance of the system when multiple reference signals and multiple input signals are present at the input plane. The correlation tests are performed for four different orientations of the capital letter F used as reference signals. The input scene will contain one or more of these characters. The correlation tests are performed for two cases: the classical joint transform image correlator and the bipolar joint transform correlator. The correlation signals when the input character F with 30^o orientation is used are shown in Fig. 2. Figure 2(a) shows the input signal and the reference signals, Fig. 2(b) shows the correlation result for the classical joint transform correlator when the Fourier transforms' interference intensity is not binarized, and Fig. 2(c) shows the correlation result for the bipolar optical correlator when the interference intensity is binarized. It is evident from this figure that the correlation signals corresponding to the thresholded interference intensity are substantially superior.

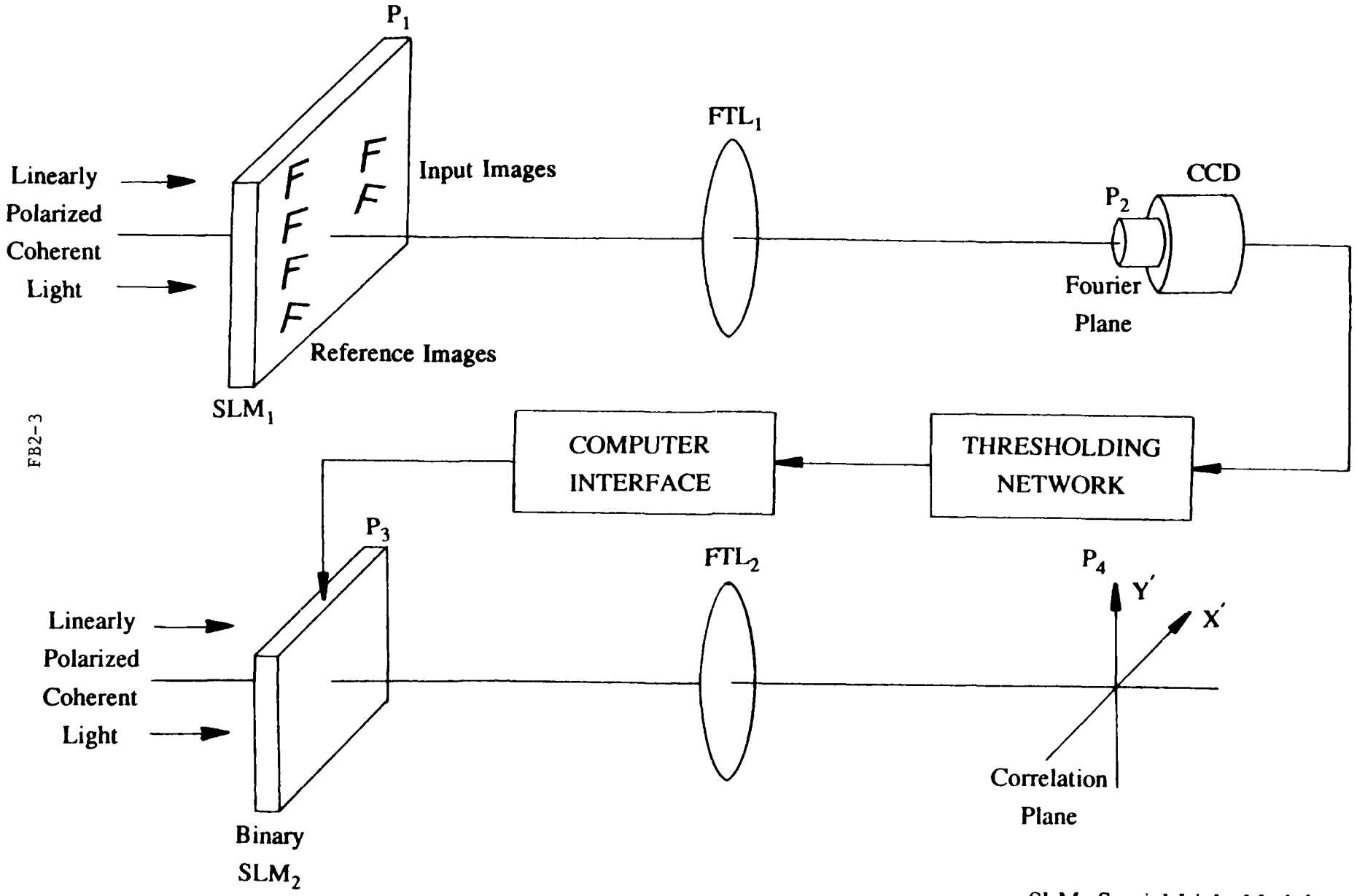

FB2-3

232

Figure 1. Bipolar joint transform image correlator using an electrically addressed binary SLM at the Fourier plaen.

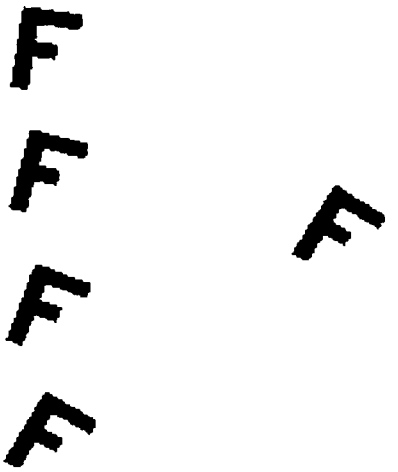

(a)

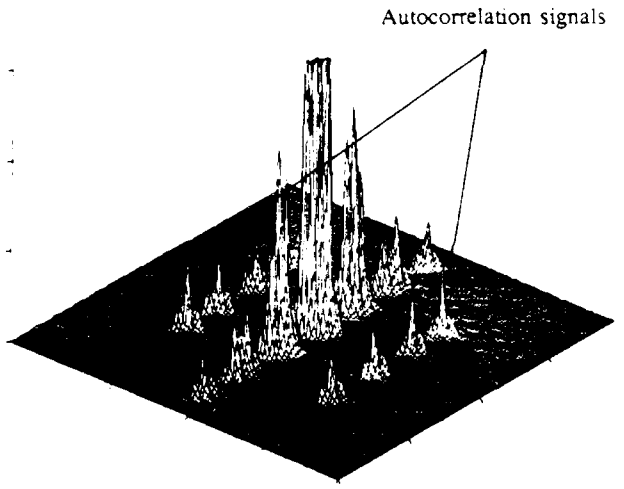

(b)

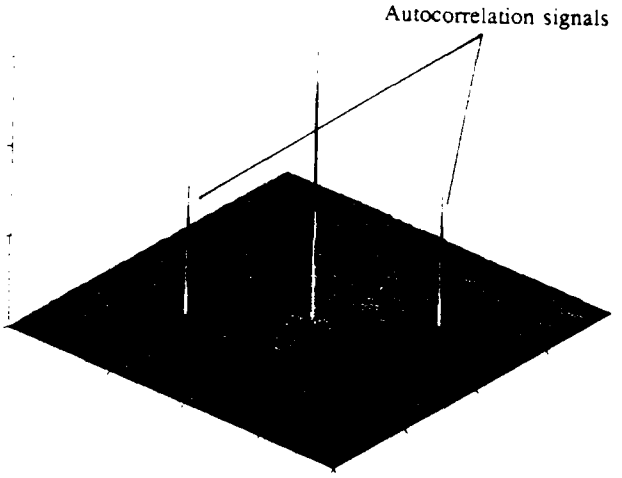

(c)

Figure 2. Correlation results when the character F with orientation of 30^0 is used as the input signal.

(a) The input signal and the reference signals.

(b) Correlation results obtained by the classical joint transform correlator.

(c) Correlation results obtained by the bipolar joint transform correlator.

GENERATING TANDEM COMPONENT CORRELATION FILTERS FOR PROGRAMMABLE SPATIAL LIGHT MODULATORS

Stanley E. Monroe, Jr.
Lockheed/EMSCO
2400 NASA Road 1
Houston, Texas 77058

INTRODUCTION

Bartelt and Horner [1,2,3] have described an iterative procedure for constructing Tandem Component (TC) filters, which are a series of phase-only, passive elements distributed through an optical system. Of the several applications considered, the one of interest to this author is that of optical correlators. Since the elements do not affect the amplitude of the optical beam (ie, there is no absorption), the optical efficiency of these systems is higher than systems using conventional matched filters. By using more than one element, more than one degree of freedom can be influenced and an iterative technique can be used to force a desired response in the correlation plane for a given input.

Consider the architecture of the basic 4-f correlator shown in figure 1. An input signal incident from the left is filtered by the first element of the TC filter, F1, before it is transformed by the lens, L1. The second element of this TC pair, F2, lies in the Fourier plane. The filtered signal is then

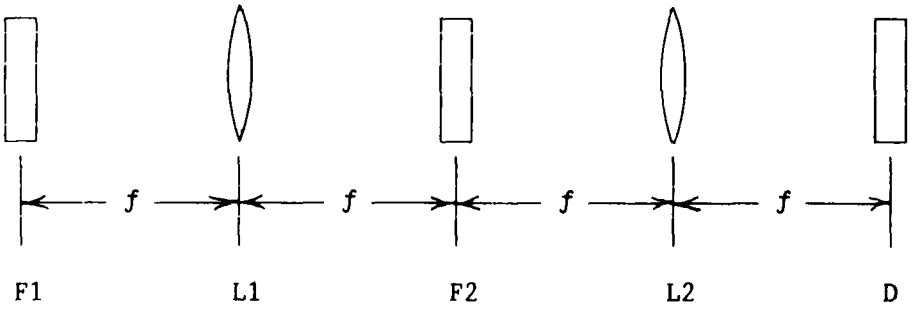

Figure 1. Placement of the elements of a simple tandem component filter in a 4-f correlator, after Bartelt [1].

retransformed by the second lens, L2, and the correlator output is detected by a CCD imager, D.

The basic algorithm to generate the elements of this implementation of the TC filters is summarized below:

1) Start with an arbitrary filter F1.

2) Calculate the Fourier transform of the product of the first filter element, F1, and the reference input image, I, $\mathcal{F}\{F1_{ij} \cdot I_{ij}\}$.

3) The expression calculated in step 2) is the signal which will be incident on F2. The desired functional form of the product of filter F2 and the signal is a plane wave (ie, the function which will produce a δ-function in the correlation plane). Thus, the function F2 can be calculated from

$$F2 = \frac{(1+0\cdot j)}{F\{F1\cdot I\}}$$

4) A further constraint is that the function F2 should be the matched filter of the input product F1·I,

$$F2 = [F\{F1\cdot I\}]^{*}$$

or, solving for F1,

$$F1 = \frac{F^{-1}\{F2^{*}\}}{I}$$

5) Calculate the correlation resulting from this pair of filters and repeat from step 2) as required.

PHASE INPUT, PHASE-ONLY FILTER

The TC filters discussed by Bartelt and Horner were constructed for input images which were amplitude modulated and then processed with two phase-only filtering elements. Consider a system in which the input image is phase rather than amplitude modulated: the product of the image and the first filter can now be realized by simply adding the filter to the image, pixel by pixel, before the input phase modulation.

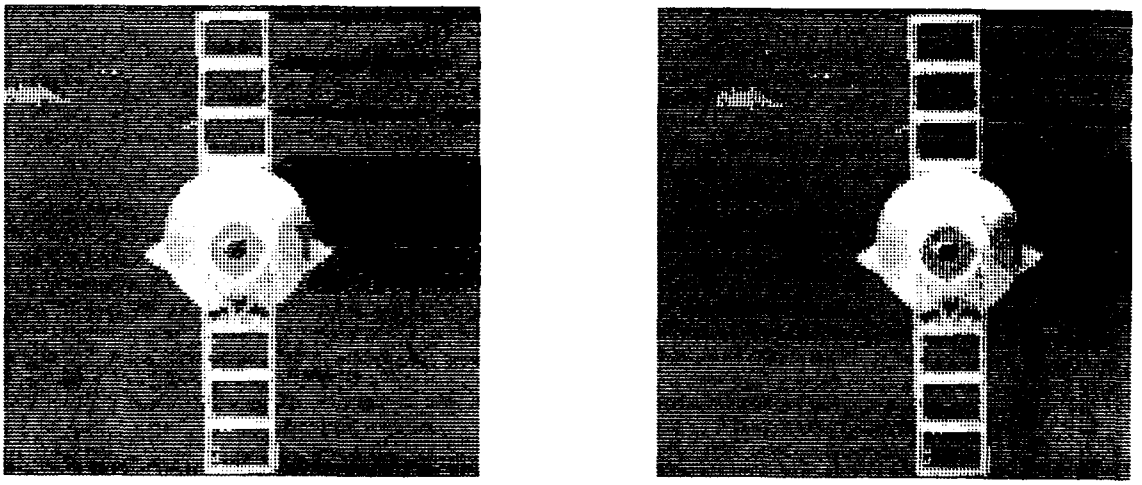

Figure 2. 2a) is the original input image and b) is the shifted image.

A TC filter was calculated for the input image shown in figure 2a, which is a frame-grabbed video image of a model spacecraft. Table 1 contains the computer simulated correlation results obtained from TC filters constructed with one to four iterations of the above algorithm. The units of the

correlation intensity are relative to an input intensity of 1 at each input pixel. The correlation peak is seen to rise rapidly for the first two filters, and more slowly for the rest. The next column shows the value of the second highest peak in the correlation plane, which decreases with filter iteration.

NUMBER OF ITERAT. USED IN FILTER	CORRELATION OUTPUT				DYNAMIC RANGE (Db)
	IMAGE INPUT		NULL INPUT		
	FIRST MAX	SECOND MAX	FIRST MAX	SECOND MAX	
1	6478	25.0	2069	25.2	5.0
2	14365	1.9	9876	25.6	1.6
3	15532	0.6	11054	21.2	1.5
4	15855	0.4	11423	18.8	1.4

Table 1. Correlator results of tandem component filters calculated for the input image shown in figure 2a.

Because the total light intensity in the input image is always the same for phase-encoded input systems, large background offsets are usually predicted in the correlation plane. For this reason, null images (complex input image pixel values all equal to [1,0]) were input to the correlator as a check of the system's dynamic range ($10 \cdot \log\{[\text{max response}]/[\text{null image response}]\}$). The correlation results (columns 4 & 5) and the dynamic range (column 6) are shown in table 1.

The correlation intensity output of the second tandem component filter is a little over an order of magnitude greater than a continuous phase-only filter. The gains in intensity of further iterations would not seem to be justified by the corresponding loss of dynamic range. Thus, the second TC filter pair was used in the correlation simulations below.

TRANSLATION INVARIANCE

Since part of the filter is incorporated into the input image, the TC filter is space-variant. If, however, the input plane filter is moved with an object, translation invariance should be maintained. The use of electrically addressable SLM easily accommodates the shifting of the first filter before it is combined with the input image.

To illustrate this point, the input image was shifted (using the computer) 16 pixels to the right (figure 2b) and the correlation was calculated using the TC filters constructed from the original image. The peak value in the correlation plane dropped to 8885, or 2.1 dB (Note that the correlation intensity for the offset image is less than that for the null input image). The first filter element, F1, was then shifted to the right one pixel at a time and the correlation recalculated. Of course, the second filter component, F2, was not shifted. The results are shown in figure 3. As expected, when F1 is shifted 16 pixels to the right, a value close to the original correlation is again obtained.

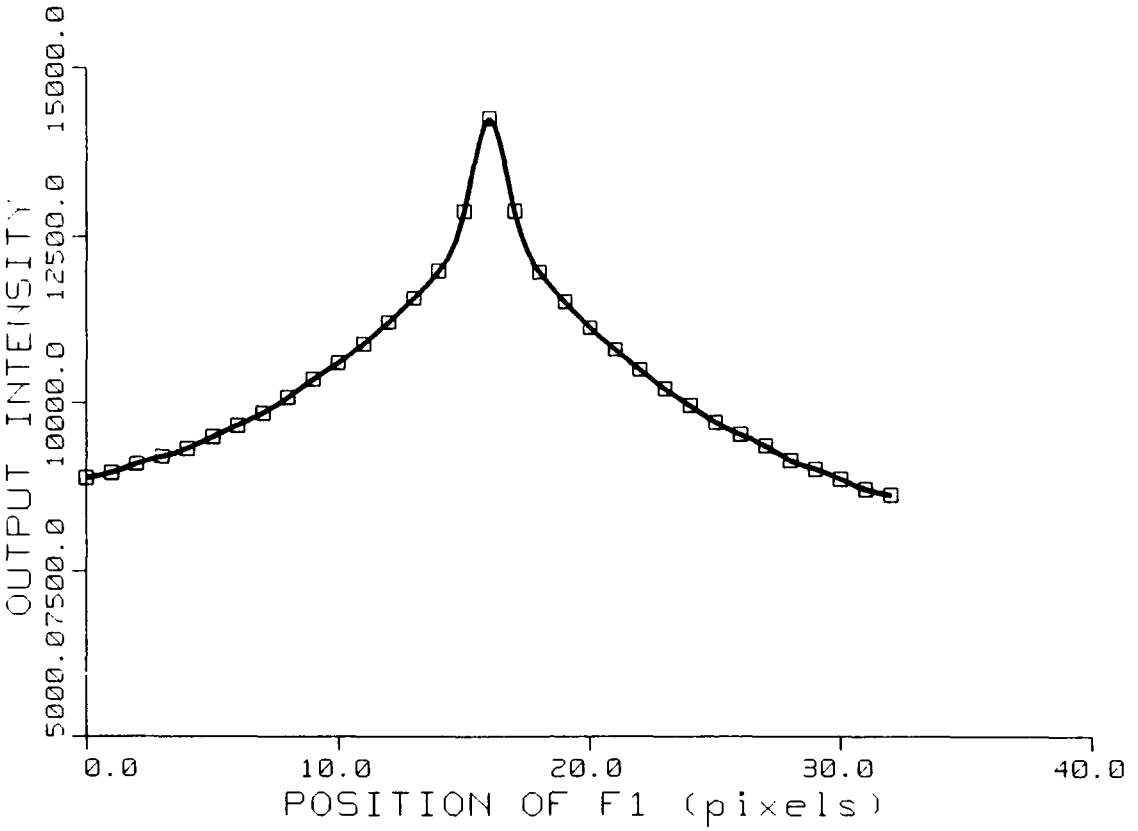

Figure 3. Calculated correlation output for shifted positions of F1.

CONCLUSIONS

The higher optical output intensity provided by the tandem component filter may be applicable to a phase-encoded, phase-filtered correlation system. The lack of spatial invariance can be overcome by using a simple shift of the first of the filter pair.

ACKNOWLEDGMENTS

This work was done in cooperation with the National Aeronautics and Space Administration at the Johnson Space Center and the U. S. Army Missile Command at the Redstone Arsenal. NASA's and MICOM's technical and financial support is gratefully acknowledged.

REFERENCES

1. Bartelt, H., 1984. Computer-generated holographic component with optimum light efficiency, **Applied Optics 23**, 1499-1502.

2. Bartelt, Hartmut and Joseph Horner, 1985. Improving binary phase correlation filters using iterative techniques, **Applied Optics 24**, 2894-2897.

3. Bartelt, Hartmut O., 1985. Applications of the tandem component: an element with optimum light efficiency, **Applied Optics 24**, 3811-3816.

OPTICAL CORRELATION WITH A CROSS-COUPLED SPATIAL LIGHT MODULATOR

Richard D. Juday
NASA Johnson Space Center
Tracking and Communications Division
Houston, Texas 77089

ABSTRACT

In correlation filtering a spatial light modulator (SLM) is usually modeled as affecting only the phase or only the amplitude of light. Usually it is a one-parameter combination of phase and amplitude that correctly describes the action. We develop an integral equation as a necessary condition that includes the phase and amplitude cross-coupling while optimizing a correlation filter. The phase-only filter is shown as a special case. A technique for solving the integral equation is outlined for a phase-mostly SLM.

INTRODUCTION

There are programmable continuously variable spatial light modulators (SLMs) that are driven by a single parameter (voltage or charge in electrically addressed SLMs, intensity in light-addressed SLMs). Hughes' liquid crystal light valve (LCLV) is an example of the light-addressed variety, Texas Instruments' deformable mirror device (DMD) is an electrically-addressed SLM. An SLM affects both phase and amplitude to varying degree. The cross-coupling between phase and amplitude may be adjusted during the manufacture of the device, or in the details of how it is inserted into the stream of the correlation. But given that the SLM is controlled through a single parameter, one cannot achieve any arbitrary combination of phase and amplitude. Once an SLM is installed in a correlator, the cross-coupling is not usually adjustable, and there is never pixel-by-pixel independence of the cross-coupling. Most previous work in simulating correlations has not included an SLM's cross-coupling between phase and amplitude, and none known to this author has explicitly included the cross-coupling while optimizing the filter. In this paper we develop the formulation for explicit inclusion of the (presumed known) cross-coupling while creating an optimum correlation filter. The results are dependent on the cross-coupling, whose modeling can be varied to seek an optimum combination of cross-coupling and filter signal for the cases in which the cross-coupling can be adjusted.

FORMULATION OF THE SOLUTION

Suppose we wish to filter a signal to recognize the presence of a reference pattern $x(t)$ whose transform is $X(w)$.

$$x(t) \quad \text{-->} \quad X(w) = A(w)\ e^{j\phi(w)}$$

by using a SLM constrained to the values

$$H(w) = f[s(w)]\ e^{jg[s(w)]}$$

in which $s(w)$ is the control value for the filter at frequency w , and $f(s)$ and $g(s)$ are respectively the modulator's resulting amplitude and phase. The problem is to determine the scalar function $s(w)$ for the filtering, if given $A(w)$, $\phi(w)$, and the functionals $f(\cdot)$ and $g(\cdot)$. The filtered signal presents the field E_s at the correlation plane.

$$E_s(t) = \int_{-\infty}^{\infty} e^{jwt}\ A(w)\ e^{j\phi(w)}\ f[s(w)]\ e^{jg[s(w)]}\ dw$$

Signal E_s is intensity-detected. Among many other possibilities, we take the criterion for choice of $s(w)$ that it shall maximize the central intensity, I_s .

We can develop *necessary conditions* for $s(w)$ by variational calculus. A necessary condition for maximum central intensity is that the variation in I_s be zero. Since the correlation plane detection is insensitive to phase, we can permit E_s to vary in phase.

For any value of the SLM control value s , there is a real value of the expression

$$g(s) + \text{Arg}\ \{\ [\frac{\partial f(s)}{\partial s} + j\ f(s)\ \frac{\partial g(s)}{\partial s}]\ \}\ =:\ a(s)$$

which we shall call the ancillary phase of the SLM. The ancillary phase is the analogue of the phase produced in a phase-only SLM, including additionally the amplitude variation of the cross-coupled SLM as it affects the correlation process. As earlier, a practical SLM will have an invertible ancillary phase (within modulo 2π). We denote the inverse of $a(\cdot)$ by $p(\cdot)$.

For a stationary value of E_s , then, a necessary condition is that

$$\phi(w) + a[s(w)] = \theta$$

and the constant, θ , is converted to the control signal by

$$s(w) = p\ [\ \theta - \phi(w)\ ]$$

Further, though, the constant must satisfy the integral equation now shown with its full frequency dependence:

$$\int_{-\infty}^{\infty} A(w)\ e^{j[\phi(w)+g\{p[\theta-\phi(w)]\}]}\ f\{p[\theta-\phi(w)]\}\ dw \;=\; \frac{1}{j}\ D\ e^{j\theta}$$

where the only condition on D is that it be real. This is the integral equation to be solved for the constant θ to produce the optimum correlation with the pattern whose transform is $A(w)\ \exp\ [j\ \phi(w)]$.

RELATIONSHIP TO THE PHASE-ONLY FILTER

We can easily particularize this result for the POF by letting $f \equiv 1$.

$$\text{Arg}\ \{\ [\frac{\partial f(s)}{\partial s} + j\ f(s)\ \frac{\partial g(s)}{\partial s}]\ \} \;=\; \pi/2$$

inasmuch as $f(\cdot)$ and $g(\cdot)$ are real. Continuing,

$$\phi + g(s) + \pi/2 \;=\; \theta$$

$$g(s) \;=\; \theta - \phi - \pi/2$$

$$E_s = \int_{-\infty}^{\infty} A\ e^{j\phi}\ e^{j(\theta\ -\ \phi\ -\ \pi/2)}\ dw$$

$$E_s = \frac{1}{j}\ e^{j\theta} \int_{-\infty}^{\infty} A\ dw$$

and we identify D with the integral of the amplitude, a real quantity as required. The integral equation is satisfied by <u>any</u> value of θ, a well-known result. The POF cancels the phase of the transformed reference image if that image occurs, centered, in the input plane. Any value for θ will do, since adding a constant phase at the filtering plane has no effect on the intensity-detected correlation. Note also that the amplitude of the reference image's spectrum does not enter the formulation for the POF, consistent with the POF's inability to alter amplitude.

A distinction between the optimum filter realized in a coupled SLM and in a phase-only SLM is apparent in the integral equation for the coupled SLM. In the coupled SLM the amplitude spectrum of the reference image's transform enters explicitly. If the phase of the coupled filter is changed by a uniform amount, the correlation strength can be affected. Such is not the case for the phase-only filter.

DISCUSSION

Though not carried through to completion here, the optimization of the constrained filter in the presence of noise would be done by considering the relative spectral dependences of noise and signal, with the solution of s chosen to give a large value of $f[s(w)]$ where signal amplitude is relatively large compared with noise, and conversely. In further work we will carry noise considerations further.

We explicitly assumed knowledge of the amplitude response $f(s)$ and the phase response $g(s)$ as functions of the control signal s. We require those functions' derivatives as well. (As a result this method does not readily extend to binary SLMs.) Knowing a function to high accuracy, though, does not guarantee knowledge of its derivative to equivalent accuracy. Direct measurement of the derivatives, as opposed to inference from the form of the functions themselves, is a difficult task. No SLM is known to the author to have been so completely characterized. If an optimum control value can be determined for a set of arbitrary reference signals, it may be possible to infer the derivatives by beginning with the direct measurements of $f(s)$ and $g(s)$. Thus this method could become a tool in the characterization of SLMs.

CONCLUSIONS

We have developed the necessary condition for one criterion of optimizing an optical correlation filter realized with a one-parameter coupled phase and amplitude SLM filter. The optimum filter explicitly involves the amplitude spectrum of the pattern to be recognized. Details of the solution vary strongly with the form of the coupling. The phase-only filter is a special case. We have outlined an iterative solution for the filter, and we have indicated areas for further research on coupled filters optimized for signal-to-noise performance.

Andersson, P.O. — ThA2
Armitage D. — WA2
Ashley, Paul R. — WA5
Asthana, P. — WE1
Athale, Ravindra A. — ThC4
Aull, Brian F. — ThA3

Barbier, E. — ThA4
Bernstein, Mark S. — ThC1
Boughton, R. Scott — WB2
Brinker, W. — ThE2
Burke, Barry E. — ThA3

Casasent, David P. — FA
Caulfield, H. John — ThE15
Chao, Tien-Hsin — WA, WB4, ThD1
Cheng, Li-Jen — WC2
Chiou, Arthur E. — FA1
Chipman, R. — ThE16
Clark, Noel A. — ThD3
Coldren, L. A. — ThA2
Collings, N. — ThD2
Collins, Dean R. — ThB1
Crossland, W. A. — ThD2

Dasgupta, S. — ThC2, ThC3
Davis, Jack H. — WA5
Davis, Jeffrey — ThD
Delboulbe, A. — ThA4
Dellenback, Paul A. — FA3

Eades, W. D. — WA2
Efron, Uzi — WA1, WB1
El-Sherif, Mahmoud A. — ThE14
Eng, S. T. — ThA2
Esener, Sadik C. — ThC2, ThC3, ThC4

Fainman, Yeshaiahu — WC1
Faller, Calton S. — ThE3
Farber, Ira — WA3
Fisher, Arthur D. — WD2
Fisli, Tibor — ThC1
Fiannery, David — FA4
Florence, James M. — ThB1
Ford, Joseph E. — WC1
Fromont, C. — ThA4
Fronek, Donald K. — ThE3

Gately, Michael T. — ThB1
Gerhard-Multhaupt, R. — ThE2
Gheen, Gregory — WC2
Giles, C. Lee — ThC
Glaser, I. — ThE12
Goodhue, William D. — ThA3
Goodwin, N. W. — WA1
Gossard, A. C. — ThA2
Gregory, Don A. — ThB3, ThE11
Grunthaner, F. J. — ThA2
Guilfoyle, P. S. — ThE9, ThE10

Hancock, B. R. — ThA2
Handschy, Mark A. — ThD3
Hara, T. — WD3
Hecht, David L. — ThC1
Hill, Robert E. — ThE3
Hirleman, E. Dan — FA3
Hirsch, Peter W. — WA3
Hirtz, J. P. — ThA4
Holtz, P.O. — ThA2
Hong, John — WB2
Hornbeck, Larry J. — ThB2
Horner, Joseph L. — ThE5
Huignard, J. P. — ThA4

Iannelli, J. M. — ThA2

Jannson, Tomasz — WD1
Javidi, B. — ThE13, FB2
Johnson, Kristina M. — WE2
Johnson, R. V. — WE1
Juday, Richard D. — FB4
Jutamulia, S. — ThE11

Kaminski, Joseph W. — ThC1
Khoo, Iam-choon — ThD5
Khoshnevisan, Monte — FA1
Kirsch, James C. — ThB3
Kuhlow, B. — ThB4
Kuo, C. J. — FB2
Kyriakakis, C. — WE1

Lane, Richard A. — ThE3
Law, K.-K. — ThA2
Lee, John N. — WD2, ThE7
Lee, Sing H. — WC1, ThC2, ThC3, ThC4
Lehmen, A. von — FA2
Li, X. — ThE11
Lin, Shih-Chun — WB2
Lin, Shing-Hong — WD1, ThE1
Lin, T. H. — ThC2, ThC3
Liu, Hua-Kuang — WB4, ThD1, ThE
Liu, Tsuen-Hsi — WC2
Loomis, John — FA4
Ludwig, Lester F. — ThE4

Mahler, G. — ThB4
Marrakchi, Abdellatif — WC3
Maserjian, J. — ThA2
McKnight, Douglas J. — ThD4
Merz, J. L. — ThA2
Miceli, William — ThA
Milkovitch, Mary — FA4
Molzow, W.-D. — ThE2
Monroe, Stanley Jr. — FB3

Neff, John A. — WE1
Neil, Mark A. A. — ThE8
Nelson, William E. — ThB2
Nichols, Kirby B. — ThA3

Odeh, S. F. — ThE13, FB2
Oh, Tae-Kwan — WA5, ThE7

Paek, Eung Gi — FA2
Pagano-Stauffer, Laura A. — ThD3
Pape, Dennis R. — ThE6
Patel, J. S. — WB3
Penz, P. Andrew — ThB1
Pocholle, J. P. ThA4
Psaltis, Demetri — WE

Raffy, J. — ThA4
Reichman, Joe — WB2
Reif, P. G. — WA1
Rolsma, Peter B. — ThE7
Roosen, G. — WC4
Rouse, I. D. — WA1

Sampsell, Jeffrey B. — ThB1
Sawchuk, A. A. — ThE12
Sayyah, K. — WA4
Schnell, J. P. — ThA4
Sillitto, R. M. — ThD4
Simes, R. J. — ThA2
Sokoloski, Martin — FB
Song, Q. W. — FB1
Soref, Richard A. — ThE5
Sprague, Robert A. — ThB, ThC1
Stanchina, W. E. — WA1
Steinmetz, David L. — ThC1
Suzuki, Y. — WD3, FB1

Tam, E. — ThE11
Tanguay, Armand R. Jr. — WE3
Tepe, R. — ThB4, ThE2
Thackara, J. I. — WA2
Turner, William D. — ThC1

Vaerewyck, Janine M. — ThE15
Vass, D. G. — ThD2, ThD4

Walpita, L. M. — ThA1
Wang, J. H. — ThC2, ThC3
Warde, Cardinal — WA3, WD
Welkowsky, M. S. — WA1, WA4
Wheeler, E. R. — ThE9, ThE10
White, Ian H. — ThE8
Wu, M. — FB1
Wu, M. H. — WD3
Wu, Shin-Tson — WA1, WB1
Wu, W. Y. — WA1

Yeh, Pochi — WC, FA1
Yu, Francis T. S. — WB, ThE11, FB1

Zeise, F. F. — ThE9, ThE10